LANCASTER UNIVERSITY

The use of Small Neutron Detector Arrays for the Assessment of Nuclear Materials Comprising ^{235}U, ^{238}U and ^{240}Pu

Author:
Helen Maria O'DONNELL
BEng, MSc

Supervisor:
Prof. Malcolm J. JOYCE

A thesis submitted in partial fulfilment of the requirements

for the degree of Doctor of Philosophy

in the

Department of Engineering

June 16, 2020

Declaration of Authorship

I, Helen Maria O'DONNELL *BEng, MSc*, declare that this thesis titled, "The use of Small Neutron Detector Arrays for the Assessment of Nuclear Materials Comprising ^{235}U, ^{238}U and ^{240}Pu" and the work presented in it are my own. I confirm that:

- This work was done wholly or mainly while in candidature for a research degree at this University.

- No parts of this thesis have previously been submitted for a degree or any other qualification at this University or any other institution.

- Where I have consulted the published work of others, this is always clearly attributed.

- Where I have quoted from the work of others, the source is always given. With the exception of such quotations, this thesis is entirely my own work.

- I have acknowledged all main sources of help.

- Where the thesis is based on work done by myself jointly with others, I have made clear exactly what was done by others and what I have contributed myself.

Signed:
_____

Date:
_____

Abstract

Neutron metrology has important applications in areas such as nuclear safeguards, quality assurance, and nuclear power operations. To date, the most common detectors for performing neutron metrology have been ^{3}He detectors. With ^{3}He production in decline, it has become supply-constrained and alternatives are being sought as potential replacements. Liquid organic scintillation detectors are an option, and in particular the relatively recent development of EJ-309 liquid scintillant is a forerunner for the replacement of ^{3}He. This thesis is a study of the appropriateness of small arrays of organic liquid scintillation detectors for the characterisation of ^{235}U, ^{238}U, and ^{240}Pu using total-neutron-counting and coincidence counting during active and passive assessments. Constraints of the equipment and methods are also reported.

To do this, five studies have been carried out with a number of cubic EJ-309 detectors; comprising a combination of experimental investigations and MCNP simulations. They have assessed: optimal detector geometries; the use of a neutron shielding cube for measurements of forensic-style samples; an investigation into the applicability of the detectors for total-neutron-counting during the active assay of a broad-range of ^{235}U enrichments; the measurement of total-neutron-count of spontaneous fission neutrons from ^{238}U and a proof-of-concept of a plutonium-contaminated material drum monitor using coincidence counting. The neutron shielding cube and broad-range of ^{235}U experiments suggest that the EJ-309 detectors are suitable for measuring small samples of ^{235}U actively using total-neutron-count. The investigations into measuring the ultra-low-level emission of spontaneous fission neutrons from ^{238}U, and the assessment of 1 mg of PuO_2/PuF_4 in a 200 litre drum, are evidence of the system's ability to measure particularly small neutron fluxes, in total-neutron-counting-mode and coincidence-mode. The detectors performed well in all investigations when the length of time of assay was chosen appropriately. In most tests, the EJ-309 detectors outperform comparable ^{3}He detector-based systems, due to their ability to detect fast neutrons directly. The lack of efficiency of the detectors below 0.5 MeV does discount them for thermal neutron detection.

Acknowledgements

Contents

List of Figures

List of Tables

List of Abbreviations

CCFE	Culham Centre for Fusion Energy
CPS	Counts Per Second
DC	Direct Current
DLM	Detection Limit Mass
DU	Depleted Uranium
EC	Electron Capture
ENDF	Evaluated Nuclear Data File
EPSRC	Engineering and Physical Sciences Research Council
FPGA	Field Programmable Gate Array
FWHM	Full Width Half Maximum
GUI	Graphical User Interface
HDPE	High Density Poly Ethylene
HEU	High Enriched Uranium
HV	High Voltage
IAEA	International Atomic Energy Agency
ILW	Intermediate Level Waste
LANL	Los Alamos Nuclear Laboratory
LEU	Low Enriched Uranium
LLW	Low Level Waste
LS-UNCL	Liquid Scintillator Uranium Neutron Counting coLlar
LOCA	Loss Of Coolant Accident
MCA	Multi Channel Analyser
MCNP	Monte Carlo Neutron Particle code

MFA	Mixed Field Analyser
NNPT	Nuclear Non Proliferation Treaty
NPL	Naional Physical Laboratory
ONR	Office for Nuclear Regulation
ORNL	Oak Ridge National Laboratory
PCM	Plutonium Contaminated Material
PFNS	Prompt Fission Neutron Spectrum
PGA	Pulse Gradient Analysis
PHS	Pulse Height Spectra
PMT	Photo Multiplier Tube
PSC	Pajarito Scientific Corporation
PSD	Pulse Shape Discrimination
PWR	Pressurised Water Reactor
QA	Quality Assurance
SF	Spontaneous Fission
SFM	Special Fissionable Material
SNS	Spallation Neutron Source
TOF	Time Of Flight
TTL	Transistor Transistor Logic
UNCL	Uranium Neutron Counting coLlar
UV	Ultra Violet
VLLW	Very Low Level Waste
WGPu	Weapons Grade Plutonium

Dedicated to my Parents . . .

1 Introduction

The detection of neutrons has predominantly been done with ^{3}He detectors (Runkle, Chichester, and Thompson, 2012). With the supply of ^{3}He becoming increasingly constrained, alternative methods are sought to replace the current fleet of ^{3}He detectors (Pickrell, M. M. et al., 2013). One possible solution for a replacement is the organic liquid scintillation detector (Enqvist et al., 2013; Tomanin et al., 2014; Pino et al., 2014). The research reported in this thesis is a study on the appropriateness of organic liquid scintillation detectors for use in a number of uranium and plutonium characterisation scenarios. It compliments topical research published recently in (Pozzi et al., 2019), and is particularly relevant given the recent development in stabilised forms of plastic scintillation detectors.

A suite of non-destructive assessments of nuclear material has been undertaken, for which scintillation detectors appear to have a number of benefits over ^{3}He detectors. Firstly, the ability to detect fast neutrons directly without thermalisation, provides the user with information about the spectrum, and can make the detectors less bulky than equivalent ^{3}He detectors (Enqvist et al., 2012). Secondly, organic scintillation detectors are effectively blind to low energy neutrons, thus removing the effects of thermal neutrons, and reducing uncertainty for active measurements (Dolan et al., 2014). Thirdly, their nano-second-scale time resolution, affords the user a much narrower gate for coincident neutron measurements, again reducing uncertainty. This is particularly apparent in scenarios with large uncorrelated neutron fluxes, such as (α, n) neutrons (Hamel et al., 2017) and large ambient background cases. For a number of years, scintillation detectors were deemed too hazardous for many industrial environments due to their low flash point; for EJ-301 liquid it is a mere $26°$ C. The advent of EJ-309 liquid has reduced the issue of flashpoints, with an increase up to $144°$ C, making the technology safe to be

utilised in more places than before.

Detecting neutrons is important because of their properties in comparison to other forms of radiation. Unlike γ rays, they are not attenuated very significantly by high-Z materials and metals and, as such, they are useful particles for probing nuclear materials and their containers. This property can be exploited in a variety of applications such as safeguards (Tagziria et al., 2012; Chichester and Seabury, 2009), quality assurance (Lousteau et al., 2018), waste assay (Davidson and Martin, 1993; Aryaeinejad et al., 1996; Raoux et al., 2003; Ohzu et al., 2016), environmental monitoring (Nakamura, Kosako, and Iwai, 1984; Kim et al., 2011; Jha et al., 2016), forensics (Jallu et al., 2011; Osborn et al., 2018), and the investigation of nuclear power accidents (Gromov et al., 1993; Grosse et al., 2013).

Since special fissionable material (SFM) has the potential to cause serious disasters, and to be particularly detrimental to health (Ojovan and Lee, 2005), strict controls are in place over its whereabouts and usage, known as safeguards. The nuclear non-proliferation treaty (NNPT) was devised and accepted internationally to safeguard nuclear material and to prevent its misuse (UN, 1968). Neutrons can be utilised in safeguards for processes such as characterising fuel (Dolan et al., 2014), identifying defects (Hausladen, 2013; Lee et al., 2001), verifying warheads (Göttsche and Kirchner, 2014), verifying UF_6 cylinder heels (Kiff et al., 2013), and for detecting illicit transport or storage of nuclear materials (International Atomic Energy Agency, 2002; Slaughter et al., 2003; Valkovic et al., 2016).

Quality assurance within the nuclear sector is paramount in avoiding nuclear accidents and maintaining high levels of reliability in nuclear reactors. Neutrons can be used to measure uranium enrichment (Lousteau et al., 2018) and to assess inclusions of foreign bodies and homogeneity of fresh fuel (Tremsin et al., 2013; Panakkal, Ghosh, and Roy, 1992; Lehmann, Vontobel, and Hermann, 2003). They can also be used to detect fuel plug failures in spent fuel. And in order to increase reactor efficiency, as well as fuel lifetime, neutrons can be used to assess spent fuel burn-up (Prokopowicz and Pytel, 2016; Sim et al., 2013).

Chapter 2 presents the scientific background to the research in this thesis. The concepts of nuclear enrichment and radiation are introduced. Specific types of radiation are discussed, including the neutron, as well as related methods of detection.

Chapter 3 describes the equipment, methods and techniques employed in this research. Detectors, analysers, data acquisition and ancillary equipment are all presented. The simulation software, Monte-Carlo neutron particle tracking code (MCNP) is introduced, along with a brief overview of how it works and has been utilised.

The assessment of ^{235}U is covered in chapter 4. Three experiments are introduced, and discussed. The first is an optimisation study of the most likely EJ-309 detector geometries. The second item presented is an investigation of the efficacy of a neutron reflector cube placed around an active neutron measurement of various enrichments of UO_2. Thirdly, a broad-range of U_3O_8 enrichments from 0.03166 % to 93.1 % have been measured actively and compared using three detector geometries.

Design, methods, results and analysis of two further experiments are also included in this thesis. A passive measurement of the neutron emission of ^{238}U is presented in chapter 5. The ultra-low-level neutron emission was measured for masses of 0.3 % wt. depleted uranium up to 16.45 g. Chapter 6 introduces a passive neutron measurement system for investigating waste drums containing ^{240}Pu.

Finally, conclusions pertaining to the entire experimental suite are included in chapter 7. This chapter also includes discussion about potential applications of the methods presented in this thesis, as well as further work required to bring the techniques to fruition in real-world scenarios.

1.1 Aims

The aim of the research presented in this thesis is to prove the ability of a modular organic liquid scintillation neutron detection system for use in neutron measurements of materials containing the radioactive isotopes ^{235}U, ^{238}U and ^{240}Pu. Using just one set of portable equipment for measurements of neutrons from these isotopes, is hoped to

provide a suitable basis from which to apply the techniques described in applications where ^{3}He is currently deployed. In particular, the system should be able to:

- Count neutrons accurately in singles-counting and coincidence-counting modes

- Detect neutrons in high background environments

- Detect ultra-low-level neutron fluxes

- To significantly reduce the cost of accurate NDA measurement of fissile materials in (solid) orphan wastes/residues, and high [alpha, neutron] materials such as PuF$_4$ that has traditionally been extremely difficult and expensive to characterise

1.2 Publications

The research included in this thesis has led to a number of scientific papers and conference proceedings. Spin-out research, not fitting the remit of this thesis, was also carried out and details of the full list of publications is included below. Items of particular interest, that do not fit within this thesis, are a review paper covering all aspects of imaging nuclear fuel using ionising radiation, and more recently, the design, build, and test of a neutron back-scattering measurement rig to assess oil-pipeline wall thickness. A paper covering this research was recently accepted into Nature's *Scientific Reports*.

1.2.1 Peer-Reviewed Journal Articles

- M. Licata, M. D. Aspinall, M. Bandala, F. D. Cave, S. Conway, D. Gerta, **H. M. O. Parker**, N. J. Roberts, G. C. Taylor and M. J. Joyce, *Depicting corrosion-born defects in pipelines with combined neutron/γ-ray backscatter: a biomimetic approach.* Sci Rep 10, 1486 (2020). `DOI: https://doi.org/10.1038/s41598-020-58122-3` [I.F. 4.525] (Licata et al., 2020).

- **H. M. O. Parker**, J. S. Beaumont, and M. J. Joyce, *Passive, non-intrusive assay of depleted uranium.* Journal of Hazardous Materials 364 (2019) 293-299. `DOI: 10.1016/j.jhazmat.2018.08.018` [I.F. 6.64] (Parker, Beaumont, and Joyce, 2019).

- M. D. Aspinall, M. J. Joyce, A. Lavietes, R. Plenteda, F. D. Cave, **H. M. O. Parker**, A. Jones, and V. Astromskas, *Real-Time Capabilities of a Digital Analyzer for Mixed-Field Assay Using Scintillation Detectors.* IEEE Transactions on Nuclear Science 64 (2017) 945-950. DOI: 10.1109/TNS.2017.2654512 [I.F. 1.65] (Aspinall et al., 2017).

- **H. M. O. Parker**, M. D. Aspinall, A. Couture, F. D. Cave, C. Orr, B. Swinson, and M. J. Joyce, *Active fast neutron singles assay of ^{235}U enrichment in small samples of triuranium octoxide.* Progress in Nuclear Energy 93 (2016) 59-66. DOI: 10.1016/j.pnucene.2016.07.022 [I.F. 1.45] (Parker et al., 2016).

- **H. M. O. Parker** and M. J. Joyce, *The Use of Ionising Radiation to Image Nuclear Fuel: A Review.* Progress in Nuclear Energy 85 (2015) 297-318. DOI: 10.1016/j.pnucene.2015.06.006 [I.F. 1.45] (Parker and Joyce, 2015).

1.2.2 International Conference Proceedings

- M. Licata, **H. M. O. Parker**, M. D. Aspinall, M. S. Bandala, F. D. Cave, S. Conway, D. Gerta, M. J. Joyce, *Fast neutron and γ-ray backscatter radiography for the characterisation of corrosion-born defects in oil pipelines.* (2019) 6th International Conference on Advancements in Nuclear Instrumentation Measurement Methods and their Applications (ANIMMA).

- **H. M. O. Parker**, M. Licata, M. D. Aspinall, F. D. Cave, and M. J. Joyce, *Characterizing corrosion-born defects in oil pipelines using fast-neutron elastic scattering.* (2018) IEEE nuclear Science Symposium and Medical Imaging Conference. Conference record submitted.

- **H. M. O. Parker**, A. Jones, and M. J. Joyce, *Counting neutrons from the spontaneous fission of ^{238}U using scintillation detectors and mixed field analysers.* (2015) 4th International Conference on Advancements in Nuclear Instrumentation Measurement Methods and their Applications (ANIMMA) DOI: 10.1109/ANIMMA.2015.7465617.

2 Background

Nuclear materials are broadly understood to comprise at least one of the elements uranium, plutonium or thorium. Isotopes of these elements are often either fissile, fertile, fissionable or capable of spontaneous fission. These elements come from the actinides range of the periodic table that extends from actinium (atomic number 89) to lawrencium (atomic number 103). Fissile isotopes can sustain a nuclear chain reaction with incident neutrons of thermal energy. Fertile isotopes can be transmuted (transformed) into fissile materials with the bombardment of neutrons, usually inside a reactor core. Fissionable isotopes can only be made to fission when interacting with high-energy (fast) neutrons (OU, 2019). Special fissionable material (SFM) is more definitively understood to comprise plutonium-239, uranium-233 and uranium enriched in isotopes 235 (IAEA, 2002). SFM does not refer to source material, which is uranium containing the proportion of isotopes occurring in nature. SFM is to be accounted for by any IAEA member state that may be in ownership or guardianship of such material, also known as safeguarding. In the UK, safeguarding is overseen by the Office for Nuclear Regulation (ONR), as part of the Euratom treaty (Louka, 2011). Elsewhere, internationally, safeguarding is under the jurisdiction of the International Atomic Energy Agency (IAEA).

2.1 Enrichment

Enrichment of material refers to a process whereby a particular isotope's percentage of composition (usually uranium-235) is increased with respect to the other isotopic components of the material. For example, natural uranium is abundant on earth in the following isotopic percentages: ^{234}U at 0.0057$\pm$0.0002 %, ^{235}U at 0.7204$\pm$0.0007 %,

and ^{238}U at 99.2739$\pm$0.0007 % wt. (Lounsbury, 1956), and when uranium is described as enriched, it simply means that the percentage of uranium-235 has been artificially increased. Uranium is enriched using a gas centrifuge, whereby UF$_6$ at natural abundances is spun and the mass of the uranium isotopes determines whether the compound is more or less affected by the centripetal force. This results in a layer of heavier ^{238}UF$_6$ at the bottom of the centrifuge tube, ^{235}UF$_6$ in the middle and lighter ^{234}UF$_6$ on top (ignoring trace amounts of ^{233}UF$_6$). These layers can then be harvested and recombined into the enrichment desired; for nuclear reactor fuel the enrichments are usually between 3-4 % wt. ^{235}U (Yue et al., 2016).

2.2 Radiation

Radioactivity is a descriptor relating to the propensity to radioactive decay of a material comprising unstable atomic nuclei. This decay also results in the loss of energy from the atom, usually in the form of an elementary particle or alpha (α) particle from the nucleus. Elementary particles include beta (β), gamma photon (γ-ray), and neutron (n). Radiation from electron shells includes Auger electrons and X-rays. A full history of the discovery and characterisation of radioactivity can be found in (L'Annunziata, 2007). Radioactivity is measured in becquerels (Bq), where one becquerel corresponds to one nuclear decay per second. Therefore the number of becquerels a material is measured to have, denotes the average amount of decays per second that that material is undergoing.

The following descriptions of the different types of radiation listed above, are all adapted from (L'Annunziata, 2012). Alpha particles are simply helium nuclei, comprised of two neutrons and two protons. As they are relatively heavy, and highly charged, they are highly ionising, and thus have a low penetrability in matter. For example, a 5.5 MeV alpha particle will be halted in less than 5 cm of air, acquiring two electrons through coulombic attraction and being converted to helium. Alpha particles are often high energy, with for example, a ^{241}Am decay resulting in a 5.638 MeV alpha particle. Beta decay describes any nuclear decay process when the mass number of the

nucleus (A) remains the same, but the atomic number (Z) changes. This may occur via three processes: electron emission (β^-), positron emission (β^+), or electron capture (EC). Electron emission is when a negative β particle, or a negative electron is emitted from a nucleus. It occurs due to there being a neutron imbalance in the nucleus, associated with an excess of neutrons. Tritium (^{3}H) decays by β^- emission, releasing a maximum of 0.0186 MeV of energy.

Positron emission occurs when a proton excess is present, in the form of an excess of protons in comparison to neutrons. The transformation of a proton to a neutron releases a positive electron (β^+). The energy required for this process must significantly exceed 1.02 MeV in order to surpass the energy barriers of both a β^-, and a β^+ required for the transformation. Electron capture (EC) is a mechanism that competes with positron emission. This process involves the nucleus gaining an electron to combine with a proton, thus creating a neutron. This mechanism predominates at energies below 1.02 MeV where positron emission cannot occur; usually for nuclides of higher atomic number. Finally either Auger electrons or X-ray photons are produced after an EC capture has occurred. The EC process leaves vacancies in electron shells. As electrons from higher shells drop into these vacancies they release energy as photons of X-radiation. This X-ray may escape the nucleus as radiation in its own right, or it may interact with an electron, transferring its energy and allowing the electron to break-free of its shell, being released as an Auger electron.

Gamma-ray photons and neutrons have been omitted from the previous paragraph as they constitute the largest proportion of radiation studied in this thesis, and will be discussed in more detail in the following sections. Both neutrons and γ rays are usually described by the energy they possess. This energy is denoted using the SI unit of electron volts (eV), where one eV is the amount of energy an electron has when accelerated by a potential difference of one volt. In real terms one eV is equal to 1.602×10^{-19} J.

2.3 Gamma-ray photons

Gamma-ray (γ-ray) photons are often perceived to be particles, however they have zero rest-mass (Harkness-Brennan, 2018). They are electromagnetic radiation photons, i.e., purely electromagnetic energy. They are identical to X-rays, other than that they originate in an atom's nucleus as opposed to its electron shells. They are produced when an excited nucleus; an isomer; transitions to a lower energy state, either directly or in a number of steps. They are released with discrete quantities of energy which correspond to the transition made by the isomer. Due to their lack of charge and rest-mass, they are generally more penetrating than either α or β radiation. However, they are increasingly likely to interact with matter of increasing Z-number due to the greater number of electrons present in the electron cloud, and the distance these electrons are from the nucleus. A γ ray has three methods of interaction with matter: the photoelectric effect, the Compton effect, and pair production. The photoelectric effect is a mechanism whereby the energy from a γ ray is entirely absorbed by an atom. This energy is transferred to an electron from the atom which is then released, resulting in an ion pair. The energy of the emitted electron is equal to the energy of the incoming γ-ray, minus the binding energy of the electron.

The Compton effect, also known as Compton scattering, involves a γ ray impacting upon an atomic orbital electron, being deflected and imparting a fraction of its energy with the orbital electron. The electron is ejected at an angle to the incident γ-ray. This interaction leads to the formation of an ion pair, with the deflected γ-ray continuing on its course and dissipating its energy via the host of interaction mechanisms discussed in this section. The ejected electron loses its energy through secondary ionisation. The angle of deflection of the γ-ray is a function of the energy imparted. A γ ray that is scattered back upon itself imparts the maximum energy, this is called the Compton edge.

Pair production is a mechanism by which energy from the γ-ray results in the creation of matter, and in particular an electron and a positron. This occurs when a photon

Descriptor	Energy range
Cold neutrons	<0.003 eV
Slow (thermal) neutrons	0.003 - 0.4 eV
Slow (epithermal) neutrons	0.4 - 100 eV
Intermediate neutrons	100 eV - 200 keV
Fast neutrons	200 keV - 10 MeV
High energy (relativistic) neutrons	>10 MeV

TABLE 2.1: Classification of neutrons based upon their energy, where energy is related to the speed of the particle using $E = \frac{1}{2}mv^2$, $1\ eV = 1.6 \times 10^{-19}$ J, and the mass of 1 neutron is equal to 1.67×10^{-27} kg. Here E is energy, m is mass, and v is speed. Adapted from (L'Annunziata, 2012).

interacts with the Coulomb field of a nucleus. It requires an initial γ-ray energy, or combined rest energy of an electron and positron, of at least 1.02 MeV, in order to provide enough energy to create the particles, as defined by Einstein's equation for the equivalence of mass and energy: $E = m_e c^2$. It occurs in nuclei bombarded with a γ-ray field, but may also be instigated when a nucleus emits a γ-ray with energy greater than 1.02 MeV; also known as internal pair production.

2.4 Neutrons

Neutrons have a mass of 1.009 amu (atomic mass unit), and, as the name suggests, they have a neutral charge. They were discovered by James Chadwick in 1932 (Chadwick, 1932), after being hypothesised by Chadwick's contemporary Ernest Rutherford over a decade earlier (Rutherford Ernest, 1920). They are often classified by the kinetic energy they possess, Table 2.1 provides an approximation of each category.

2.4.1 Passive Neutron Emission

Neutrons are emitted without intervention (passively) in (α, n) reactions or via spontaneous fission.

2.4.1.1 The (α, n) reaction

The (α, n) reaction predominates in low-Z materials, when an α particle combines with a low-Z atom giving one neutron and two protons to the atom and releasing one neutron as well as an amount of energy. The energy released Q, can be calculated by inferring Einstein's $E = mc^2$ equation: $Q = m_{reactants}c^2 - m_{products}c^2$. For example, the reaction between beryllium and an α particle releases 5.701 MeV of energy, with both the resulting neutron and the new atom having some fraction of this energy. As α decay is random, so too is the (α, n)-induced neutron emission. It can be described as *not time-correlated*.

2.4.1.2 Spontaneous Fission

Spontaneous fission (SF) is documented to be prevalent in 100 radionuclides (Magill and Galy, 2005, pg. 76). It is described as the non-induced splitting of a nucleus into fission fragments with the release of at least one neutron, and is depicted in Fig. 2.1. It occurs for radionuclides with atomic mass numbers greater than 230. These radionuclides often undergo both (α, n) and SF. Popular commercial SF sources include ^{252}Cf and ^{248}Cm. From a safeguarding perspective, SF is prevalent for even-numbered isotopes of Pu: ^{238}Pu, ^{240}Pu, and ^{242}Pu. Although these three isotopes decay primarily by α-emission, they still decay by SF at rates of 1100, 471 and 800 SF.s^{-1}.g^{-1} respectively. As fission neutrons from the same fission event are released at the same time, they are considered to be *time-correlated*.

2.4.2 Induced Neutron Emission

Neutrons can also be emitted in induced reactions such as induced fission, or spallation reactions. In induced fission reactions, a neutron impacts upon a nucleus causing that nucleus to become unstable. The nucleus then splits, usually into two fission fragments releasing at least one neutron. The released neutrons are often called prompt neutrons. These prompt neutrons may themselves go on to cause fission in other nuclei, such is the case for most human-made nuclear processes. This process is possible for almost all
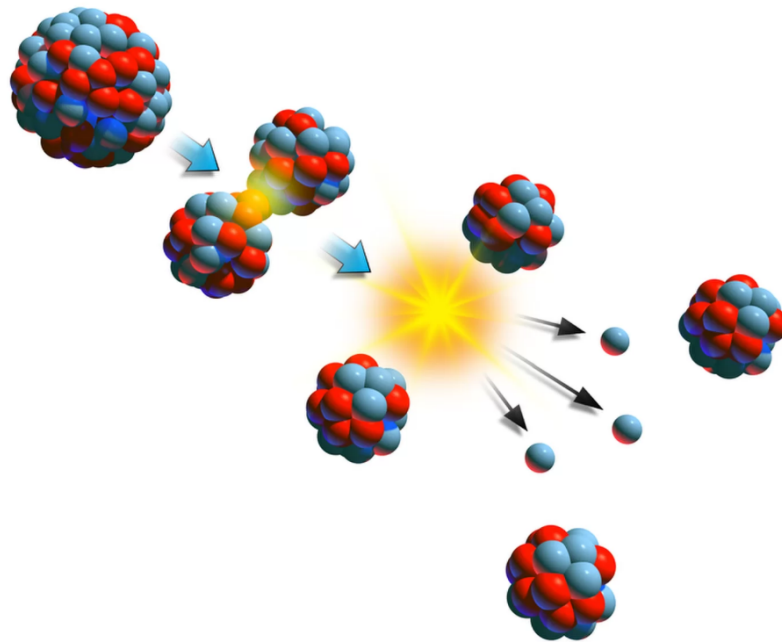
FIG. 2.1: Depiction of spontaneous fission (SF), when a nucleus splits spontaneously into two fission fragments releasing at least one neutron. Adapted from (Redd, September 19, and ET, 2012).

nuclei, however, nuclei with high fission neutron cross-sections are much more likely to undergo induced fission.

2.4.2.1 Spallation Reactions

Spallation neutrons are produced when a material is impacted upon on an atomic or nuclear scale. Often, proton beams are used as the projectile. Negative hydrogen ions are produced by a source and then accelerated in a linear accelerator up to speeds of 90% of the speed of light. The ions are then injected into an accumulator ring where they are initially stripped of their two electrons creating a positive hydrogen ion, a proton. As the protons complete loops of the accelerator ring they begin to bunch together. The proton lump is then ejected from the loop and delivered to a target. The Oak Ridge National Laboratory (ORNL) spallation neutron source (SNS) uses a target of liquid mercury, whilst the Los Alamos neutron science centre (LANSCE) SNS uses a

(A) $(^2H - {}^2H)$ reaction produc-   (B) $(^2H - {}^2H)$ reaction produc-   (C) $(^2H - {}^3H)$ reaction produc-
ing a neutron   ing a proton   ing a neutron
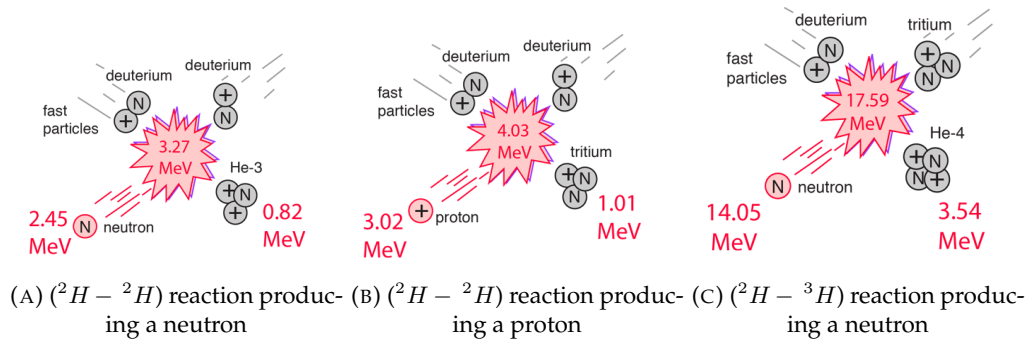
FIG. 2.2: Mechanisms for fusion reactions proposed for energy generation. Adapted from (Nave, 2019b).

tungsten target (Nowicki, Wender, and Mocko, 2017); the former creating between 20-30 neutrons when a high energy proton hits the nucleus of a mercury atom (Henderson et al., 2014). The neutrons produced in spallation are often very fast and may have to be moderated before use.

2.4.3 Fusion Reactions

Fusion reactions are those in which two smaller particles react together to form a larger particle and usually some other reaction products. Although they do not require any inducing particles, the mass of the resulting particle dictates whether the reaction is exothermic or endothermic. If the initial particles combine to create a nucleus with an atomic mass of less than 56, then the reaction is exothermic. For resulting masses of greater than 60, the reaction is endothermic. In terms of power generation it can be inferred that we are only interested in the former, exothermic reactions. In terms of nuclear power and energy production the deuterium-deuterium (^{2}H - ^{2}H), and deuterium-tritium (^{2}H - ^{3}H) reactions are most prevalent. The (^{2}H - ^{2}H) reaction has two possible outcomes, one releasing a ^{3}He atom, a neutron and 3.27 MeV of energy, and the other releasing a ^{3}H atom, a proton, and 4.03 MeV of energy. In the (^{2}H - ^{3}H) reaction, ^{4}He, one neutron and 17.59 MeV are released. Fig. 2.2 depicts these reactions. Fusion power generation is still a major area of research with the aim of harvesting an almost carbon free, highly-efficient source of energy (Verberck, 2016; Nian, 2018).

2.4.4 Neutron Cross-Sections

The term *neutron cross-section* (σ) refers to the probability of a nuclear interaction with an incoming neutron (Knoll, 1999). It is measured in *barns* with one barn being equal to 10^{-28} m^2. The *area* of the neutron cross-section is analogous to a target, and thus, the bigger the target, the more likely it will interact with an incoming neutron. The neutron cross-section for various interaction mechanisms with a ^{235}U nucleus is depicted in Fig. 2.3, here the actual geometric cross-sectional area is compared to the probabilistic areas for neutron interaction. Multiplying the neutron cross-section by the number of nuclei per unit volume of material (N) gives us the macroscopic cross-section: $\Sigma_{tot} = N\sigma$. Each neutron interaction mechanism has its own microscopic neutron cross-section, and these are summed to produce the total macroscopic cross-section (Σ_{tot}):

$$\Sigma_{tot} = \Sigma_{scatter} + \Sigma_{radcapture} + ... \tag{2.4.1}$$

Σ_{tot} is then the probability per unit path length that any type of interaction will occur. Fig. 2.4 depicts the elastic scattering cross-section, the (n, 2n) cross-section and the total cross section for both ^{2}H and ^{235}U. ^{2}H and ^{235}U have been chosen because they are common isotopes that are used in neutron interactions. Fig. 2.4-(A) shows that ^{2}H has no fission cross-section, and for elastic scattering the cross-section increases exponentially as incident neutron energy decreases. For ^{235}U, the cross-section for elastic scattering also increases as incident neutron energy decreases. Along with this there is a window between incident neutron energies of 1 eV - 1.4 keV where the neutron cross-section is large for fission reactions.

2.4.5 Attenuation

For a beam-neutron-source Σ_{tot} can be used to calculate neutron attenuation using the *Beer-Lambert law*, where I_0 is the initial neutron flux, I is the attenuated neutron flux, and d is the depth of the material through which the neutrons have passed, as depicted in Fig. 2.5.
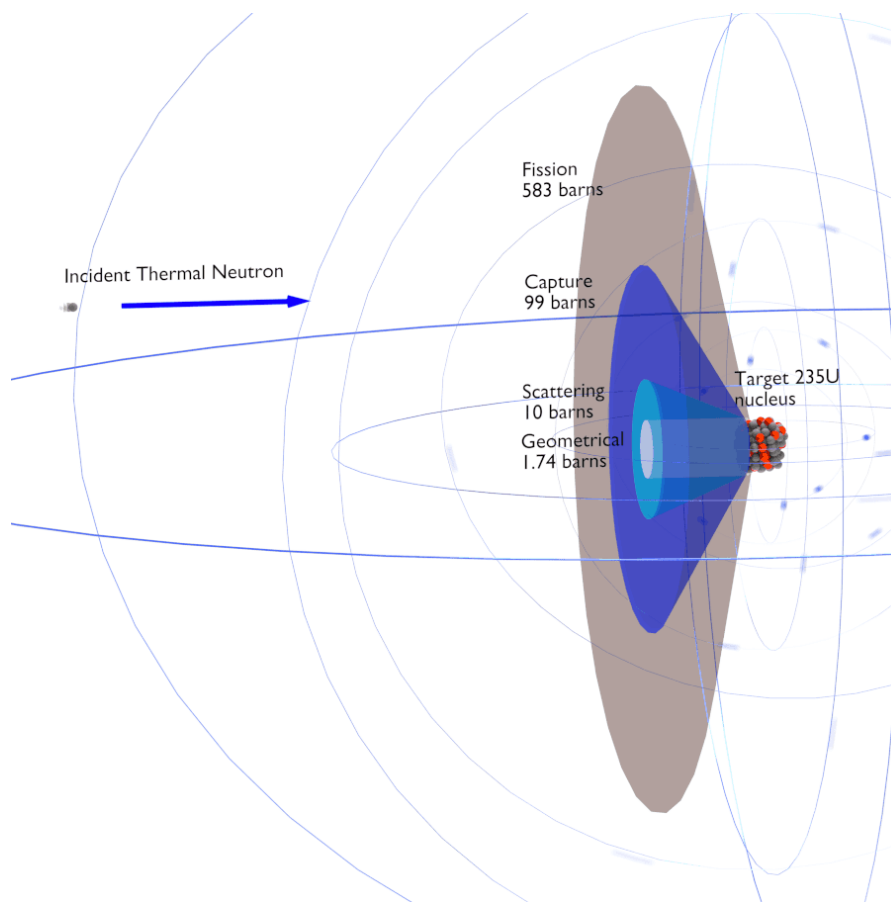
FIG. 2.3: Representation of four different neutron interaction mecha-nism cross-sections when a thermal neutron is incident on a ^{235}U atom (*Neutron Cross-section* 2014).
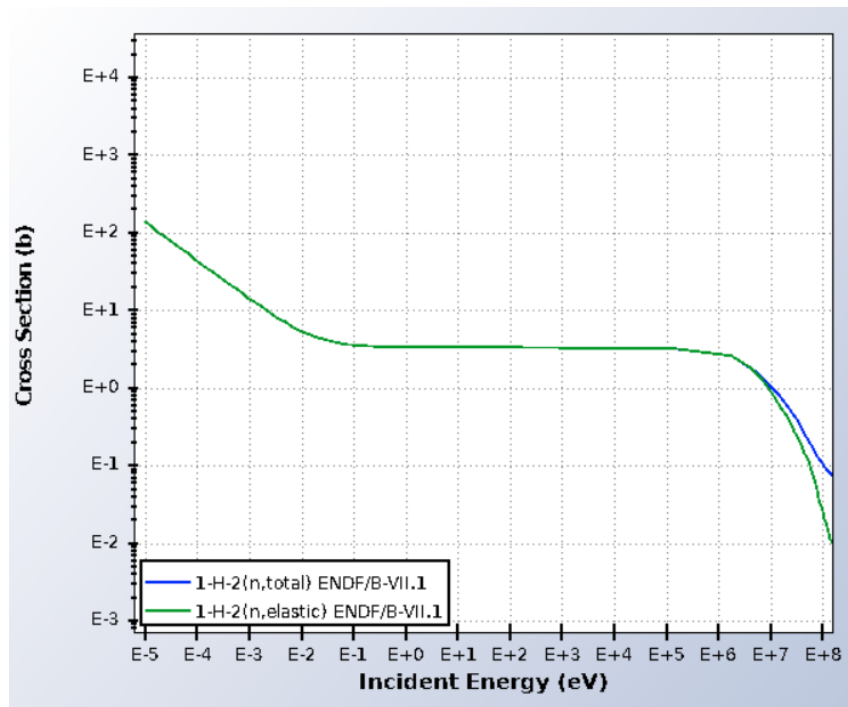
(A) Hydrogen-2
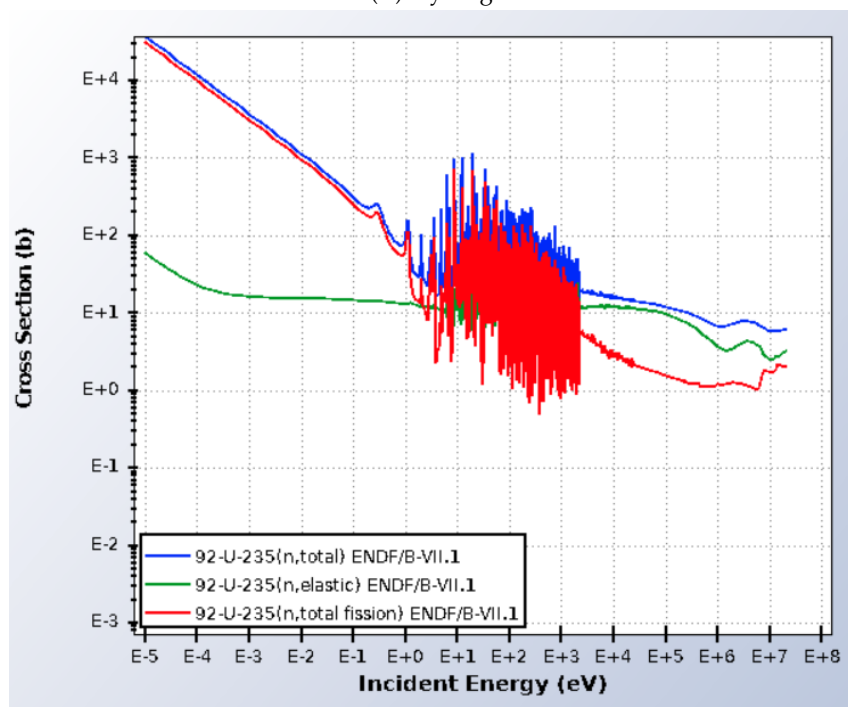
(B) Uranium-235

FIG. 2.4: Total, elastic, and fission neutron cross-sections for (A) hydrogen-2 (deuterium) and (B) uranium-235 nuclei. ^{2}H and ^{235}U have been chosen because they are common isotopes that are used in neutron interactions. Data provided from the ENDF/B-VII.1 library (Chadwick et al., 2011). (Graphs should be viewed in colour).
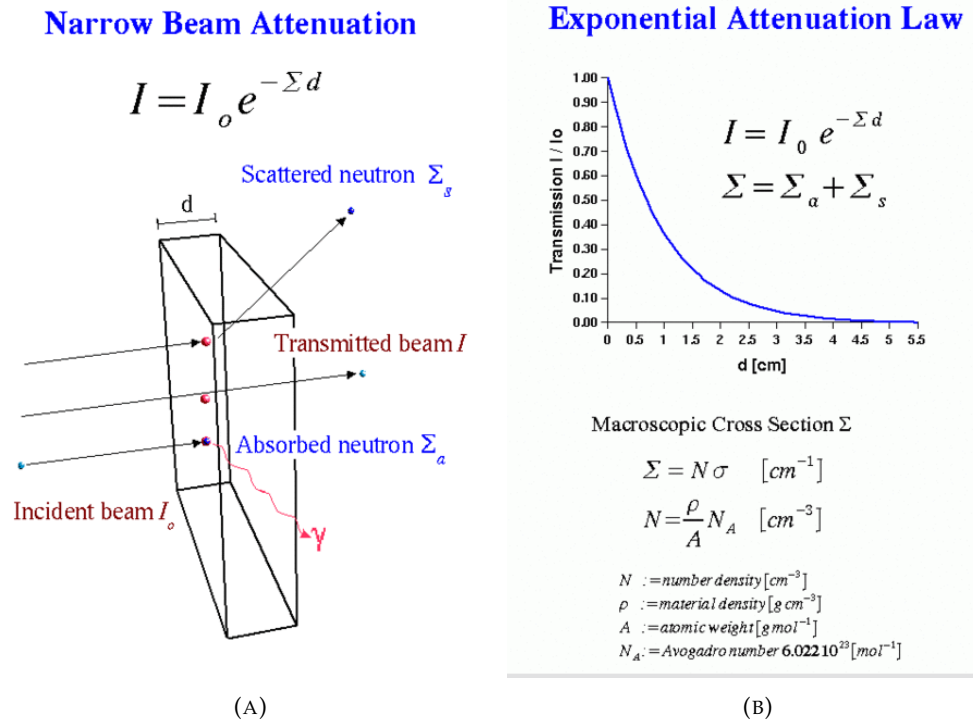
FIG. 2.5: Depiction of the exponential relationship of how neutrons are attenuated in material (A), and a plot of the Beer-Lambert law (B) (**strobl_neutron_2018**).

$$I = I_0 e^{-\Sigma_{tot} d} \tag{2.4.2}$$

The Beer-Lambert law is a useful approximation in a variety of situations within neutron metrology. It can be used to design collimators, shielding, and moderators.

2.4.5.1 Collimation

Collimation is the process of modifying a beam of radiation into a particular shape, like a fan, or beam (Joyce et al., 2016; Beaumont, Mellor, and Joyce, 2014; Gamage, Joyce, and Taylor, 2012). This is done by using highly attenuating material with a vacancy of the desired shape and then aiming a neutron source at the vacancy. Putting a lamp-shade over a light bulb to direct the electromagnetic rays is an example of collimation. Shielding is simply the use of highly-attenuating material to protect items within a radiation shine-path, like the use of lead-aprons to protect radiographers.

2.4.5.2 Moderation

Moderation of neutrons is the process of reducing the average energy of neutron radiation. It is often used to obtain neutrons of a particular energy that will increase the cross-section of a sample material and therefore increase the reaction rate (Chao and Niu, 1997; Sharma, 2001; Licata and Joyce, 2018). In the case of neutron detection, moderation of neutrons is often required when ^{3}He detectors are being used, to shift the neutrons into an energy range that will cause reactions with the ^{3}He atom due to the favourable cross-section at low energies. Moderation can sometimes be unhelpful, as it changes the direction of neutrons and in the case of neutron detection, it removes most of the information about the energy of the original incoming neutron. Even for neutron detectors that do not require moderation, such as scintillation detectors, moderation within the scintillation material itself may cause issues with detection due to the possibility of a scattered neutron being detected twice or more within the material. This is particularly prevalent in large arrays of scintillation detectors (Sarwar et al., 2018; Shin et al., 2015; Verbeke, Prasad, and Snyderman, 2015).

2.4.6 Neutron Distributions

For both spontaneous and induced fission, the number of emitted neutrons varies stochastically. The most commonly-used parameter to describe this is the average number of neutrons emitted in a fission reaction ($\bar{v}$), and this is reasonable due to the probabilistic nature. As more reactions are considered, the number of neutrons emitted per reaction tends towards the mean. Measured distributions of prompt fission multiplicity for a number of well known sources are included in Table 2.2. Coincidence counting, where multiple neutrons from the same fission event are detected, is a well-used method of material assay due to the unique multiplicity distributions, as presented in Table 2.2 (Reilly et al., 1993). In comparison with total-neutron-counting, multiplicity counting affords greater protection against background neutron counting. Conversely, total-neutron-counting can lead to more precise results than coincidence in the same measurement time (Stewart and Reilly, 1991). As neutrons from fission are ejected in

Probability	^{235}U Induced fission [a]	^{238}Pu SF [b]	^{239}Pu Induced fission [a]	^{240}Pu SF [a]	^{242}Pu SF [a]	^{252}Cf SF [a]
P(0)	0.033	0.054	0.011	0.066	0.068	0.002
P(1)	0.174	0.205	0.101	0.232	0.230	0.026
P(2)	0.335	0.380	0.275	0.329	0.334	0.127
P(3)	0.303	0.225	0.324	0.251	0.247	0.273
P(4)	0.123	0.108	0.199	0.102	0.099	0.304
P(5)	0.028	0.028	0.083	0.018	0.018	0.185
P(6)	0.003		0.008	0.002	0.003	0.066
P(7)						0.015
P(8)						0.002
$(\bar{v})$	2.406	2.210	2.879	2.156	2.145	3.757

TABLE 2.2: Measured probability distributions for prompt fission multiplicity, where SF refers to spontaneous fission. Adapted from (Reilly et al., 1993), [a](Boldeman and Hines, 1985), [b](Hicks, Ise, and Pyle, 1956)

.

all directions of 4-π space in the laboratory frame, the likelihood of detecting two neutrons from the same event is proportional to ε^2, where ε is the detector efficiency.

2.4.6.1 Neutron Energy Distributions

Prompt fission neutrons are emitted from nuclei in a predictable manner. Their spectra have been a regular aim of investigation from the earliest and simplest model; the Maxwell-Boltzmann distribution (a.k.a the Maxwellian); to today's Nuclear Data Sheets compiling deterministic models along with experimental data and simulated data (Capote et al., 2016). The prompt fission neutron spectrum (PFNS) is important in neutronics, as the spectrum, when combined with the neutron cross-section of a material, dictates how a material and neutron fluence will interact (Capote et al., 2016). The fission spectra commonly utilised in the evaluated nuclear data file (ENDF) (Chadwick et al., 2011) are defined by the Watt spectrum equation given in equation 2.4.3, where $C = \sqrt{\pi \frac{b}{4a}} \frac{e^{\frac{b}{4a}}}{a}$ (Dokania et al., 2015). Here E' is the energy of the fission neutron and coefficients a and b vary weakly between isotopes and incident neutron energy.

$$W(a,b,E') = Ce^{-E'/a}\sinh(\sqrt{bE'}) \qquad (2.4.3)$$

Isotope	$(\bar{v})$	a (MeV^{-1})	b (MeV^{-1})
^{235}U	1.86	1.29080	4.85231
^{238}U	2.01	1.19985	4.24147
^{239}Pu	2.16	1.12963	3.80269

TABLE 2.3: Coefficients corresponding to the spontaneous Watt fission spectra of three isotopes from (Werner, 2017, Tab: 9.1.2.2). Spontaneous fission multiplicity values as provided in (Langner et al., 1998, Tab: 5.1).
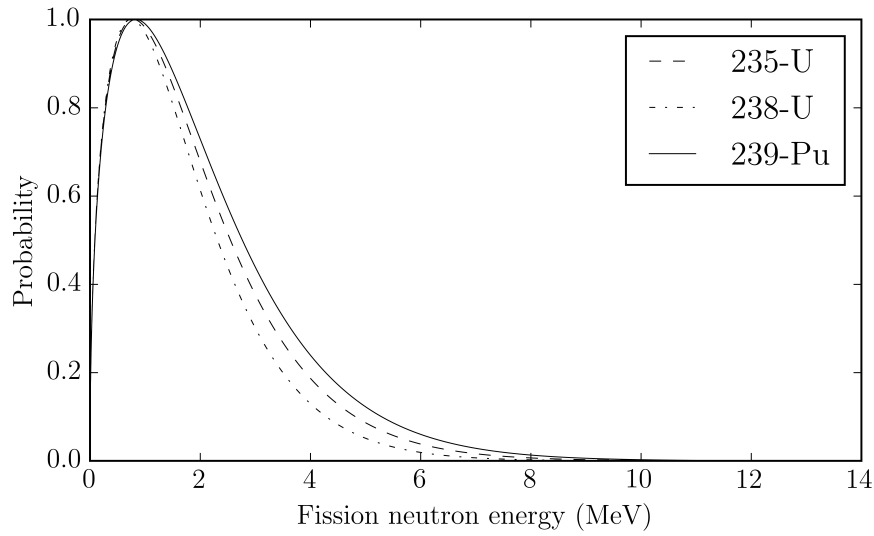
FIG. 2.6: Spontaneous fission neutron spectra calculated using the Watt spectrum equation with fit parameters provided in SF is (Werner, 2017, Tab: 9.1.2.2). SF is not significant for ^{235}U and ^{239}Pu, they are included for completeness. All three isotopes display a positively skewed distribution.

Coefficients for spontaneous fission reactions of common isotopes can be found in (Langner et al., 1998) and for the purposes of this thesis ^{235}U, ^{238}U and ^{239}Pu have been included in Table 2.3, and plots can be seen in Fig. 2.6. For induced fission, a and b are also weakly dependant upon the energy of the incident neutron. Here, b is set equal to 1.0 and a becomes $a(E) = a_0 + a_1 E + a_2 E^2$, with E being the energy of the incident neutron and coefficients of a_0, a_1, and a_2, found in Table 2.4. Plots of the induced fission Watt spectrum of these three isotopes can be seen in Fig. 2.7. The spontaneous fission and induced fission spectra for all three isotopes display a positively skewed distribution.

Isotope	a_0 (MeV^{-1})	a_1 (MeV^{-2})	a_2 (MeV^{-3})
^{235}U	0.920108	-0.00936909	7.32627×10^{-5}
^{238}U	0.925469	-0.0106491	8.96945×10^{-5}
^{239}Pu	0.887305	-0.0101099	8.50642×10^{-5}

TABLE 2.4: Coefficients corresponding to the induced Watt fission spectra of three isotopes. Adapted from (Cullen, 2004).
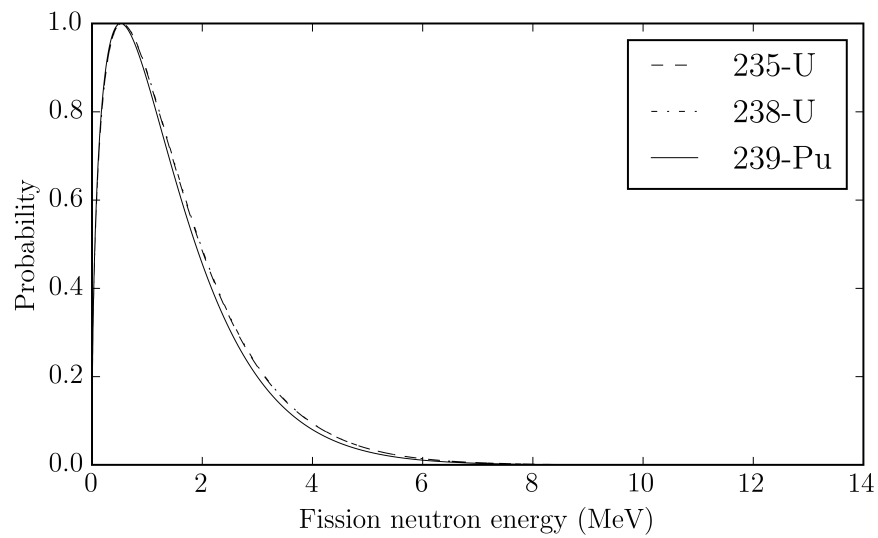
FIG. 2.7: Induced fission neutron spectra as calculated using the Watt spectrum equation with fit parameters provided in (Cullen, 2004). All three isotopes display a positively skewed distribution.

2.4.7 Delayed Neutrons

Delayed neutrons are those which have been released from a reaction after a relatively long time in comparison to prompt neutrons. This time period may be hundredths of a second up to tens of seconds. Delayed neutrons account for approximately 0.7 % of neutrons produced in PWR reactors. They are important as they allow control systems within nuclear power stations to modify the control-rod status to account for positive variations of the chain reaction criticality which must remain equal to one. For radiation detection purposes described in this thesis, delayed neutrons can be ignored due to their small proportion of the total neutron flux observed, as well as being too slow and not correlated in time.

2.4.8 Statistical Nature of Radiation Emission

Distribution functions of radiation fields can be estimated using statistical models. Three models are applicable to radiation fields and these are the Binomial distribution, the Gaussian distribution and the Poisson distribution. The latter two distributions are approximations of the Binomial distribution, and can be used to reduce computational power requirements in certain circumstances. For processes that can be characterised by a small and constant probability of success, the Poisson distribution is the most appropriate, and for almost all radiation measurement activities, this is sufficient. The distribution is described using equation 2.4.4, where P_n = the probability of μ events within an interval, μ = the average number of events per interval, and n = the number of events measured in the interval. For distributions of this type, the standard deviation is simply the square root of the mean of the datum (Knoll, 1999, p. 73).

$$P_n = e^{-\mu}\, \frac{\mu^n}{n!} \tag{2.4.4}$$

2.5   Neutron Measurements

2.5.1   Neutron Detection Methods

Neutrons and their interaction mechanisms have been discussed in section 2.4. Since their discovery in 1932, they have been measured in a variety of ways, using a number of different detectors. *Neutron measurements* is a catch-all phrase used to cover processes whereby information about neutrons is measured, this may be the number of neutrons present (total-neutron-counting or fluence measurements), the energy of a neutron or population of neutrons (time-of-flight or spectroscopy), and the ratio of released neutron multiplets in fission (coincidence counting). Table 2.5 provides a comparison of 19 different types of neutron detector.

Mechanism	Detector type	Neutron energy	Pros	Cons
Boron-10 Reaction	BF$_3$ proportional tubes	S	Superior gamma discrimination when compared to other Boron reaction mechanisms	Wall effects apparent with proportional counters
				PHS not related to energy
				Temperature dependant
				May degrade in high gamma fields
	Boron-lined proportional counters	S	Less pulse pile up in high gamma environments than BF$_3$	Hazardous if leaks occur
	Boron-loaded scintillators	S	Time-of-flight achievable due to small volumes used	
Other Conversion Reactions	Lithium-6-containing slow neutron detectors	S	Good gamma pulse-pile-up discrimination	Highly hygroscopic; not suitable near traces of water vapour
			Single peak PHS, regardless of wall effects	
	^{3}He Proportional counters	F, S	Only detector sensitive to both fast and slow neutrons	Gaseous filling means failure due to leak-age is common

Mechanism	Detector type	Neutron energy	Pros	Cons
			Can work in temperatures up to 250°C	- PHS spectra are affected by the wall effect - γ-ray discrimination is lower than than for BF_3 tubes
	Fission counters	F	Function in very low background measurements due to fission fragments exhibiting so much energy	- Almost always α-radioactive - Management of small quantities of fissile material, manufacture.
Neutron Moderators	Bonner sphere	F	Flat(tish) response across whole spectra	Interactions remove low energy neutrons from count and often any directional information
	The long counter	F	Flat(tish) response across spectra Can acquire directional information due to geometry and material used	0.25% efficiency
Lithium (α,n) reaction	LiI scintillators	F	Reaction Q-value makes for easy energy calibration	^{6}Li(n, n'd)^{4}He reaction competes for neutrons Low resolution at room temperature

Mechanism	Detector type	Neutron energy	Pros	Cons
	Lithium glass scintillators	F	Reaction Q-value makes for easy energy calibration; Effective for time-of-flight measurements	^{6}Li(n, n'd)^{4}He reaction competes for neutrons
^{3}He(n,p) Reaction	^{3}He Ionisation chamber	F	Better resolution than the proportional counter	
	^{3}He Scintillator	F	Very fast pulse rise-time	Poorer PSD resolution compared to other ^{3}He detectors
Fast neutron scattering detectors	Anthracene	F	Largest light output of any organic scintillator; Faster than most detectors; Easily scaleable	Difficult to discriminate between neutrons and γ-rays below a few hundred keV; Expensive when larger than 2 cm; Easily damaged thermally and mechanically; Direction dependent; light output range of 25% depending on direction of neutrons
	Stilbene	F	Superior γ-ray rejection than anthracene	Same as anthracene

Mechanism	Detector type	Neutron energy	Pros	Cons
	Liquid scintillators	F	Relatively inexpensive to produce	Larger sizes have greater neutron interaction but lower light yield and greater γ-ray pile-up
			Non-directional response	Neutron spectrum must be unfolded for complex response functions
			PSD capability to suppress γ-ray response	Light output is non-linear with respect to neutron energy
			Linear light response to γ-ray energy allows for easy energy calibration in MeVee	Carbon scattering, followed by Hydrogen scattering can affect response function
				Some are flammable and/or toxic
				Energy cut-offs for noise also affect γ-ray response
	Plastic Scintillators	F	Same as liquid scintillators	Same as liquid scintillators plus...
				High radiation environments degrade plastics and surface crazing can significantly impact light output

Mechanism	Detector type	Neutron energy	Pros	Cons
Gas Recoil Proportional Counters	F		Reduced multiple scattering effects Similar response between neutrons and γ-rays Differences in neutron and γ-ray ionisation tracks allow for easy discrimination Tunable via pressure across energy	Low density, therefore less efficient than organic scintillators Gaseous filling means failure due to leakage is common More difficult assembly than organic scintillators γ-rays are very likely to interact with detector walls and construction materials Non-linearity of response at anode ends: called the tip-effect Energy calibration is more difficult than for organic scintillators
Proton Recoil Telescopes	F		Spectra can be acquired without unfolding	Very inefficient compared to other techniques
Capture-Gated Neutron Spectrometer	F		Gives a single peak for mono-energetic neutrons sources	Non-linearity of response lead to peak-broadening

Mechanism	Detector type	Neutron energy	Pros	Cons
				Carbon scattering effects are apparent above 5-6 MeV

TABLE 2.5: Comparison of various neutron detector technologies. Where neutron energy is either slow (S) or fast (F). Adapted from (Knoll, 1999)

It can be inferred that for purposes of detecting neutrons, as opposed to spectroscopy, the two main techniques use ^{3}He detectors, and scintillation detectors. ^{3}He detectors utilise the reaction shown in equation 2.5.1, whereby 765 keV of energy is released as charged particles. The ionisation produced by these charged particles triggers the multiplication process which leads to detection. When the counters are run in proportional mode, the energy deposited is equal to that released in the reaction (Reilly et al., 1993, p. 386).

$$^3\text{He} + \text{n} \rightarrow\ ^3\text{H} +\ ^1\text{H} + 765\ \text{keV} \qquad (2.5.1)$$

Scintillation detectors utilise the elastic scattering mechanism with hydrogen nuclei to transform neutron energy into visible light. A neutron impacts a hydrogen nucleus, transmitting up to 100 % of its energy. The recoiling proton then deposits its kinetic energy in the scintillation material and this is converted to heat and visible light. This light can then be converted to an electrical signal directly by a photomultiplier. This recoiling process is similar for detecting γ rays, except that they interact with the electron shells of the carbon and hydrogen atoms. The ability of scintillation material to detect neutrons and γ rays at the same time is beneficial in mixed-field measurements, but has certain drawbacks. In intense radiation fields the detectors can be affected by pulse pile-up, where the instrumentation cannot discriminate between pulses of light quick enough to identify them independently of one another. At low neutron energies there may also be *bleed through* where γ rays are incorrectly identified as neutrons because they appear similar as their peak light output and tail light output have similar ratios. Typical light outputs from neutrons and γ rays can be seen in Fig. 2.8.

There are a variety of ways of interpreting these pulses, with discussions available in (Gamage, Joyce, and Hawkes, 2011; Balmer, Gamage, and Taylor, 2015; Jamili, Bayat, and Ghal–Eh, 2017). For all research described in this thesis, an analysis method called pulse gradient analysis (PGA) is used. This method analyses the gradient of the falling edge of the pulse to obtain the peak of the light output, and then at some user-defined time later (in the order of ns) the amplitude of the pulse is taken again, this is often
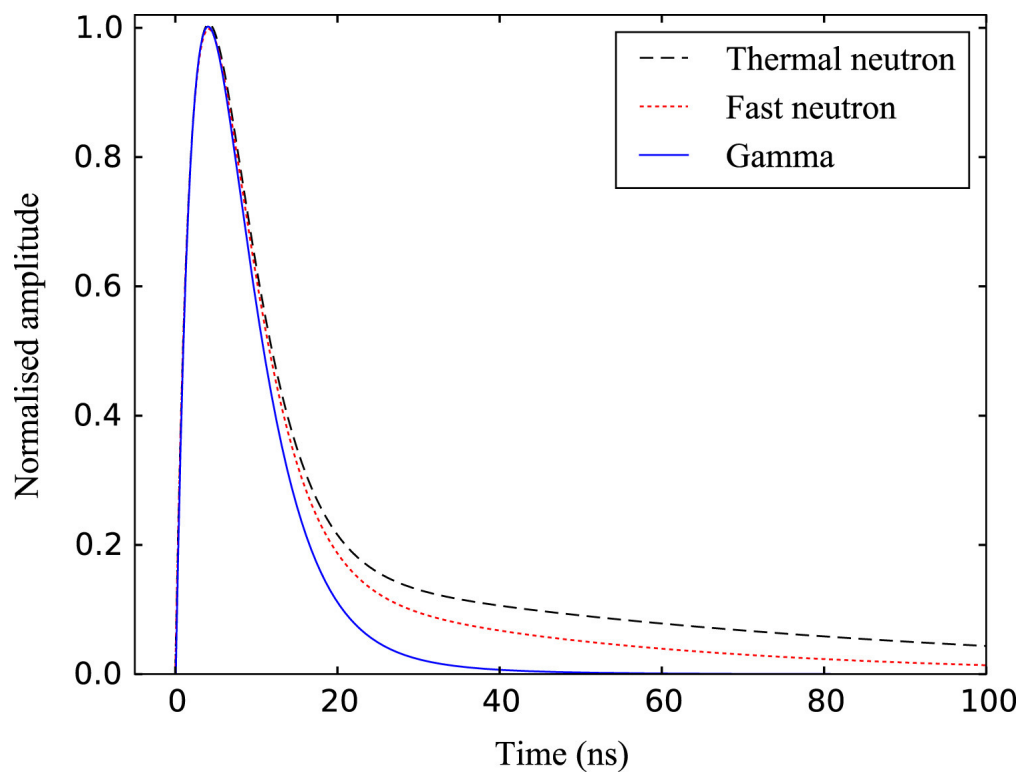
FIG. 2.8: Typical light output of liquid scintillation material after interaction with a thermal neutron, fast neutron and a γ-ray (Balmer, Gamage, and Taylor, 2015), based upon (Zaitseva et al., 2013).
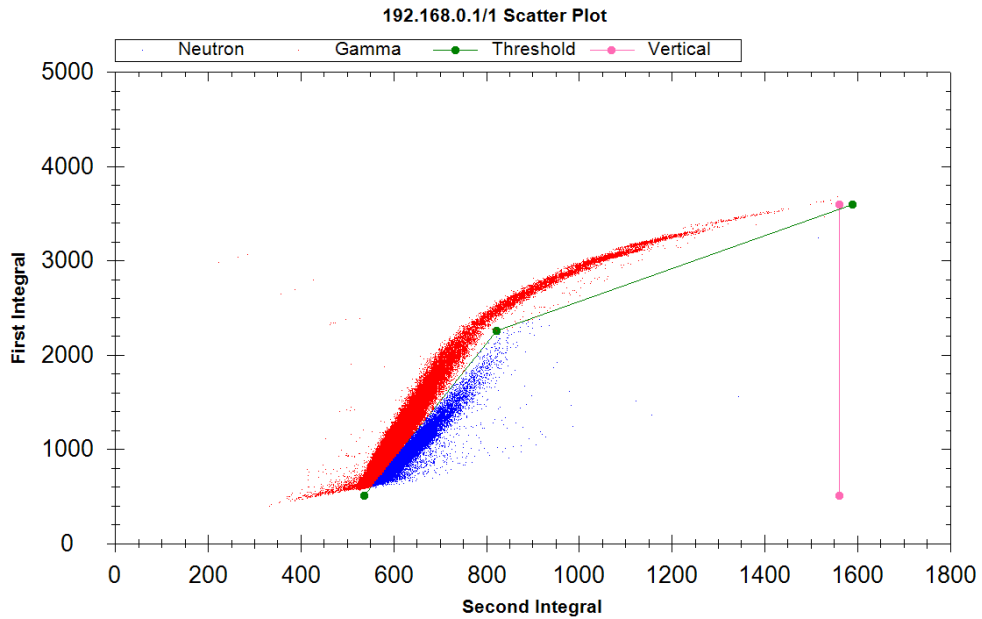
FIG. 2.9: Plumes of γ rays (above threshold) and neutrons (below threshold) in a PSD scatter plot of a mixed field of radiation. Data is provided from a 60 s measurement of a ^{252}Cf source with a cubic EJ-309 detector and a single channel Hybrid MFA.

referred to as the *discrimination* amplitude. From Fig. 2.8 it can be seen that neutron and γ-ray light outputs have differing decay profiles. When a ratio of the peak and discrimination amplitude is calculated, a neutron will generate a higher ratio than a γ ray (D'Mellow et al., 2007). Fig. 2.9 compares the plumes of γ rays and neutrons in a PSD plot of a mixed field of radiation.

2.5.2 Background Measurements

Prior to carrying out a measurement of radiation, a background measurement must usually be taken to provide a baseline data level. Following the experimental radiation measurements, this background level can be subtracted to give a *true* measurement of the field as desired. Ambient neutrons predominantly come from atmospheric reactions by protons from the cosmos and may be scattered or reflected by nearby materials such as concrete (Bethe, Korff, and Placzek, 1940; Neumann, 2006). As well as ambient neutrons, the process of measuring neutrons may introduce further neutrons

into the measurement space. Processes that may lead to a greater number of neutrons are discussed henceforth. Cosmically-induced neutrons occur when a cosmic neutron reacts with a sample material creating fission, thus a single neutron may cause the release of a number of neutrons that may be measured (Noonan, 2014). Spontaneous fission of very low level neutron emitters such as ^{238}U, which releases neutrons at rate of 0.0136 n.s^{-1}.g^{-1}, can become significant for large samples, and very high sensitivity measurements (Reilly et al., 1993, p. 339).

2.5.2.1 Active Neutron Assay

A common method of carrying out a neutron measurement of a material, is to induce fission in the material and measure the number of induced fission neutrons (Runkle, Chichester, and Thompson, 2012). This method is described as active, in comparison to detecting neutrons directly which is called passive measurement. The neutron source used to induce fission in a sample can lead to these interrogating neutrons being detected as well as the induced fission neutrons. In addition to carrying out a background measurement, the effect of the interrogating neutron source can be minimised in scintillation detectors by using a neutron source with a low energy (<0.5 MeV), where the detector is essentially blind (Pino et al., 2014). Fig. 2.10 compares an americium-lithium (AmLi) neutron spectrum to the efficiency of an EJ-309 detector. It can be seen that the detector is unlikely to detect a significant number of neutrons from an AmLi source.

2.5.2.2 Multiplication in Samples

Ejection of multiple neutrons from a single reaction was introduced in section 2.4. The neutrons released from a reaction may themselves go on to cause another reaction, and so on and so forth. This process is called multiplication and, depending upon the multiplication factor, it may create a sustainable nuclear reaction or an uncontrolled excursion (Kaneko and Sumita, 1967; Endo, Yamamoto, and Yamane, 2011). Multiplication is highly dependent upon the overlap between the spectrum of emitted neutrons and the fission neutron cross-section of the sample material.
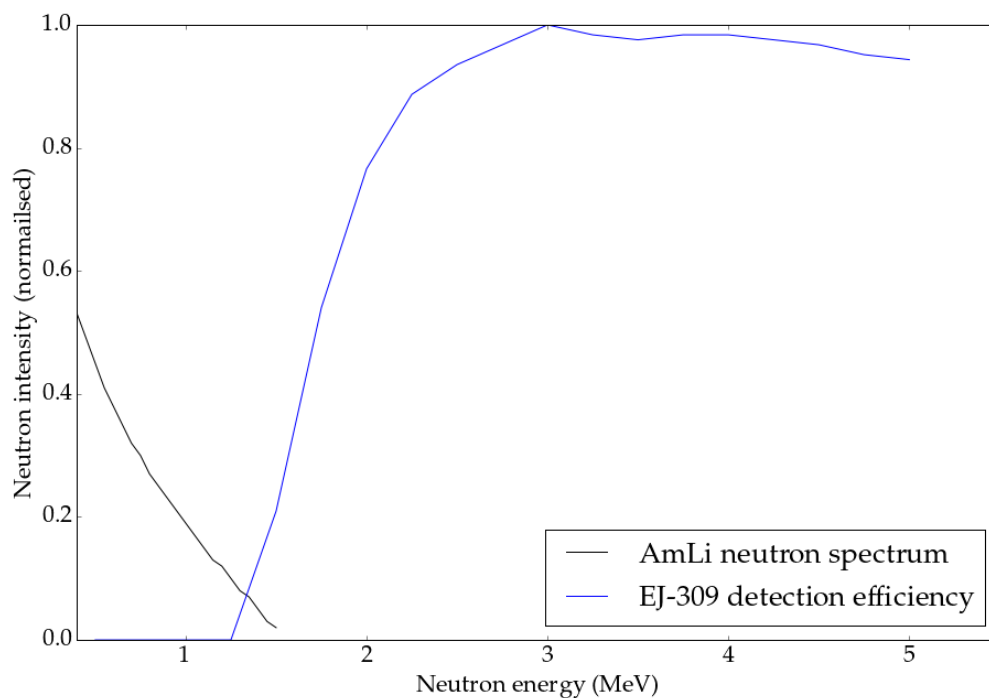
FIG. 2.10: Comparison between a measured AmLi neutron spectrum (Reilly et al., 1993), and experimental EJ-309 detector efficiency (Pino et al., 2014).

2.5.2.3 The Observer Effect

Measuring neutron fields from samples of nuclear material is a process that can be influenced heavily by the observer effect. Introducing lumps of dense, nuclear material with large neutron cross-sections, creates a lot of new possibilities for neutron interaction and therefore changes the number of neutrons measured. Self attenuation is an example, whereby a sample may be of a shape or size that inhibits neutron emission due to the mean free path being less than the depth of the material. In this case, a neutron emitted from a reaction may dissipate all of its energy and be reabsorbed by the material and therefore not leave the material and be detected. Similarly, during active measurements, carrying out a background measurement of the neutron source, the lack of the sample material may result in a higher background neutron count than will be the case when a sample is present. This effect may be overcome with the use of a shadow cone. Fig. 2.11 depicts an interrogating neutron field incident upon a detector, alone, with a sample present, and with a shadow cone present. A shadow cone is a

piece of material with a similar form and preferably a similar neutron cross-section to that of the sample that is to be measured, but that does not undergo induced fission. A shadow cone allows for a more accurate background measurement of the inducing neutron field to be taken than measuring the field alone (Kim et al., 2015).

2.5.2.4 Background Error Propagation

Following a background measurement, or measurements, the uncertainty of these data must be estimated and propagated through any calculations whereby the background is subtracted from a sample measurement. The background measurement and the sample measurement will both have their own errors. Combining these is done by invoking equation 2.5.2, where Q is the difference in each measurement, described using the form $a + \delta a$, $b + \delta b$ (Tsoulfanidis and Landsberger, 2010, p. 42).

$$
\begin{aligned}
Q &= a - b \\
\delta Q &= \sqrt{(\delta a)^2 + (\delta b)^2}
\end{aligned}
\tag{2.5.2}
$$

2.5.3 Further Considerations

Neutron measurement experiments must be designed carefully if the efficiency of the measurement is to be maximised. Neutron emitters used for research in this thesis all exhibit neutron isotropy ejection in 4-π space (laboratory frame), thus the solid angle of any detection equipment is important. The solid angle can be calculated using equation $\Omega = A/r^2$, where Ω is the solid angle in steradians, A is the spherical surface area and r is the radius of the sphere in question. Fig. 2.12 shows how increasing a radius reduces the intensity of radiation from a central point within a sphere. In order to increase the solid angle a detector can be placed as close to the neutron source as possible, but then fewer detectors can be used. Failing that, the length of time of the measurement can be increased.
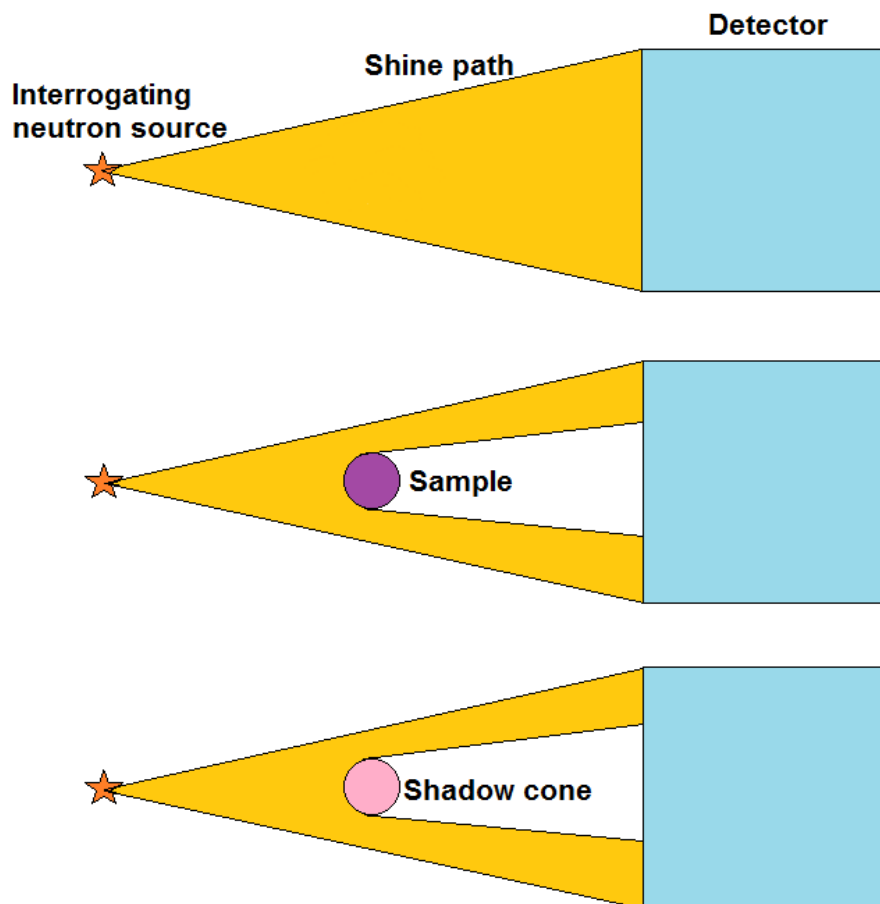
FIG. 2.11: Depictions of the impact of a sample's presence on a background measurement of an interrogating neutron source. A shadow cone is introduced to mimic the sample and make the background measurement more accurate. The shadow cone should not emit neutrons of its own or undergo fission.
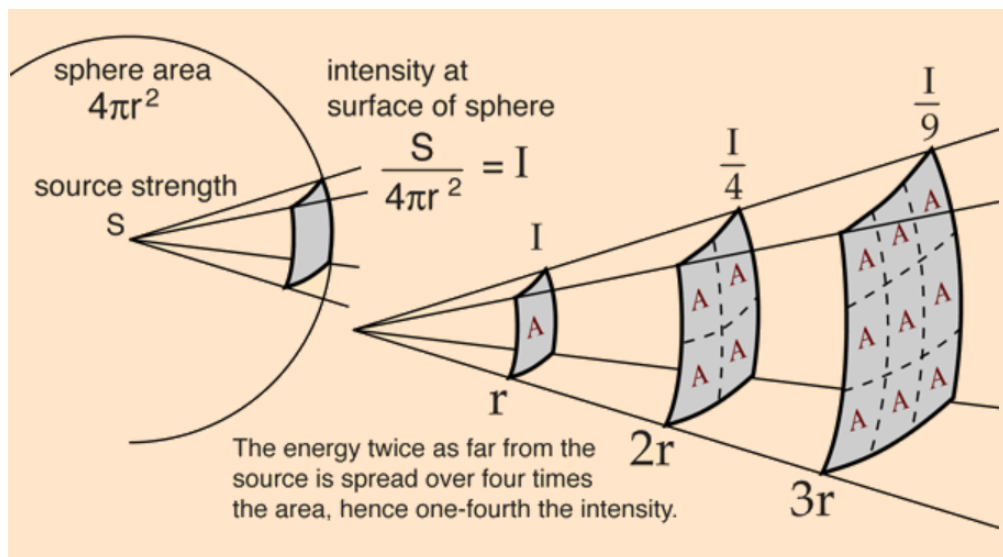
FIG. 2.12: Relationship between radiation intensity and distance from a
point source (Nave, 2019a)

3 Materials and Methods

3.1 Radiation Detection Equipment

The radiation equipment used throughout the research presented in this thesis included VS-1105-21 EJ-309 Eljen organic scintillation detectors (Scionix, Neth.) with coupled photo multiplier tubes of the type 9821 FLB (ADIT Electron Tubes, Sweetwater, TX) (Enqvist et al., 2013), a Hybrid Instruments mixed field analyser MFAx4.3 (*MFAX4.3*), signal counting boards, and off-the-shelf ancillary equipment. Each of these technologies will be described and discussed henceforth.

3.1.1 Detectors

Detector selection for the projects discussed in this thesis was carried out by comparing current detector technologies to find an appropriate variety. As discussed in chapter 1 the main drivers of these research projects were to have small, modular detector arrays that were not comprised of ^{3}He detectors. ^{3}He production is supply constrained and therefore it is becoming more and more difficult to acquire cost-effectively. Reactor instrumentation was not taken into account when choosing detectors, due to the extreme working conditions not aligning with those planned as part of this work. An in-depth review of the current technologies available for neutron detection can be found in section 2.5.1, Table 2.5.

For the research described in this thesis, cubic EJ-309 liquid organic scintillation detectors were chosen due to their modular design, pulse-shape discrimination capability and low hazard characteristics. These detectors have been proven in a variety of applications similar to those planned (Lawrence et al., 2010; Enqvist et al., 2012; Stevanato

et al., 2012; Joyce et al., 2014; Marcath et al., 2017). The Eljen EJ-309 material is a recent development of the longer established EJ-301. However the EJ-309; with its higher flashpoint (144°C) and lower toxicological risk; have made the technology suitable for long-term use in some industrial applications (Tomanin et al., 2014). Fig. 3.1 depicts the detector unit with its associated photo multiplier tube. The detectors are sealed unlike other forms of liquid scintillation detector that mix the sample within the scintillant (Gaca, Warwick, and Croudace, 2017).

Detectors using the Eljen EJ-309 liquid organic scintillator material have been studied at length (Aspinall et al., 2007; D'Mellow et al., 2007; Pino et al., 2014; Tomanin et al., 2014; Shin et al., 2015; Astromskas and Joyce, 2018). (Enqvist et al., 2013) reports that differences in size and shape of the detector material have a significant effect on light output, this is confirmed in (Tomanin et al., 2014), which describes the cubic EJ-309 detectors used throughout this research. Here, pulse height spectra of the cubic ($0.1 \times 0.1 \times 0.12$ m) EJ-309 are presented for four different mono-energetic neutron sources, as reproduced in Fig. 3.2. (Enqvist et al., 2013) reports the neutron response on light output functions of the EJ-309 liquid, with the most appropriate here being reproduced in Fig. 3.3, using a rational and an exponential fit, the empirical functions are respectively: $L_p = \frac{0.90E_p^2}{E_p + 5.95}$ and $L_p = 0.817E_p - 2.63(1 - exp^{(-0.297E_p)})$ where $E_p =$ photon energy (or transferred neutron energy), and $L_p =$ light output.

The light output emitted by a scintillation detector is linearly dependant upon the energy of the incident radiation, for γ rays. However, for a neutron this is not true. Evidence of this can be found in (Pozzi, 2003; Czirr, Nygren, and Zafiratos, 1964), where the relationship between the energy of the incoming particle and that of the light produced in the scintillation material is given by an equation of the form:

light output $= C_1 \ E_n^2 \ + \ C_2 \ E_n$, where C_1 and C_2 are constants. Fig. 3.4 shows the relationship between incoming particle energy and light output for γ rays (electron recoil) and neutrons (proton recoil) reacting with BC-501 liquid scintillant (closely related EJ-301).
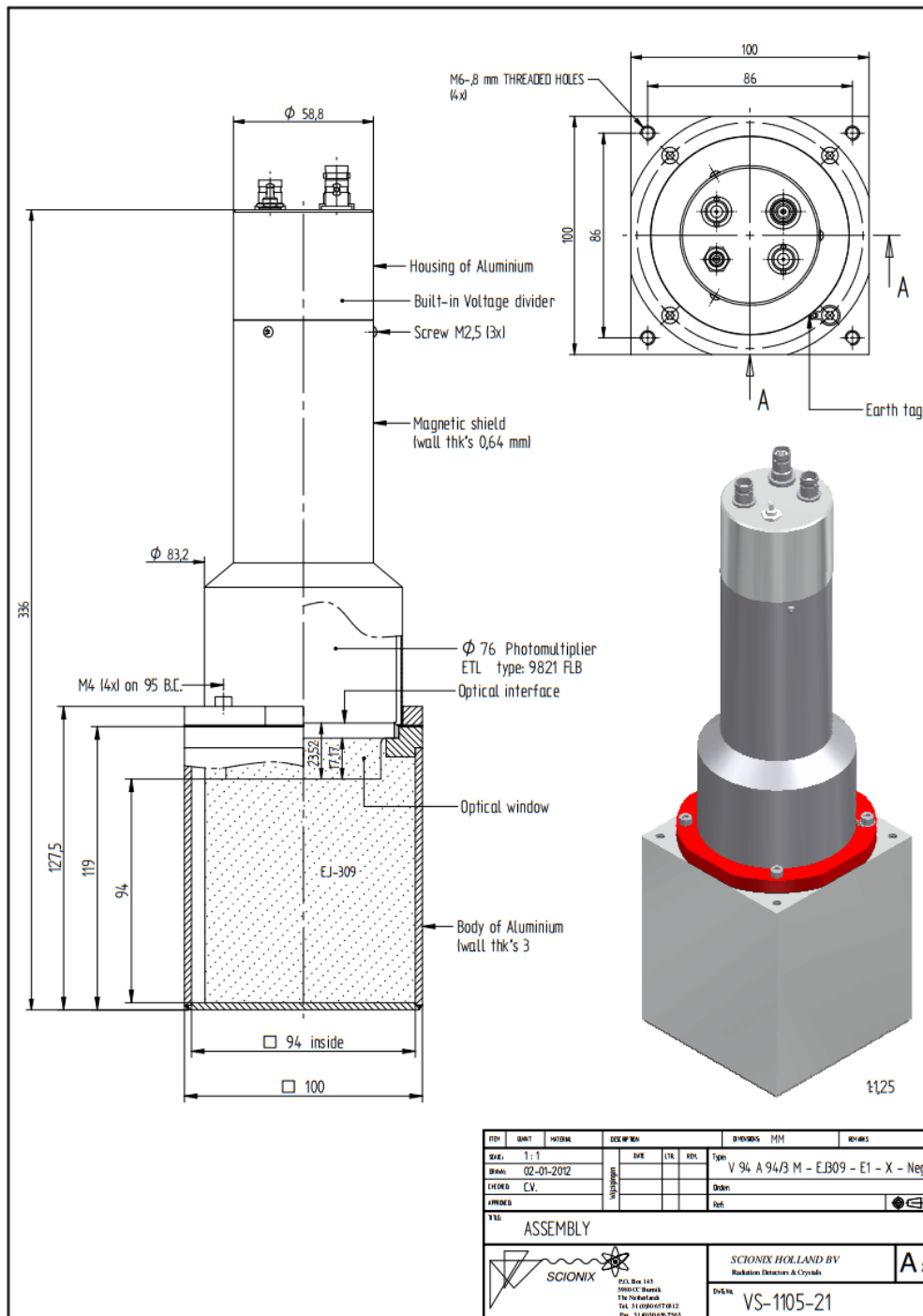
FIG. 3.1: A $10 \times 10 \times 12$ cm Scionix EJ-309 cubic liquid organic scintillation detector assembly diagram (BV", 2012).
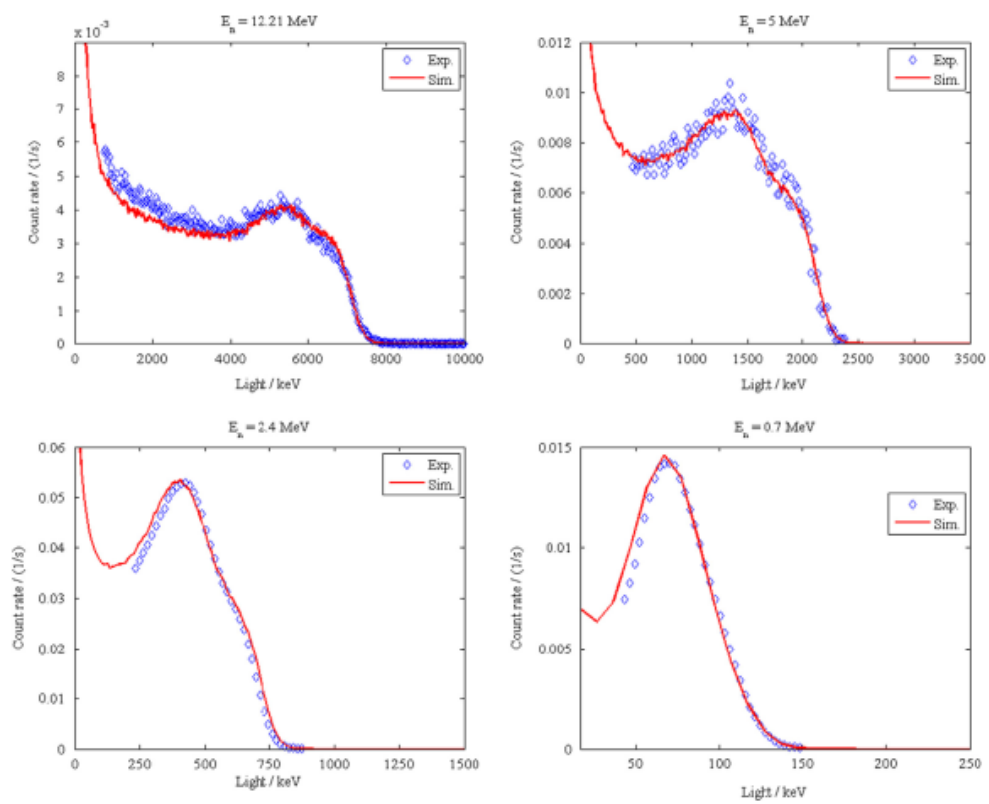
FIG. 3.2: Experimental and simulated pulse height spectra of a cubic EJ-309 detector at four initial neutron energies. (Tomanin et al., 2014).
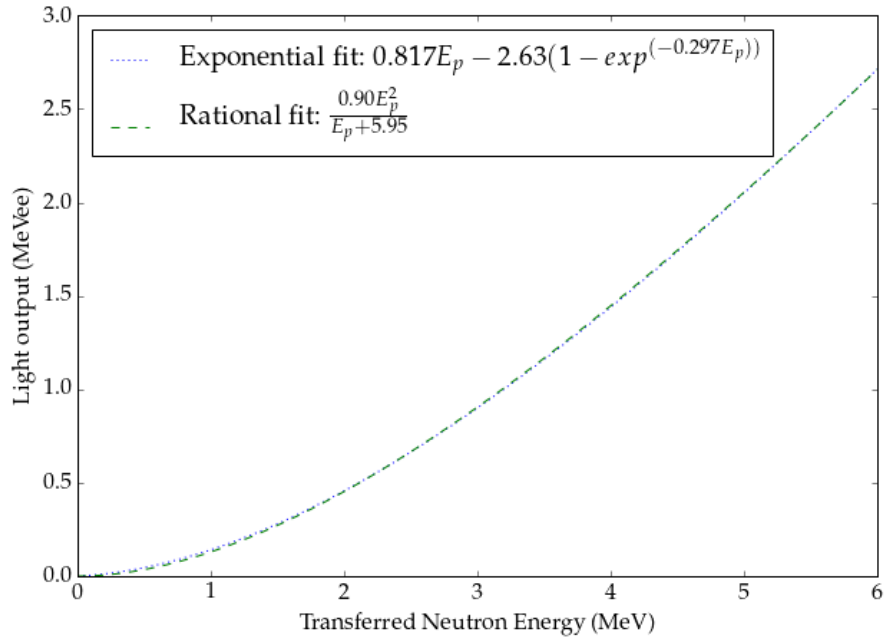
FIG. 3.3: Light output response of neutron interactions in a EJ-309 detector, where E_p = photon energy (or transferred neutron energy), and L_p = light output. Adapted from (Enqvist et al., 2013).
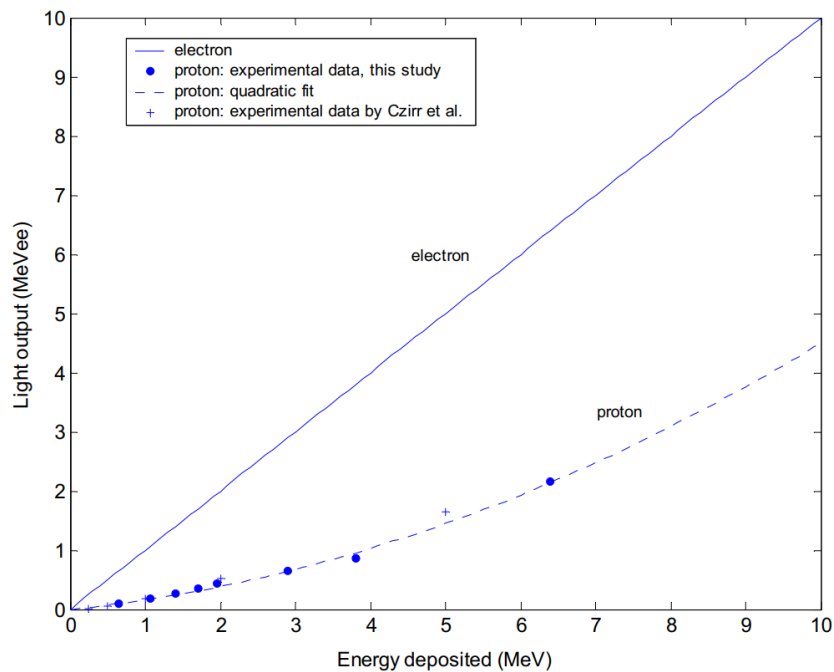
FIG. 3.4: Measured and theoretical light output energy following interactions with neutrons (proton recoil) and γ rays (electron recoil) for BC-501 liquid scintillant (Pozzi, 2003).

Detectors efficiencies are measured inn terms of absolute efficiency or intrinsic efficiency. Absolute efficiency is the ratio of radiation emissions to detections. Intrinsic efficiency is the ratio of radiation incident upon the detector Vs the number of detections that that detector makes. Absolute efficiencies of organic scintillation detectors are dependent upon the shape, size, scintillant material response, PMT, solid-angle of measurement, and processing equipment used. Therefore, each detector assembly will have its own absolute efficiency. Intrinsic efficiency can be measured and compared with other systems. (Pino et al., 2014) reports on the efficiency of a cylindrical EJ-309 detector system, and even though the same detector is used throughout, efficiencies still vary with the energy threshold applied to the measurements, and the energy of the incoming neutrons and γ rays. This still remains a comprehensive measurement of efficiency of any EJ-309 detector system. For neutron measurements, a maximum intrinsic efficiency of $\sim$40% is measured at a neutron energy of 1.5 MeV with an energy threshold of 0.1 MeVee, however this low threshold would not remove signals resulting from isomeric states of the fission products. It is suggested that a 0.2 MeVee threshold be used as a minimum. Using this threshold, Fig. 3.5 was obtained, which also brings together research reported in (Enqvist et al., 2013; Takada et al., 2011).

A detailed overview of how PMTs work and their operating parameters can be found in (Enterprises, 2011b), with a diagrammatic representation provided in Fig. 3.6. Electrons are emitted by the PMT upon sensing light. These electrons are multiplied by a number of dynodes and then summed at the anode. When used with a scintillant in a mixed field, the PMT will produce light outputs similar to that seen in Fig. 3.6. Electron Tubes' 9821 FLB Photo Multiplier Tubes (PMTs) are connected directly to the detectors discussed above (Enterprises, 2011a, pg. 21). These are 76 mm diameter PMTs with bialkali (K-Cs-Sb) sensitive to blue-green light with a low dark current. The wavelength of maximum emission for EJ-309 detectors is 424 nm. They have a quantum efficiency peak typically of 30 %, a gain of 7×10^6, a pulse rise time of 2.1 ns, and a pulse FWHM of 3.2 ns. These types of PMTs have been used extensively with organic scintillation
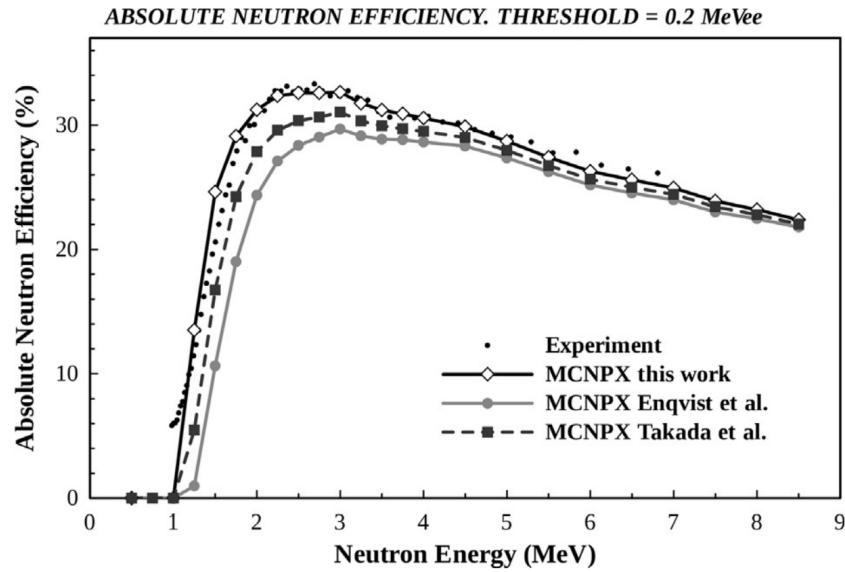
FIG. 3.5: Measured and simulated neutron efficiency of a cylindrical EJ-309 organic scintillation detector (Pino et al., 2014).

detectors and are more than adequate to provide suitable pulse height traces for discrimination in an MFA (Enqvist et al., 2013; Mirzoyan, Laatiaoui, and Teshima, 2006).

3.1.2 Mixed Field Analysers

A Hybrid Instruments Ltd. Mixed Field Analyser 4.3 provides real-time pulse shape discrimination (PSD) and multi-channel analyser (MCA) capabilities for fields of radiation including neutrons and γ rays from scintillation and CLYC detectors, in real-time and synchronised. An MFAx4.3 can be seen in Fig. 3.7. The MFAx4.3 version has capacity for four detectors to be used at once, and multiple MFAx4.3 systems can be used simultaneously if a fast Ethernet switcher is used for calibration. The MFAx4.3 modules are supplied with power supplies at 28 - 40 V DC and produce HV supplies to the detectors of between -2000 V and 0 V.

The MFAx4.3 system is coupled to a detection unit's PMT with one HV and one signal co-axial cable per detector. An Ethernet cable is used between the MFAx4.3 and a conventional PC running the MFA GUI in order to calibrate the detectors. Co-axial signal cables are used between the neutron and γ-ray transistor-transistor logic (TTL)
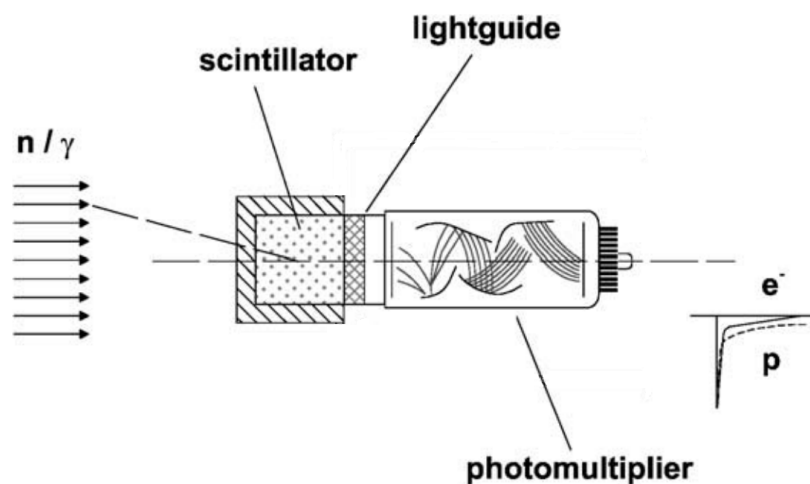
FIG. 3.6: Representation of how a PMT works, and the output created
for neutron and γ-ray interactions in a scintillant material. Adapted from
(Klein and Neumann, 2002).

FIG. 3.7: Photgraph of a Hybrid Instruments Mixed Field Analyser
MFAx4.3, with capacity for four scintillation detectors in a mixed field
of radiation including neutrons and γ rays.

ports, and a signal counter to count in real-time the number of neutrons and γ rays being detected by the system. The process of calibration begins by organising the required detectors in position and attaching the cabling required from the detectors to the MFA unit. If using EJ-309 organic scintillation detectors, the potentiometers upon the top of the units should be screwed to maximum, to ensure an equitable starting position to begin calibration. The MFA is then powered up, along with the PC and Hybrid's software graphical user interface (GUI). The software will automatically detect the presence of the Ethernet cable, and will sync to the MFA. Once up and running the GUI can be used to switch between PSD and MCA mode.

To begin with, MCA mode is selected and the equipment will begin to plot an MCA plot peak energy deposition (channel number) vs sum of particles present at this energy (counts). Next, a known γ-ray source, preferably with one γ-ray emission, is placed near to the detectors. Throughout the work described in this thesis, a ^{137}Cs source is used which has a primary γ-ray peak at 662 keV. With the known γ-ray source in place, an MCA plot should be acquired until Compton edges for all detectors are clear. Aligning these Compton edges is done by changing the high voltage (HV) provided to each detector separately. The aim is to have all detector Compton edges at the same channel number, where channel number is analogous to energy. To reduce the channel number of a Compton edge, the amplitude of the HV should be reduced, and to increase the channel number of a Compton edge, the HV should be increased. Increasing the HV increases the potential difference between the dynodes of the PMT and thus results in a greater signal at the anode. Fig 3.8 depicts a Compton edge for the same ^{137}Cs source at various HV. This process is iterative and the more detectors used in a system, the longer the process takes. Hybrid Instruments Ltd. state that this process can be done automatically with the auto-calibration option on the GUI. For the experiments described within this thesis, manual calibration was carried out, due to the relatively low number of detectors.

As discussed in section 3.1.1, the energy-dependent light response by a scintillator is linear for a γ ray but not for a neutron. Therefore, if the calibration method detailed

(A) HV at (-1645) (B) HV at (-1745)

(C) HV at (-1845) (D) HV at (-1900)
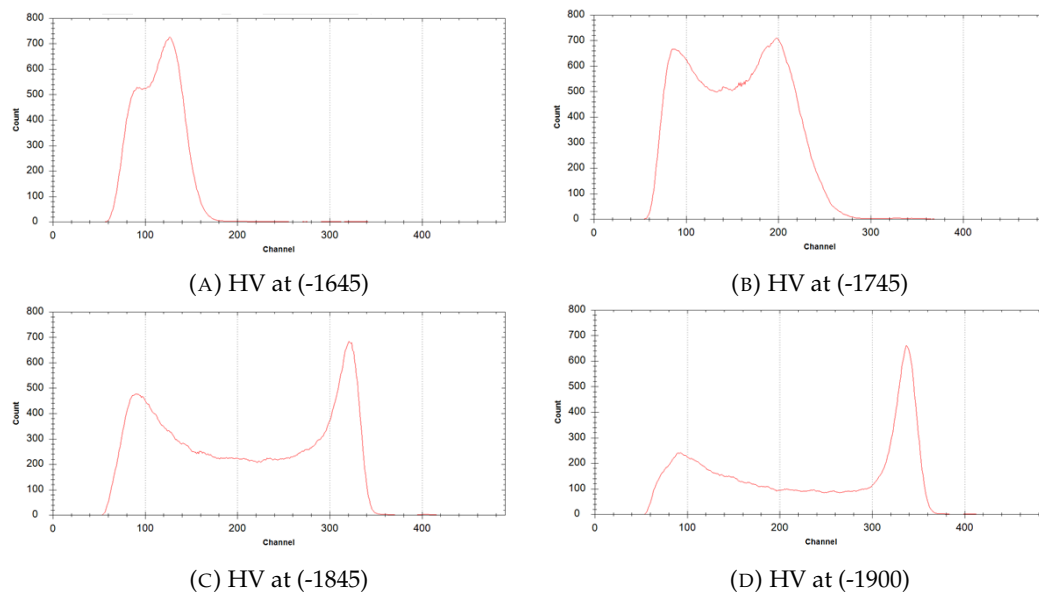
FIG. 3.8: Compton edges of a ^{137}Cs γ-ray source measured with the same EJ-309 organic scintillation detector, at various high voltages (HV).

above is only carried out with a single γ-ray source, an interpretation of the energy of the measured light pulses may be made for all energies of γ ray. However, if only γ-ray sources are used or even, a single neutron source is used to calibrate, then interpretation of any measurements of neutrons that are not identical to that used to calibrate may be erroneous due to a lack of a complete neutron calibration curve.

When the Compton edges are all calibrated to the same channel number, the user can switch to PSD mode in the GUI to set the neutron/γ-ray threshold. This is easier to do if a neutron source is available to the detectors, however, if necessary, it can be done with only a γ-ray source. In PSD mode, plots should be produced that clearly show the γ-ray plume and neutron plume if a neutron source is being used. The user can now drag the three discrimination points to suitable positions to give the best discrimination between the neutron and γ-ray events. There is also a cut-off point that can be changed to remove any extraneous high-energy particles from the ensuing counts. This process is done by eye, Fig. 3.9 portrays an example PSD plot with a neutron-γ threshold and energy cut-off applied. The neutron/γ-ray ratio may be different for each detector, even if these two calibration steps are carried out correctly. As discussed earlier, as neutron
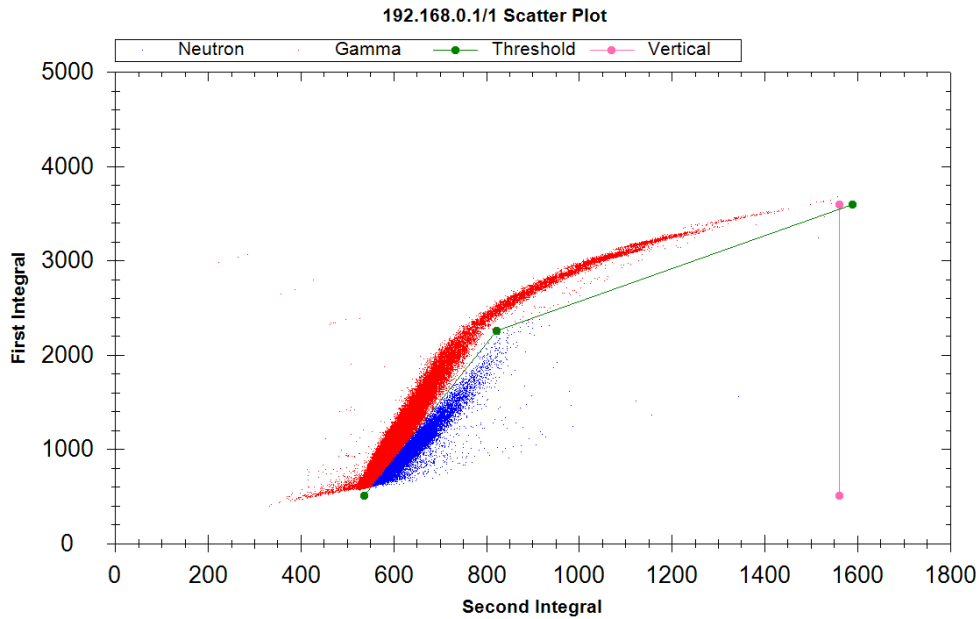
FIG. 3.9: PSD scatter plot with neutron-γ threshold and cut-off included.
This is a 60 s measurement of a ^{252}Cf source with a cubic EJ-309 detector
and single channel MFA unit.

energy deposition is non-linear with regards to the incoming energy of the neutron, any difference in HV between two detectors can dramatically effect the number of neutrons counted. In comparison to γ rays, which have a linear relationship and therefore, a change in HV results in a linear change in the number of γ rays detected.

For a passive assay, a background measurement is taken of ambient radiation and will often be carried out overnight due to the low counting rate. For active assay the background measurement is taken with the activating source in place, as well as ambient background, although any ambient radiation is usually negligible in comparison to the source. These measurements are required to allow the user to correct for background radiation after the sample measurements have been taken, and therefore makes the research more comparable with others in the field and subject to fewer systematic influences.

When the MFAs are running, the GUI can be left to plot PSDs of one or all of the detector signals. During post processing, these plots can be very useful to provide the user with assurance that plumes of neutrons and γ rays are being separated as

(A) 2-D PSD plot

(B) 3-D PSD plot
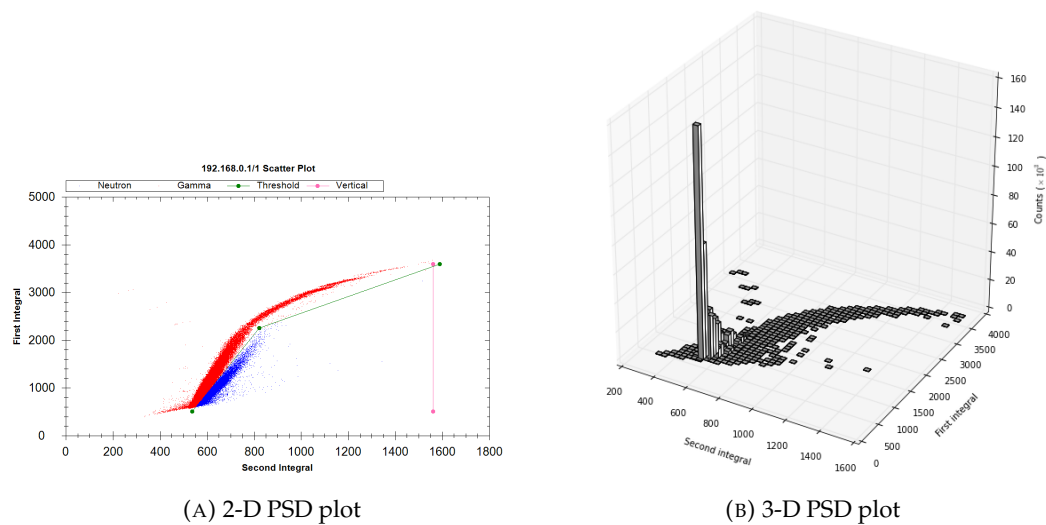
FIG. 3.10: 2-D and 3-D renderings of the same set of PSD scatter plot data; a ^{252}Cf source measured for 60 seconds with a cubic EJ-309 detector. The 2-D image allows clearer threshold placement. The 3-D image gives a clearer indication of where the majority of incidences of radiation have been plotted.

expected. Sometimes this is not the case, and as the PSD plots are 2-dimensional, some information is lost about how *deep* the plumes are. The MFAs have an option to create a text file containing information about the signals that it has processed. These text files must be switched on by the user and are not automatic. They reproduce information about the cable number, particle type, peak amplitude and discrimination amplitude for roughly 10% of the signals that the MFA processes. The data in the text file can be plotted in 3-dimensions to give a better understanding of the plumes measured with the MFAs. The difference between a GUI plot and a 3-D plot is demonstrated in Fig 3.10.

Figure 3.10 makes clear one of the major drawbacks with using PSD. At low pulse amplitudes there can be bleed-or breakthrough between the γ-ray events and the neutron events. This bleed through has been shown to vary between 3-5% of the γ-ray count. In radiation fields which have a large number of γ rays in relation to neutrons, this 3-5% can be rather significant (Sarwar et al., 2018). The worst case scenario for a bleed through issue is a field of radiation with a relatively low-energy neutron source and a large ratio of γ rays to neutrons, such as ^{252}Cf.

3.1.3 Ancillary Equipment

3.1.3.1 TTL Counters

The MFAx4.3 does not count the number of neutrons and γ-rays it processes, and instead sorts the events and sends real-time signals via its transistor transistor logic ports (TTL), one for each type of radiation. Through co-axial cables the signals can be sent to bespoke counting equipment. Two different types of TTL counters have been utilised in the research presented in this thesis, an Arduino-based counter, and an FPGA-based counter. The Arduino counter board simply provides totals of the number of signals it receives from the TTL ports. The development of this system and its embedded software are included in (Beaumont, 2017). The output is via an RS-232 cable to an off-the-shelf serial communication software on a PC. The cumulative total number of counts seen on each TTL port is updated onto the software each 1.15 s and a separate output file can be ascertained with the second-by-second data. This output file may be used to confirm the nature of the radiation emission that has been detected is within expected statistical parameters, i.e., that a Poisson distribution has been measured. The FPGA counter board is a time-based tagging system which affords the ability to carry out coincidence counting anf time-of-flight measurements. It is discussed in greater detail in (Sarwar, 2019). For the purposes of the research covered in this thesis, the FPGA board was used exclusively in counting mode with no time-stamped-data.

3.1.3.2 Ethernet Cables

Although a rather mundane piece of equipment, Ethernet cables afford the user the ability to connect to the MFA systems and any increase in data through-put will aid the user in equipment set-up and data retrieval. The category of Ethernet cable, which can be read along the side of the cable, should be sufficiently high-enough to relay the amount of information that the MFA can output. It is recommended that a minimum of category 5e cable be used. These cables have a maximum data transmission speed of 1000 Mbps and maximum bandwidth of 100 MHz. More preferable is a category 6

cable which has a maximum data transmission speed of 1000 Mbps but an increased maximum bandwidth of 250 MHz.

3.1.3.3 Attenuating Materials

HDPE and lead (Pb) have both been employed to attenuate ionising radiation during experimental research carried out in fulfilment of this thesis. HDPE has been used to attenuate cosmic neutrons, and reflect neutrons back into a sytem that may have otherwise escaped. HDPE has a high neutron cross-section due to its large number of hydrogen nuclei which each have a larger than average neutron scattering cross-section. HDPE is also a useful reflecting material, as it has a low propensity to interact with γ rays, which, for the purposes of research reported here, can be described as interference. Conversely, lead is used in this research to attenuate γ-ray fields, optimise PSD processing, and therefore increase neutron detection efficiencies.

3.2 Monte-Carlo N-Particle code: MCNP

MCNP is an internationally-recognised programming code that is designed for neutron, photon (γ-ray) and electron simulations (Werner, 2017). It is owned and updated by Los Alamos National Laboratory (LANL) and has had a series of iterations since its conception, in 1947. What began as a monte-carlo method for tracing neutron movements through fissionable materials (Metropolis, 1987) has grown into a multi-particle tracking code that is currently being used to design fusion tokamaks and new fission reactors (López-Revelles et al., 2018; Sun et al., 2018). Fig 3.11 shows the timeline of all iterations within MNCP's history. Research within this thesis has been carried out in MCNP-X, MCNP-5 and MCNP-6. The code, in its current form, is run in FORTRAN, and sample codes have been included in Appendices B and C.

The Monte-Carlo method is a class of algorithms that use stochastic sampling to garner numerical results from problems with many coupled degrees of freedom. In its earliest form, the Monte-Carlo method was adopted in the Buffon's needle experiment to obtain Pi (π) by dropping needles onto a surface of stripes (Hwang et al., 2017).
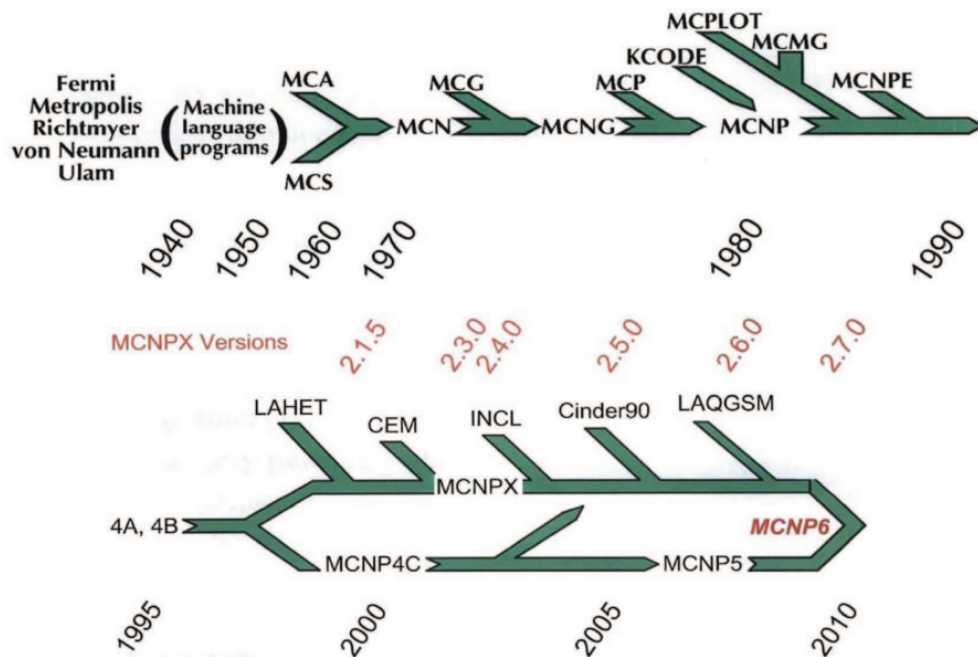
FIG. 3.11: A timeline of the historical versions of MCNP, from conception to present-day. Adapted from (Mashnik et al., 2013).

Buffon devised a formula $\pi = \frac{2l.n}{th}$ where l is the length of the needle thrown, n is the number of needles dropped, t is the width of the stripes, and h is the number of needles crossing the stripes. This formula gave way to the world's shortest rational approximation of π, when Lazzarini dropped 3408 needles, obtaining $\frac{355}{113}$ which is π to 6 s.f. (Lucas, 2005).

For radiation transport, probabilistic events are simulated in turn with the output of MCNP being the most likely outcome of the problem. If you can imagine hitting the same snooker ball 1,000,000 times and coming up with an approximation of the angle and speed at which it moves off, you could then estimate whether it would be likely to impact upon any other balls on the snooker table. This step by step process is what MCNP does, on a molecular level, at an incredible speed. For example, interrogating a 230 g disc of PuO_2 with an AmBe source, with 1800 cm^3 of organic scintillator surrounding the disc, takes only 144 minutes when running on a single core with an Intel Xeon processor. In order to assess each individual nuclear interaction, the code calls upon

nuclear data tables, and in particular ENDF/B-VII.1 (Chadwick et al., 2011) to provide nuclear cross-sections, fission product yields and decay data. The user specifies certain aspects of the simulation, such as geometry, materials, and source particles. The geometry is simulated using a series of surfaces and volumes, each volume is called a cell and is categorised as being important to the simulation or not. Materials are simulated by using their mass proportions and densities. Radiation sources are simulated in various forms. They can be mono-energetic, depicted with a Watt spectrum intrinsic to MCNP, represented with a probability distribution measured experimentally, or created using the *spontaneous fission (SF)* function that MCNP-6 has. These three methods have been utilised for research reported in this thesis.

The user also has to specify what information is required to be produced in the output, from details about the source particles' mass and velocity to flux tallies across detectors. *Tallies* are the most used method of gaining results from MCNP and they can be run in various forms. Tallies F2, and F4 are perhaps the most commonly-used tallies, and the only ones used in this thesis. Descriptions of the tallies are presented in Table 3.1. For both F2 and F4 tallies, the results are presented as neutron flux (per unit of area or volume respectively) per source neutron simulated, i.e., the results are normalised to one neutron being emitted from the source. This removes any impact of the source strength from the results, although this can be overcome by either multiplying the results by the source strength per sec after they are obtained, or by including an FMn card into the code that contains the source strength. An FMn card is a multiplying constant that can be apllied to any result within MCNP. Throughout the research discussed here, the former approach has been taken, in order to make the user contemplate the results rather than accepting them as given. Another tally which is used extensively within this thesis is the *FMESH* tally. This tally places a 3-D mesh into a system and measures the flux within each mesh element separately. FMESH tallies are useful to view flux across volumes such as detectors and samples without having to define multiple tiny cells within which to measure. Over the volume of a standard EJ-309 organic scintillation detector there are 120 cm^3, and it can be foreseen that neutron flux would

Mnemonic	Tally type	Particles pl	Units	Notes
F2:pl	Average surface flux	N, P, NP or E	# cm^{-2}	Average track-length can be used freely as area flux
F4:pl	Average flux in a cell	N, P, NP or E	# cm^{-2}	Average track-length can be used freely as volume flux

TABLE 3.1: Description of F1, F2, and F4 tallies called in MCNP and utilised for work within this thesis (Werner, 2017).

not be the same across this volume size. Energy and time variances can be investigated easily with the tallies mentioned here, simply by adding extra lines of code to describe the energy and time bins required. For example, a request to have fluxes binned at 0.5, 5 and 50 MeV would result in three fluxes being presented, 0 to 0.5 MeV, 0.5 to 5 MeV and 5 to 50 MeV.

MCNP has various methods of letting the user know that input code is incorrect. Firstly, the user should check the geometry and materials are correct by plotting the code in a suitable plotter. When the geometry and materials are understood to be correct, the user may run the file through MCNP and see if any warnings or fatal errors are detected. If the warnings are acceptable and there are no fatal errors detected the code will run and create an output file. Once results have been obtained from the output file checks must be made to ensure that the code has done what is expected. These checks include: ensuring that particles have been created at the correct location (i.e., usually where the source is supposed to be), that they have begun travelling in the specified direction, and that any induced radiation has been released in an appropriate location (usually where the sample material is). There are many other tables in the output of MCNP files that have useful information that corroborate that the file has executed as expected and all information should be taken in before accepting the results.

MCNP carries out a number of statistical tests to clarify whether a sufficient number of particles have been run to trust the output results. These statistical tests run automatically and are presented for each separate tally that has been executed underneath the tally results. If multiple tallies are included in the simulation, each one must be

checked as a number of them may have run perfectly, whilst just one may need more particles to be simulated in order to provide trustworthy results (Hussein, Esam M. A., 2007).

For MCNP to simulate radiation transport systems consistently, the user must try to ensure that the environment is simulated as closely as possible to the real-life scenario. In an ideal scenario as much information as possible would be included in the simulation. In reality, the extra computational effort to run simulations of vast building structures and almost infinite numbers of everyday objects is of little benefit. The user must assess each situation and simulate any important materials as they see fit.

4 Assessment of ^{235}U

Methodologies by which to measure the abundance of ^{235}U in a sample are continually sought, due to its abundance in nuclear materials, and its status as a special fissionable material (SFM). Three experiments carried out in this research to investigate the use of small detector arrays for the assessment of nuclear materials comprising ^{235}U are set out within this chapter. Each experiment is detailed with regards to the methods, the results and analysis of these results. A broader conclusion about the analysis of these results, and how they fit with the wider findings of this thesis can be found in the conclusion (chapter 7).

Firstly, simulations were carried out in Monte Carlo Neutron Particle code (MCNP) version 5 (*MCNP - A general Monte Carlo N-Particle Transport Code, Version 5. Volume 2: User Guide* 2003) to quantify the most efficient geometry for an array of EJ-309 detectors for an active assay. The aim of the experiments was to simulate various detector geometries, from one detector, to 32 detectors, during an active assay of a mass of uranium oxide.

Secondly, the Orr-Box was investigated. The Orr-Box is a high density polyethylene (HDPE), hollow cube in which active neutron singles measurements can be taken (Parker et al., 2016). The box design was intended to prevent the escape of neutrons from a measurement volume and reflect them back in to be detected. It also attenuates cosmic and background neutrons, thus increasing the accuracy of the measurements.

Finally, investigations of various detector arrangements for the active assessment of uranium from 0.3166 - 93.23 % ^{235}U wt. enrichment were carried out. The aim of this investigation was to show that the detectors and ancillary equipment have the ability to discern different enrichments of uranium over a broad range of enrichments, using only singles measurements, as opposed to coincidence counting. The experiments described

in this section were performed experimentally and simulated. The experimental work was carried out by Dr Rashed Sarwar, Dr Vytautas Astromskas and Prof. Malcolm J. JOYCE at Oak Ridge National Laboratory (ORNL), grant number EP/P008062/1. The experimental and simulated work will both be described here.

4.1 Methods

4.1.1 Geometry Optimisation

To investigate the efficiency of various detector geometries, the active assay of low enriched uranium was simulated with a number of proposed geometries. The sample mass of uranium oxide was increased from 0 g to 368 g, whilst remaining at 3 % wt. enrichment. This increase in mass of UO_2 at a steady enrichment led to an increase in the amount of ^{235}U present, which is key to the active interrogation process. The ^{235}U undergoes induced fission (n, f), when interrogated by a slow or thermal neutron source (Knoll, 1999). Therefore, as the mass of ^{235}U increases, the probability of interaction between the incoming slow neutrons and the ^{235}U increases, not withstanding the bulk, and the ensuing number of fast-fission neutrons emitted from the sample increases too. The simulated UO_2 was spherical in shape and its mass was increased by increasing the radius of the sphere in 1 mm increments from 5 mm to 20 mm. The sphere was modelled to contain ^{235}U, ^{238}U, and ^{16}O, with a density of 10.97 g.cm^3. Details of the composition of each UO_2 sphere are included in Table 4.1. The UO_2 sphere was always placed at the centre of the MCNP universe.

The detectors were modelled as 100 mm $\times$ 100 mm $\times$ 100 mm cubes of hydrocarbon material as per the materials compendium for an organic scintillator (McConn Jr et al., 2011). The geometries used were based on a system of placing layers of detectors around the sample, equidistant in both angular and radial space. The detectors were placed with a minimum of 25 mm between them, to reduce effects of scatter, and therefore cross-talk, between them (this figure was chosen, after carrying out a separate scattering study in MCNP), as per Fig. 4.1. The layered system was chosen, as in

Radius (mm)	Mass (g)	Mass of ^{235}U (g)
5	6	0.15
6	10	0.26
7	16	0.42
8	24	0.62
9	34	0.88
10	46	1.21
11	61	1.61
12	79	2.10
13	101	2.67
14	126	3.33
15	155	4.09
16	188	4.97
17	226	5.96
18	268	7.07
19	315	8.32
20	368	9.70

TABLE 4.1: Details of ^{235}U 3 % wt. UO_2 samples simulated in MCNP. Samples were used in various detector geometries during an active interrogation with an AmLi source.

practice it is the most simple and likely set-up for a detector array. Other geometries including 4π-spherical detector arrays have been investigated elsewhere, for example (Schmitt et al., 1995), but due to the need for bespoke rigs, these types of more sophisticated arrays were discounted for this investigation. In the geometries within which the detectors were very close to the UO_2 source (i.e., low numbers of detectors where the 25 mm separation rule did not apply), the detector front-faces were placed at 15 mm from the edge of the UO_2 sphere. This meant that as the sphere increased in diameter, the distance between the detector and the centre of the sample increased, equal to the radius of the sphere plus the 15 mm.

The only array that does not follow the convention of equidistant layers of detectors around the sample, is the liquid scintillator uranium neutron coincidence collar (LS-UNCL). This geometry is based upon a liquid scintillator (EJ-309) version of the IAEA's UNCL (Joyce et al., 2015). This was included in the investigation to show what has been seen experimentally at the IAEA, that ^{235}U mass cannot be measured successfully using the UNCL device. The purposes of this are twofold, one, to provide information to the

Name	Detectors in circumference	Layers of detectors	Total number of detectors
1 Det mov	1	1	1
1 Det stat	1	1	1
2 Det	2	1	2
3 Det	3	1	3
4 Det	4	1	4
4 by 2 Det	4	2	8
8 Det	8	1	8
8 by 2 Det	8	2	16
8 by 4 Det	8	4	32
16 Det	16	1	16
16 by 2 Det	16	2	32
LS-UNCL*	6	2	12

TABLE 4.2: Details of various detector geometries assessed for efficiency by simulating an active interrogation of UO_2 with an AmLi source. *LS-UNCL arrangement is not circumferential, this set-up is shown in Fig 4.1.

IAEA about the mechanisms of the interactions, and therefore why the UNCL does not seem to differentiate between ^{235}U at small masses, and two, to allow for a benchmark of a real-world system, against which to compare any geometries investigated in this work. The geometries used during this investigation are detailed in Table 4.2, with *1 Det mov* pertaining to an arrangement within which the detector was always 15 mm from the edge of the sphere of UO_2 and in *1 Det stat* the detector was always in the same location (30 mm from the centre of the arrangement). Fig. 4.1 shows a selection of the geometries as made up in MCNP.

Neutron tallies (F2 for neutron-flux and FMesh for image production) were run across the front faces of each of the detectors (from the perspective of the sample). A simulation was run with no sample present, to give a neutron-count of the AmLi stimulating source. This figure was later subtracted from the results of the measurement of the samples to provide a background-corrected result. The AmLi interrogating source was modelled as a point source 1 cm below the UO_2 sphere. It was modelled using measured data provided by the UK's National Physical Laboratory (NPL). A sample of one of the codes used can be found in Appendix A. FMesh tallies were also run within the volume of the UO_2 volume to investigate the flux of fast and slower neutrons within

(A) 1 Det stat

(B) 4 by 2 Det

(C) 8 by 4 Det

(D) LS-UNCL
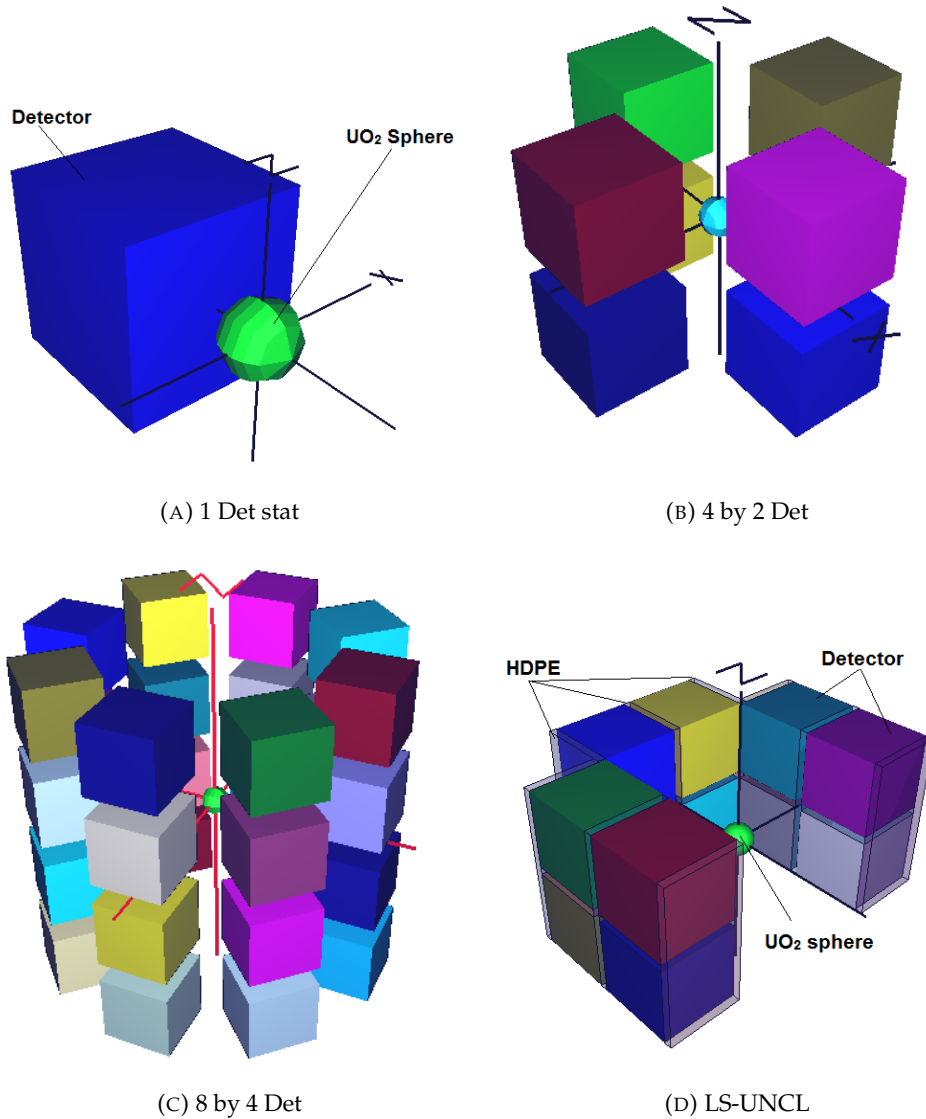
FIG. 4.1: Diagrams of four of the geometries investigated with regards to efficiency, using MCNP-5. Each geometry contains a sphere of UO_2 in the centre, and a number of EJ-309 detectors placed in close proximity. The interrogating AmLi neutron source is always placed 1 cm below the sphere of UO_2 (in the z-plane). *1 Det stat, 4 by 2 Det, 8 by 4 Det*, and *LS-UNCL* geometries are depicted, with axes labelled. The LS-UNCL geometry has 1 cm of HDPE between each detector, this is included transparently.

the sample.

4.1.2 Orr-Box Shielded Measurements

Investigations into the efficacy of the Orr-Box were carried out both experimentally and in simulations in MCNP-5 (*MCNP - A general Monte Carlo N-Particle Transport Code, Version 5. Volume 2: User Guide* 2003). The methods of both sets of investigations are described here sequentially. The experimental methods were carried out by Prof. Malcolm J. JOYCE and Dr Francis D. CAVE at Los Alamos National Laboratory (LANL), whilst the simulations were completed by the author. Analysis of both sets of data were carried out by the author.

4.1.2.1 Experimental methods

The Orr-box dimensions as seen in Fig. 4.2, are 750 mm $\times$ 750 mm $\times$ 760 mm, and the container houses an aluminium table upon which the detectors are placed. This table has a height of 460 mm. A photgraph of the box and table can be seen in Fig. 4.3. The elevated position of the table, and therefore detectors, reduces neutron scatter from the surroundings and the floor, in particular.

Four VS-1105-21 EJ-309 organic scintillation detectors were placed orthogonally on the aluminium table, level with, and equidistant to the sample (Enqvist et al., 2013). The detector volumes were 100 mm $\times$ 100 mm $\times$ 120 mm, and photo multiplier tubes (PMTs) of the type 9821 FLB (ADIT Electron Tubes, Sweetwater, TX) were coupled directly. Signal and power cables were routed through a small port in the box, to a four-channel Mixed Field Analyser (MFA) x4.3 real-time pulse-shape discrimination analyser (Hybrid Instruments Ltd., UK) (*MFAX4.3*).

After the equipment was set up and calibrated using the methods detailed in section 3.1, measurements of the two major sources of background neutrons were taken. For this experiment these were the neutrons emanating from the ^{241}AmLi stimulating source, and neutrons from the spontaneous fission (SF) of ^{238}U in the U_3O_8. To measure the former, the AmLi source container was placed into the Orr-Box and measurements
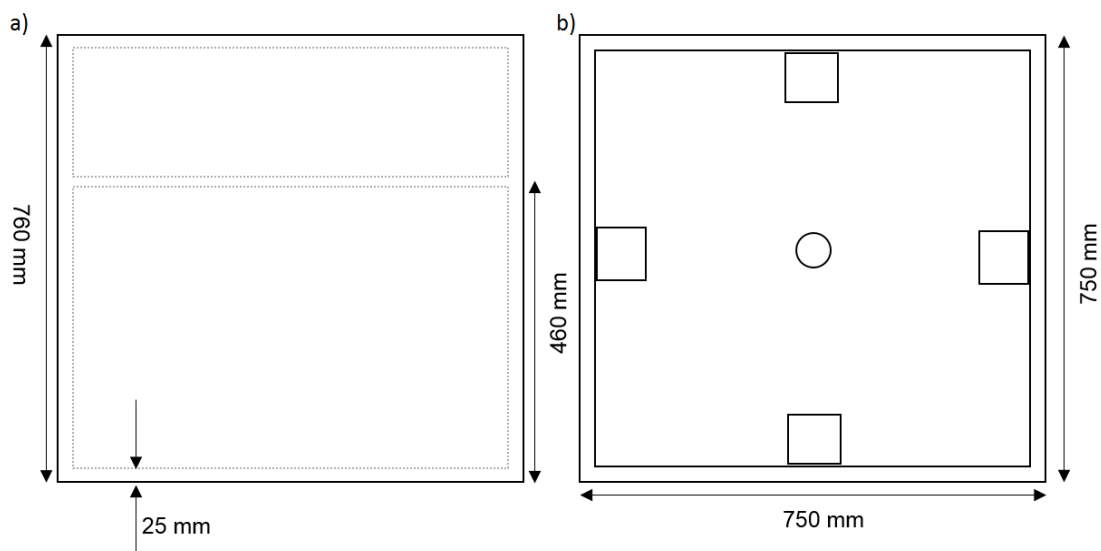
FIG. 4.2: A schematic diagram of the experimental set-up used in this research, a) side elevation (detectors omitted) and b) plan view, showing the high-density polyethylene box of thickness 25 mm and dimensions 750 mm × 750 mm × 760 mm, the thin sheet aluminium stand of height 460 mm, central circular sample container and the four organic liquid scintillation detectors (PMTs not shown for clarity).
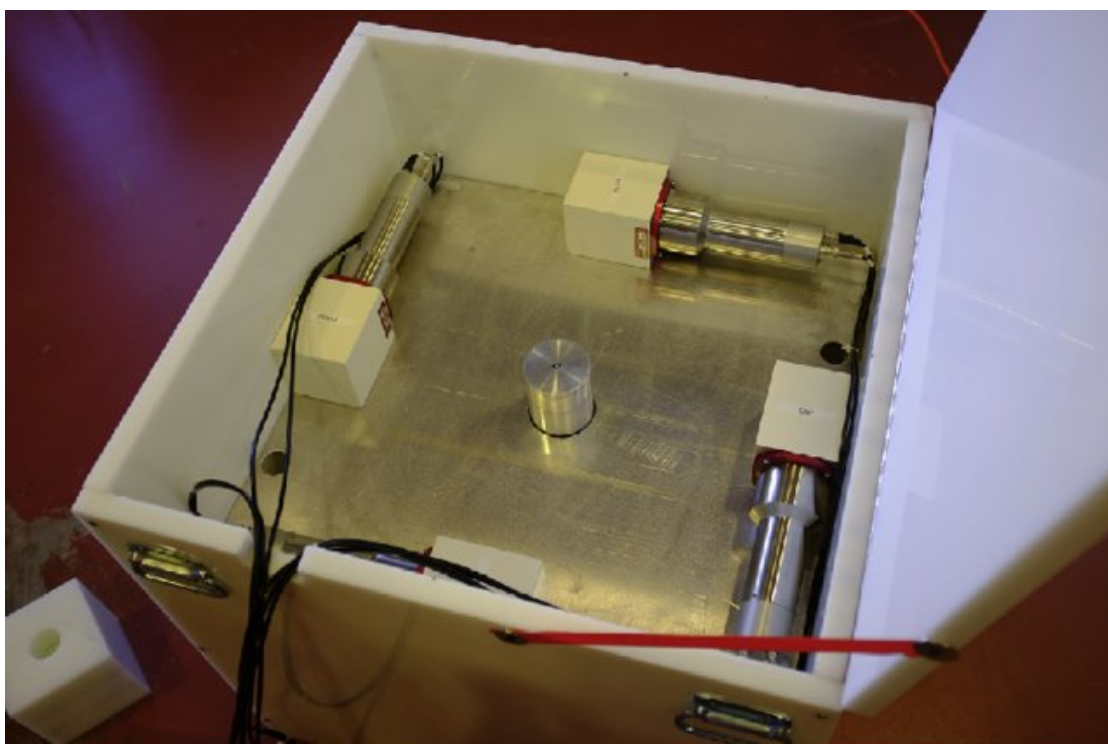
FIG. 4.3: A photgraph of the experimental set-up, showing the HDPE box, thin aluminium stand, and four EJ-309 detectors surrounding a central sample container.

Enrichment (% wt.)	Acquisition time (s)
4.46	1200
2.95	7200
1.94	3600
0.71	3600
0.31	3600

TABLE 4.3: Details of U_3O_8 samples measured during active assay with an AmLi stimulating source. All samples are 200 g. Acquisition times of the measurements are included.

were taken for 1800 s, with no sample present. To measure the SF neutrons from ^{238}U, a sample of U_3O_8 of 2.95 % wt. ^{235}U enrichment was measured for 10 hours (overnight). It was assumed that a measurement of 2.95 % wt. enrichment would provide a suitable count rate for all enrichments from 0.31-4.46 % due to the limited difference in ^{238}U mass as a function of ^{235}U enrichment. These overnight measurements were also used to compensate for any spurious neutrons from cosmic rays, building materials etc.

The AmLi source used had a neutron emission rate of 87,900 n s^{-1} into 4π. The source was a cylindrical Gammatron AN-HP series model 9 with diameter 31.75 mm and length 63.5 mm, doubly encapsulated in type 17-4 stainless steel. The source was presented as 0.222 TBq $^{241}AmO_2$ powder combined with lithium. The source capsule was then contained in a 40.6 mm diameter, 90.0 mm tall well inside a 150 mm high HDPE cube.

Five samples of 200 g U_3O_8 were measured. Details of the enrichments along with acquisition times can be seen in Table 4.3. The samples were housed in a polyethylene cylinder to increase thermalisation of the emitted neutrons.

In the experimental work, no correction for cross-talk between detectors was made. As the arrangement dimensions were kept the same for all measurements, i.e., the solid angle between the sample and each detector remained the same, it is assumed that the prevalence of cross-talk would remain in a linear relationship to neutron count (Joyce et al., 2019; Enqvist et al., 2011). These measurements were also based on the use of a calibration trend. Therefore, scattering can be assumed to be constant for all enrichments when the small change in count rate, from sample to sample is taken into account.

4.1.2.2 Monte-Carlo simulations

The details described above were simulated in Monte Carlo Neutron Particle code (MCNP) version 5 (*MCNP - A general Monte Carlo N-Particle Transport Code, Version 5. Volume 2: User Guide* 2003). Due to the flexibility of the software, it was also decided to simulate an alternative geometry that has been used in industry in the past, known as the liquid scintillator uranium neutron coincidence collar (LS-UNCL) (Joyce et al., 2015). This was done to provide a benchmark of the the Orr-Box system but also to gain more understanding about the apparent lack of suitability of the neutron collar to assay small masses of fresh fuel.

The samples described above were simulated along with a sample of 200 g U_3O_8 at 0 % wt. ^{235}U enrichment. A simulation was run without any sample present, in order to provide a count that would be attributed to the ^{241}AmLi source. The small contribution from SF neutrons from ^{238}U were measured, but the environmental settings were not simulated, nor was their contribution to the background count. The background measurement of the neutrons from the ^{241}AmLi and SF neutrons from ^{238}U is subtracted from the measurements with U_3O_8 sample present to give a net neutron count. The Orr-Box geometry was simulated according to the dimensions and descriptions given above. The LS-UNCL arrangement was simulated by placing three blocks of four detectors in a square shape around a sample placed at the centre of the square. One side of this square is inevitably empty and this is where the AmLi source is presented. The detectors for both sets of simulations were depicted using scintillant blocks, with no PMTs or associated wiring. In both cases the AmLi was simulated as a point source and the U_3O_8 is encased in polyethylene to thermalise incoming neutrons. For the LS-UNCL arrangement, 1 cm of polyethylene was sandwiched between any neighbouring detectors to maintain its similarity, and allow for comparison between previous works (Joyce et al., 2015). The AmLi source was positioned 5 cm below the U_3O_8 discs. Details of the set ups can be seen in Fig. 4.4, where the star shape represents the location of the AmLi source. Labels for each of the detector sets are included in the figure and these labels will be used furthermore to describe the methods and results. For each

(A) Orr-Box geometry

(B) Labelling system for Orr-Box

(C) LS-UNCL geometry

(D) Labelling system for LS-UNCL
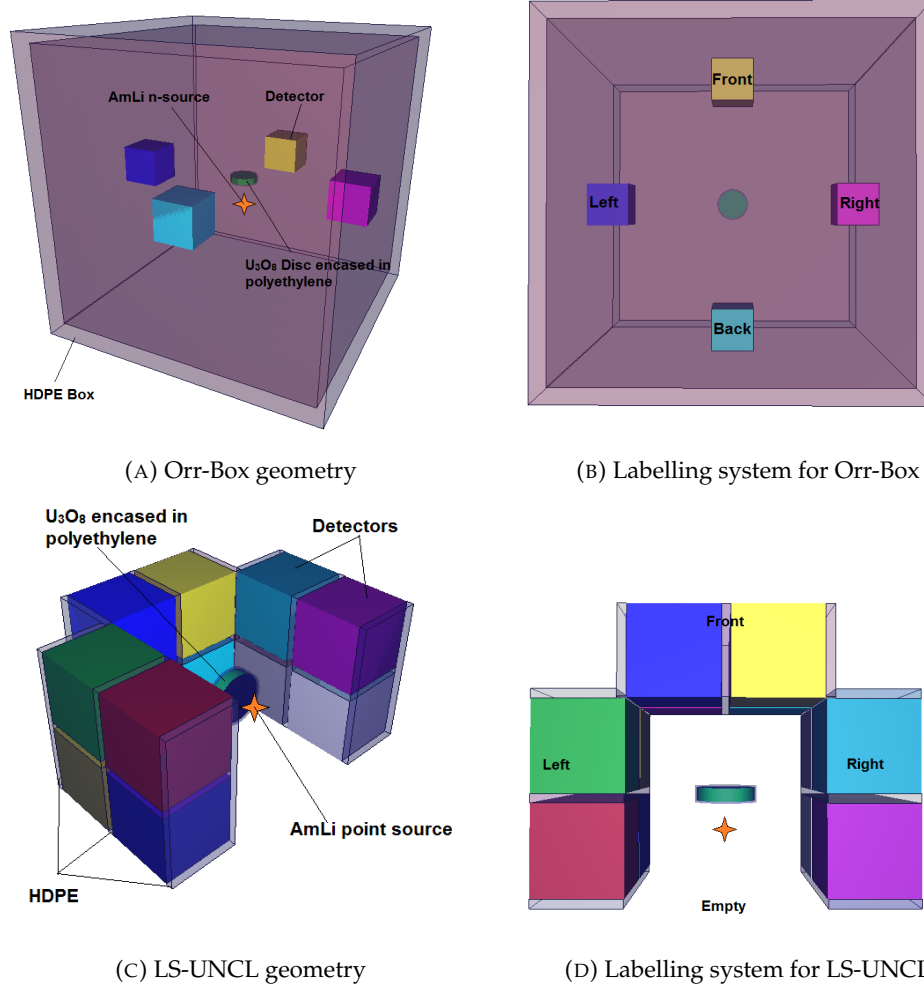
FIG. 4.4: Geometries of MCNP-5 simulations used to compare the Orr-Box geometry with the LS-UNCL geometry. Labels for each side of the geometries are included. The orange star-shape depicts the place where the AmLi point source is simulated.

simulation, a neutron tally was measured across the front face of each detector (from the perspective of the sample). A neutron tally was also carried out on the *empty* side of the LS-UNCL arrangement to provide insight into the neutron flux crossing this plane. All simulations were carried out with an adequate number of neutrons to provide confidence statistically.

Title	Number of detectors	Radius of detectors (cm)	Thickness of polyethylene thermaliser (cm)
8 Det 6 cm	8	20.5	6
15 Det 6 cm	15	26.25	6
15 Det 3 cm	15	25.25	3
UNCL	12	10	3

TABLE 4.4: Descriptions of four geometries of EJ-309 detectors used to measure neutron count during the simulated and experimental active assay of U_3O_8 with a thermalised AmLi source. Titles are derived from the number of detectors in the set-up, as well as the thickness of the HDPE neutron-thermaliser.

4.1.3 Broad Range Enrichment Investigation

This investigation focused on the measurement of singles neutron-counts from a sample, activated by four AmLi sources summed together, in four different geometries. The four geometries used are described in Table 4.4 and can be seen in Fig. 4.5 and 4.6, where the titles are derived from the number of detectors in the set-up, as well as the thickness of the HDPE neutron-thermaliser. As per previous research discussed in this thesis, the UNCL set-up is not circular and takes the shape of a three-sided cube (S. Beaumont et al., 2017). This set-up was included here to provide comparison with a real-world example, and to shed further light upon this system.

The U_3O_8 samples ranged from 0.03166 % wt. to 93.1 % wt. ^{235}U enrichment. Further details of the samples can be seen in Table 4.5. The samples were presented in powder form, sealed into separate aluminium canisters. The canisters each have an internal vacancy within which the powder resides, the sample shape is a short but wide cylinder or disc shape. AmLi neutron sources were used to stimulate fission in the samples. Four AmLi sources were used in this research, all of emission rate 3.32×10^5 nps. Each source canister was placed upon the polyethylene neutron thermaliser, above the U_3O_8 samples to reduce AmLi neutron counts in the detectors. For each of the circular arrangements, another hollow polyethylene cylinder was placed at radius 20 cm to reflect neutrons from the source back towards the sample to induce probability of fission. Another use of this cylinder is to soften (reduce) the energy spectrum of the neutrons

Elevation of 8 Det 6 cm arrangement

AmLi canister

Polyethylene
thermaliser

Detector and
PMT

Polyethylene
cylinder

U_3O_8 sample

Aluminium
canister

Plan of 8 Det 6 cm arrangement

U_3O_8 sample

Detector
and PMT

Polyethylene
cylinder

Elevation of 15 Det 6 cm arrangement

Plan of 15 Det 6 cm arrangement

Elevation of 15 Det 3 cm arrangment

Plan of 15 Det 3 cm arrangement

Elevation of UNCL arrangement

Plan of UNCL arrangement

FIG. 4.5: Detector elevations and plans from top to bottom: 8 Det 6 cm,
15 Det 6 cm, 15 Det 3 cm, UNCL. The 15 Det and UNCL images show
slices of the edge of the PMTs across the centre of the arrangement.
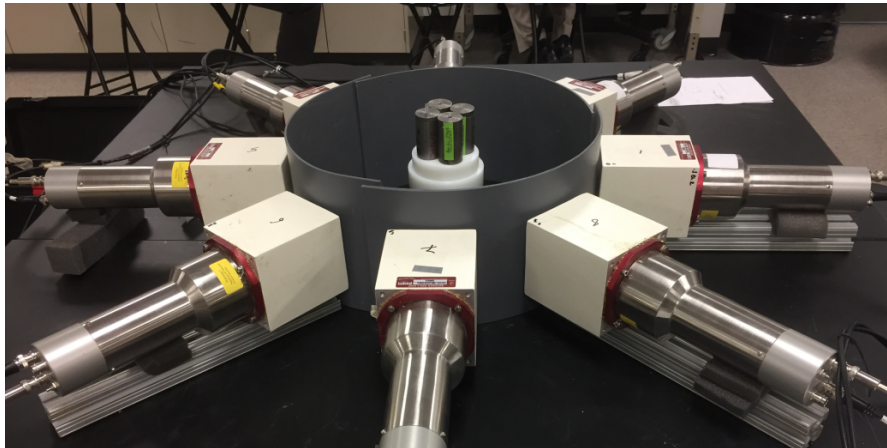
(A) 8 Det 6 cm, shown with lead (Pb).
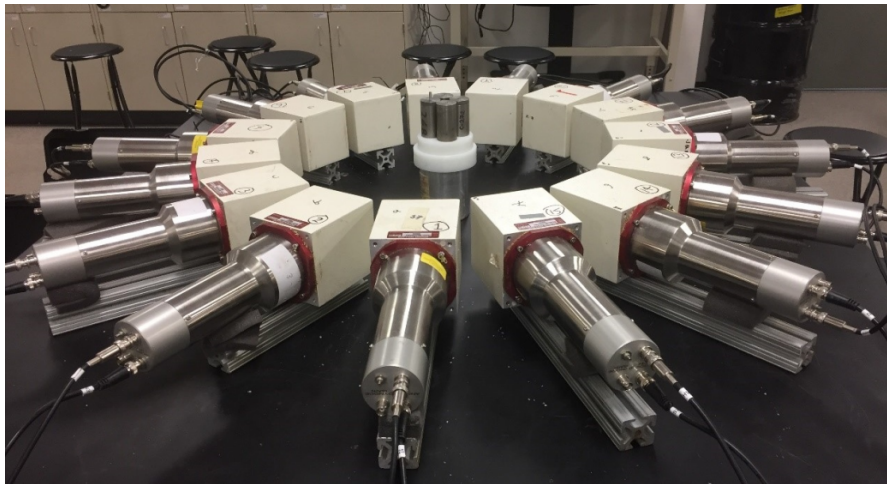
(B) 15 Det setup, shown without lead (Pb) for clarity.
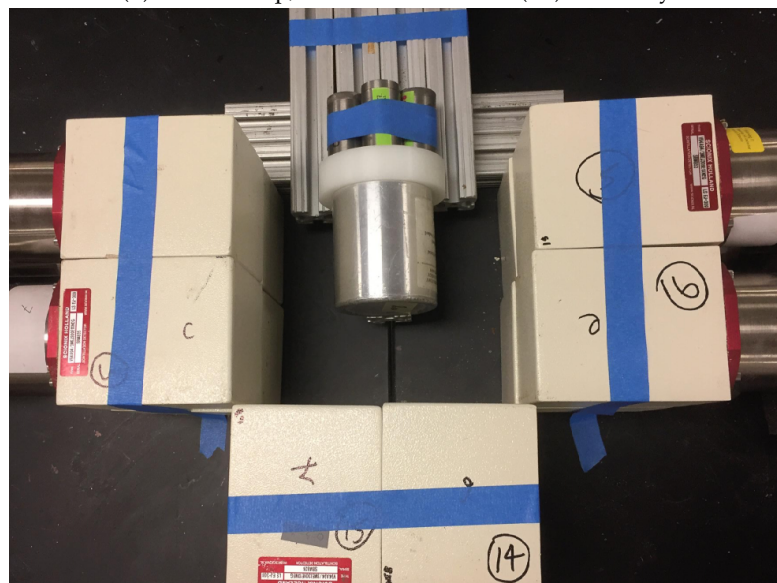
(C) UNCL setup.

FIG. 4.6: Detector arrangements as used in the active interrogation of a broad-range of enrichments of U_3O_8 samples. The 15 Det setup in (b) is applicable to the 15 Det 3 cm, and 15 Det 6 cm arrangements, as the thickness of the polyethylene neutron thermaliser cannot be seen. Photographs courtesy of Dr. R. Sarwar.

Mass percent (%)	Mass U_3O_8 (g)	U_3O_8 Density (g cm^{-1})	Mass ^{235}U (g)
0.3166	200.00 ± 0.2	5.2 ± 0.3	0.52
0.7119	200.00 ± 0.2	5.2 ± 0.3	1.2
1.9420	200.00 ± 0.2	5.2 ± 0.3	3.28
2.9492	200.00 ± 0.2	5.2 ± 0.3	4.99
4.4623	200.00 ± 0.2	5.2 ± 0.3	7.54
20.31	229.99 ± 0.1		39.31
52.80	229.99 ± 0.1		102.61
93.23	229.99 ± 0.1		182.15

TABLE 4.5: Details of eight samples of U_3O_8, assessed actively with AmLi for induced neutron count.

from the AmLi as the detectors have lower efficiency at low energies (Verbinski et al., 1968) and it is not these neutrons that we are interested in.

4.1.3.1 Experimental methods

EJ-309 organic scintillation detectors were utilised (Enqvist et al., 2013) in each of these experimental runs. As per previous research described in this thesis, the EJ-309 detectors were coupled directly to PMTs which are powered and send signals via coaxial cables to Hybrid Instruments Ltd. MFAx4.3 (*MFAX4.3*). As these experiments ran eight, 12 or 15 detectors, a number of MFAx4.3 units were used to accommodate the correct number of detectors. Calibration and background correction measurements were taken as described in section 3.1. The TTL outputs for the neutron count were coupled to a custom FPGA board which accumulated neutron counts for all detectors at once and output the sum of all neutrons counted in real-time (Sarwar, 2019). Samples were placed into the geometry in turn and measured for lengths of time from 445 s to 6342 s. After all eight samples were measured in one geometry the equipment would be reassembled into another geometry and the process repeated again until all eight samples had been measured in all four set-up geometries.

4.1.3.2   Monte-Carlo simulations

The four geometries and eight samples used experimentally were simulated in MCNP-6 (Goorley and al., 2012). Each geometry was simulated in the centre of a domed universe with no environmental parameters but a concrete floor 150 cm below the equipment. The AmLi sources were simulated using an AmLi neutron spectrum (Reilly et al., 1993), as four point sources located at the centre of where each canister was situated during experimental work. Fig. 4.5 shows an example geometry. Neutron tallies were implemented within all detector volumes, at various energies and time intervals. Energy data were collected from 0 MeV to 100 MeV, and time data from 2×10^{-1} shakes to 1×10^{10} shakes (or 100 s). As well as simulating the eight samples being actively measured, a simulation was carried out with no sample present, to mimic the background measurement done experimentally. This background measurement was subtracted from the active measurements of the samples to give a comparable background-corrected assessment to those presented elsewhere within this thesis.

4.2   Results

4.2.1   Geometry optimisation

Firstly, surface plots of the net-neutron flux across a number of specific detector geometries are presented. These images show fluxes across the front surfaces of the detectors in 1 cm intervals. The images are colour graded and show both negative and positive neutron fluxes. A negative, net neutron flux suggests that more neutrons are detected during a background assay than when a sample is present, this possibility is discussed at length in section 4.3. Three geometry results are presented diagrammatically, 4 by 2 Det (Fig. 4.7), 8 by 2 Det (Fig. 4.8), and LS-UNCL (Fig. 4.9).

When each of the total net-neutron flux levels across the surfaces of the detectors are summed we obtain a more suitable method of comparing the results between the geometries. Fig. 4.10 shows the net-neutron flux for each geometry at the various masses of UO_2 simulated.
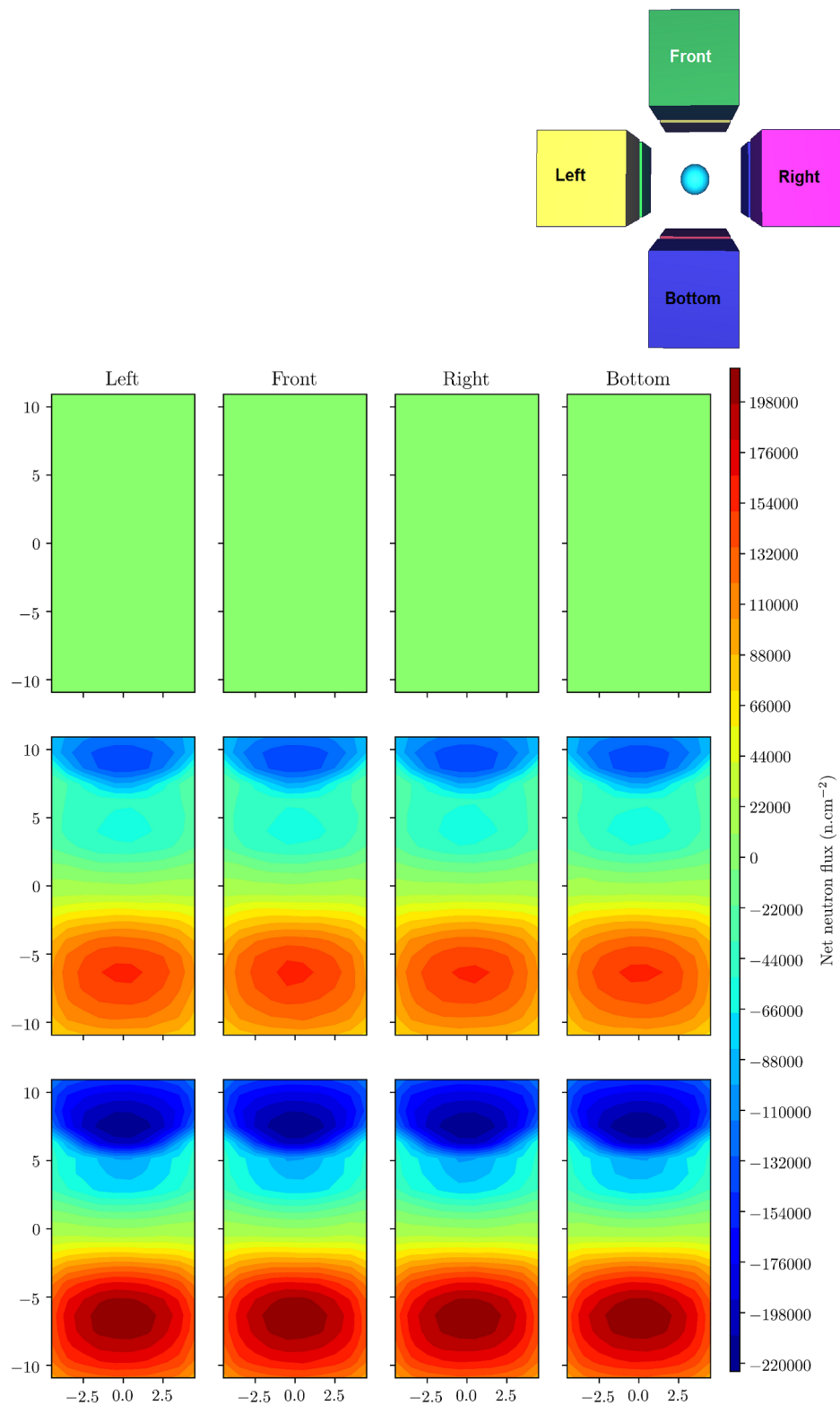
FIG. 4.7: Simulated, net singles surface neutron flux in a 4 by 2 detector geometry during active assay with AmLi, at masses of UO$_2$ at 0 g (top), 101 g (middle), and 368 g (bottom). The axes represent the dimensions of the detector faces in centimetres. The detector labelling system is depicted in the sub-figure. Images of all masses of UO$_2$ can be found in Appendix A, Fig. A.2.
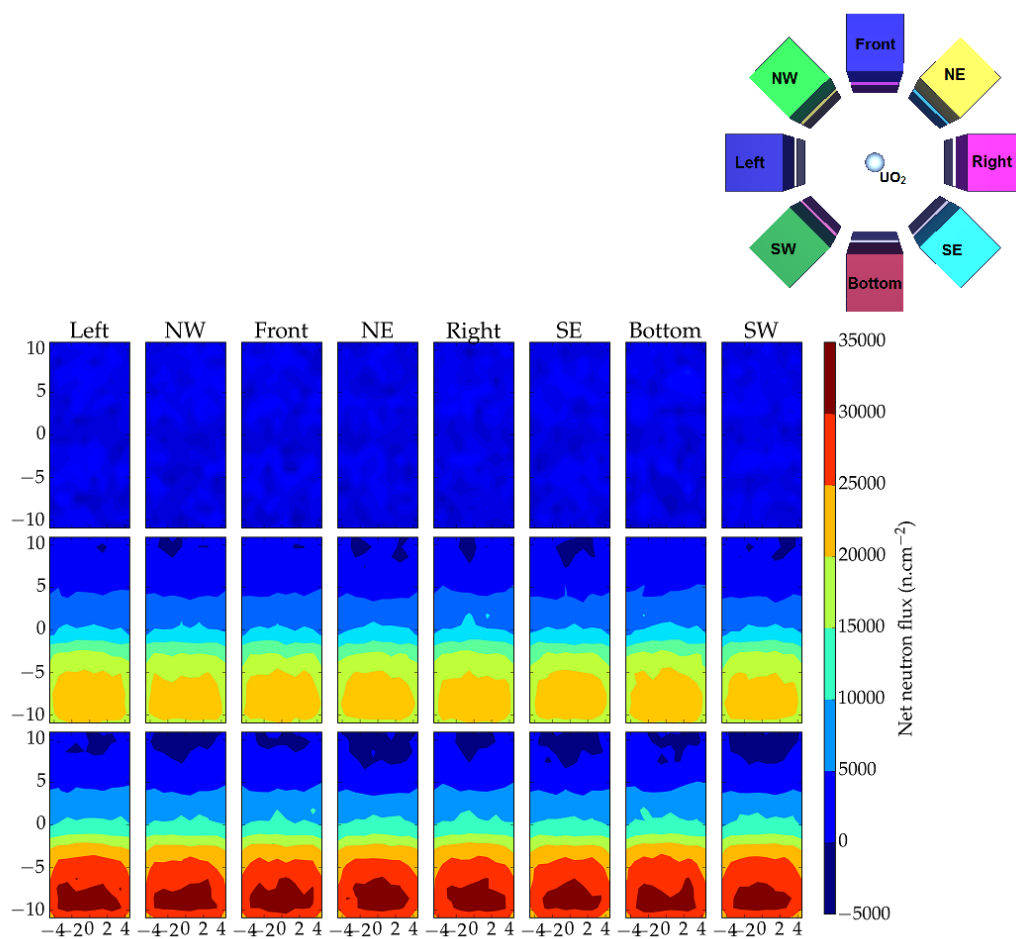
FIG. 4.8: Simulated, net singles surface neutron flux in a 8 by 2 detector geometry during active assay with AmLi, at masses of UO$_2$ at 0 g (top), 101 g (middle), and 368 g (bottom). The axes represent the dimensions of the detector faces in centimetres. The detector labelling system is depicted in the sub-figure. Images of all masses of UO$_2$ can be found in Appendix A, Fig. A.4.
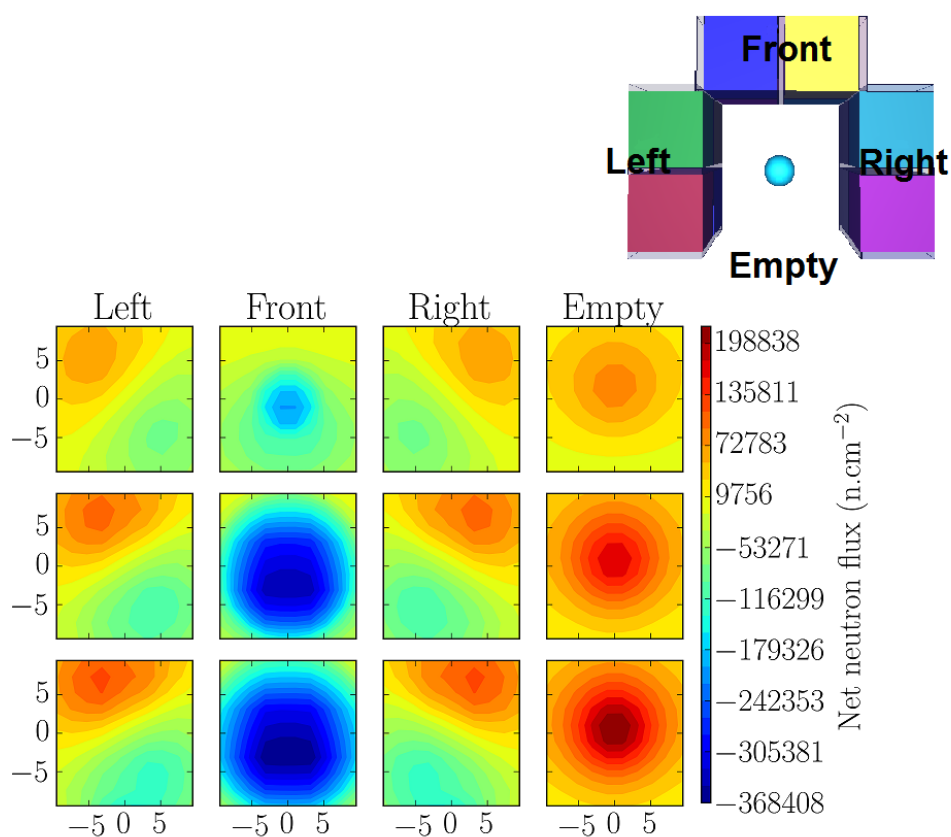
FIG. 4.9: Simulated, net singles surface neutron flux in a LS-UNCL detector geometry during active assay with AmLi, at masses of UO$_2$ at 0 g (top), 101 g (middle), and 368 g (bottom). The axes represent the dimensions of the detector faces in centimetres. The detector labelling system is depicted in the sub-figure. Images of all masses of UO$_2$ can be found in Appendix A, Fig. A.6.
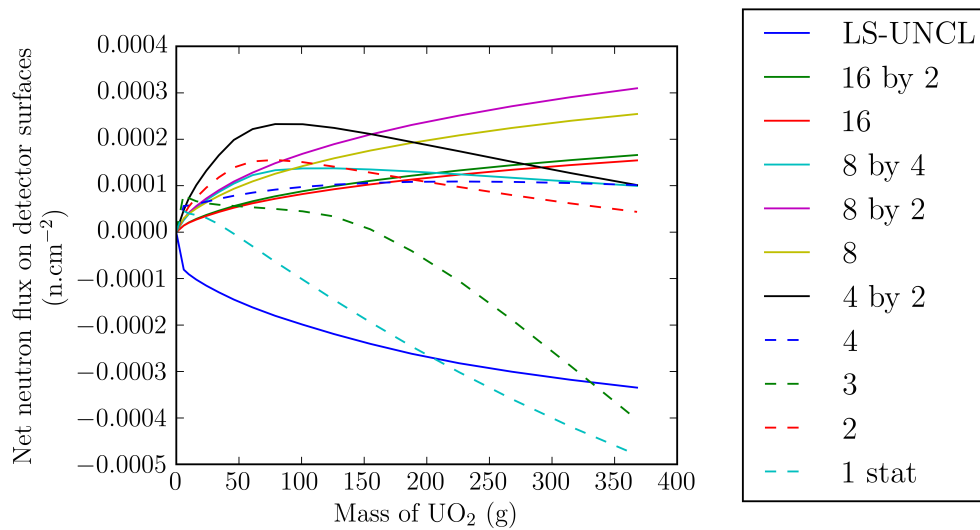
FIG. 4.10: Simulated, net singles surface neutron flux for a variety of detector geometries during active assay with AmLi, at masses of UO$_2$ from 0 g to 368 g

Neutron flux within the sphere of UO$_2$ was simulated. An energy threshold of 1.5 MeV was implemented to specify fast neutrons. Fig. 4.11 presents the neutron flux within the UO$_2$ sphere with all neutron energies considered. Fig. 4.12 shows the neutron flux in the UO$_2$ sphere at energies above 1.5 MeV.

4.2.2 Orr-Box Shielded Measurements

Results of the experimental research carried out are included here for comparison. Fig. 4.13 shows the experimental results, whilst Fig. 4.14 presents the results calculated from the simulations ran in MCNP.

Results from the FMesh tallies within MCNP were plotted to produce the images in Fig. 4.15. The column headings refer to the side of the detector geometry upon which the neutron flux was measured. The axes represent the dimensions of the detector faces in centimetres, with the LS-UNCL surfaces being 20 cm $\times$ 20 cm and the PSC surfaces being 10 cm $\times$ 10 cm.

Neutron fluxes within the U$_3$O$_8$ samples were measured with an FMesh[1] tally to investigate the depth of penetration of the AmLi interrogating neutrons. The FMESH

---

[1]a tally of neuron flux across a 3-D mesh super-imposed over each sample, as per section 3.2
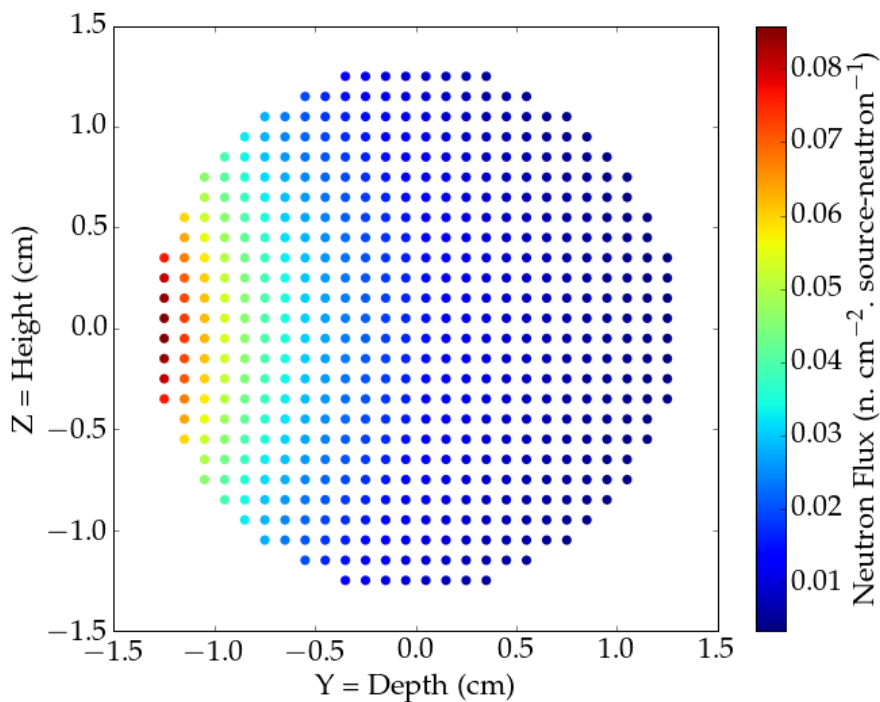
FIG. 4.11: Simulated neutron flux within a 101 g sphere of UO$_2$ when stimulated with an AmLi point source. The AmLi source is positioned at Y=-2.3, Z=0, or 1cm to the left of this slice of sphere. All neutron energies are considered here.
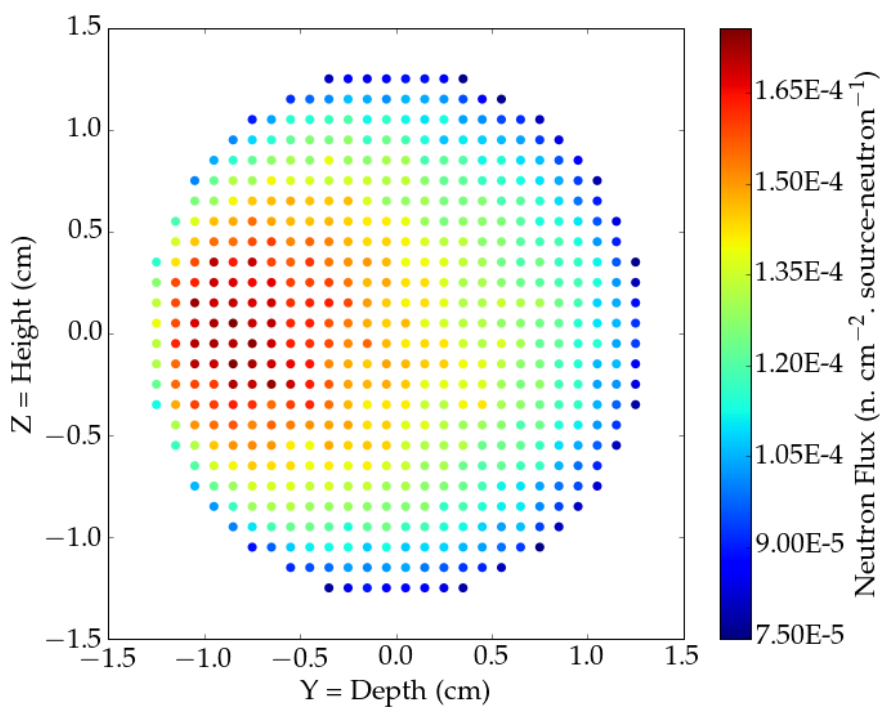
FIG. 4.12: Simulated neutron flux within a 101 g sphere of UO$_2$ when stimulated with an AmLi point source. Neutron energies above 1.5 MeV.
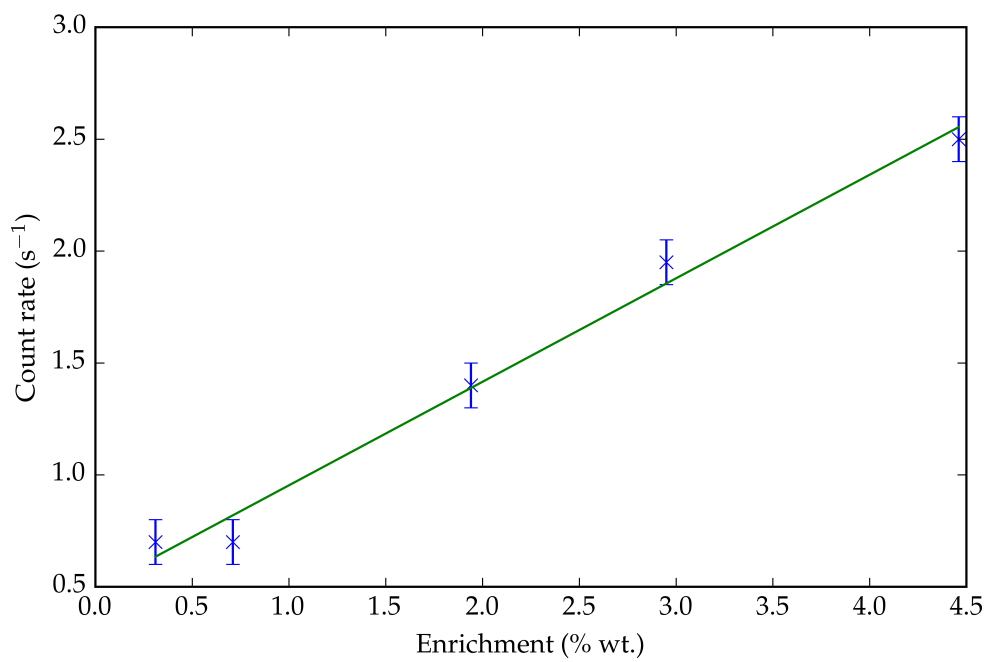
FIG. 4.13: Experimental results of net-singles neutron flux versus ^{235}U enrichment from 0.00 % to 4.46 % for the PSC geometry during active assay with an AmLi source. Linear fit included with parameters: gradient = 0.46 cps % wt.$^{-1}$, intercept = 0.49 cps, and a reduced chi-squared value of 0.008.
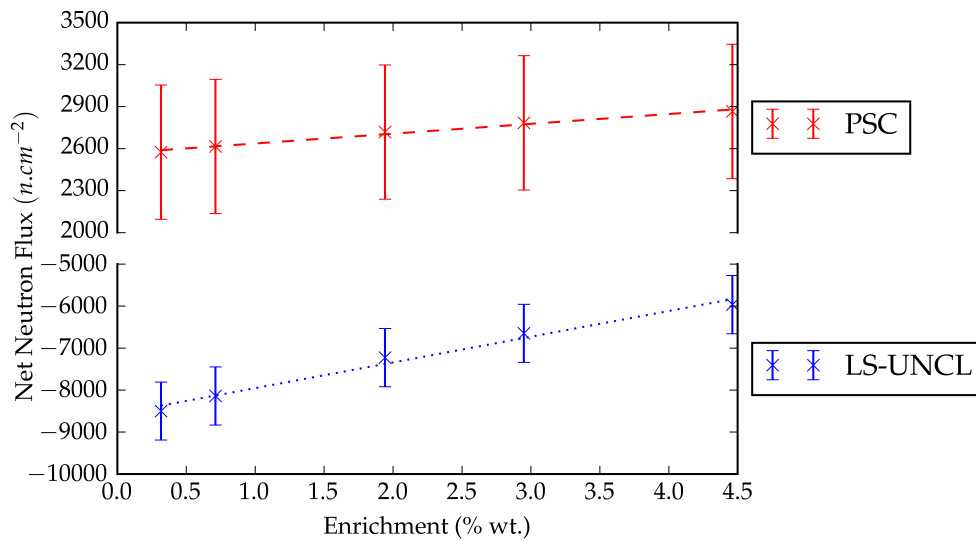
FIG. 4.14: Simulated net-singles surface neutron flux versus ^{235}U enrichment from 0.00 % to 4.46 % for PSC and LS-UNCL geometries during active assay with an AmLi source. PSC graph linear fit included with parameters: gradient = 70 cps % wt.$^{-1}$, intercept = 2566 cps, and an adjusted R^2 value of 0.98. LS-UNCL graph linear fit included with parameters: gradient =612 cps % wt.$^{-1}$, intercept = -8567 cps, and an adjusted R^2 value of 0.98. (Adjusted R^2 is used here as the chi-squared test is unsuitable for data sets that are expected to be negative.)

was a 1mm mesh imposed over the whole disc of U_3O_8. As well as this, a tally was carried out above a 1.5 MeV threshold to ascertain where within the sample the fast-fission neutrons were being produced. The 1.5 MeV threshold was chosen due to the AmLi neutron spectrum, which has very few neutrons above this energy. The results from these measurements are presented in Fig. 4.16.

4.2.3 Broad Range Enrichment Investigation

The data; net neutron cps from the experimental and simulated work carried out can be seen plotted in Fig. 4.17. The data are presented with lines-of-best-fit using a natural logarithmic function of the form $y = a.log_2(x + b) - c$. Table 4.6 contains the fit parameters for both sets of data.

Using the highest available mass of ^{235}U, 182.15 g, plots were created of the net-neutron flux upon the surfaces of each of the detectors in each geometry. Fig. 4.18 presents this information. The UNCL geometry can be seen in the top row with the
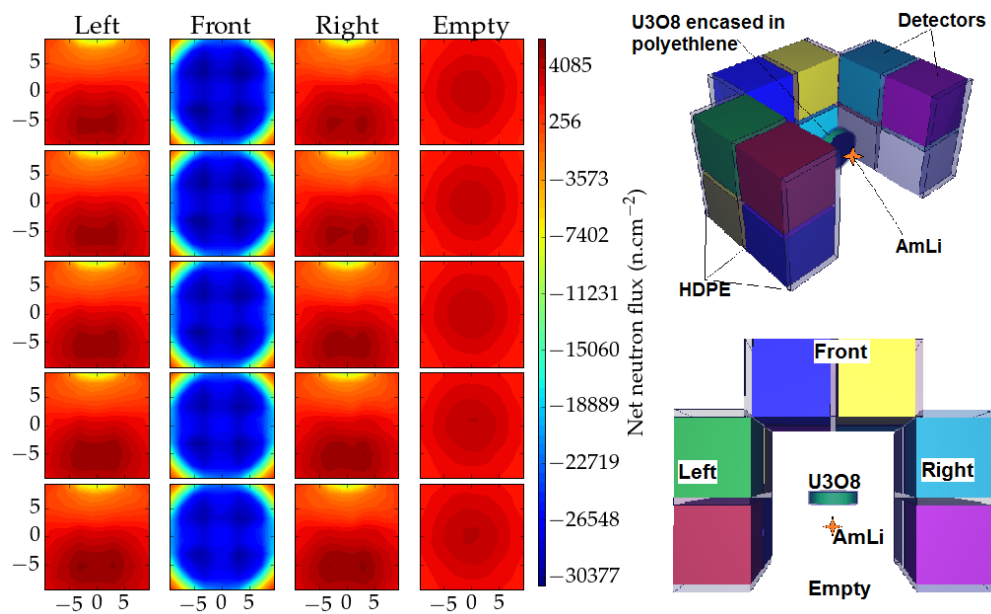
(A) LS-UNCL data
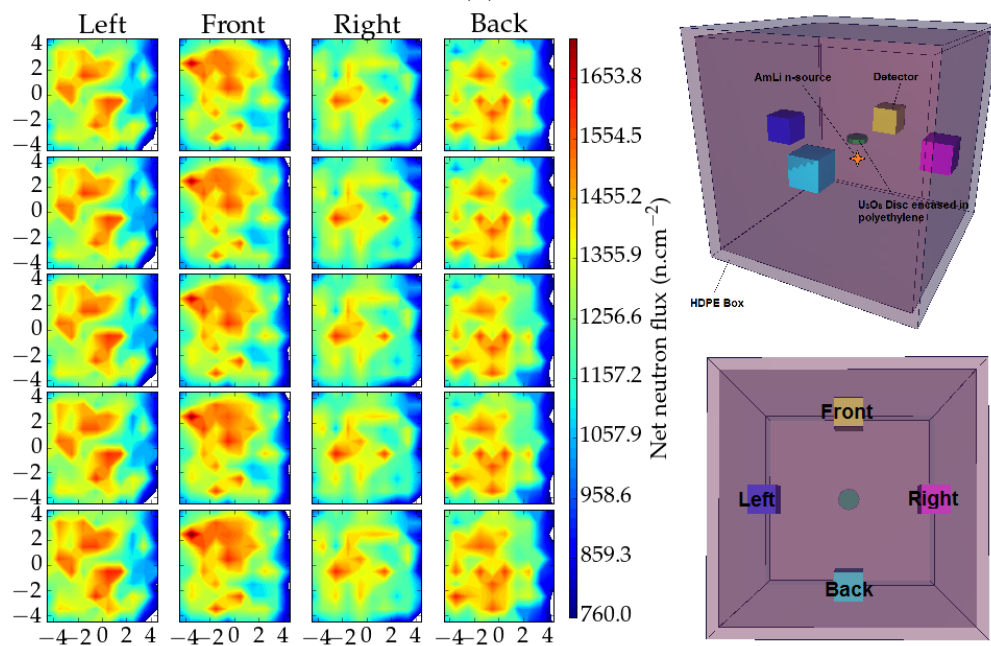
(B) PSC data

FIG. 4.15: Simulated net-neutron flux upon each side of two detector geometries during the active interrogation of 0.31-4.46 % wt. samples (top to bottom) with an AmLi source. The column headings infer the corresponding side of the detector geometry, as shown in the subfigures. The axes represent the dimensions of the detector faces in centimetres, where each face of the LS-UNCL system is 20×20 cm, and the faces of the PSC system are 10×10 cm.
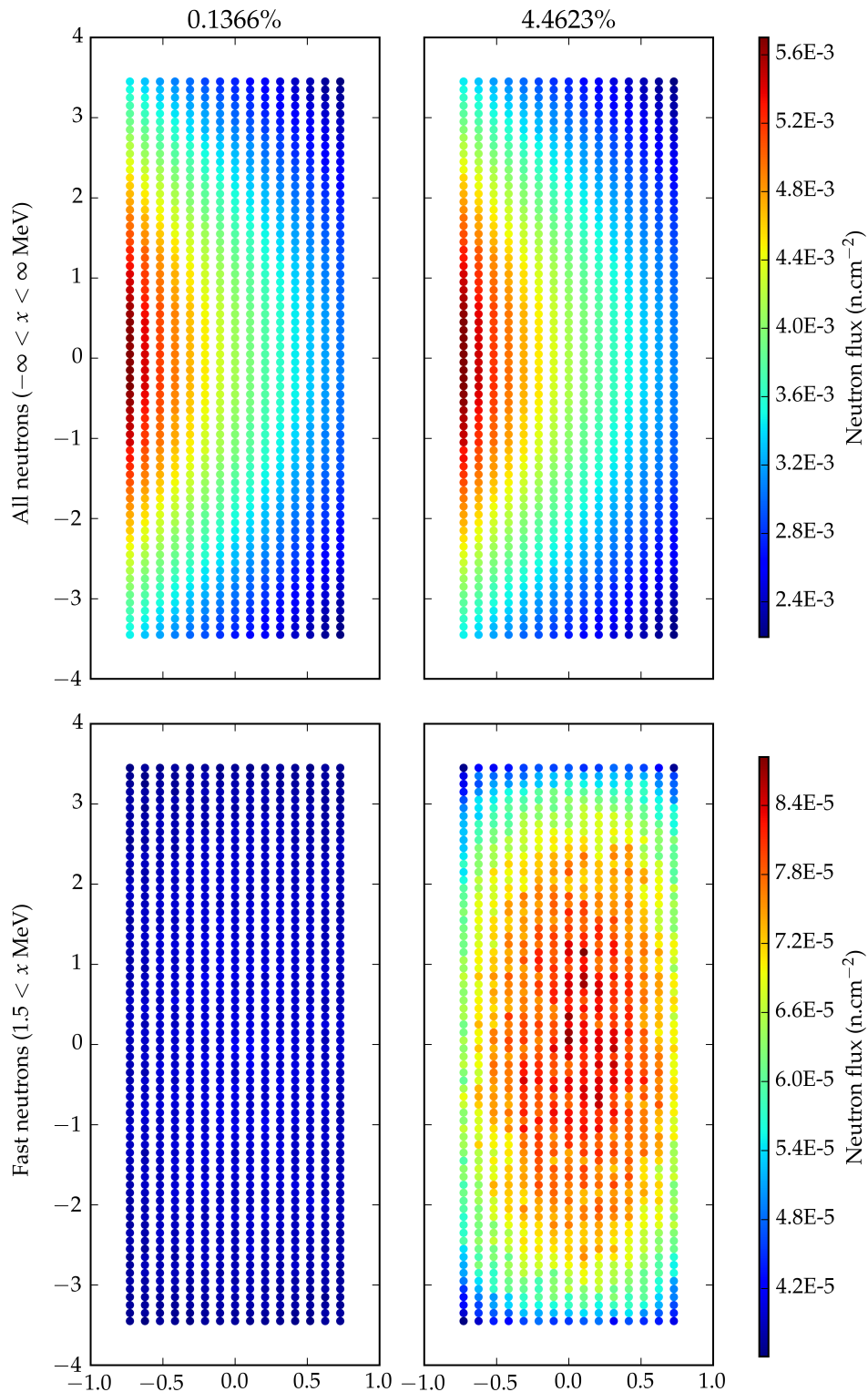
FIG. 4.16: Neutron flux within the central slice of the U_3O_8 samples at 0.1366 % and 4.4623 % wt. enrichment. Top row shows all neutron energies, including the interrogating AmLi neutrons. Bottom row shows neutron energies above a 1.5 MeV threshold, attributed to neutrons created during fission. The axes represent the dimensions of the slice of the U_3O_8 disc in centimetres, depth of the disc on the x axis and radial position of the disc on the y axis.
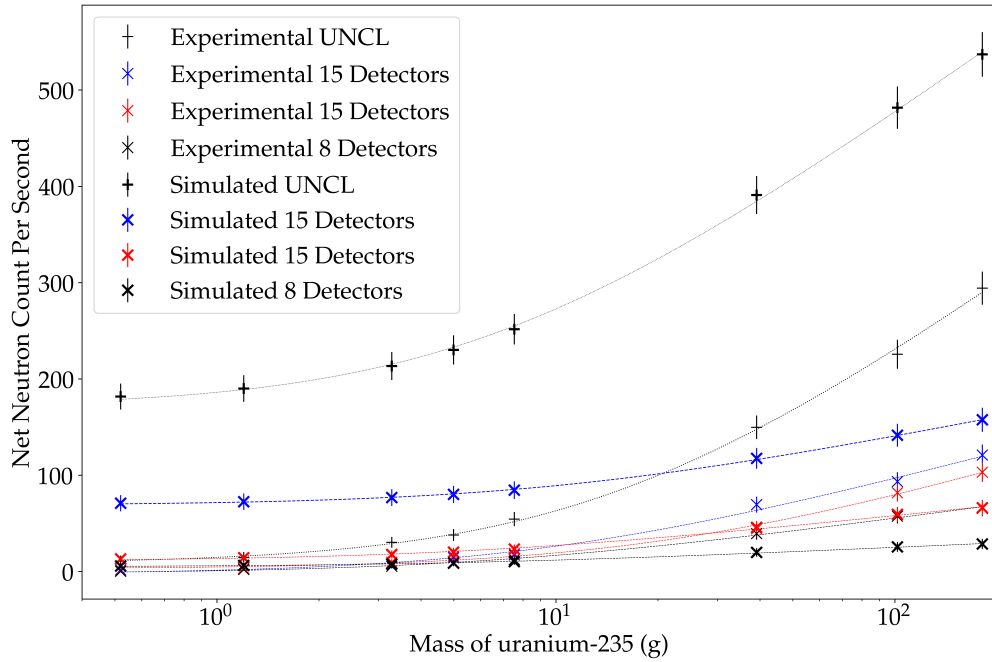
FIG. 4.17: Experimental and simulated net-neutron CPS for four detector geometries during the active assay of masses of ^{235}U from 0.52 g to 182.15 g with four AmLi sources. Lines of best fit of the form $y = a.log_2(x + b) - c$ are included. Fit parameters can be found in Table 4.6.

Net-neutron CPS per g (^{235}U) in the form $y = a.log_2(x + b) - c$					
Experimental data	a	b	c	$\chi_\nu{}^2$	*p-value*
8 Det 6 cm	14.48	6.82	42.18	-0.05	1.0
15 Det 6 cm	31.75	22.86	140.61	5.85	0.55
15 Det 3 cm	28.59	9.82	96.86	-7.65	1.00
UNCL	77.00	15.49	296.64	0.67	0.99
Simulated data	a	b	c	$\chi_\nu{}^2$	*p-value*
8 Det 6 cm	4.82	5.74	7.32	0.09	0.9$\dot{9}$
15 Det 6 cm	11.34	5.93	18.19	0.24	0.9$\dot{9}$
15 Det 3 cm	21.30	10.62	3.83	0.03	0.9$\dot{9}$
UNCL	76.11	6.49	34.95	0.27	0.9$\dot{9}$

TABLE 4.6: Fit parameters, in the form $y = a.log_2(x + b) - c$, for normalised-net-neutron counts per second (CPS) detected in four detector geometries during an active assay of ^{235}U with AmLi neutrons. $\chi_\nu{}^2$ and p values for each line-of-fit are also included.

volumes of the 12 detectors represented, 4 detectors for the left, bottom, and right side. For the circular detector arrangements, only one detector is shown as the symmetry of the arrangements dictates that all detectors would statistically receive a consistent flux.

Using results from the highest and lowest efficiency arrangements; UNCL and 8 Det 6 cm respectively; plots were computed of the neutron spectra of the lowest and highest masses of ^{235}U over a 100 second window. These plots aim to show the worst case and best case scenarios in terms of efficiency and neutron counts. Each plot contains a threshold at 0.5 MeV as per the cut-off of detection for the EJ-309 detectors. The plots can be seen in Fig. 4.19. Fig. 4.20 depicts the same data in a different way, summing the flux over all of the energies. These are then plotted against the time elapsed since the source neutrons were released.

4.3 Analysis

Three experiments have been carried out with respect to the active assessment of ^{235}U: an optimisation of multiple detector geometries, a boxed-array assessment, and an assessment of a broad-range of enriched samples in various geometries. The results of said experiments have been presented in Section 4.2. This section will analyse this research, in comparison with previous research and, in places, theoretically expected results.

4.3.1 Geometry Optimisation

The ideal system would produce a directly proportional correlation in order to be useful for these types of measurements. Best practice would suggest a linear trend affording the user the ability to extrapolate the neutron detection rate with increasing mass size (PINCKNEY and GNAEGY, 1986). Fig. 4.10 confirms that not all detector geometries investigated are equally suitable for measuring fast neutrons during an active assay of UO$_2$. Five of the geometries investigated produce a positive correlation, in order of efficiency using the gradient of the result lines, these are: *8 by 2 Det, 8 Det, 16 by 2 Det,*
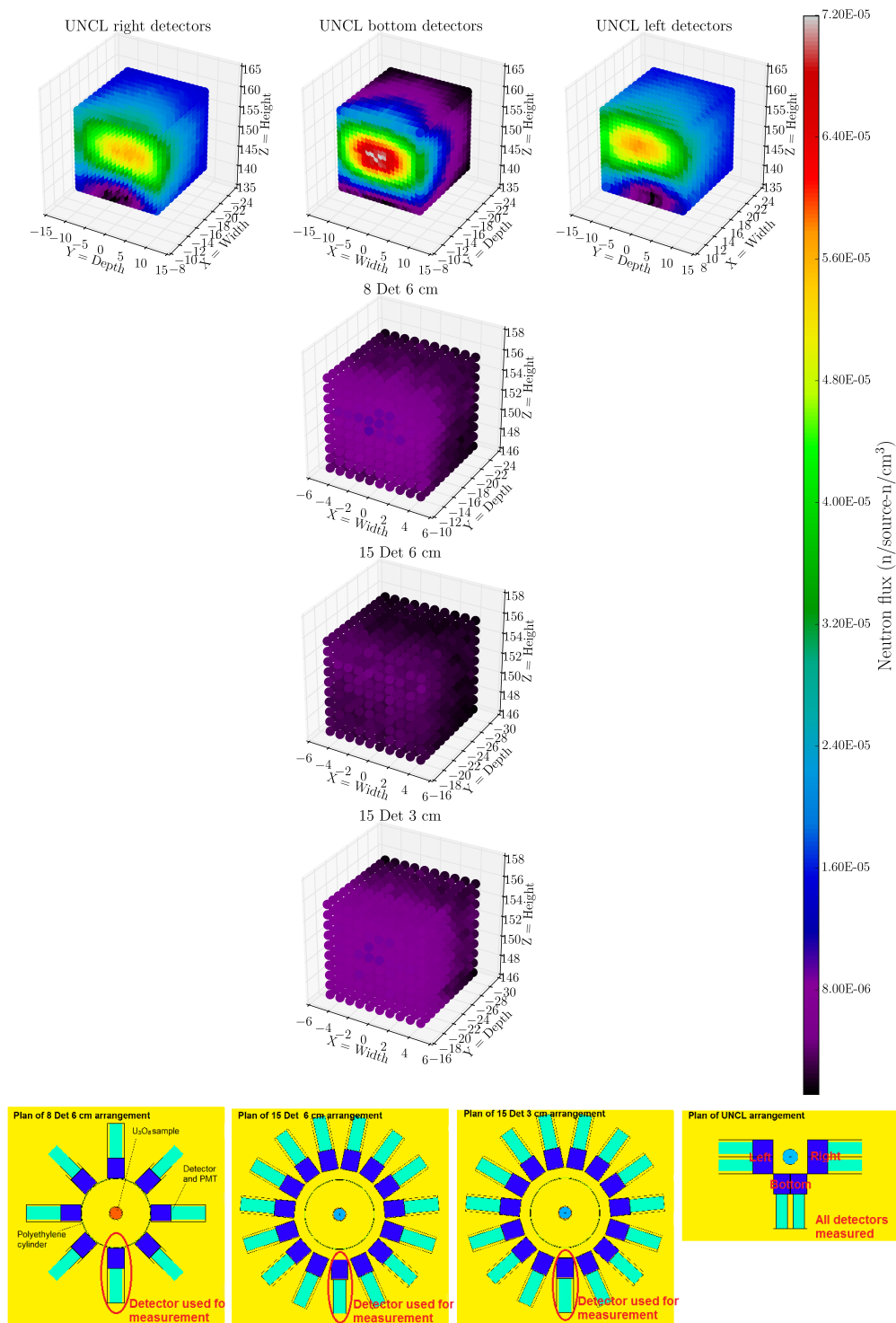
FIG. 4.18: Simulated, net-neutron flux in four detector geometries during the active assay of masses of ^{235}U at 182.15 g (maximum flux) with four AmLi sources. Top row: UNCL geometry, right detectors, bottom detectors and left detectors. Bottom row: 8 detectors with 6 cm of HDPE, 15 detectors with 6 cm of HDPE, and 15 detectors with 3 cm of HDPE, respectively. The circular geometries have only one detector plotted due to the symmetry of the set-ups. All images share the same colour-bar.
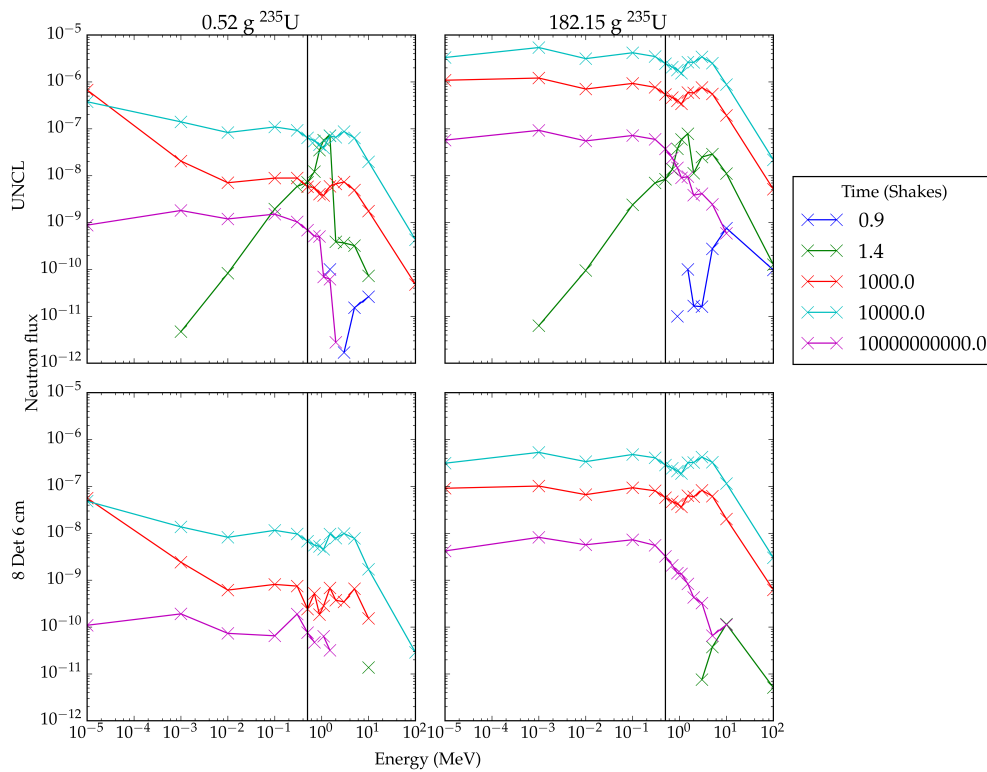
FIG. 4.19: Simulated neutron spectra for the lowest efficiency geometry (8 Det 6 cm) and highest efficiency geometry (UNCL) during the active assay of masses of U-235 at 0.52 g to 182.15 g with four AmLi sources. Fast neutrons reach the detector volumes first, then flux increases across the spectrum until a maximum at 10,000 shakes when the spectrum softens for all arrangements and masses of ^{235}U. A 0.5 MeV threshold is applied in black on all four plots.
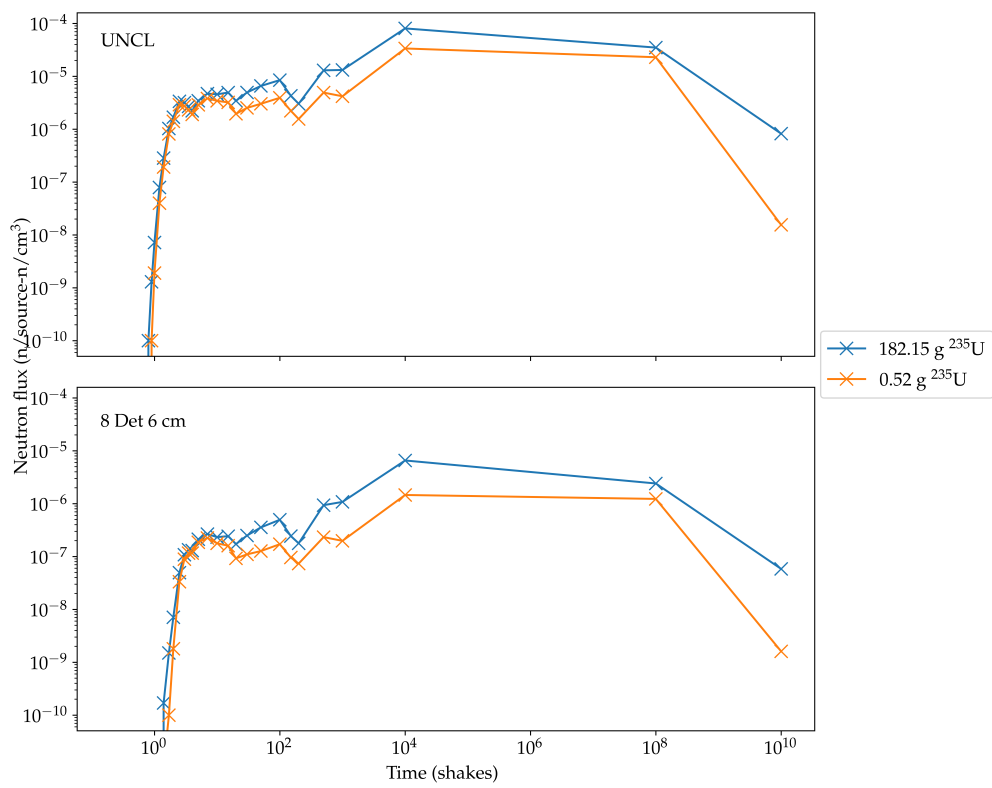
FIG. 4.20

16 Det and *4 Det*. The geometries tested that do not garner useful results include: *LS-UNCL, 8 by 4 Det, 4 by 2 Det, 3 Det, 2 Det* and *1 Det stat*. The trends of these results either have negative correlations or are parabolic, both qualities rendering them insufficient to discern suitable correlations between UO_2 mass and neutron flux. Arrangements with low numbers of detectors (*3 Det, 2 Det* and *1 Det stat*) all suffer from a low counting efficiency purely due to the lack of detector surface present. The solid angle subtended by the detectors in each of these scenarios is small in comparison to the full 4-π space available.

Upon further investigation, when considering the flux across each detector in each geometry it can be seen that the detectors above the UO_2 samples measure significantly fewer neutrons than those below the sample. Figs. 4.7, 4.8 and 4.9 all show these traits. This can be attributed to self attenuation within the sample, and the inability of the slow-interrogating-neutrons to penetrate the sample to produce fission events in the *top-half* of the sample. This is confirmed by Figs. 4.11 and 4.12, with the former showing that the incoming slow neutrons only penetrate into the first millimetre of the sphere's depth, and the latter portraying the fast-neutrons produced from fission, that are mostly concentrated in the first half of the sample. When this information is overlaid onto the geometries used in these experiments we can create a demonstration using the *8 by 4 Det* geometry as shown in Fig. 4.21. The attenuation factor (G) of a sphere of 0.3 % wt. UO_2 can be calculated using the following formula (Glaser, 2004):

$$G = \frac{3}{4r\mu}(1 - e^{\frac{-4}{3r\mu}})$$

where μ is the linear attenuation coefficient, and r is the radius of the sphere. Using (Sears, 1992) data tabulated in (*Neutron Scattering & Activation Estimation*), μ is calculated to be 0.047 cm^{-1} for 0.3 % wt. UO_2 of density 10.97 g cm^{-1} with neutrons of 2.5 MeV (or wavelength 5.72 Å). Letting r range from 5 mm to 20 mm as per the experiments carried out, the attenuation of the spheres used here, normalised to the 5 mm sphere can be calculated and plotted, as per Fig. 4.22. In real terms, assuming that 100 % of neutrons escape the 5 mm sphere, only 19.6 % would escape the 20 mm sphere, which
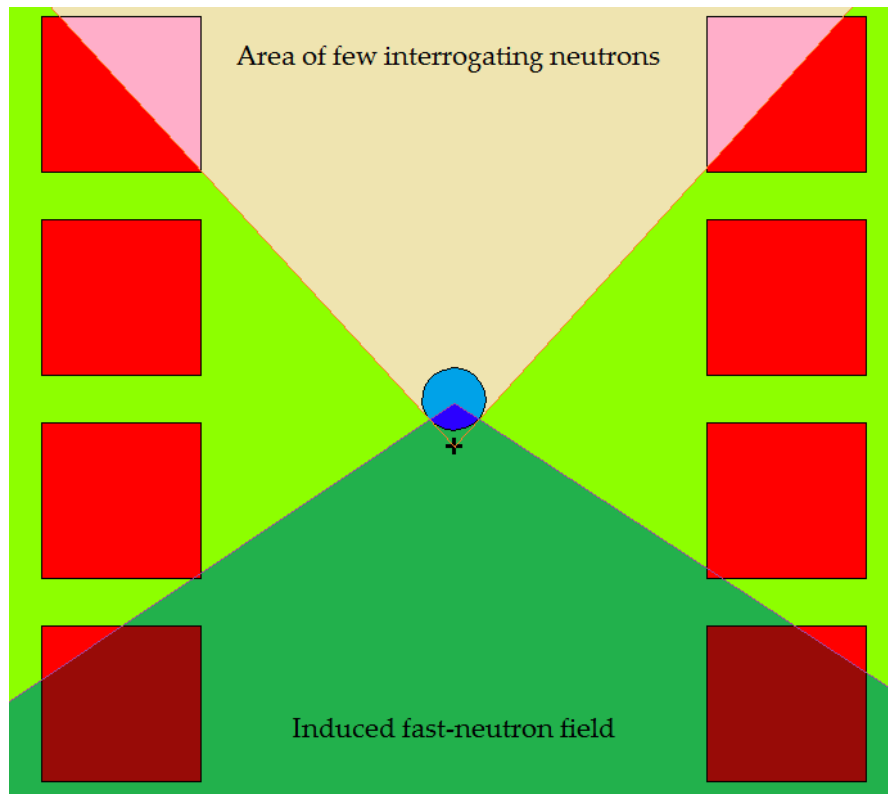
FIG. 4.21: Demonstration of the effects of self attenuation and low penetrability of UO_2 when stimulated with an AmLi point source, where the + symbol denotes the location of the AmLi source. Due to self-shielding within the sample, the thermal-interrogating field is prevented from reaching certain areas of detector material, as seen in the lighter colours. Using the penetrability study of the sample (Fig, 4.12), the induced fast-neutron flux was shown to be concentrated within the first half of the UO_2 sphere. Overlaying this information onto the image allows for a crude interpretation of the fast-neutron flux, seen here in darker colours.

is not insignificant when being taken into account for these experiments.

The areas of negative net-flux, as seen in blue in Figs. 4.7, 4.8 and 4.9, are due to the background measurements performed, which were carried out with the AmLi stimulating-source present, but no sample. In the no-sample scenarios the AmLi neutrons are unperturbed and exert a neutron flux on each detector surface inversely proportional to the distance between the AmLi source and detector. When a sample is placed into the arrangement, 1.5 cm from the AmLi, the slow neutrons no longer have a free-path to the detectors above where the sample is placed as can be deduced from
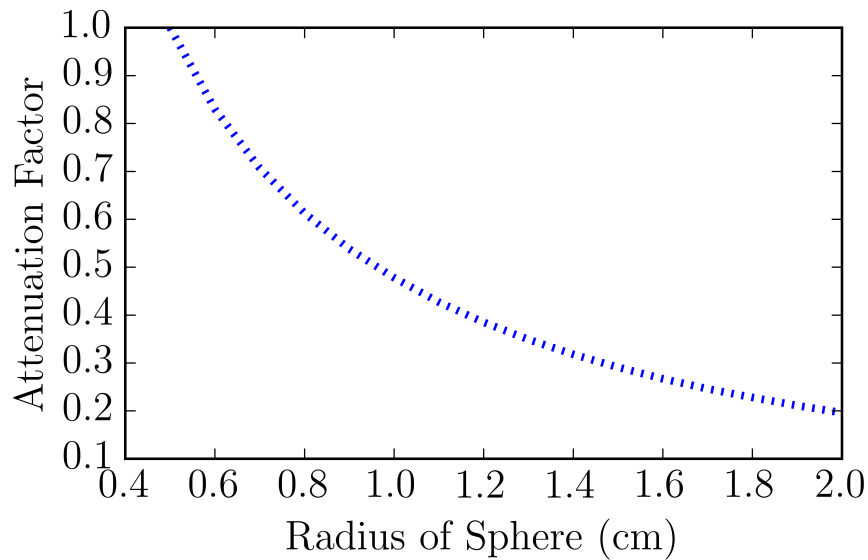
FIG. 4.22: Normailsed attenuation factor of a sphere of 0.3 % wt. UO_2 of density 10.97 g cm^{-1}, ranging in radius from 5 mm to 20 mm.

Fig. 4.21. This phenomenon has a greater effect the closer the detectors are to the sample, due to the solid angle covered by the UO_2 sphere as shown by the shine paths visible in Fig. 4.23. As mentioned in 4.1.1 the background (AmLi) measurement is subtracted from all measurements with a sample. Thus some geometries can have a significantly negative net-flux depending upon the arrangement and how large this solid angle is. This has significant consequences for which geometries are more suitable to measure UO_2 masses using fission neutrons. In real-life scenarios, the differences between the background and measured flux would be less polarised than here, as the EJ-309 detector response is lower at energies below 0.5 MeV, and therefore the slow-interrogating-AmLi neutrons would be less likely to be detected in the first place (Pino et al., 2014). It is still recommended that for UO_2 measurements with a stimulating source, arrangements *8 by 2 Det, 8 Det, 16 by 2 Det, 16 Det* and *4 Det* are used to minimise this effect altogether, and that the potential for shine paths of any interrogating neutrons are carefully considered during experimental design.

The results from the *LS-UNCL* are the most unexpected. Fig. 4.9 presents the surface flux on each side of the geometry at 0 g, 101 g and 368 g of UO_2. It is important to note that the side with the highest flux, the *Empty* side, does not have any detectors,

4 Det

4 by 2 Det

8 by 2 Det

8 by 4 Det
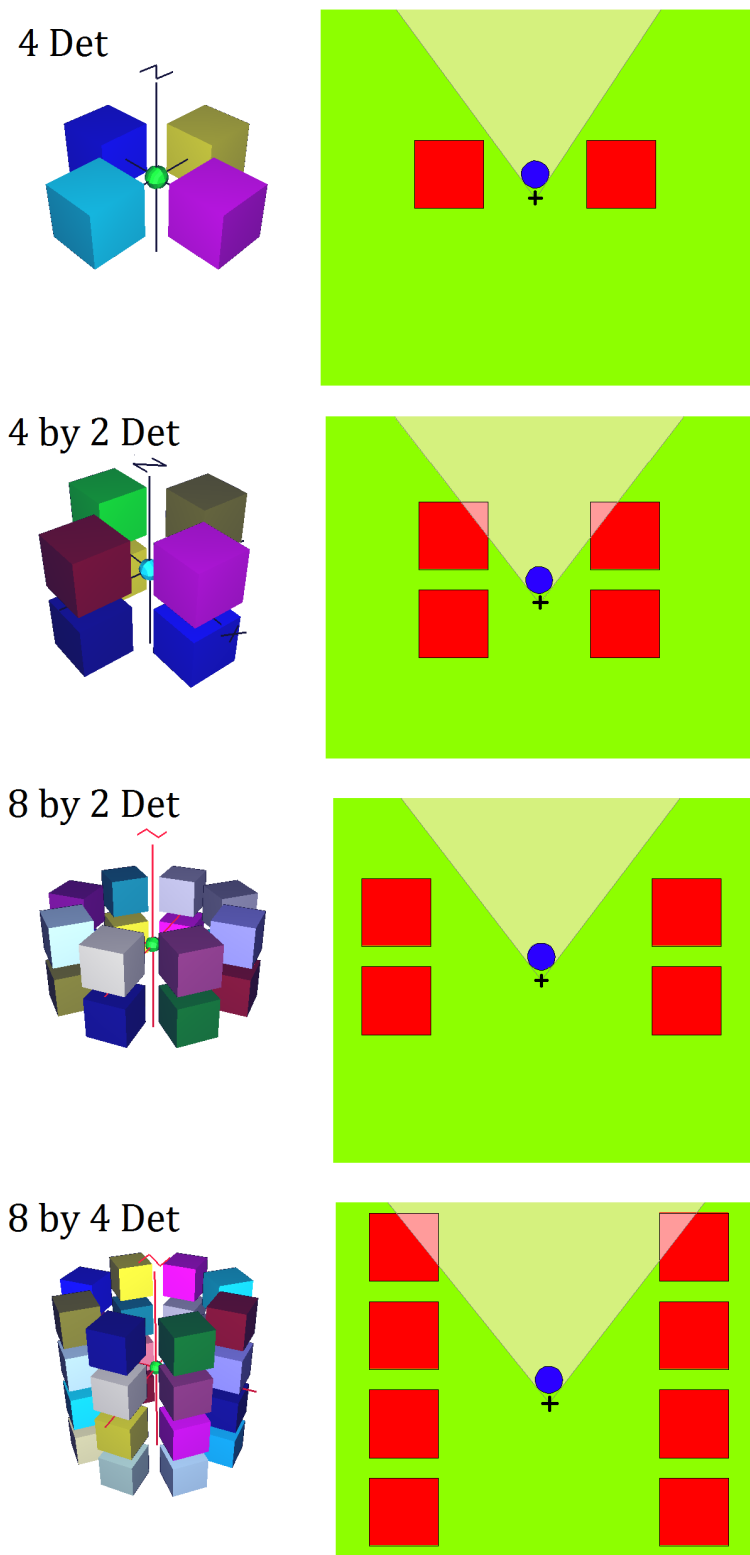
FIG. 4.23: Shine paths of interrogating AmLi neutrons for four geometries investigated within this research, where the + symbol denotes the location of the AmLi source. *8 by 4* and *4 by 2* geometries (top row) are both not suitable for UO$_2$ measurements and can be seen here to have a problem with the solid angle of the UO$_2$ affecting the AmLi neutrons. *8 by 2* and *4 Det* geometries (bottom row) have both been measured to be suitable to measure UO$_2$ and can be seen here to have un-perturbed AmLi shine paths when a sample is present.

and the side which has a significant negative net-neutron flux, the *Front* side, has four detectors. This is again due to the placement of the AmLi stimulating source. Due to the geometry of the UNCL, any stimulating sources have been located at the *Empty* side due to access constraints, i.e., the *Empty* side is a door and can be opened to provide access (S. Beaumont et al., 2017). It is proffered that if the AmLi stimulating source was presented to the sample between the sample and the *Front* side, then the net-neutron count measured may be much more inclined to give a positive-linear correlation, as is usually desired.

Throughout these investigations only the surface flux of the detectors was used. It is proposed that similar simulations are run with a neutron tally across the volumes of the detectors. There may be some cases whereby neutrons enter the detectors from the sides, particularly in the arrangements with four layers of detectors.

4.3.2 Orr-Box Shielded Measurements

The method investigated here, with the use of four detectors in a polyethylene box has been shown here to measure ^{235}U enrichment at levels below 5 % wt. Experimentally, singles measurements and doubles were taken concurrently; coincidence measurements usually affording better resolution for active measurements (Ensslin et al., 2007). The author is only interested in singles measurements here due to their quicker assay times and the simplicity of the circuitry required. Also, due to the small solid-angle subtended by the four detectors here, coincidence measurements would be difficult and lengthy, with coincidence count rate proportional to ε^2, and total count rate proportional to ε, where ε is the absolute efficiency of the detector system (Stewart and Reilly, 1991). When comparing this method to previous work (Chichester et al., 2009) a sensitivity of 0.115 per detector, per second, per % wt. below 5 % wt. shows an increase of a factor of $\times$ 3-5. This is achieved with a smaller array and notably smaller sample masses. Results of the singles assay are presented in Fig. 4.13, a line of fit is included for the reader, with fit parameters: gradient = 0.46 cps % wt.$^{-1}$, intercept = 0.49 cps, and a reduced chi-squared value of 0.008.

MCNP-5 simulations of the PSC geometry and the LS-UNCL geometry produce interesting results with regard to surface flux on the detectors. Fig 4.14 presents the results obtained, and at first glance the PSC system is far superior to the LS-UNCL system. The PSC system has a positive linear trend, with all results garnering positive net-fluxes. The line of fit included has fit parameters: gradient = 70 cps % wt.$^{-1}$, intercept = 2566 cps, and an adjusted R^2 value of 0.98. The LS-UNCL system has a positive linear trend, however all of the results have a negative net-neutron flux. The line of fit included here has fit parameters: gradient = 612 cps % wt.$^{-1}$, intercept = -8567 cps, and an adjusted R^2 value of 0.98 (adjusted R^2 is used here instead of chi-squared because chi-squared is not suitable for negative sets of data). When FMesh results for the front surfaces of the detectors are plotted, Fig. 4.15 is produced. This shows a surface-by-surface breakdown of the fluxes measured on the detector faces. The PSC system results have a roughly ubiquitous flux across each face, at all enrichments of U_3O_8. A slight increase in flux can be seen in the images as the enrichment of U_3O_8 increases, as would be expected. The LS-UNCL system however shows large disparities between each side of the system. The only side with a positive net-flux across the whole surface is the *empty* side, where there are no detectors measuring flux. The *front* side has a particularly negative net-neutron flux at all enrichments of U_3O_8. As the enrichment of the U_3O_8 increases, the positive fluxes become more positive and the negative fluxes become more negative. The reasons for this will be discussed further below.

Comparison between the experimental measurements and the MCNP simulations is not straightforward due to the tallies run in MCNP. Surface flux tallies were measured in MCNP and these identify the number of neutrons passing through a surface. For the geometries investigated here, the front faces of the detectors were used, from the perspective of the samples. The number of neutrons crossing a detector face is not equal to the number of neutrons detected within that detector. The relationship is expected to be linear, and as such, the trend lines for the simulation work carried out are thought to be sound. There is still a vast difference between the measured and simulated results. This difference is thought to be an artefact of the way that the background measurement

in MCNP is taken. As mentioned in 4.1.2, a background-count simulation was run for each geometry, with the AmLi point source present, but no sample. The self-attenuation of the samples is thought to play a large part in deflecting the AmLi neutrons towards the detectors and increasing the neutron count on the detectors. This is not corrected when subtracting the background measurement, as the deflection of these neutrons does not occur when there is no sample present. Therefore the net-neutron count is still measured higher than a real-life measurement would be. In real-life this effect is mitigated due to the low response of the EJ-309 detectors at energies below 0.5 MeV and not withstanding any threshold (Pino et al., 2014).

Due to the self attenuation of neutrons in the measured samples, as seen in 4.2.1, similar investigations were carried out for these sample geometries, i.e., disc-shaped samples. Fig. 4.16 presents the results of these investigations. It can be seen that the interrogating AmLi neutrons penetrate well through 80 % of the samples, due to the large surface area and slim profile of the samples. This ensures that fission neutrons are created in over 90 % of the sample, as can be seen in the *Fast neutron* image at 4.4623 % wt. enrichment (bottom-right image). This sample geometry is an improvement on the sphere shape investigated in 4.1.1. (Menlove and Bosler, 1981) looked at the effect of sample shapes for active assay with neutrons. They found that as the surface-to-volume ratio increased, neutron self-shielding decreases, giving a higher neutron response. However, neutron multiplication also decreased, and these two effects almost cancelled each other out in the mass range 1-3 kg of ^{235}U. However they did record a decrease in response of 5 % when the same sample discs were assessed in a stack (rod-shape), than when laid-out flat in a pancake shape. It is recommended that more sample shapes are investigated to increase penetration of interrogating neutrons. Hemi-spherical samples seem to be quite suitable, purely from assessing the flux of slow-neutrons, seen in the top row of Fig. 4.16.

The shine path of the AmLi interrogating neutrons was also investigated. As the method used here benefits from the background count being subtracted from the sample measurements, the AmLi neutron-flux on each detector is critical to the results. The

shine path of the AmLi neutrons in the PSC geometry is in a different plane to that of the detectors, and therefore perturbation of these neutrons makes a unifrom, and relatively insignificant difference to the flux on the detector surfaces. However, in the LS-UNCL geometry, the AmLi shine path between the source and detectors is highly affected by the sample due to the geometry of the sample. Fig. 4.24, shows the AmLi interrogating-neutron shine path for both of the arrangements investigated here. From Fig. 4.24a it can be seen that over one third of the detector faces are obscured by the sample. When the background measurement is taken, with no sample present, the slow-neutron flux on these surfaces is much higher than when a sample is present. These measurements heavily affect the net-neutron calculations carried out after the sample measurements have been taken. Experimentally, the neutron flux measured during the background count would be much lower due to the low efficiency of the EJ-309 detectors at low energies (Pino et al., 2014). There is a trade-off that can be seen between having a sample that covers a large solid-angle, in order to increase the number of interactions between the incoming AmLi neutrons, and that same large solid-angle causing perturbation, affecting the measurements of background count.

It is recommended that a more realistic simulated measurement method is devised to account for the detector response to the neutron spectra of the interrogating neutron source. This would reduce the systematic errors throughout the simulation work carried out here. A shadow cone arrangement such as those used in (Ende et al., 2016) is also recommended.

4.3.3   Broad Range Enrichment Investigation

We might expect that as ^{235}U abundance increases in the sample, the number of neutrons detected due to fission would increase. This can be observed in each of the experimental and simulated runs described here. Quantitatively, the superior system here is the UNCL geometry. In both the experimental research, and simulated work, the UNCL outstrips the neutron count of the nearest competitor by between 60-80 % respectively, when using the highest enrichment of ^{235}U measured.
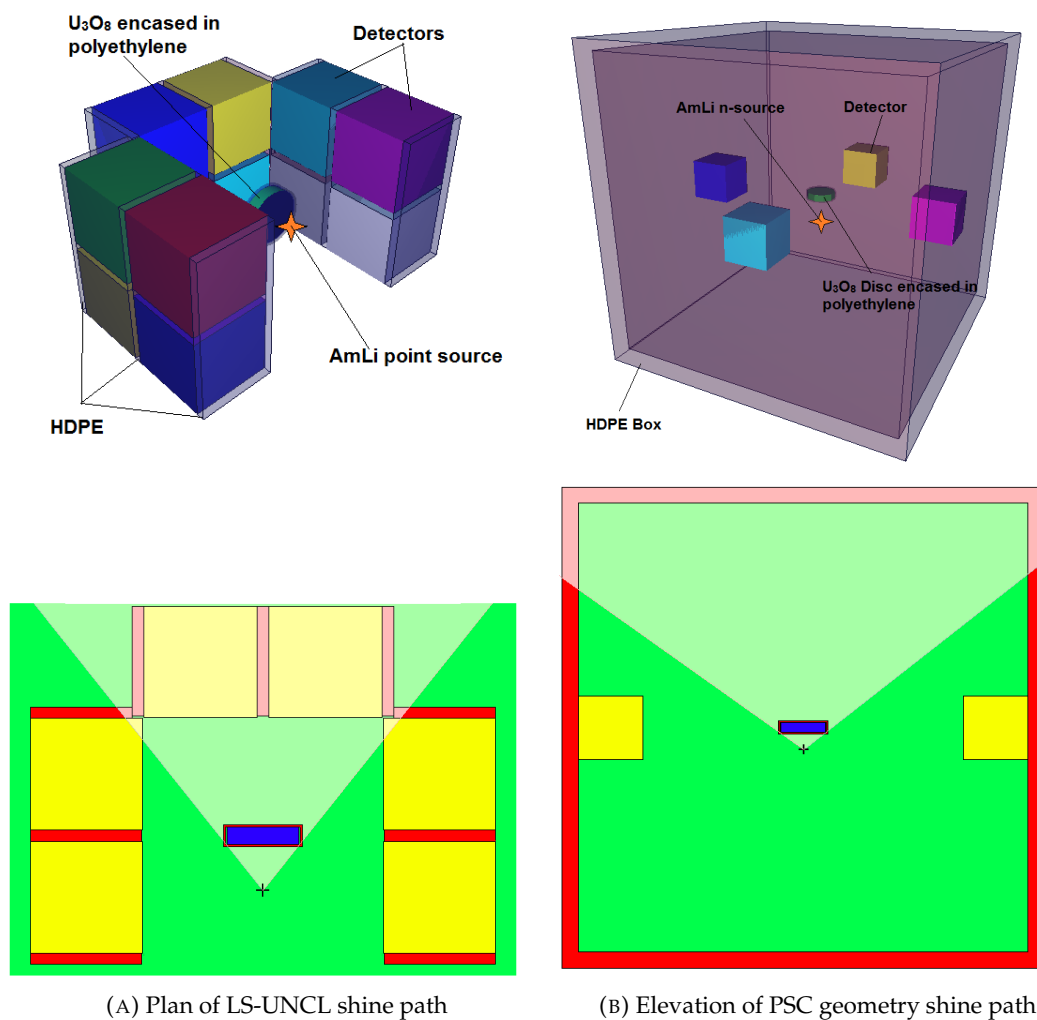
(A) Plan of LS-UNCL shine path

(B) Elevation of PSC geometry shine path

FIG. 4.24: Shine path of interrogating AmLi neutrons for the LS-UNCL geometry (A) and PSC geometry (B), where the + symbol denotes the location of the AmLi source. In (A) the U_3O_8 sample subtends a large solid-angle of the AmLi shine path. This interaction prevents AmLi neutrons being measured on all of the *front* detectors and skews the results of the background measurement in this geometry by a not-insignificant amount. In (B) the path between the AmLi neutron source and the detectors is completely un-perturbed, so background measurements are far more similar to real-life measurements.

Despite active-singles-neutron measurements resulting in greater precision of measurements in comparison to coincidence counting using the same assay time, it is a relatively underused technique (Stewart and Reilly, 1991). Comparisons between this research and existing research are discussed henceforth. (Parker et al., 2016) includes results from the active interrogation of U_3O_8 with AmLi neutrons, although only LEU samples were measured. The results are presented with a linear line-of-fit, in contrast to the research presented here which has an exponential fit. This may be due to the range of samples used in this research, which provide enrichment levels up to 93 %. An exponential fit is suitable for the process investigated here due to the effects of multiplication, where fission neutrons cause further fissions after they have scattered and acquired a softened energy spectrum that will easily cause fission in another ^{235}U nucleus. The process would suggest that an increase in fissions leads to positive feedback and therefore more fissions, which appears to be the case. It should be noted here that a chain reaction is not being suggested, and instead that there is a small increase in probability of (n, fission) occurring when more neutrons are present in a given material. If the results for low enrichments of U_3O_8 are plotted against the results in (Parker et al., 2016), Fig. 4.25 is obtained. All four of our sets of results how higher count rates than (Parker et al., 2016). This is to be expected when taking into account the numbers of detectors used. Parker uses four detectors, 27.5 cm away from the centre of the sample, whereas the investgation in this thesis used 8-15 detectors between 10, and 26 cm away from the centre of the sample. The intercepts of all the lines-of-best-fit are close to zero, except the results for the UNCL system. This system intercepts the y-axis at 7.8. This may suggest that cross-talk is ocurring within the detectors, with background counts being counted twice or more in the detectors. This is more liekly in that set-up due to the close proximity of the three walls each with four detectors.

Linear-lines-of-fit are presented in (Lakosi, Tam Nguyen, and Bagi, 2008; Tomar et al., 2013), however, these papers use a die-away active interrogation technique using a pulsed source, rather than a continuous active neutron source being present. AmLi interrogation arises in (Miller et al., 2013), for the assessment of UF_6 cylinders. Here the
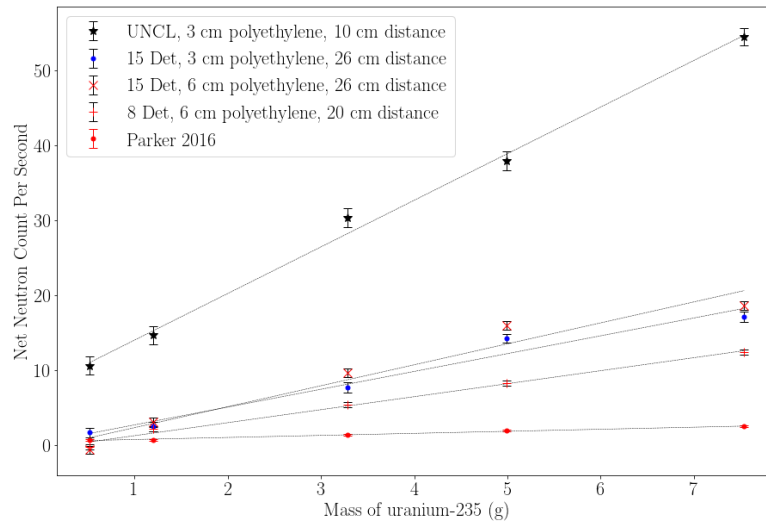
FIG. 4.25: LEU results of interrogation the of U_3O_8 with AmLi neutrons moderated with polyethylene. Lines of best fit aree included

doubles count is non-linear, and can instead be calculated to be an inverse exponential rate of increase, with enrichment. This is in contrast to the experimental and simulated results presented in this thesis, which have a line-of-fit of the type $y = a.log_2(x + b) - c$. The effects of the bulk sample may be attenuating and moderating neutrons in their experiments, which would account for the leveling out of the counts as the enrichment/mass of ^{235}U increases. Again, the enrichments looked at in (Miller et al., 2013) only go up to enrichments of 5 %, as opposed to 93.1 % as investigated here.

(Goddard et al., 2016) actively interrogates the same HEU UO_2 samples as the research presented in this thesis. The AmLi sources used ranged from 48,850 to 49,950 nps, which is an emission rate 26 times smaller than ours. Their background corrected experimental measurements are observed from Fig. 17 to be: 20 % wt. enrichment = 221 cps, 52 % wt. enrichment = 243 cps, and 93 % wt. enrichment = 272 cps. A linear line-of-best fit can be applied, with equation $y = 0.3574x + 206.73$ where x is the mass of ^{235}U, and y is the counts per second. Again, this is in contrast to our line of fit with a natural logarithm. Our results can be modelled with a linear line-of-fit over these three data points. Between (Goddard et al., 2016) and our data, two of the data points overlap with each other, giving good agreement between the measurements.The detection system used here was the large volume active well coincidence counter (LV-AWCC), which

is a ^{3}He type detector with 48, 1-in tubes at 4 atm. Comparing this data to our UNCL data, Fig. 4.26 can be produced. Two of the data points seem to be in agreeance, but the 39.31 g of ^{235}U point does not. There is also the discrepancy between the interrogating AmLi source strength to take into account. The total strength of the 4 AmLi sources used in our research is 26 times greater than that described in (Goddard et al., 2016), so we might expect our measurements to be 26 times greater. The difference in detector as well as the use of thermalising polyethylene in our research are thought to be the cause of the discrepancies between the two sets of measured data. ^{3}He detectors have a broader range of energies within which they can detect neutrons. This may lead to a greater number of scattered neutrons being detected. For the thermalising polyethylene used in our research, it is shown in Fig. 4.17 that for the 15 Det systems, increasing the thickness of the thermalising polyethylene reduces the number of counts for high enrichment samples. The aim of (Goddard et al., 2016) is to consolidate lots of data around AmLi spectra which is largely misunderstood, and as such, our research which uses polyethylene to soften the AmLi spectra may have had a detrimental effect, either by reducing the number of interrogating neutrons or softening them too much to cause fission. It is recommended that further studies into the spectra of AmLi sources are carried out, and the effects of polyethylene upon these spectra with regards to causing fission in ^{235}U.

In contrast to previous simulation work which has suggested that the UNCL detection system is inadequate to actively assay small masses of ^{235}U (section 4.2.1), it is the most efficient system at all enrichments investigated here, both experimentally and in simulations. The obvious major difference between this set of experiments and previous research reported in this thesis is the proximity of the detectors to the sample during each assay carried out. In previous research in this thesis, all detectors have been placed as closely as possible to the sample, in order to increase the solid-angle. Here, the three circular geometries are set at a distance of at least 20 cm due to the diameter of the polyethylene neutron-thermaliser used. For the 8 Det 6 cm system, this is rather significant in terms of the solid-angle subtended by the detectors. In section 4.1.1
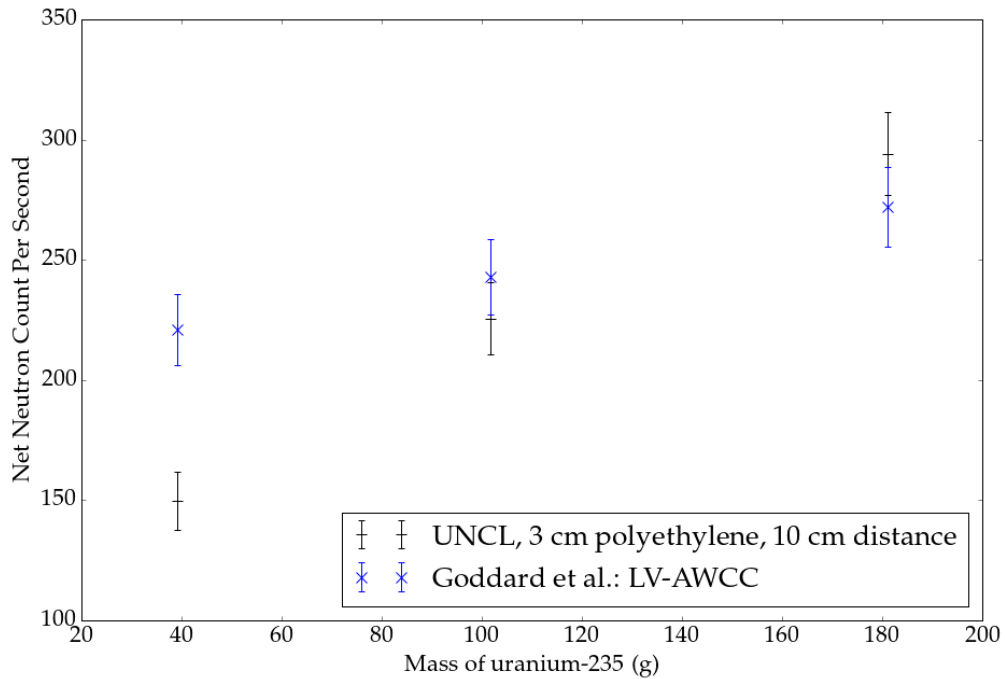
FIG. 4.26: UNCL measurements of ^{235}U mass plotted alongside data purported in (Goddard et al., 2016).

the 8 detector system has a radius of 16 cm, and thus the surface area of the detectors facing the sample (where tallies have been simulated) is 8 % higher than here where the diameter is 20 cm. As well as the differences in detector solid-angle, the position of the AmLi sources used here are different to that described in 4.1.1. The shine path of the four AmLi sources is mostly unaffected by the sample itself, as the polyethylene thermaliser (at either 3 cm or 6 cm thickness) is situated between the two. Therefore, during simulation in-particular, the AmLi (slow/thermal) flux measured in the detectors during the background assay is very similar to that measured when a sample is present and thus the 0.5 MeV detector response threshold discussed elsewhere (Pino et al., 2014) has less of an impact here. Fig. 4.27 shows the effect of having the polyethylene neutron thermaliser between the AmLi sources and the sample. The detectors in both scenarios will receive similar amounts of AmLi neutrons in contrast to the results from MCNP depicted in sections 4.2.1 and 4.2.2.

When comparing the experimental results with the simulated results, they are mostly similar, with a few exceptions. The trends are similar for both sets of results, and the
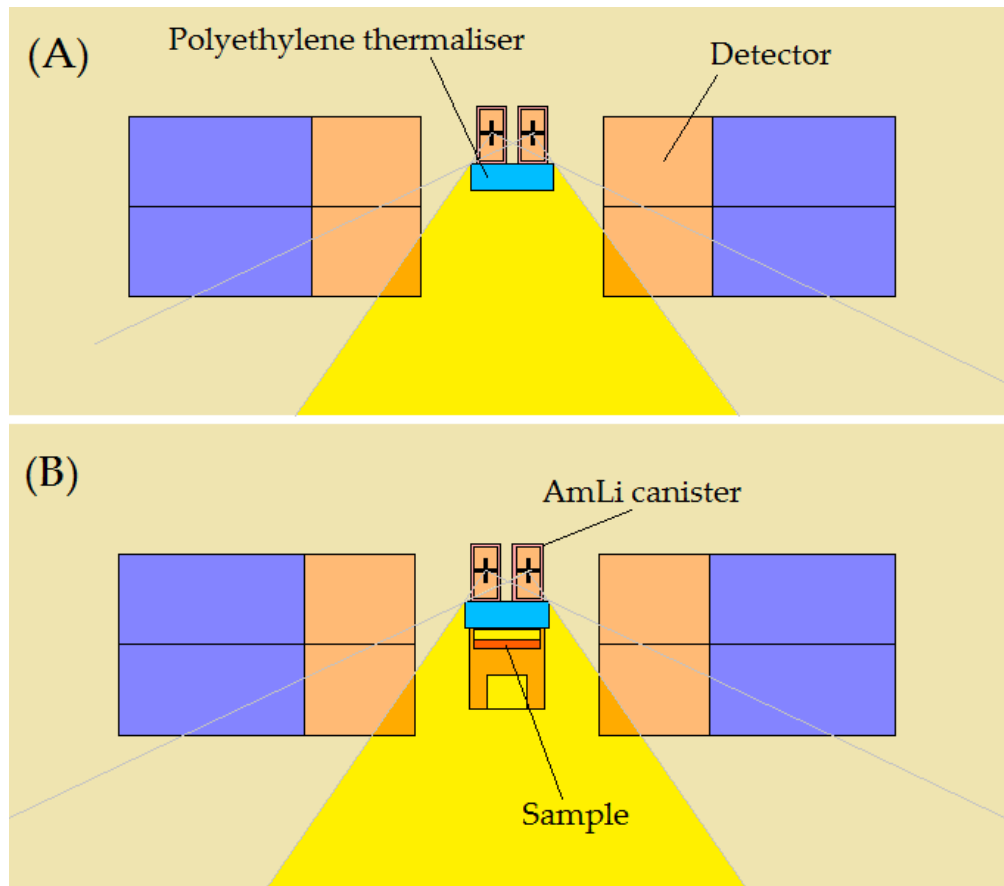
FIG. 4.27: Shine-paths of neutrons from AmLi sources in the UNCL arrangement, with (A) no sample present, and (B) a sample of U_3O_8 at the centre of the geometry. Where the $+$ symbol denotes the location of the AmLi neutron source. The detector faces/volumes receive the same amount of flux in each case.

order of efficiency ranking from best to worst as: UNCL, 15 Det 3 cm, 15 Det 6 cm, and 8 Det 6 cm. However, the magnitude of difference between each geometry is not the same for both sets of experiments. In the experimental results, the 15 Det and 8 Det system's responses are very similar at low masses of ^{235}U, and only really become discernible from each other at masses of ^{235}U greater than 10 g. The simulated results show a much more pronounced difference between the 15 Det 3 cm arrangement and the 15 Det 6 cm and 8 Det 6 cm arrangements throughout the range of masses. Both sets of results present the UNCL as superior across the range of masses of ^{235}U. However, this difference is far more pronounced in the simulated results than the experimental. The simulations yield the flux of the neutrons within each detector volume and the detector response is not factored in. The inherent detector efficiency (Tomanin et al., 2014), scintillant response to energy spectra (Colonna and Tagliente, 1998), and PMT response (Enterprises, 2011b) could account for the difference between the two sets of results here.

The inconsistency of having a polyethylene cylinder to thermalise neutrons from the AmLi source in the three circular arrangements and not in the UNCL arrangement may be significant in the results obtained both experimentally and with MCNP. This polyethylene cylinder attenuates neutrons and reduces the number of slow/thermal neutrons reaching the detectors. If the cylinder is not in place, the full AmLi neutron-spectrum reaches the detectors, however, with the cylinder in place the number of AmLi neutrons impacting the detectors changes. Simulations in MCNP-6 show that the AmLi cylinder reduces the number of neutrons > 0.5 MeV by 16 $\pm$0.15% assuming an assay length of 6342 seconds as per our longest experimental test. There are two ways of considering this reduction, firstly, with the purpose of the cylinder being to reduce the number of AmLi neutrons directly impacting in the detectors, a 16$\pm$0.15 % reduction is low. Secondly, a 16$\pm$0.15 % reduction in AmLi neutrons reaching the detectors only when the cylinder is used (i.e. in the circular arrangements) must have an impact on the differences between these results and the UNCL results, where no cylinder was used.

When the flux within the detector volumes is visualised, Fig. 4.18 (page 82) is obtained, using MCNP results for 182.15 g of ^{235}U. This is the maximum flux seen by each of the detectors. The UNCL arrangement has three images (seen on the top row of this figure), due to there being three banks of detectors and the non-symmetry of the system leading to flux differences between these detector banks. The other arrangements; 15 Det 3 cm, 15 Det 6 cm, and 8 Det 6 cm; are imaged using the results from just one detector as the symmetry of these systems implies all detectors would see an almost identical flux (Langford et al., 2016). Sharing a colour-bar between the images allows for quick and easy comparison to be made between the results. The effects of scatter can be seen in the UNCL images. Where the detectors are close together, at the junctions of the left and top detectors, along with the top and right detectors, a higher flux of neutrons can be seen. This is to be expected and is in line with results reported elsewhere (Shin et al., 2015). However, the non-symmetrical nature of the UNCL setup, means that cross-talk between the three different banks of detector may differ from that seen within the circular arrangements of detectors. This may be one explanation of why the UNCL system appears to have a much higher efficiency here than the other geometries investigated. Fig. 4.28 shows the areas in question and the subsequent flux profile of each detector block. Clearly the corner-detectors which are in close proximity, have a higher flux than those detectors on the edge of the arrangement.

The maximum net-neutron fluxes within each of these images have been summarised in Table 4.7. This clarifies that the UNCL system has a higher net-neutron flux than the other systems, by an order of magnitude in most cases. It is interesting that the 8 Det 6 cm system has a higher flux here than the 15 Det 6 cm arrangement, when the full results (seen in Fig. 4.17) depict the 8 Det 6 cm geometry as having the lowest net-neutron count. The fluxes detailed here are per cm^3 of the detector material, whereas the results detailed in Fig. 4.17 are for the whole system of detectors. i.e., the results in Table 4.7 need to be multiplied by the number of cubic centimetres of detector volume in order to obtain the flux of the whole system, which then give us the results presented in Fig. 4.17. This would suggest that if another layer of detectors was included in the
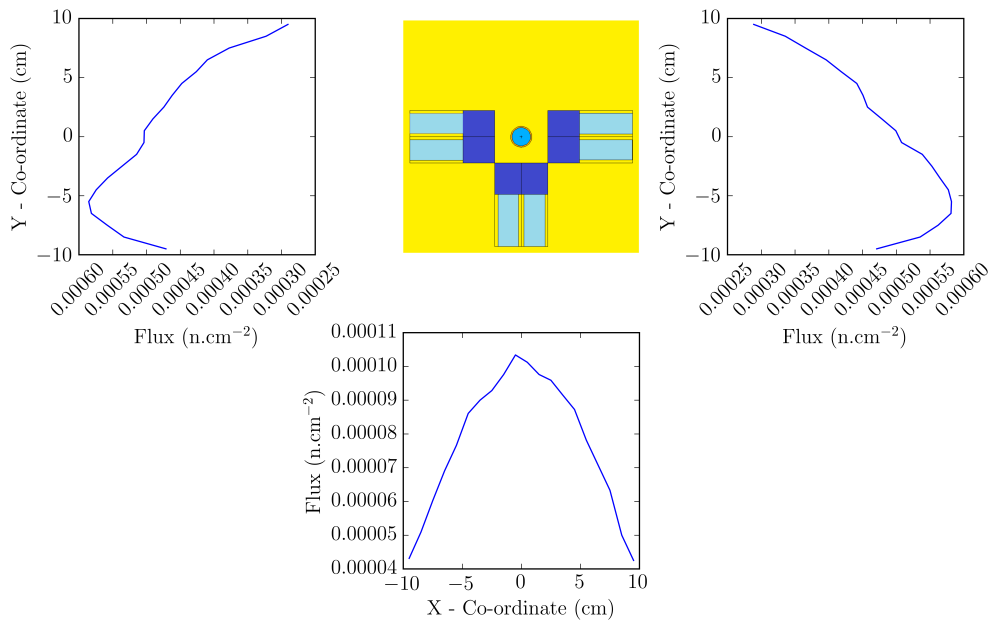
FIG. 4.28: Flux profiles of the front face of each side of the UNCL system. The *left* and *right* detectors have a greater flux nearer the *bottom* detectors, which can be atributed to scattering between the low-Z materials in the detector materials. NOTE: the x-axis of the *left* plot is reversed to show the symmetrical profiles of the *left* and *right* detectors.

8 Det 6 cm geometry, i.e., two layers of 8 detectors instead of one, that the net-neutron flux detected in this system may be comparable to the 15 Det 6 cm and even the 15 Det 3 cm systems.

MCNP allows the user to carry out temporal experiments by measuring the amount of time between each interaction. Ordinarily the code *releases* all source-neutrons at the same time. Neutron spectra at various time periods after neutron release were calculated in MCNP, as shown in Fig. 4.19. These plots show a variety of artefacts of the process. Measurements were taken in all simulated configurations, but only the results with the highest and lowest neutron CPS have been included in the graph for brevity, i.e., the lowest efficiency with the lowest sample ^{235}U mass and the highest efficiency system with the highest ^{235}U mass. The author had assumed that a spectrum shift over time from an AmLi spectrum to a fission spectrum would be observed. To clarify this, time-of-flight (TOF) calculations were carried out. Fig. 4.29 shows the average pathways that the neutrons must traverse in order to be detected in the scintillation

Detector arrangement	Maximum flux (n/source-n/cm^3)
UNCL left detectors	5.31×10^{-5}
UNCL bottom detectors	7.19×10^{-5}
UNCL right detectors	5.39×10^{-5}
8 Det 6 cm	9.75×10^{-6}
15 Det 6 cm	4.48×10^{-6}
15 Det 3 cm	1.08×10^{-5}

TABLE 4.7: Maximum net-neutron fluxes simulated within detector volumes, resulting from the active assay of 182.15 g of ^{235}U with four AmLi neutron sources.

material. These distances, along with the speed of the neutrons in question (AmLi and fission), can then be turned into TOF for comparison. It can be inferred that in order for a fission neutron to reach the detector, an AmLi neutron must complete pathway A, as well as a fission neutron completing pathway B. This is in comparison to an AmLi neutron reaching a detector, which only requires an AmLi neutron to complete pathway C.

Calculating the average speed of the AmLi neutrons and fission neutrons; for the AmLi neutrons the mode energy was chosen, 0.125 keV (Reilly et al., 1993, pg. 349). Simulated fission neutrons were calculated at 2 MeV. A neutron mass of 1.675×10^{-27} kg was used (L'Annunziata, 2012, pg. 73).

AmLi neutrons

$$0.125 \; keV = 2 \times 10^{-17} \; joules$$

$$Energy = \frac{1}{2}mv^2$$

$$2 \times 10^{-17} = \frac{1}{2}(1.675 \times 10^{-27})v^2$$

$$4 \times 10^{-17} = (1.675 \times 10^{-27})v^2$$

$$2.39 \times 10^{10} = v^2$$

$$154533 \; ms^{-1} = v$$

Fission neutrons

$$2 \; MeV = 3.2 \times 10^{-13} \; joules$$

$$Energy = \frac{1}{2}mv^2$$

$$3.2 \times 10^{-13} = \frac{1}{2}(1.675 \times 10^{-27})v^2$$

$$6.4 \times 10^{-13} = (1.675 \times 10^{-27})v^2$$

$$3.82 \times 10^{14} = v^2$$

$$19547111 \; ms^{-1} = v$$

When the distances and speeds of the neutrons are combined using $speed = \frac{distance}{time}$ results calculated in Table 4.8 are obtained.
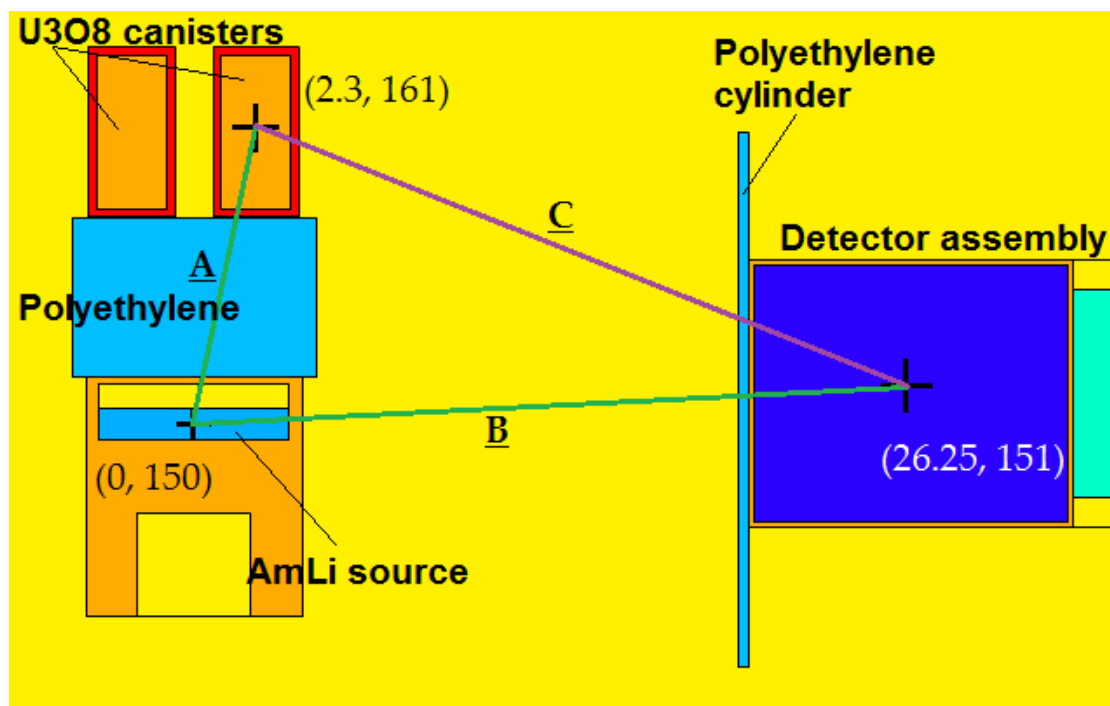
(A) Average paths of AmLi (A, B) and fission neutrons (C) in the 8 Det 6 cm arrangement.
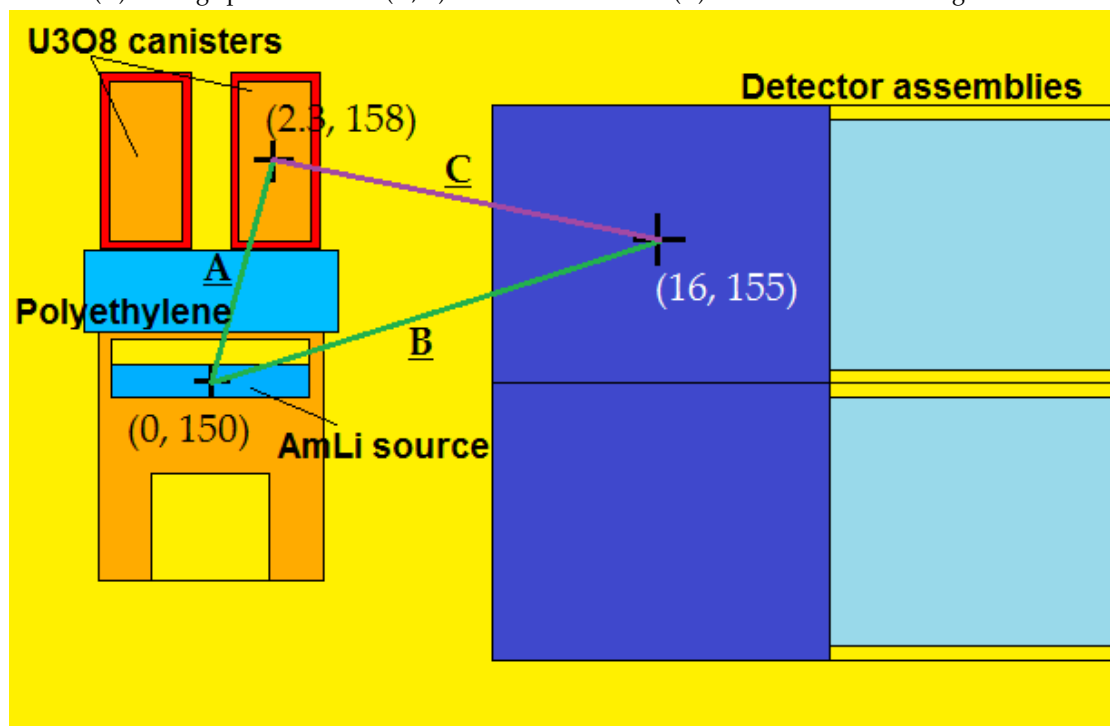
(B) Average paths of AmLi (A, B) and fission neutrons (C) in the UNCL arrangement.

FIG. 4.29: Co-ordinates of the average pathway lengths that must be traversed by neutrons in order to create a neutron count in the detector. Due to the symmetry of the systems, these calculations are the average lengths for all detectors in each arrangement. Lengths A, B, and C are presented in Table 4.8, along with the time-of-flights for each distance.

	8 Det 6 cm system			UNCL system		
	A	C	B	A	C	B
Distance (cm)	11.24	25.96	26.28	8.32	14.02	16.76
TOF (shakes)	72.74	1.33	170.06	53.84	0.71	108.46
Total flight time (shakes)	74.07		170.06	54.55		108.46

TABLE 4.8: Average neutron flight times for pathways depicted in Fig 4.29. These data confirm that neutrons from fission (A + C) reach the detector before direct AmLi neutrons (B), in both arrangements investigated.

From these calculations, it can be seen that in the 8 Det 6 cm and the UNCL arrangements both neutron pathways are complete by 200 shakes. To analyse the time-of-flight data further we can use Figs. 4.19 and 4.20. For all cases, faster neutrons are detected earlier in the systems, which is to be expected. Energies higher than those calculated above are seen very early (0.9 and 1.4 shakes) which, again, is to be expected as neutrons are released from AmLi in a spectrum of which we chose the mode common energy to use for the calculations above. For all cases, fast neutrons are produced, reaching a maximum flux at 10,000 shakes after which the number of neutrons at all energies dies away. As time passes, the spectra can be seen to soften, this is due to neutrons scattering and losing energy during their interactions (Simpson and Chichester, 2011). In Fig. 4.20 the difference between the amount of flux for the UNCL and 8 Det 6 cm systems can be seen, at both 182.15 g and 0.52 g ^{235}U. The results fit with what woud be expected; the UNCL system has a higher flux than the 8 Det 6 cm system, by an order of magnitude. Similarly, the 182.15 g ^{235}U sample leads to a greater flux than a 0.52 g sample, in both systems, again sometimes up to an order of magnitude of difference can be measured. Interestingly, from the calculations carried out in Table 4.8 it becomes apparent that on average neutrons from fission reach the detector before those directly from AmLi, in both arrangements. This may explain why neutrons can be observed in the detector material from as little as 0.9 shakes.

It was realised after the experimental work was completed, that an incorrect power supply had been used to power the FPGA TTL counter system. Instead of a 12 V supply, a 5 V supply was used. Further investigation into the effect of this was carried out at

Lancaster University and a neutron count was measured for the same arrangement with both power supplies. The 5 V supply lead to a reduction in neutron count to 74 % of the amount measured with the 12 V supply. The effects of pulse-pile up and deadtime were not taken into account during this minor investigation, and thus, the differences between the counts may not be as severe as 74 % As all experimental measurements taken here were carried out with the same 5 V supply, the results are deemed to be reliable as the inconsistencies within the measurements are relative throughout.

5 Assessment of ^{238}U

^{238}U undergoes spontaneous fission to produce neutrons at a rate of 0.0136 n s^{-1} g^{-1}. This low rate of neutron production, when compared to neighbouring even-numbered isotopes ^{238}Pu, ^{240}Pu, and ^{242}Pu, has resulted in relatively less focus being paid to radiation measurement of this phenomenon. ^{238}U is important as, by mass, it makes up the majority of about all refined uranium. Measuring the spontaneous neutron flux passively is carries less risk than active interrogation of SFM and could be useful for measurements of things like heels and UF$_6$ cylinders. The benefit of using neutrons over γ rays in these scenarios is that neutrons are far more penetrating than γ rays, particularly in dense, high-Z materials like those found in SFM. The 186 keV γ-ray has a mean free path length of between 0.39 and 0.7 cm in UO$_2$ (Reilly et al., 1993, Table 7.2). The range of significant γ-ray emmissions is between 63 keV and 1831 keV. The research reported here has been published in (Parker, Beaumont, and Joyce, 2019); figures, tables, and text have been reproduced here, with text being included in quotation marks.

5.1 Methods

To measure neutron counts from depleted uranium (DU), a suitable geometry was required to optimise detection efficiency. The results, seen in section 4.2.1 of experiments described in 4.1.1 were used to identify a suitable detector geometry, with a *4 by 1* layout being utilised here. This arrangement exhibited a positive linear trend, with a suitable efficiency in comparison to other arrangements tested.

In order to measure neutron counts from the spontaneous fission of ^{238}U, various masses of 0.3 % wt. DU were assessed using similar equipment to that discussed in

section 4.1.2. Four organic scintillation detectors (EJ-309) (Enqvist et al., 2013), and associated PMTs were placed orthogonally around a void in which DU samples were placed, as can be seen in Fig. 5.1. The detectors were sandwiched between two layers of 1-cm thickness HDPE. The HDPE was included to reduce ambient background radiation, in particular, that from cosmic sources. The detectors were coupled to a four-channel Mixed Field Analyser (MFA) x 4.3 real-time pulse-shape discriminator (Hybrid Instruments Ltd., UK) (*MFAX4.3*). The MFA TTL outputs for neutrons and γ-rays were connected to a custom data acquisition module (Beaumont, 2017) and then to a conventional PC. The data acquisition module had eight TTL input connections, one each for the neutron and γ-ray signals from each of the four detectors. Through an arduino (*Arduino Uno*) interface on the PC, the module displayed the neutron and γ-ray count in 1.15 s intervals. An output file was also created with the second-by-second data which was analysed in Python (Python Software Foundation, V2.7). The use of this logging function reduced systematic errors in the system in comparison to the use of a real-time counter, as it allowed for analysis of the second-by-second data. These data were used to confirm that the detected radiation exhibited a Poisson distribution, and it enabled the stability of the electronic systems to be checked periodically. This was particularly pertinent due to the length of time that the assessments took.

"Due to the close proximity of the four detectors, the effect of inter-detector scattering (cross-talk between detectors) was investigated experimentally and in MCNP-6 (Goorley and al., 2012). The data from a single detector were compared to a four-detector array in order to quantify the number of extra neutrons observed with the four-detector array as a result. However, the neutron count (per detector) was consistently higher for the single detector arrangement, by approximately 25%. It is proposed that the increase in hydrogenous material from one to four detectors moderates neutrons within the geometry and down-scatters them below the detector threshold at approximately 0.5 MeV (Pino et al., 2014). This spectrum softening was tested in two MCNP-6 models, one with an array of four detectors and one with just one detector, the results of which can be seen in Fig. 5.2. The model measured the neutron flux in
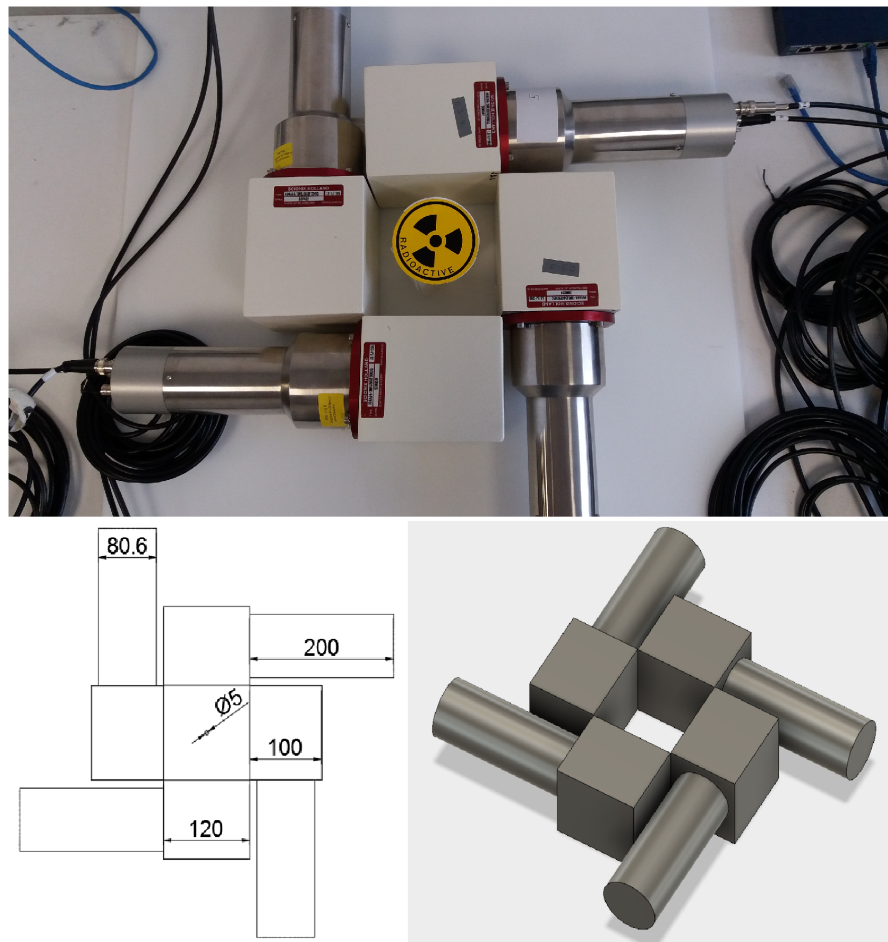
FIG. 5.1: A photograph and associated drawings of the detector array used to assess spontaneous fission neutrons from 0.3 % wt. UO$_2$. The dimensions stated here (in mm) were also used in MCNP simulations of the experiment.

one detector when on its own, and when in a four-detector array, the results of which passed all inherent MCNP statistical tests and had acceptable fractional standard deviations in line with (Hussein, Esam M. A., 2007). The neutron flux below 0.5 MeV was shown to be greater in the four-detector array, and above 0.5 MeV the neutron flux was greater in the single-detector, thus the softening of the spectrum was shown to be plausible; an intrinsic influence of the measuring system on the field as measured. The mean flux was calculated to be 11.35% higher for the single detector alone, than when in a four-detector arrangement, broadly in agreement with the 25% measured experimentally. The difference between these two results could be attributed to photon bleedthrough in the PSD at low energies, where neutrons and γ rays can be confused. In contrast, MCNP-6 does not have this issue, and reports definitive numbers of neutrons and γ rays. There have been multiple papers published providing correction factors for cross-talk measurements (Wang et al., 1997; Marqués et al., 2000; Shin et al., 2015; Verbeke, Prasad, and Snyderman, 2015; Sarwar et al., 2018). Our sample emission rates were deemed too low to be able to correct for the scattered neutrons statistically with confidence. For the purposes of this experiment, the measured factor of 25% and the simulated factor of 11.35% imply that the effects of scatter are not a significant source of over-response for our four-detector array, but are in fact depressing the number of counts measured here. Self shielding within the samples was not investigated due to the small volumes of the samples used. Such scattering results open a debate as to whether increasing the solid angle of detector coverage is outweighed by the spectrum softening that will occur, when trying to increase detection efficiency of systems similar to that used here."

Once the equipment had been set up and calibrated in the same fashion as described in 4.1.2, a background radiation count was carried out, overnight, for 18 hours. These neutron and γ-ray counts were then subtracted from results obtained during the assessment of the samples. Details of the samples used in this research are given in Table 5.1 along with predicted neutron emission rates for each sample. The samples were placed into the void in the detector array sequentially and each assessed for 18 hours. The
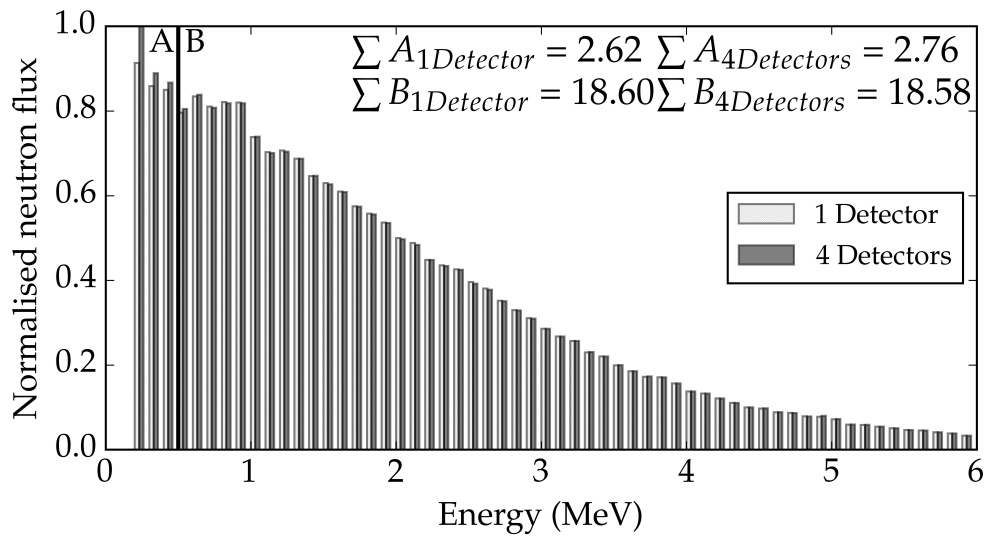
(a) Neutron energies < 10 MeV.
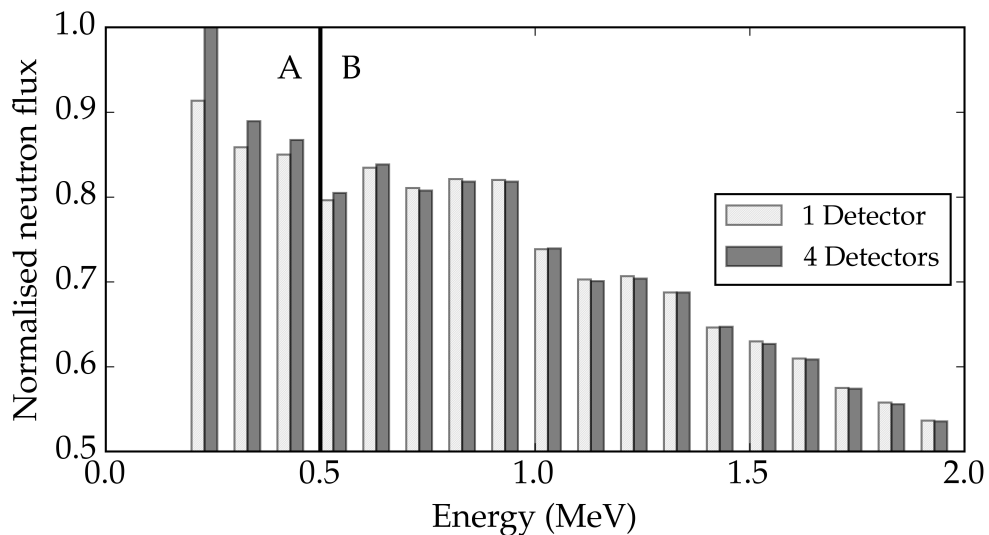
(b) Zoom in of image (a): neutron energies < 2 MeV.

FIG. 5.2: Results from an MCNP-6 model showing a spectral softening of the neutron flux in the same detector when four detectors are present in comparison to just one detector. This validates the experimental test which concluded that scattering of neutrons within the four-detector array was not increasing the number of neutrons detected per detector, but reducing them, due to the EJ-309 detectors having low efficiencies at low neutron energies. The neutron flux below 0.5 MeV was shown to be greater in the four-detector array, and above 0.5 MeV the neutron flux was greater in the single-detector. The mean neutron flux across the range of energy 0-10 MeV was calculated to be 11.35% higher for the same detector alone, than within a four-detector array. At 0.7 MeV the single detector overtakes the efficiency of the same detector in a four-detector array.

Mass UO$_2$ (g)	Mass of ^{238}U (g)	Predicted SF neutron emission (n s^{-1})	Predicted α-n neutron emission (n s^{-1})
4.20	3.69	0.050	3.69×10^{-4}
7.97	7.00	0.095	7.00×10^{-4}
12.25	10.77	0.146	10.77×10^{-4}
16.45	14.46	0.197	14.46×10^{-4}

TABLE 5.1: Details of 0.3 % wt. UO$_2$ samples assessed in this research, along with associated spontaneous fission (SF) and alpha-n (α-n) predicted emission rates. Predicted emission rates use data from (Reilly et al., 1993, p. 413-414)

samples were presented as slices of a DU pellet, of mass up to 2 g, combined to produce the masses assessed here. For radiation protection the pellet slices were sealed individually into air-tight plastic bags which were then stored in a plastic box.

5.2 Results

Results from this experiment were simply the neutron and γ-ray count from the passive assay of each sample. The raw data collected is presented in Table 5.2, in terms of: gross neutron count, gross γ-ray count, and γ-ray/neutron ratios. Errors of 1σ are provided for the gross counts, and these errors are propagated for the ratios. It is apparent that the background measurement is large in comparison to the sample measurements. When this background is subtracted from the sample measurements the results presented in Table 5.3 are obtained. These results are described henceforth as *net* results. The errors provided in this table are propagated to account for the double error on the background and sample measurements.

The net-neutron count is presented graphically in Fig. 5.3, net-γ-ray count in Fig. 5.4 and a ratio of the two can be seen in Fig. 5.5. A plot of the ratio between gross γ-ray and neutrons is also included in Fig. 5.6.

Mass UO$_2$ (g)	Mass of ^{238}U (g)	Gross Neutron Count	Gross γ-ray Count / $\times 10^7$	γ-ray/Neutron Ratio
Background		3330 ± 60	$1.59 \pm 0.025\,\%$	4764 ± 86
4.20	3.69	3600 ± 60	$3.30 \pm 0.018\,\%$	9159 ± 153
7.97	7.00	3660 ± 60	$4.59 \pm 0.015\,\%$	12539 ± 206
12.25	10.77	3920 ± 60	$6.32 \pm 0.013\,\%$	16124 ± 247
16.45	14.46	4240 ± 70	$8.14 \pm 0.011\,\%$	19194 ± 317

TABLE 5.2: Gross counts of neutrons and γ rays during 18-hour passive assessments as a function of UO$_2$ masses.

Mass of ^{238}U (g)	Net Neutron Count	Net Neutron CPS	Net γ-ray Count / $\times 10^7$	Net γ-ray CPS
Background	0 ± 82	0.000 ± 0.001	0.00 ± 6000	0.00 ± 0.1
3.69	274 ± 83	0.004 ± 0.001	$1.71 \pm 0.04\,\%$	264.6 ± 0.1
7.00	333 ± 84	0.005 ± 0.001	$3.01 \pm 0.03\,\%$	464.0 ± 0.1
10.77	591 ± 85	0.009 ± 0.001	$4.73 \pm 0.02\,\%$	730.7 ± 0.1
14.46	911 ± 87	0.014 ± 0.001	$6.55 \pm 0.02\,\%$	1011.2 ± 0.2

TABLE 5.3: Net counts of neutron and γ rays during 18-hour passive assessments as a function of UO$_2$ mass. Data are also presented in CPS (counts per second).
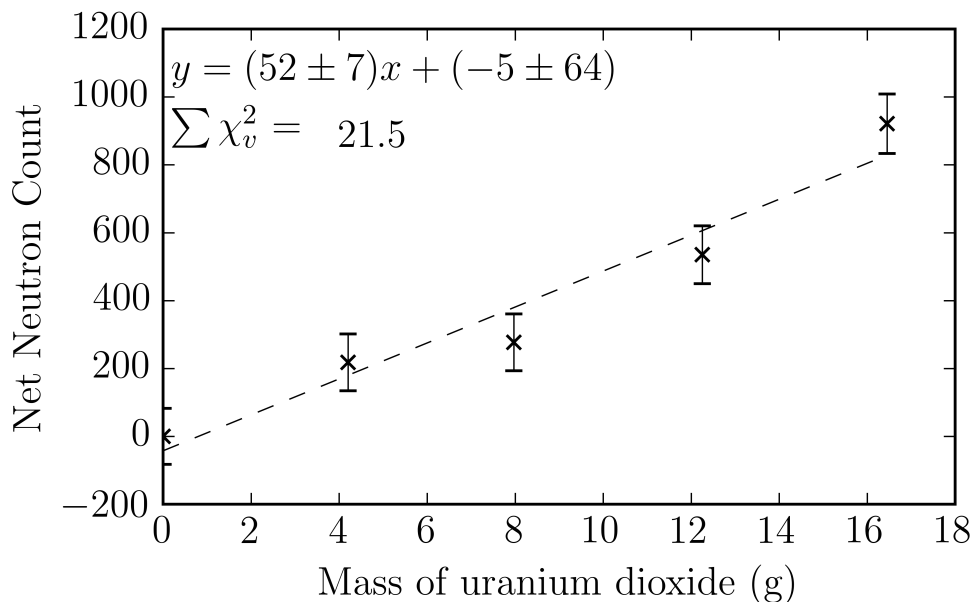
FIG. 5.3: Passive net-neutron count summed over four detectors from the assay of various masses of 0.3 % wt. depleted uranium over 18 hours (a line of best fit, errors of 1σ and reduced chi-squared are included; where x equals the mass of uranium dioxide (g) and y equals the Net neutron counts).
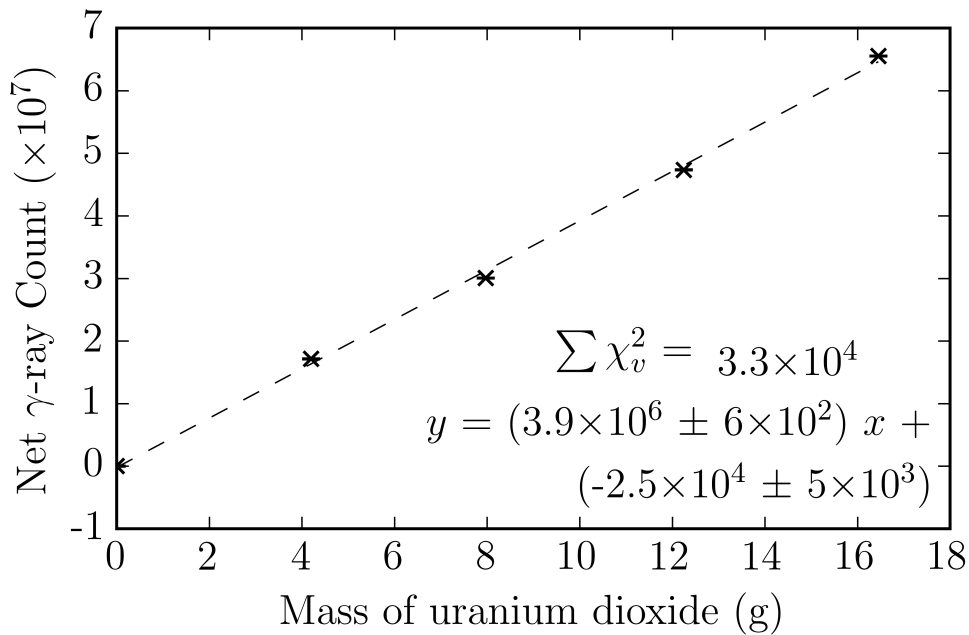
FIG. 5.4: Passive, net γ-ray count summed over four detectors, from the assay of varying masses of 0.3 % wt. depleted uranium, over 18 hours (a line of best fit, errors of 1σ and reduced chi-squared are included; where x equals the mass of uranium dioxide (g) and y equals the net γ-ray counts). The size of the reduced chi-squared value is discussed in Section 5.3; the dashed line is used here to guide the reader's eye.

	CPS per detector per g (UO$_2$)				
	Form of equation of line: $y = (m \pm \Delta m)x + (c \pm \Delta c)$				
Result type	m	Δ m	c	Δ c	$\chi_\nu{}^2$
Net neutron: Fig. 5.3	2.01E-04	3E-05	-2.05E-05	2E-04	8E-05
Net γ-ray: Fig. 5.4	1.51E+01	2E-03	-9.65E-02	2E-02	0.128
	Form of equation of line: $y = m(x) + c$				
	m	c		$\chi_\nu{}^2$	
Net γ/n ratio: Fig. 5.5	-1.1E+03	9.8E+04			7.6E+03
	Form of equation of line: $y = a + b\exp^{cx}$				
	a	b	c		$\chi_\nu{}^2$
γ/n Ratio: Fig. 5.6	0.14	-0.13	-1.4E-07		8.55E-02

TABLE 5.4: Fit parameters for the results obtained in Tables 5.2 and 5.3, normalised to their Counts Per Second (CPS) per detector per gram of UO$_2$. Subsections within these give the fit parameters for different shapes of fit-line as described above each section. $\chi_\nu{}^2$ values for each line-of-fit are also included, the large values are discussed and analysed in section 5.3.
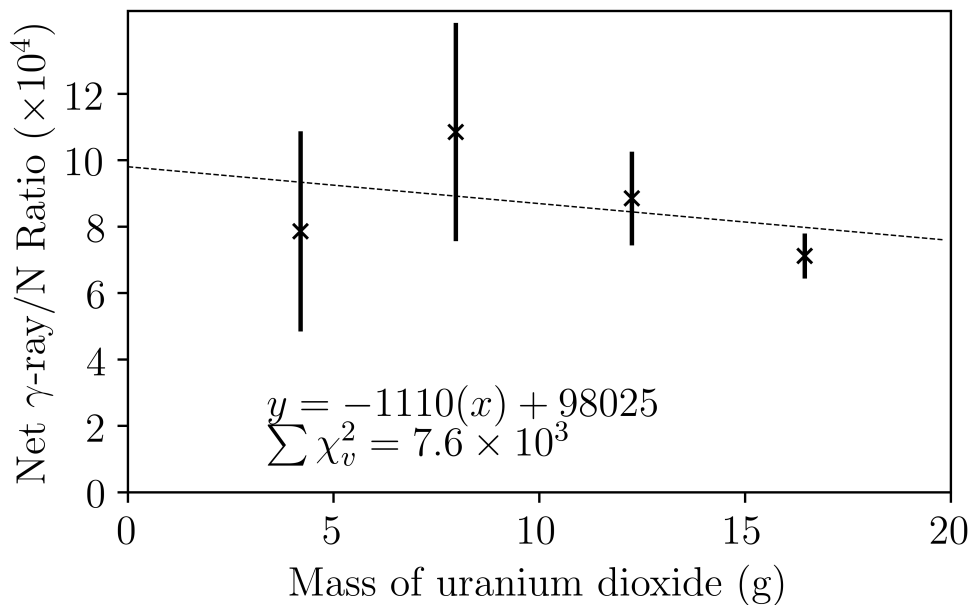
FIG. 5.5: The ratio of net γ-ray count to net-neutron count summed over four detectors, from the passive assay of various masses of 0.3 % wt. depleted uranium, over 18 hours. A reduced chi-squared is included, calculated using a linear line-of-fit. The relationship between the γ/neutron ratio is likely to be linear and slightly negative due to the positive linear correlations canceling each other out and the ability of each type of particle to penetrate the sample of UO_2. The high chi-squared is discussed and analysed in section 5.3. (Propagated errors of 1σ are included; where *x* equals the mass of uranium dioxide (g) and *y* equals the net γ/neutron ratio).

$$y = 37128 - 32443e^{(-0.04x)}$$
$$\sum \chi_v^2 = 0.29$$
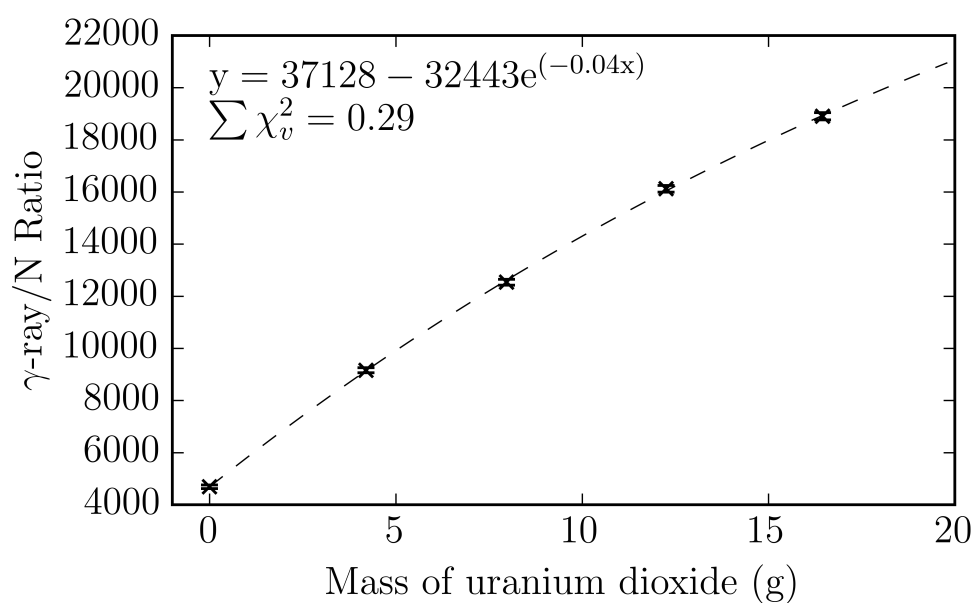
FIG. 5.6: The ratio of γ-ray counts to neutron counts summed over four detectors, from the assay of various masses of 0.3 % wt. depleted uranium, over 18 hours. A reduced chi-squared is included, calculated using an exponential line-of-fit. The relationship between the γ/neutron ratio is unlikely to be linear due to the ability of each type of particle to penetrate the sample of UO_2. (Errors of 1σ are included; where x equals the mass of uranium dioxide (g) and y equals the γ/neutron ratio).

5.3 Analysis

The net neutron count from each of the samples studied in this research exhibits a positive trend with mass with a line-of-best-fit equal to $y = (52.20 \pm 6.51)\, x + (-5.32 \pm 63.83)$; where x equals the mass of uranium dioxide (g) and y equals the net neutron count. As well as neutron detection the equipment detects γ-rays, concurrently. The net γ-ray count also shows a positive trend, with a line of best fit equal to $y = (3918288 \pm 589.19)\, x + (-2500 \pm 4809)$; where x equals the mass of uranium dioxide (g) and y equals the net γ-ray count. The ratio between neutron and γ-ray events has been calculated and exhibits a positive trend; the line of best fit for this relationship has been calculated to be $y = 37128.42 - 32443.46e^{(-0.035x)}$; where x equals the mass of uranium dioxide (g) and y equals the γ-ray/neutron ratio. However, this uses gross counts rather than net counts. This relationship between neutrons and γ rays could be a potentially useful marker of ^{238}U mass without the need for background correction. The very slight exponential function observed here can be attributed, in part, to γ-ray attenuation at high masses of UO_2. This is calculated to be up to 12 % at the highest mass of UO_2.

When the net γ-ray/neutron ratio is plotted, the result is somewhat different to the trends presented elsewhere in this section. The trend exhibited by this ratio appears to be slightly negative, and linear, and has been fitted here with a line-of-best-fit. The equation of this line is calculated as $y = -1110(x) + 98025$, where x equals the mass of uranium dioxide (g) y equals the net-γ-ray/neutron ratio. The large reduced chi-squared value here suggests that this fit is not ideal, however, it was the best fit in comparison to alternatives. This line-of-fit for the ratio is expected as the linear lines of fit for the net neutron, and net γ-ray results, would cancel each other out when divided by one another. The slight negative slope is likely to be due to the fact that neutrons are more penetrating than γ rays, so as the sample size increases self-attenuation of the γ rays is greater than that of the neutrons.

The dense sample material inhibits the emission of γ rays due to self-attenuation, as touched upon in the previous paragraph. The case is less so for neutrons and as sample

size increases this artefact would become more pronounced. The samples used in this study were 5 mm radius and had maximum lengths of 2.5 mm. It can be foreseen that if these samples were scaled up the attenuation of the γ rays could become far more limiting than in this experiment. It is in that scenario that the detection of neutrons comes to the fore.

"Plotting the predicted neutron emission rate of each sample against the measured neutron count rate produces Fig. 5.7. This positive correlation gives an absolute efficiency of the detector system of ∼7%. Given that the solid angle of the detector system is roughly 2/3 of 4-π space (four sides of a cube around the samples are comprised of detector material), the average energy of a ^{238}U spontaneous fission neutron is 0.8 MeV (Alexandrov et al., 2016), and EJ-309 detection efficiency at this energy is ∼20% with a 0.1 MeVee threshold (Pino et al., 2014), we would expect an average absolute efficiency in the region of 13.3%. This average absolute efficiency ignores errors with each of these measurements (predicted neutron emission rate, measured neutron rate, efficiency of detector system, and average neutron energy emitted) that would require intensive computational effort to convolute and combine, for little benefit. The simplistic predicted efficiency of the system also fails to take into account errors associated with using PSD techniques, particularly at low neutron energies, self-shielding, and induced fission neutron energies. With this knowledge of the inadequacies of our predicted efficiency, we believe our measured 7% efficiency and the predicted 13% efficiency are suitably similar."

"There are limited comparisons to be drawn between this method and previous reports due to the low fission neutron emission rate of ^{238}U, resulting in there being relatively little investigation of its potential for uranium assessment. Research into the detection of neutron emissions from the spontaneous fission of ^{238}U has focussed predominantly on measuring the decay constant (Roberts, Gold, and Armani, 1968; Popeko and Ter-Akopian, 1980; Guedes et al., 2003; Yoshioka et al., 2005). An ionization chamber has been used for similar studies using low-mass, heavy-element samples (Ivanov et al., 1985). In that report, 2800 events of ^{238}U spontaneous fission were measured. The
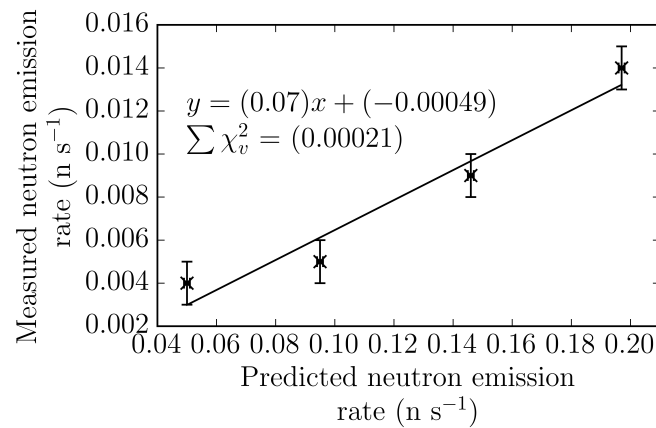
FIG. 5.7: Predicted and measured neutron emission and detection rates at various masses of 0.3 % wt. depleted uranium (errors of 1 standard deviation, a line of best fit, and reduced chi-squared are included; where *x* equals the predicted neutron emission rate from Table 5.1 (n s^{-1}) and *y* equals the measured neutron count rate from Table 5.3 (n s^{-1})).

results have a similar count rate to that measured here. However, the applications of such technology are not readily comparable with the methods discussed here. Most ionisation chambers are stationary and have samples brought to them. Whilst portable ionisation chambers exist, they have much lower efficiencies than the detector system described here. It is feasible for the system described in this paper to be packed up and transported onto nuclear sites for the passive assessment of materials, in-situ. Goddard and Croft (Goddard and Croft, 2013) assayed U_3O_8 passively, concluding that nuclear data available at that time was insufficient to create useful models of the reactions. The paper focused on multiplicity measurements and aligns with the work in this paper with regards to the SF and (α, n) reaction rates. Of the neutron-singles data presented, the research suggests that MCNPX models align well with measured data, although there is negative trend in the ratio as enrichment increases (Goddard and Croft, 2013, Fig. 8). At 0.3% wt. enrichment, as utilised in the work carried out for this paper, there are no data, and the closest point to this has a ratio of ~1.022 between the measured and MCNPX values. This suggests that the MCNP-6 model used in this work is reliable. There are inconsistencies between the research presented here, and (Goddard and Croft, 2013, Fig. 11) with respect to the declared singles count rate efficiencies.

Goddard and Croft (Goddard and Croft, 2013) states that efficiencies for SF neutrons are between 66.5% and 67.0% for all enrichments of U_3O_8, and we declare efficiency of $\sim$7%. However the detection systems are different, and (Goddard and Croft, 2013) uses the Los Alamos Epithermal Neutron Multiplicity Counter (ENMC). The ENMC is constructed of ^{3}He tubes which detect neutrons across the whole spectrum of energies. It would be expected that the ENMC would have a much greater efficiency than the EJ-309 detectors utilised in this research given the spectrum of SF neutrons from ^{238}U (Alexandrov et al., 2016)." The spectrum has a not-insignificant proportion of neutrons below 0.5 MeV, where the EJ-309 scintillant has low efficiency (Pino et al., 2014).

"The PSD data produced during each of the assessments that comprise this experiment were plotted to ensure that the neutron and γ-ray plumes were as expected. Each of the five assays contained patches of noise above the γ-ray plume, as presented in Fig. 5.8. It is expected that these patches of noise are an artefact of running the assessments for long periods of time, and the effects of the noise can be seen clearly in the chi-squared values for the net-γ-ray count (Fig. 5.4). As all the noise artefacts (*clouds*) are manifested above the neutron/γ-ray threshold, in the γ-ray region, the neutron data presented here are considered to be sound and unaffected by this effect. Calculations show that these clouds account for less than 0.16% of the radiation events counted here. Further research is under way to identify the origin of this noise and eliminate the clouds all together. Given what I have observed, I recommend a study of long-sample-time assessments of mixed fields of radiation, in both high and low emission rate enviroments. The results from this will then dictate how to progress further research or suggest a method of removing the *noise*-clouds.

In order to quantify the proportion of neutrons from the (α, n) reaction, a *SOURCES* simulation of this sample was conducted (LANL, 2002). The neutron production rate of 0.3% wt. DUO_2 is given as 7.17×10^{-5} n g^{-1} s^{-1}. This rate of neutron production is a factor of $\sim$189 less than the neutron production rate of spontaneous neutrons from ^{238}U, and so, when considering the results it is reasonable to consider the neutron flux from the (α, n) reaction as negligible relative to that from spontaneous fission."
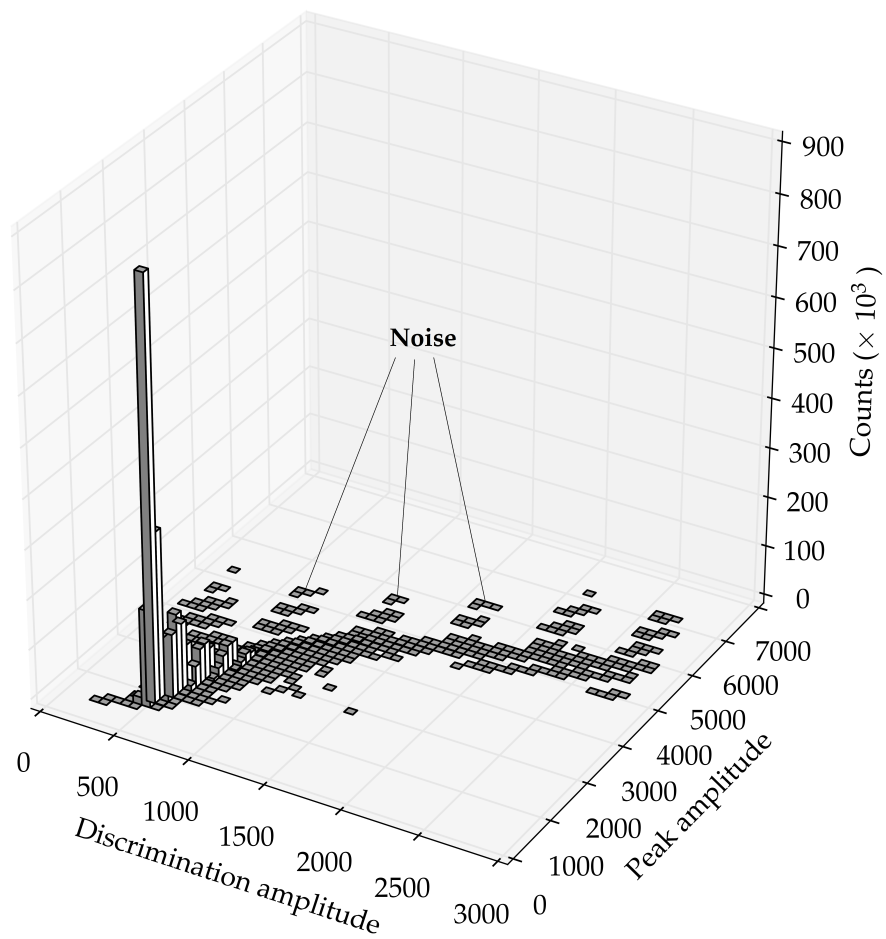
FIG. 5.8: A histogram of PSD data from long term measurement (46 hours) of background radiation showing *clouds* of noise in the γ-ray region. No neutron/γ-ray threshold is plotted as no neutron source was present.

6 Assessment of ^{240}Pu

In collaboration with Hybrid Instruments Ltd., Pajarito Scientific Corporation (PSC) and under an Innovus UK grant, a drum measuring rig was designed. The aims of the project were:

To significantly reduce the cost of accurate NDA measurement of fissile materials in (solid) orphan wastes/residues, and high (α, n) materials such as PuF$_4$ that has traditionally been extremely difficult and expensive to characterise (Ltd., 2017).

Plutonium contaminated material (PCM) is a major α emitter so the drums must remain sealed during characterisation activities. An overview of PCM handling is that by Sills in (Sills, 1984). The drum-rig was designed to measure mixed fields of radiation from legacy PCM drums. The drums, of which there are at least 3000 predicted to increase to 24,000 from Sellafield Sites Limited (SSL) (NDA, 2013), are standard industrial 200 l steel drums. The content of these drums varies from concreted chopped hulls of spent fuel, to standard industrial waste that has come from a plutonium plant consisting of plastics, metals and building materials. The consignment of these drums as low level waste (LLW) instead of intermediate level waste (ILW) has significant cost benefits to the UK tax payer. Inhomogeneous distribution of radioactivity is the largest contributor to the uncertainty of drum measurements (Gillespie, 1994). LLW is classified as havinng radioactivity not exceeding 4 GBq per tonne (α), or 12 GBq per tonne (β/γ). ILW is waste that exceeds the boundaries of LLW, but does not generate a significant amount of heat.

The plutonium in PCM is composed of various plutonium isotopes often formed into compounds with fluorine and oxygen, having been produced in the nuclear cycle. The mixture of plutonium-oxides and plutonium-fluorides makes the process of identification difficult. As plutonium isotopes emit α particles they can induce (α, n) neutron

Isotope	SF (n.s^{-1}.g^{-1})	Oxygen (α, n) (n.s^{-1}.g^{-1})	Fluorine (α, n) (n.s^{-1}.g^{-1})
^{238}Pu	2590	13400	2,200,000
^{239}Pu	0.0218	3.81	5600
^{240}Pu	1020	141	21,000
^{241}Pu	0.05	1.3	170
^{242}Pu	1720	2	270

TABLE 6.1: Specific neutron production rate for isotopes of plutonium. SF denotes spontaneous fission neutrons, and (α, n) neutron production rates are also included for compounds of oxygen and fluorine (Reilly et al., 1993).

emissions and the (α, n) production rate can vary significantly dependant upon the plutonium compound. Table 6.1 gives neutron production rates for various plutonium containing compounds. Compounds containing fluorine have a much greater (α, n) neutron production rate than those containing oxygen. Therefore a small increase in the amount of PuF$_4$ in a PCM drum can significantly change the number of neutrons counted in a tota- neutron-counting scenario. For this reason, coincidence counting is understood to give a better indication of the plutonium content, as it relies upon the spontaneous fission neutron count to determine the composition. It is routine to measure ^{240}Pu$_{eff}$ mass, which, in this research, is equal to 2.49(^{238}Pu) + (^{240}Pu) + 1.57(^{242}Pu) (Stewart and Eccleston, 1993). For the remainder of the chapter ^{240}Pu and ^{240}Pu$_{eff}$ shall both be understood to contain PuF$_4$ and PuO$_2$, unless otherwise stated.

The system designed in this research was benchmarked against a piece of current technology that is available for PCM drum measurements. We chose the Antech N2024-220 *Drum Decommissioning Piece Monitor* which is an off-the-shelf drum monitor for 220 l drums, utilising both coincidence neutron counting and total-neutron-counting. The system comprises 24 ^{3}He tubes surrounded by large slabs of moderating polyethylene. The literature states the lower limit of detection for ^{240}Pu$_{eff}$ as 60-100 mg in a 600 s measurement time (Antech, 2019). Certain requirements of our proposed system were decided upon: that the system would be able to measure masses of 1 mg of PuO$_2$/PuF$_4$ within the drum, and the system would be comprised of detectors that

were compatible with Hybrid Instruments Ltd. MFAx4.3 analysers. Due to the nature of the materials within the drums, it was decided to measure radiation passively rather than actively. Any interrogating source would have to be extremely penetrating or geometrically ubiquitous throughout the sample in order to assay a drum filled with plutonium oxide materials and concrete due to the high neutron cross-section of the sample materials proposed.

Detecting neutrons instead of γ rays is advantageous when measuring radiation from large drums of unknown materials because, as mentioned in earlier chapters, neutrons are more penetrating than γ rays. If a drum were to contain lead or even an amount of steel, then γ rays would be far less likely to reach the detectors than neutrons.

Drum-rig monitors are not a new technology, however the large majority measure γ rays, which are perturbed by high-Z materials within the drum. Off-the-shelf drum monitors measuring γ rays are widely available from companies such as Antech, Mirion Technologies, and Scannix. Of the minority of drum monitors that detect neutrons, it is most commonplace to do so with ^{3}He (Armitage et al., 1995; Jallu and Loche, 2008; Slaninka, Slávik, and Nečas, 2010; Jallu, Passard, and Brackx, 2011; Thanh et al., 2016). As discussed previously, our neutron-detection rig using EJ-309 detectors affords many benefits over a ^{3}He system, including: manoeuvrability, cost, simultaneous γ-ray detection, and spectral information, but is sensitive to γ rays.

6.1 Methods

Two experiments were run in MCNP-6 (Goorley and al., 2012), one to determine the effect of increasing ^{240}Pu % wt. enrichment, and another to determine the effects of increasing the proportion of PuF$_4$ within the sample. Simulations included 200 l steel drums filled with a lattice of PCM materials (metals, plastics, rubber, and soft organics), as per the NDA inventory (NDA, 2016). Throughout the lattice of PCM, 1 mg of PuO$_2$/PuF$_4$ was dispersed, with equal proportions of each isotope of plutonium in the PuO$_2$ and PuF$_4$.

In the first experiment, the enrichment of ^{240}Pu was increased from 0 % wt. up to 8 % wt. (^{240}Pu$_{eff}$ 0.18 - 7.23 % wt.), and PuF$_4$ contamination of 0 % and 1 % were included. The pure PuO$_2$ at 0 % wt. to 8 % wt. had activities of 0.01 Bq to 0.09 Bq respectively. When there was a contamination f 1 % PuF$_4$, the activities increase to 0.07 Bq at 0 % wt. enrichment up to 0.16 Bq at 8 % wt. enrichment. The region of interest for weapons grade plutonium (WGPu) is between ^{240}Pu enrichments of 4-8 % (3.7-7.2 % wt. ^{240}Pu$_{eff}$). Neutrons were counted in coincidence, and in a separate simulation, they were counted as totals. In the second experiment the enrichment of ^{240}Pu was maintained at 6 % wt. to represent weapons-grade plutonium (WGPu) (DOE, 2013, Table 1). The plutonium compounds were initially set to be 100 % PuO$_2$, and then PuF$_4$ was introduced up to a percentage of 15 % wt. The activity of the 0 % PuF$_4$ samples are proportional to the enrichment by a factor of 10.21. The activity of the 1 % PuF$_4$ samples are proportional to the enrichment by a factor of 11.55.

These drums were assessed by our proposed rig, a ring of 16 EJ-309 detectors. This was placed around the drum, affording a suitable radius to have the detector ring translate the height of the drum with clearance from the drum chimes, and by the Antech N2024-220. Fig. 6.1 depicts the geometries of the two detector systems utilised in this research. The neutron-sources were modelled using the neutron production rates given in Table 6.1 multiplied by the relative content within 1 mg of the substance being simulated. Each plutonium compound that we measured contained ^{16}O, ^{19}F, ^{238}Pu, ^{239}Pu, ^{240}Pu, ^{241}Pu, and ^{242}Pu (excluding the 100 % PuO$_2$ samples, which had no ^{19}F).

The neutrons from the dispersed PuO$_2$/PuF$_4$ sources were released in such a way that they mimicked the real-life emission and detection of spontaneous fission (SF) neutrons alongside (α, n) neutrons. To do this in coincidence mode, we introduced a continuous fluence of (α, n) neutrons being emitted from the sources, equal to the amount expected in one second. Then we released a burst of SF neutrons that would be equivalent to the amount released in one second. This produced a Rossi-alpha distribution similar to that in Fig. 6.2. The burst of SF neutrons is mimetic to an event-triggered neutron detection system, whereby a neutron has just been detected and thus the coincident
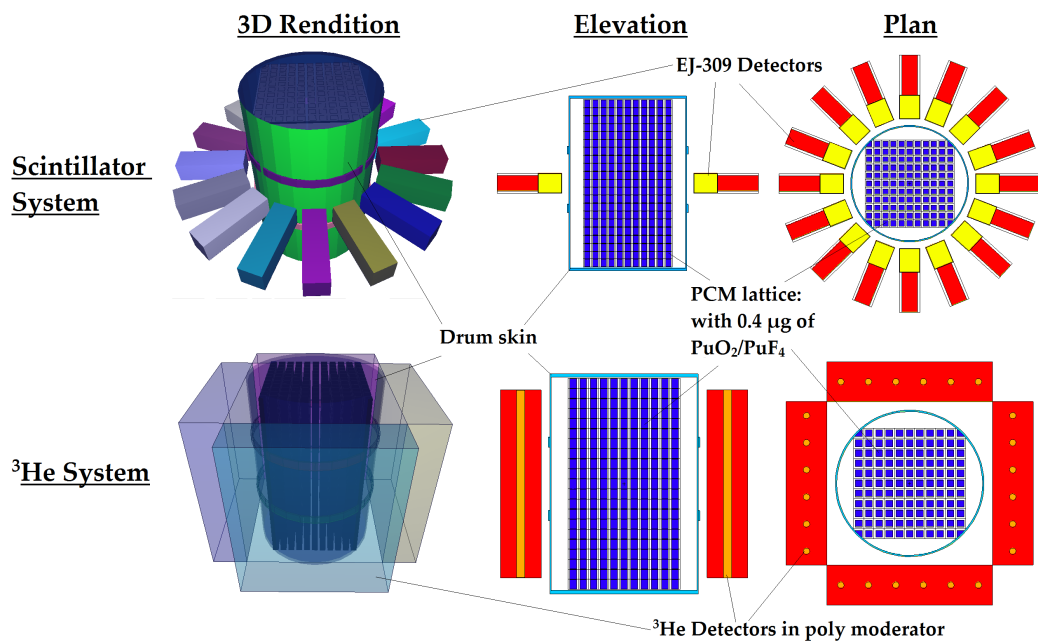
FIG. 6.1: Elevations and plans for a simulated drum-rig monitoring system comprised of scintillation detectors, and an off-the-shelf system comprising ^{3}He detectors; the Antech N2024-220. The drums are filled with a matrix of PCM material with 1 mg of PuO_2 and PuF_4 dispersed throughout the 2541 lattice elements. EJ-309 scintillation detectors are shown at their position of half-drum height (40 cm from the base of the drum). ^{3}He tubes are 2.54 cm in diameter and 75 cm tall.
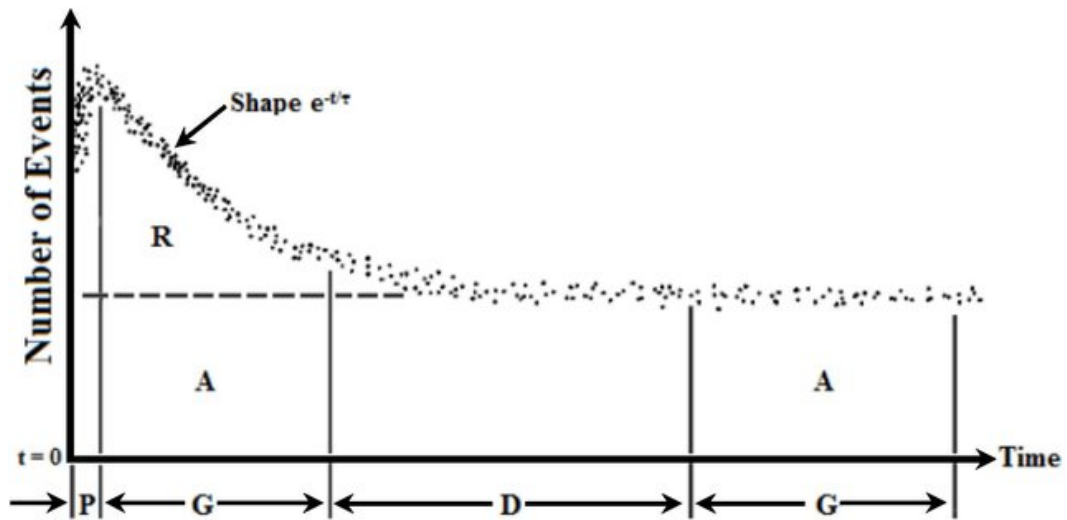
FIG. 6.2: The Rossi-alpha distribution of detected radiation plotted against time. Coincidence counting, with two measurement gates, aims to calculate the *reals* from the accidentals by subtracting a delayed gate from a prompt gate (Reilly et al., 1993, p. 461).

SF neutrons would be imminent. As the burst of SF neutrons is released in our model, each detector-system opens a detection gate. For the scintillation system, this gate was set to 60 ns, double the gate required as detailed in (Sarwar et al., 2018). For the ^{3}He system the gate was set to 81 μs which was based upon a detection window of 64 μs multiplied by 1.27 to take into account the neutron die away time (Mirion, 2019). 4 ms after the initial event-triggering and SF burst, the second detection gates are opened in each system, for the same length of time as the first. The purpose of the second gate is to measure any uncorrelated events, which in the case of PCM drums, could be high due to (α, n) contributions. The difference between the second gate and the first gate is equal to the background corrected neutron count, where we are classing (α, n) neutrons as background. The gate timings for each system are depicted graphically in Fig. 6.2, with Table 6.2 detailing the lengths.

Neutron flux in the detector volumes (F4 tallies) were ran in each detector for all simulations (F4 tallies have been described in further detail in section 3.2). The scintillation detection system had an energy threshold of 0.5 MeV, whilst the ^{3}He system measured neutrons of all energies. An example of one of the codes is available in Appendix C.

	Prompt gate: G	Delay: D	Delayed gate: G
Scintillation system	60 ns	4 ms	60 ns
^{3}He system	81 μs	4 ms	81μs

TABLE 6.2: Gate lengths for a scintillation detector system and a ^{3}He detector system. The ^{3}He system gates must be much longer than those in the scintillation system due to the requirement to thermalise the incoming neutrons to increase detection efficiency.

The raw results from MCNP, in terms of neutrons per source-neutron per cm^3, were corrected to portray each of the detector-systems. The results were multiplied by the detector areas, and the neutron emission rate for each PuO$_2$/PuF$_4$ sample.

6.2 Results

For 1 mg of plutonium-oxide/fluoride mixture, the results of the first experiment are presented in Fig. 6.3. Here, the enrichment level of ^{240}Pu$_{eff}$ is plotted against the net-coincident-neutron count (the difference between the first time-gate and the second time-gate) in each scenario. Propagated uncertainties are included, of one standard deviation. Systematic error associated with the length of coincedence window is omitted due to the window being the same length for all experiments discussed here. The data plotted are for measurement times of 3600 s. If we aim for an uncertainty level of less than 3 % of the net-neutron count, between ^{240}Pu$_{eff}$ enrichments of 3.7-7.2 % wt. (^{240}Pu enrichments of 4-8 % wt.), the measurement times given in Table 6.3 are calculated. The 3 % figure comes from a compromise between accuracy and realistic counting times for these types of experiment, when considering a poisson approximation. For the total-neutron-counting simulations over a 3600 s measurement time, the data presented in Fig. 6.4 are obtained. The time in hours to reach an uncertainty of less than 3 % on these measurements is given in Table 6.4. These total-neutron-count measurements do not have any associated background, as environmental background has not been included in any of the simulations in this chapter. The associated uncertainties are therefore smaller than for the coincidence measurements.
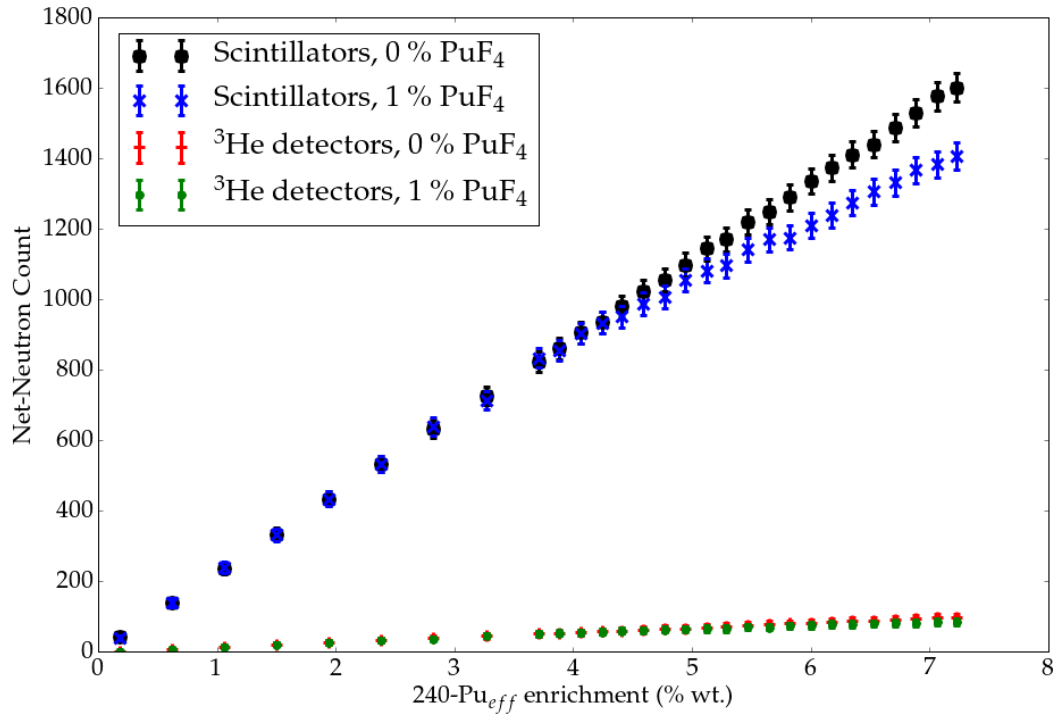
FIG. 6.3: 3600 s Coincidence measurements of 1 mg of plutonium oxide and plutonium oxide/fluoride materials dispersed throughout a 200 l drum of PCM. Net-neutron counts are plotted against the independent variable $^{240}Pu_{eff}$ ($^{240}Pu_{eff}$ includes PuF_4 and PuO_2). Results for a ring of 16 scintillation detectors are plotted against an off-the-shelf ^{3}He monitor; the Antech N2024-220. Propagated errors of one standard deviation are included.

PuF_4 abundance	Scintillation system	^{3}He system
0 % wt.	1.35	21.99
1 % wt.	1.33	23.19

TABLE 6.3: The number of hours of coincidence measurement required to reach an uncertainty level less than 3 % between $^{240}Pu_{eff}$ enrichments of 3.7-7.2 % wt. (^{240}Pu enrichments of 4-8 % wt.). $^{240}Pu_{eff}$ enrichment is formed from both PuF_4 and PuO_2, and the sample is 1mg spread over a 200 l drum.

PuF_4 abundance	Scintillation system	^{3}He system
0 % wt.	0.95	16.05
1 % wt.	0.42	7.29

TABLE 6.4: The number of hours of total-neutron-counts required to reach an uncertainty level less than 3 % between $^{240}Pu_{eff}$ enrichments of 3.7-7.2 % wt. (^{240}Pu enrichments of 4-8 % wt.). $^{240}Pu_{eff}$ enrichment is formed from both PuF_4 and PuO_2, and the sample is 1mg spread over a 200 l drum.
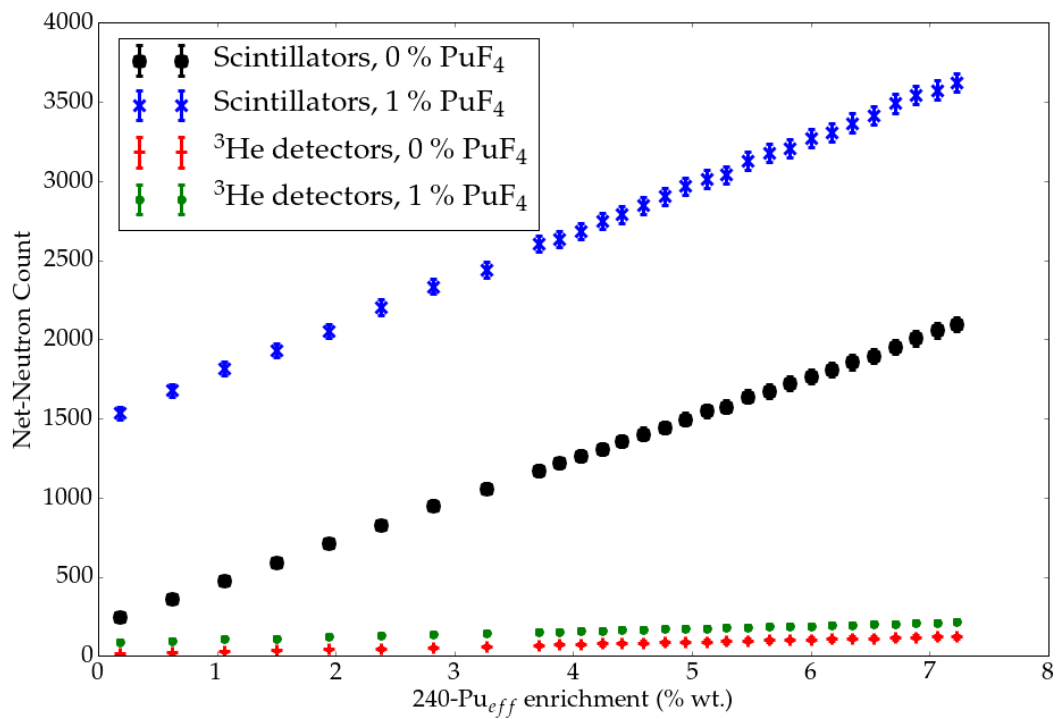
FIG. 6.4: 3600 s Total-neutron-counts of 1 mg of plutonium oxide and plutonium oxide/fluoride materials dispersed throughout a 200 l drum of PCM. Neutron counts are plotted against the independent variable $^{240}Pu_{eff}$. Results for a ring of 16 scintillation detectors are plotted against an off-the-shelf ^{3}He monitor; the Antech N2024-220. Errors of one standard deviation are included.
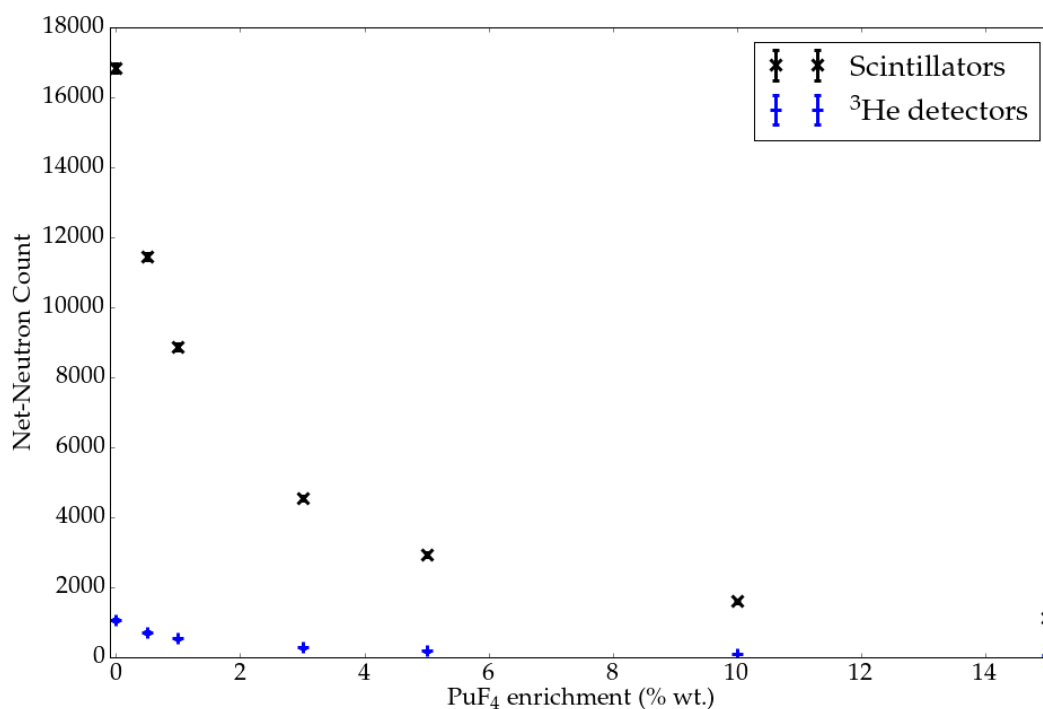
FIG. 6.5: 3600 s coincidence measurements of 1 mg of plutonium ox-
ide/fluoride materials dispersed throughout a 200 l drum of PCM. ^{240}Pu
enrichment is a constant 6 % wt., net-neutron counts are plotted against
the independent variable the PuF_4. Results for a ring of 16 scintillation
detectors are plotted against an off-the-shelf ^3He monitor; the Antech
N2024-220. Propagated errors of one standard deviation are included.

Scintillation system	^3He system
0.97	27.84

TABLE 6.5: The number of hours of measurement required to reach an
uncertainty level less than 3 % between PuF_4 enrichments of 0-15 % wt.

In the second experiment, for 1 mg of plutonium-oxide/fluoride mixture at a con-
stant ^{240}Pu enrichment of 6 % wt., the abundance of PuF_4 between 0-15 % wt. is plotted
against the net-neutron count. The results are presented in Fig. 6.5 for a measurement
time of 3600 s. If we vary the measurement time to achieve an uncertainty level of less
than 3 %, the times provided in Table 6.5 are obtained.

6.3 Analysis

Fig. 6.3 presents the effects of increasing ^{240}Pu enrichment on the net-coincident-neutron count during coincidence counting. The two detector systems; scintillators and ^{3}He have been simulated with 1 mg of PuO$_2$ dispersed throughout a 200 l drum of PCM, and also with an inclusion of 1 % wt. PuF$_4$. It can be seen that over a 3600 s measurement time, the scintillation detectors produce a much higher net-neutron count, for both the 0 % PuF$_4$ and the 1 % PuF$_4$ samples. At an enrichment of 0 % wt. ^{240}Pu, the ^{240}Pu$_{eff}$ enrichment in our sample material is 0.0017 % wt. due to the presence of ^{238}Pu and ^{242}Pu.

When no PuF$_4$ is present, as the ^{240}Pu abundance increases, the net-neutron count increases linearly with a trend of $y = 221.7x + 2.792$ with a reduced $\chi_\nu{}^2$ of 0.016. At a contamination level of 1 % wt. PuF$_4$, the net-neutron count is consistent with the 0 % wt. PuF$_4$ results, until 4.8 % wt. ^{240}Pu (4.41 % wt. ^{240}Pu$_{eff}$). Here, the effects of the (α, n) contamination in the measurements become apparent. The results begin to show an element of a logarithmic increase, which is to be expected as the (α, n) neutron emission rate for fluorines in ^{240}Pu is 21,000 n.s^{-1}.g^{-1}. This is in contrast to a spontaneous fission neutron emission rate of 1020 n.s^{-1}.g^{-1} for pure ^{240}Pu. The background correction mechanism is susceptible to a large (α, n) component, albeit to a significantly lesser degree than a total-neutron-count would be.

When PuF$_4$ is present alongside plutonium oxide, the background neutron count is significantly raised due to the (α, n) neutrons emitted at a rate of 2,200,000 and 21,000 n.s^{-1}.g^{-1} for ^{238}Pu and ^{240}Pu respectively. It is in this high-neutron-background environment that the scintillator system out-performs the ^{3}He system. The gate length of the ^{3}He system; 81 μs; provides a much higher probability of counting accidental coincidences than the scintillator system's 60 ns gate. This ability of the scintillator system to measure the coincidences in a shorter gate is a result of its capacity to detect-directly fast neutrons in comparison to the ^{3}He system which has to thermalise the fast neutrons before they can be detected.

The detection limit mass (DLM) is reported as the lower fissile mass that can be detected with a given confidence level (Jallu, Passard, and Brackx, 2011). In (Stewart and Eccleston, 1993), a DLM of 1-2 mg $^{240}Pu_{(effective)}$ is reported for a 1000 s passive measurement. Similarly, in (Antech, 2019), a DLM of 60-100 mg $^{240}Pu_{eff}$ can be obtained in 600 s. Our system has resolution down to 4.41 μg of ^{240}Pu (6.2 μg of $^{240}Pu_{eff}$, whilst measuring neutrons passively over 3600 s. Between ^{240}Pu enrichments of 4-8 % wt., the smallest increment that can be discerned with a significant statistical difference is 4 μg. This is an 80 times higher resolution than the (Stewart and Eccleston, 1993), when correcting for the difference in measurement time. Our simulations do not take into account the efficiency of the detectors, so this figure would be expected to decrease by roughly $\times$100; 10 % efficiency, squared for coincidence counting.

When total-neutron-counting is carried out with the same systems and same samples, over 3600 s, it can be seen that the time in seconds to get to an uncertainty of less than 3 % is reduced, in comparison to coincidence counting, as per Table 6.4. This is in part due to the fact that the totals counts do not have any background subtracted, and thus the uncertainties are only based upon one measurement. Mostly, the uncertainties are smaller because the total counts are much higher than the coincidence counts. Total-neutron-counting does have major drawbacks when a contamination of (α, n) neutrons is present. Fig. 6.4, clearly shows a disparity between the results for 0 % wt. PuF_4 and 1 % wt. PuF_4. For the scintillation detector system and the ^{3}He system, there is a difference of $\times$1.9 between the 0 % wt. PuF_4 and 1 % wt. PuF_4 results, in the region of interest (^{240}Pu enrichments of 4-8 % wt.). These total-neutron-counts could result in a PCM drum being classified as having a greater quantity of plutonium inside, and therefore sentenced as ILW instead of LLW or even VLLW.

The effects of contamination from (α, n) are clearly depicted in Fig. 6.5. As the ^{240}Pu enrichment is maintained at 6% wt., the PuF_4 content is increased and the net-neutron count, in coincidence mode, is measured. Even a small increase from 0-0.5 % wt. PuF_4 leads to a significant reduction in the net-neutron counts. As the (α, n) emission rate increases, the difference between the counts in gate one and the counts in gate

two reduces, and thus the net-neutron count becomes smaller as the PuF_4 abundance increases.

In (Armitage et al., 1995) a passive neutron drum-monitor is presented, with a novel approach to correct for the unknown matrix within the drum. The monitor is comprised of eight modular ^{3}He detector bundles that can be jointly coupled to a signal processor. Total-neutron-counts as well as coincidence counts are reported, however no nuclear material is measured and so no comparisons can be made between that research and the simulations reported in this thesis. A small ^{252}Cf source is used to scan the drum, it does not interrogate it in the usual manner, but is instead used for transmission radiography. If the ^{252}Cf is translated down one side of the drum, the detectors on the opposite side to the ^{252}Cf measure fewer neutrons when there is a high-neutron-cross-section material in the shine-path in the drum. Matrix composition has not been studied in depth in the simulations reported in this thesis.

Matrix effects from the drum contents and the drum itself could have a significant effect on any results obtained here. The unknown nature of the contents of the PCM drums is of particular concern when designing a system like this for the reasons that inclusions of, for example, hydrogenous materials can interfere with neutron detection. The composition of the drum in our simulations is relatively homogeneous, with a repeated lattice structure containing 2541 PuO_2/PuF_4 elements. Each repeated element has a mass of plutonium oxide/fluoride equal to 4×10^{-7} g. It is understood that a change in the make-up of the drum contents and distribution of plutonium would be likely to affect the results obtained. The worst-case scenario would be a high-activity plutonium source at the top dead-centre, or bottom dead-centre of a drum filled with attenuating material such as concrete, or plastic. To negate the possibility of missing a scenario such as that just described, a simultaneous measurement could be made of neutrons and γ rays, the detectors could be translated through the height of the drum, or extra detectors could be added to the system on the top and bottom of the drum. (Jallu, Passard, and Brackx, 2011) details a $\times$ 30 decrease in counts when a concrete annulus is introduced into the drum. This would need to be factored into to any further

investigations for our system due to the current simulation using only air as the suspension material. Alternatively if an isolated-highly-active source was located towards the periphery of a sample drum, the net-neutron count in the scintillation detectors close to the source would be higher, (Jallu, Passard, and Brackx, 2011) reports that moving a mass of ^{235}U from a central location to a radius of 17 cm, results in a three-fold increase in counts by the system. As the scintillation detectors are counted through separate TTL channels it would be easy to ascertain where the *hot spot* was.

The possibility of counting neutrons and γ rays simultaneously could provide a number of benefits over a neutron-only system. The nature of materials which can attenuate neutrons and γ rays is such that there is not a lot of cross over. γ rays are attenuated by materials with increasing Z-number, and so inclusions of lead, uranium, plutonium and even steel could attenuate γ rays from a sample within the drum. However, neutrons are attenuated mainly by hydrogenous material such as plastic, water, and H_2. It would be unlikey for a singular drum to contain lots of these materials and thus a joint measurement could identify hotspots of radioactivity negating the issues of the matrix effect.

Self attenuation and multiplication within the samples measured has been incorporated into the simulation. In the current drum configuration, the multiplication and self-attenuation do not appear to affect the results that have been measured. However, a change in the drum contents to include something like a thermal neutron source, may result in a greater neutron emission from induced fission. This would vary, dependant upon the ^{239}Pu content, and the abundance of the thermal neutron-emitter within the drum.

The effects of γ-ray interaction have not been simulated in these experiments. The activity of ^{240}Pu is 3.83×10^{6} $\gamma.s^{-1}.g^{-1}$, or 3834 $\gamma.s^{-1}$ for our 1 mg sample (Reilly et al., 1993, p. 18). The most probable energy of these γ rays is 45 keV which would not be very penetrating, although there is a small probability that they could have energies of between 45 - 969 keV (Bé et al., 2016). This low rate of γ-ray emission, along with the attenuation of γ rays in a number of PCM materials, including the drum material itself,

suggests that the EJ-309 scintillation detectors would not be overwhelmed by γ rays during this type of assessment.

The passive nature of the system, as well as the static nature of the detectors and lack of collimation, means that tomography cannot be achieved with the proposed drum rig. To achieve tomography and 3-D rendering of the results, collimation and a different set of detector locations would have to be used, with translations across the horizontal axes of the drum as well as the vertical as per (Licata and Joyce, 2018; Beaumont et al., 2015). However, this would involve introducing machinery into the system which could result in lower reliability of the system in a realistic operational context.

7 Conclusions

In this thesis, the use of small arrays of organic liquid scintillation neutron detectors for the assessment of nuclear materials comprising ^{235}U, ^{238}U and ^{240}Pu has been presented. EJ-309 detectors have been used throughout the research presented in this thesis. They are relatively new, in comparison to ^{3}He detectors, and are a possible replacement as the supply of ^{3}He becomes increasingly constrained, as well as being a potential candidate for metrology in scenarios where ^{3}He is not suited. This thesis is a study of the appropriateness of small arrays of organic liquid scintillator detectors for characterising uranium and plutonium in active and passive coincidence counting and total-neutron-counting scenarios.

The benefits of organic scintillation detectors over ^{3}He detectors, other than the increasing cost of ^{3}He, include their ability to detect neutrons and γ rays concurrently, allowing a real-time (n, γ-ray) ratio to be measured. They do not require neutrons to be thermalised, thus reducing the size and mass of the equipment needed to measure neutrons. The ability to detect fast neutrons provides the user with information on the original incoming neutron-energy, affording the user an opportunity to carry out spectroscopy of the neutron field. The *ns*-scale time resolution enables coincidence counting gates to be significantly shorter than those for ^{3}He, reducing uncertainty in coincidence measurements with large uncorrelated neutron fields, such as (α, n) and for instances where the uncorrelated component is relatively high, i.e. the detection of spontaneous fission neutrons at low emission rates. This property is useful for scenarios where (α, n) neutrons are emitted either from the sample, or when used as the interrogating active neutron source.

Pitfalls of the EJ-309 detector include bleedthrough between the neutron and γ-ray data regions, and the potential for human error in setting an optimum (neutron, γ-ray)

threshold. The low-efficiency of the detectors below ~0.5 MeV may also be advantageous or disadvantageous, depending upon the scenario.

In particular, this thesis focuses on the scenarios where organic scintillators were hypothesised to offer potential advantages over other detector modalities: AmLi-stimulated neutron assay of uranium enrichment, depleted uranium assay, and trace plutonium assay in a hypothesised drum situation. It has shown that, in general, those advantages have been realised.

The flexible nature of EJ-309 detectors used in conjunction with Hybrid Instruments Ltd. MFAx4.3 is reported. The system is often ready to be deployed by simply placing existing equipment in close proximity to the material to be assayed. The equipment used is inherently scaleable, and anywhere from one to 32 detectors can be employed easily in its guise at Lancaster. In the research presented in this thesis, active and passive neutron measurements have been made successfully. Measurements of neutron fields have also been demonstrated in high-neutron-background environments, in the presence of AmLi for example. Very low-level neutron emission rates have been measured, on the bench-top. The use of a neutron-shielding box, the Orr-box, has shown promise in active measurements of small forensic samples. Detector geometries have been assessed and ranked to provide users with information on the most appropriate set-ups to be used in future research. Experimental and simulated research have been used symbiotically, to verify results, refine experiments, and allow further investigation into idiosyncrasies that have arisen during the research.

In chapter 4 results were presented from a simulation-based investigation into the optimal detector array geometry, results from actively assaying low enriched UO_2 in a neutron-shielding box, the Orr-box, and results of actively assaying eight samples of UO_2 of low-enrichment and high-enrichment. The best three performing geometries for actively assessing a sphere of UO_2 were, in order: two layers of eight detectors, one layer of eight detectors, and two layers of 16 detectors. The Orr-box provided a suitable technique for quickly assessing typical forensic-sized samples, with simulations

showing the box to be more efficient than the industry-standard, uranium neutron co-incidence counting collar (UNCL) (Parker et al., 2016). The investigation into actively assessing a broad range of U_3O_8 enrichments with an AmLi interrogating source with four detector geometries proved successful. Experimental and simulated results were in agreement, with the UNCL arrangement being the most efficient. The difference between these findings and those reported in simulations earlier was attributed to the distance from the sample to the detector rings of the other geometries.

Chapter 5 introduced a four-detector array that was used to successfully measure neutrons from various masses of depleted UO_2. Measuring neutrons passively, from such small samples of depleted UO_2, suggest the system has a net-neutron detection rate of 2.01×10^{-4} counts per second, per detector, per gram of depleted UO_2. In chapter 6 a passive neutron drum-monitoring rig was demonstrated. The ability to detect 1 mg of PuO_2 in a high background environment of PuF_4 contamination was shown.

The use of liquid organic scintillation detectors coupled with Hybrid Instruments Ltd. mixed field analysers has been established here as a suitable method of counting neutrons in a variety of scenarios for actinide assay. The benefits of EJ-309 detectors over ^{3}He detectors is well understood, and theses such as this provide further evidence that the complimentary properties of organic scintillators may be relevant in industry, in some applications currently reliant on ^{3}He. Concluding the thesis, novel contributions to the field, applications, and further work are provided hereafter.

7.1 Fulfilment of Aims

- Count neutrons accurately in singles-counting and coincidence-counting modes Singles-counting has been successfully carried out in the Orr-box study, Broad range enrichment investgation, and assessment of ^{238}U. Coincidence-counting is evidenced in the Assessment of ^{240}Pu.

- Detect neutrons in high background environments Assessment of ^{238}U and Assessment of ^{240}Pu both display the successful detection of neutrons in high-background environments. The first in high natural background, and the second in high (α, n) environments.

- Detect ultra-low-level neutron fluxes Assessment of ^{238}U discusses the detection of ultra-low-levels of neutron flux.

- To significantly reduce the cost of accurate NDA measurement of fissile materials in (solid) orphan wastes/residues, and high (α, n) materials such as PuF$_4$ that has traditionally been extremely difficult and expensive to characterise This aim was rather specific, as it was drawn stright from the project aims. Assessment of ^{240}Pu reports specifically upon a design for a rig to measure neutrons to characterise PuF$_4$ in high (α, n) environments

7.2 Novel Contribution to Field

- Ultra-low-level singles-neutron detection from the passive assay of ^{238}U in depleted uranium samples with a mass of less than 16.45 g.

- Design of a passive drum-monitoring rig which can measure ^{240}Pu$_{eff}$ masses of 3.53 μg in 220 l drums of PCM, contaminated with a PuF$_4$ (α,n) neutron flux, using coincidence counting.

- Successfully assessed the ^{235}U enrichment of U$_3$O$_8$ samples between 0.03166 % wt. and 93.1 % wt using total-neutron-counting.

- Investigated the Orr-Box neutron reflection cuboid for the assessment of total-neutron-counts from small samples of low-enriched uranium in comparison to the LS-UNCL.

- Provided a thorough overview of optimal detector arrays for measuring neutrons from small samples.

- Showcased the modular aspect of an EJ-309 detector with Hybrid MFA system, carrying out measurements of ^{235}U, ^{238}U and ^{240}Pu in various formats, with the same equipment inventory.

7.3 Applications

The equipment, methods and techniques detailed in this thesis are prototypes and proofs-of-concept. It is anticipated that more robust, industrial equipment sets and rigs would not be difficult to construe, if required. The very nature of the modular system utilised throughout this thesis lends itself well to dynamic uses without the need for cumbersome, inflexible permanent rigs. The main drawback of applying the equipment and technology is the requirement to calibrate a system, and doing this on plant may be difficult due to background radiation. Notwithstanding this requirement, the technology is expected to be applicable in a variety of situations and scenarios. They will be detailed hereafter, focusing purely on nuclear industry applications.

- **Safeguards**

    - Characterising fresh and spent fuel.

    - Identifying full and partial defects.

    - Weapons verification.

    - Verifying UF$_6$ cylinder contents.

    - Detection of illicit transport and storage of nuclear material.

- **Quality assurance**

    - Fresh fuel enrichment measurements.

    - Detection of inclusions and homogeneity in fresh fuel.

    - Spent fuel burn-up.

    - Fuel plug failure in spent fuel.

- **Waste measurements.**

- **Investigating nuclear power accidents** including LOCA.

- **Unknown materials characterisation** of orphan wastes and forensic samples.

7.4 Further work

Each of the five experiments detailed in this thesis have resulted in recommendations for further work, some of which would strengthen the experiments themselves, and some of which would advance the field further. Details of the suggested further research for each experiment are included henceforth.

- MCNP simulations should be run for volumes of detectors, as well as surfaces. A method of correlating detector response to radiation (neutron and γ-ray spectra) should be devised and utilised. This would provide more realistic results and remove errors of human-judgement. The proper convolution of detector response to incoming radiation would also remove the effects of lower-energy neutrons (<0.5 MeV) affecting simulation results, which we have observed in a number of the simulations in this research.

- The optimal shape of sample material, during active assay, should be investigated. It has been shown in this thesis that spherical samples are less efficient than disc-shaped samples. When assessing forensic samples, for instance, a suitable measurement may be much quicker if the sample can be fashioned into a more optimal shape. Shapes to consider include; spheres, discs, hemispheres, cones, and convex discs, for example.

- Further investigation into the neutron spectrum of AmLi neutrons. (Goddard et al., 2016) suggests that a more consistent spectrum could improve nuclear table data, calculations and simulations.

- The Broad-Range experiment detailed in section 4.3.3 should be re-done with a 12 V supply to the FPGA board, as designed. The use of a 5 V supply will have

had a detrimental effect on the results reported, and likely inhibited the number of counts measured.

- Consider the use of mixed-field radiation measurements for isotopic discrimination during passive measurements. Chapters 5 and 6 both use EJ-309 detectors to passively assay nuclear material. In order to be able to use these techniques purposefully, the ability to differentiate isotopes would be beneficial. One option to increase the ability of the system to be able to do this, is to utilise the Hybrid MFA systems' ability to detect neutrons and γ rays to obtain a ratio of the two and compare this to previous data. As a minimum, this technique would require research into self-attenuation, self-shielding, multiplication, (α, n) contribution, and fission products for a wide variety of possible samples.

- Long-term running of the Hybrid MFA appears to cause patches of noise on the PSD, in the γ-ray region. These should be investigated further and efforts made to reduce the effects.

- Effects of neutron scattering (or crosstalk) should be further investigated. In section 5.1 we report a down scattering of the neutron spectrum due to the close proximity of hydrogenous detector material. Previous research has suggested that increasing neutron moderating material in a system will increase the number of neutrons counted, but we suggest the opposite, due to the EJ-309 cut-off at roughly 0.5 MeV. This artefact should be explored further.

- The drum-monitoring rig should be analysed with other lattice/matrix materials. The use of a lattice of PCM material suspended in air was suitable to show that PuO_2 could be detected in a high-background environment, however, a number of other materials may be in the proposed drums. In particular, a significant amount of concrete should be included, and the simulations re-run.

- Tomography should be considered for the drum-monitoring rig, in the first instance, to quantify the difference in assay times required and the benefits of the results obtained.

References

Alexandrov, A., T. Asada, A. Buonaura, L. Consiglio, N. D'Ambrosio, G. De Lellis, A. Di Crescenzo, et al. "Intrinsic Neutron Background of Nuclear Emulsions for Directional Dark Matter Searches." Astroparticle Physics 80 (July 2016): 16-21.

https://doi.org/10.1016/j.astropartphys.2016.03.003.

Antech. "Drum Decommissioning Piece Monitor, N2024-220." ANTECH, 2019.

http://www.antech-inc.com/products/n2024-220/.

Arduino. Arduino Uno. Accessed July 6, 2017.

http://arduino.cc/en/Main/ArduinoBoardUno.

Armitage, B. H., P. M. J. Chard, S. Croft, K. P. Lambert, and D. J. Lloyd. "A Scan a Source Matrix Correction Technique for Use with a Reconfigurable Passive Neutron Plutonium Assay System." Nuclear Instruments and Methods in Physics Research Section A: Accelerators, Spectrometers, Detectors and Associated Equipment 354, no. 2 (January 30, 1995): 522-26. https://doi.org/10.1016/0168-9002(94)01050-1.

Aryaeinejad, R., Y. X. Dardenne, J. D. Cole, and A. J. Caffrey. "Palm-Size Low-Level Neutron Sensor for Radiation Monitoring." IEEE Transactions on Nuclear Science 43, no. 3 (June 1996): 1539-43. https://doi.org/10.1109/23.507099.

Aspinall, M. D., M. J. Joyce, A. Lavietes, R. Plenteda, F. D. Cave, H. Parker, A. Jones, and V. Astromskas. "Real-Time Capabilities of a Digital Analyzer for Mixed-Field Assay Using Scintillation Detectors." IEEE Transactions on Nuclear Science 64, no. 3 (March 2017): 945-50. https://doi.org/10.1109/TNS.2017.2654512.

Aspinall, M.D., B. D'Mellow, R.O. Mackin, M.J. Joyce, Z. Jarrah, and A.J. Peyton. "The Empirical Characterization of Organic Liquid Scintillation Detectors by the Normalized Average of Digitized Pulse Shapes." Nuclear Instruments and Methods

in Physics Research Section A: Accelerators, Spectrometers, Detectors and Associated Equipment 578, no. 1 (July 21, 2007): 261-66. https://doi.org/10.1016/j.nima.2007.05.114.

Astromskas, Vytautas, and Malcolm Joyce. "Time-Dependent Characterisation of Stability Performance of EJ-309 Detector Systems," Vol. 170, 2018.
https://doi.org/10.1051/epjconf/201817001002.

Balmer, Matthew J. I., Kelum A. A. Gamage, and Graeme C. Taylor. "Comparative Analysis of Pulse Shape Discrimination Methods in a 6Li Loaded Plastic Scintillator." Nuclear Instruments and Methods in Physics Research Section A: Accelerators, Spectrometers, Detectors and Associated Equipment 788 (July 11, 2015): 146-53. https://doi.org/10.1016/j.nima.2015.03.089.

Bé, M.-M. and Chisté, V. and Dulieu, C. and Kellett, M.A. and Mougeot, X. and Arinc, A. and Chechev, V.P. and Kuzmenko, N.K. and Kibédi, T. and Luca, A. and Nichols, A.L. "Table of Radionuclides" Bureau International des Poids et Mesures, Vol. 8

Beaumont, Jonathan. "Characterisation of Radiation Fields with Combined Fast-Neutron and Gamma-Ray Imaging," 2017. https://doi.org/10.17635/lancaster/thesis/33.

Beaumont, Jonathan, Matthew P. Mellor, and Malcolm J. Joyce. "The Analysis of Complex Mixed-Radiation Fields Using near Real-Time Imaging." Radiation Protection Dosimetry 161, no. 1-4 (October 1, 2014): 331-34. https://doi.org/10.1093/rpd/ncu044.

Beaumont, Jonathan, Matthew P. Mellor, Mario Villa, and Malcolm J. Joyce. "High-Intensity Power-Resolved Radiation Imaging of an Operational Nuclear Reactor." Nature Communications 6 (October 9, 2015): 8592. https://doi.org/10.1038/ncomms9592.

Beaumont, J.S., T.H. Lee, M. Mayorov, C. Tintori, F. Rogo, B. Angelucci, and M. Corbo. "A Fast-Neutron Coincidence Collar Using Liquid Scintillators for Fresh Fuel Verification." Journal of Radioanalytical and Nuclear Chemistry 314, no. 2 (2017): 803-12. https://doi.org/10.1007/s10967-017-5412-x.

Bethe, H. A., S. A. Korff, and G. Placzek. "On the Interpretation of Neutron Measurements in Cosmic Radiation." Physical Review 57, no. 7 (April 1, 1940): 573-87. https://doi.org/10.1103/PhysRev.57.573.

Boldeman, J. W., and M. G. Hines. "Prompt Neutron Emission Probabilities Following Spontaneous and Thermal Neutron Fission." Nuclear Science and Engineering 91, no. 1 (September 1, 1985): 114-16. https://doi.org/10.13182/NSE85-A17133.

Capote, R., Y. -J. Chen, F. -J. Hambsch, N. V. Kornilov, J. P. Lestone, O. Litaize, B. Morillon, et al. "Prompt Fission Neutron Spectra of Actinides." Nuclear Data Sheets, Special Issue on Nuclear Reaction Data, 131 (January 1, 2016): 1-106.

https://doi.org/10.1016/j.nds.2015.12.002.

Chadwick, J. "Possible Existence of a Neutron." Nature 129, no. 3252 (February 1932): 312. https://doi.org/10.1038/129312a0.

Chadwick, M. B., M. Herman, P. Oblozinsky, M. E. Dunn, Y. Danon, A. C. Kahler, D. L. Smith, et al. "ENDF/B-VII.1 Nuclear Data for Science and Technology:

Cross Sections, Covariances, Fission Product Yields and Decay Data." Nuclear Data Sheets, Special Issue on ENDF/B-VII.1 Library, 112, no. 12 (December 1, 2011): 2887-2996. https://doi.org/10.1016/j.nds.2011.11.002.

Chao, Jiunn-Hsing, and Huan Niu. "Measurement of Neutron Dose by a Moderating Germanium Detector." Nuclear Instruments and Methods in Physics Research Section A: Accelerators, Spectrometers, Detectors and Associated Equipment 385, no. 1 (January 11, 1997): 161-65. https://doi.org/10.1016/S0168-9002(96)00873-X.

Chichester, D. L., and E. H. Seabury. "Active Interrogation Using Electronic Neutron Generators for Nuclear Safeguards Applications." AIP Conference Proceedings 1099, no. 1 (2009): 851-56. https://doi.org/10.1063/1.3120173.

Chichester, D. L., E. H. Seabury, J. M. Zabriskie, J. Wharton, and A. J. Caffrey. "Dose Profile Modeling of Idaho National Laboratory's Active Neutron Interrogation Laboratory." Applied Radiation and Isotopes 67, no. 6 (2009): 1013-22.

http://dx.doi.org/10.1016/j.apradiso.2009.01.002.

Colonna, N, and G Tagliente. "Response of Liquid Scintillator Detectors to Neutrons of En less than 1 MeV." Nuclear Instruments and Methods in Physics Research Section A: Accelerators, Spectrometers, Detectors and Associated Equipment 416, no. 1 (October 11, 1998): 109-14. https://doi.org/10.1016/S0168-9002(98)00485-9.

Cullen, D E. "Sampling ENDL Watt Fission Spectra." Lawrence Livermore National Laboratory, April 1, 2004. https://doi.org/10.2172/15009825.

Czirr, J. B., D. R. Nygren, and C. D. Zafiratos. "Calibration and Performance of a Neutron-Time-of-Flight Detector." Nuclear Instruments and Methods 31, no. 2 (December 2, 1964): 226-32. https://doi.org/10.1016/0029-554X(64)90163-6.

Davidson, D. R., and E. R. Martin. "Results of Low Level Waste Analysis of Plutonium with a Passive Neutron Coincidence Counter." Proceedings of the 1993 International Conference on Nuclear Waste Management and Environmental Remediation. Volume 3: Environmental Remediation and Environmental Management Issues, 1993. http://inis.iaea.org/Search/search.aspx?origq=RN:27020422.

D'Mellow, B., M.D. Aspinall, R.O. Mackin, M.J. Joyce, and A.J. Peyton. "Digital Discrimination of Neutrons and gamma -Rays in Liquid Scintillators Using Pulse Gradient Analysis." Nuclear Instruments and Methods in Physics Research Section A: Accelerators, Spectrometers, Detectors and Associated Equipment 578, no. 1 (July 21, 2007): 191-97. https://doi.org/10.1016/j.nima.2007.04.174.

DOE. "DOE Handbook: Radiological Safety Training for Plutonium Facilities." Training handbook. Washington, DC: Department of Energy, March 2013.

Dokania, N., V. Singh, S. Mathimalar, A. Garai, V. Nanal, R. G. Pillay, and K. G. Bhushan. "Estimation of Low Energy Neutron Flux (En less than 15 MeV) in India-Based Neutrino Observatory Cavern Using Monte Carlo Techniques." Journal of Instrumentation 10, no. 12 (December 2015): T12005-T12005. https://doi.org/10.1088/1748-0221/10/12/T12005.

Dolan, J. L., M. J. Marcath, M. Flaska, S. A. Pozzi, D. L. Chichester, A. Tomanin, and P. Peerani. "Active-Interrogation Measurements of Fast Neutrons from Induced Fission in Low-Enriched Uranium." Nuclear Instruments and Methods in Physics Research Section A: Accelerators, Spectrometers, Detectors and Associated Equipment 738 (February 21, 2014): 99-105. https://doi.org/10.1016/j.nima.2013.11.052.

Ende, B. M. van der, J. Atanackovic, A. Erlandson, and G. Bentoumi. "Use of GEANT4 vs. MCNPX for the Characterization of a Boron-Lined Neutron Detector."

Nuclear Instruments and Methods in Physics Research Section A: Accelerators, Spectrometers, Detectors and Associated Equipment 820 (June 1, 2016): 40-47.

https://doi.org/10.1016/j.nima.2016.02.082.

Endo, Tomohiro, Akio Yamamoto, and Yoshihiro Yamane. "Detected-Neutron Multiplication Factor Measured by Neutron Source Multiplication Method." Annals of Nuclear Energy 38, no. 11 (November 1, 2011): 2417-27.

https://doi.org/10.1016/j.anucene.2011.01.007.

Enqvist, Andreas, Marek Flaska, Jennifer L. Dolan, David L. Chichester, and Sara A. Pozzi. "A Combined Neutron and Gamma-Ray Multiplicity Counter Based on Liquid Scintillation Detectors." Nuclear Instruments and Methods in Physics Research Section A: Accelerators, Spectrometers, Detectors and Associated Equipment, Symposium on Radiation Measurements and Applications (SORMA) XII 2010, 652, no. 1 (October 1, 2011): 48-51. https://doi.org/10.1016/j.nima.2010.10.071.

Enqvist, Andreas, Christopher C. Lawrence, Brian M. Wieger, Sara A. Pozzi, and Thomas N. Massey. "Neutron Light Output Response and Resolution Functions in EJ-309 Liquid Scintillation Detectors." Nuclear Instruments and Methods in Physics Research Section A: Accelerators, Spectrometers, Detectors and Associated Equipment 715 (July 1, 2013): 79-86. https://doi.org/10.1016/j.nima.2013.03.032.

Enqvist, Andreas, Brian M. Wieger, Lu Huang, Marek Flaska, Sara A. Pozzi, Robert C. Haight, Hye Young Lee, Elaine Kwan, and Ching Yen Wu. "Neutron-Induced 235U Fission Spectrum Measurements Using Liquid Organic Scintillation Detectors." Physical Review C 86, no. 6 (December 12, 2012): 064605.

https://doi.org/10.1103/PhysRevC.86.064605.

Ensslin, N., M. S. Krick, D. G. Langner, M. M. Pickrell, T. D. Reilly, and J. E. Stewart. "Passive Neutron Multiplicity Counting." PANDA 2. LANL, 2007.

Enterprises, ET. "ET Enterprises, ADIT: Photo Multipliers Brochure.Pdf," 2011.

https://my.et-enterprises.com/pdf/Pmt%20Brochure.pdf.

ET Enterprises. "Understanding Photomultipliers." Uxbridge, UK, 2011. https://my.et-enterprises.com/pdf/Understanding%20Pmts.pdf.

Gaca, Pawel, Phillip E. Warwick, and Ian W. Croudace. "Liquid Scintillation Counters Calibration Stability over Long Timescales." Journal of Radioanalytical and Nuclear Chemistry 314, no. 2 (November 1, 2017): 753-60. https://doi.org/10.1007/s10967-017-5388-6.

Gamage, K.A.A., M.J. Joyce, and N.P. Hawkes. "A Comparison of Four Different Digital Algorithms for Pulse-Shape Discrimination in Fast Scintillators." Nuclear Instruments and Methods in Physics Research Section A: Accelerators, Spectrometers, Detectors and Associated Equipment 642, no. 1 (June 21, 2011): 78-83.

https://doi.org/10.1016/j.nima.2011.03.065.

Gamage, K.A.A., M.J. Joyce, and G.C. Taylor. "A Digital Approach to Imaging with a Narrow Tungsten Collimator Aperture and a Fast Organic Liquid Scintillator Detector." Proceedings of the 8th International Topical Meeting on Industrial Radiation and Radioisotope Measurement Applications (IRRMA-8) 70, no. 7 (July 2012): 1223-27. https://doi.org/10.1016/j.apradiso.2012.01.021.

Gillespie, B M. "Detection and Correction of Inhomogeneities in Drum Waste Assay Systems." In Waste Management, 5. Tucson, AZ., 1994.

Glaser, Alexander. "Detection of Special Nuclear Materials." 2004.

http://www.princeton.edu/aglaser/lecture2007detection.pdf.

Goddard, Braden, and Stephen Croft. "High-Fidelity Passive Neutron Multiplicity Measurements and Simulations of Uranium Oxide." Nuclear Instruments and Methods in Physics Research Section A: Accelerators, Spectrometers, Detectors and Associated Equipment 712 (June 1, 2013): 147-56. https://doi.org/10.1016/j.nima.2013.02.007.

Goddard, Braden, Stephen Croft, Angela Lousteau, and Paolo Peerani. "Evaluation of Am-Li Neutron Spectra Data for Active Well Type Neutron Multiplicity Measurements of Uranium." Nuclear Instruments and Methods in Physics Research Section A: Accelerators, Spectrometers, Detectors and Associated Equipment 830 (September 11, 2016): 256-64. https://doi.org/10.1016/j.nima.2016.05.100.

Goorley, T., and et al. Initial MCNP6 Release Overview (version MCNP6.1). Nuclear Technology, 180, pp 298-315, 2012.

Göttsche, Malte, and Gerald Kirchner. "Measurement Techniques for Warhead Authentication with Attributes: Advantages and Limitations." Science and Global Security 22, no. 2 (May 4, 2014): 83-110. https://doi.org/10.1080/08929882.2014.918805.

Gromov, A. V., A. V. Kozunov, A. S. Krivokhatskiy, V. A. Nikolaev, V. I. Yurevich, and V. S. Prokopenko. "Assessment of Neutron Spectral Characteristics of the Chernobyl NPP Failed Reactor." Nuclear Tracks and Radiation Measurements 21, no. 3 (July 1, 1993): 383-86. https://doi.org/10.1016/0969-8078(93)90234-U.

Grosse, Mirco K., Juri Stuckert, Martin Steinbrück, Anders P. Kaestner, and Stefan Hartmann. "Neutron Radiography and Tomography Investigations of the Secondary Hydriding of Zircaloy-4 during Simulated Loss of Coolant Nuclear Accidents." Physics Procedia, The 7th International Topical Meeting on Neutron Radiography (ITMNR-7), 43 (2013): 294-306. https://doi.org/10.1016/j.phpro.2013.03.035.

Guedes, S., J. C. N. Hadler, J. E. S. Sarkis, K. M. G. Oliveira, M. H. Kakazu, P. J. Iunes, M. Saiki, C. a. S. Tello, and S. R. Paulo. "Spontaneous-Fission Decay Constant of 238U Measured by Nuclear Track Techniques without Neutron Irradiation." Journal of Radioanalytical and Nuclear Chemistry 258, no. 1 (September 1, 2003): 117-22. https://doi.org/10.1023/A:1026218411554.

Hamel, Michael C., J. Kyle Polack, Marc L. Ruch, Matthew J. Marcath, Shaun D. Clarke, and Sara A. Pozzi. "Active Neutron and Gamma-Ray Imaging of Highly Enriched Uranium for Treaty Verification." Scientific Reports 7, no. 1 (August 11, 2017): 1-10. https://doi.org/10.1038/s41598-017-08253-x.

Harkness-Brennan, Laura. "An Introduction to the Physics of Nuclear Medicine." Morgan and Claypool Publishers, 2018.

Hausladen, P. A. "Demonstration of Emitted-Neutron Computed Tomography to Count Fuel Pins." USA: Oak Ridge National Lab, 2013.

http://info.ornl.gov/sites/publications/Files/Pub37069.pdf.

Henderson, S., W. Abraham, A. Aleksandrov, C. Allen, J. Alonso, D. Anderson, D. Arenius, et al. "The Spallation Neutron Source Accelerator System Design." Nuclear

Instruments and Methods in Physics Research. Section A, Accelerators, Spectrometers, Detectors and Associated Equipment 763 (2014): 610-73.

https://doi.org/10.1016/j.nima.2014.03.067.

Hicks, Donald A., John Ise, and Robert V. Pyle. "Probabilities of Prompt-Neutron Emission from Spontaneous Fission." Physical Review 101, no. 3 (February 1, 1956): 1016-20. https://doi.org/10.1103/PhysRev.101.1016.

Hussein, Esam M. A. "Monte Carlo Particle Transport with the MCNP Code." Department of Mechanical Engineering: University of New Brunswick, Canada, 2007. https://canteach.candu.org/Content%20Library/20043524.pdf.

Hwang, Chi-Ok, Yeongwon Kim, Cheolgi Im, and Sunggeun Lee. "Buffon's Needle Algorithm to Estimate pi." Applied Mathematics 08, no. 03 (2017): 275-79.

https://doi.org/10.4236/am.2017.83022.

Hybrid Instruments. "MFAX4.3." Accessed December 11, 2017.

http://hybridinstruments.com/products/mfax4.3.html.

Hybrid Instruments Ltd. Funding application. "Innovus Application for Funding via Personal Communication." Funding application, 2017.

IAEA, IAEA. "IAEA Safeguards Glossary." Vienna: International Atomic Energy Agency, 2002.

International Atomic Energy Agency. Detection of Radioactive Materials at Borders. Vienna: IAEA, 2002. http://books.google.com/books?id=IjgmAQAAMAAJ.

Ivanov, M. P., G. M. Ter-Akopian, B. V. Fefilov, and A. S. Voronin. "Study of 238U Spontaneous Fission Using a Double Ionization Chamber." Nuclear Instruments and Methods in Physics Research Section A: Accelerators, Spectrometers, Detectors and Associated Equipment 234, no. 1 (January 15, 1985): 152-57. https://doi.org/10.1016/0168-9002(85)90821-6.

Jallu, F., P. Allinei, P. Bernard, J. Loridon, P. Soyer, D. Pouyat, L. Torreblanca, and A. Reneleau. "The Use of Non-Destructive Passive Neutron Measurement Methods in Dismantling and Radioactive Waste Characterization." In 2011 2nd International Conference on Advancements in Nuclear Instrumentation, Measurement Methods and Their

Applications, 1-8, 2011. https://doi.org/10.1109/ANIMMA.2011.6172926.

Jallu, F., and F. Loche. "Improvement of Non-Destructive Fissile Mass Assays in alpha Low-Level Waste Drums: A Matrix Correction Method Based on Neutron Capture Gamma-Rays and a Neutron Generator." Nuclear Instruments and Methods in Physics Research Section B: Beam Interactions with Materials and Atoms 266, no. 16 (August 1, 2008): 3674-90. https://doi.org/10.1016/j.nimb.2008.06.013.

Jallu, F., C. Passard, and E. Brackx. "Application of Active and Passive Neutron Non Destructive Assay Methods to Concrete Radioactive Waste Drums." Nuclear Instruments and Methods in Physics Research Section B: Beam Interactions with Materials and Atoms 269, no. 18 (September 15, 2011): 1956-62.

https://doi.org/10.1016/j.nimb.2011.05.024.

Jamili, S., E. Bayat, and N. Ghal-Eh. "Digital Neutron-Gamma Discrimination with Scintillators: An Innovative Approach." Radiation Physics and Chemistry 132, no. Supplement C (March 1, 2017): 13-15. https://doi.org/10.1016/j.radphyschem.2016.11.008.

Jha, Divya, Sujata Dahal, Shikha Shukla, and Bimlendu Shahi. "RADIOACTIVE CONTAMINATION DETECTION IN WATER USING WIRELESS SENSOR NETWORK" 1, no. 5 (2016): 6.

Joyce, M. J., R. Sarwar, V. Astromskas, A. Chebboubi, S. Croft, O. Litaize, R. Vogt, and C. H. Zimmerman. "High-Order Angular Correlation of Californium-252 Fission Neutrons and the Effect of Detector Cross-Talk." Nuclear Instruments and Methods in Physics Research Section A: Accelerators, Spectrometers, Detectors and Associated Equipment, February 10, 2019. https://doi.org/10.1016/j.nima.2019.01.092.

Joyce, Malcolm J., Stewart Agar, Michael D. Aspinall, Jonathan S. Beaumont, Edmund Colley, Miriam Colling, Joseph Dykes, Phoevos Kardasopoulos, and Katie Mitton. "Fast Neutron Tomography with Real-Time Pulse-Shape Discrimination in Organic Scintillation Detectors." Nuclear Instruments and Methods in Physics Research Section A: Accelerators, Spectrometers, Detectors and Associated Equipment 834, no. Supplement C (October 21, 2016): 36-45. https://doi.org/10.1016/j.nima.2016.07.044.

Joyce, M.J., J. Adamczyk, M.D. Aspinall, F.D. Cave, and R. Plenteda. "Real-Time,

Fast Neutron Detection for Stimulated Safeguards Assay." In Proceedings of the 37th ESARDA Symposium on Safeguards and Nuclear Non-Proliferation, 54-60. Manchester, UK, 2015.

Joyce, M.J., K.A.A. Gamage, M.D. Aspinall, F.D. Cave, and A. Lavietes. "Real-Time, Fast Neutron Coincidence Assay of Plutonium With a 4-Channel Multiplexed Analyzer and Organic Scintillators." IEEE Transactions on Nuclear Science 61, no. 3 (June 2014): 1340-48. https://doi.org/10.1109/TNS.2014.2313574.

Kaneko, Yoshihiko, and Kenji Sumita. "Determination of Neutron Multiplication, (I): Concept." Journal of Nuclear Science and Technology 4, no. 8 (August 1967): 400-407. https://doi.org/10.1080/18811248.1967.9732775.

Kiff, Scott, Erik Brubaker, Mark Gerling, and Peter Marleau. "Using Fast Neutron Signatures for Improved UF6 Cylinder Enrichment Measurements.," September 1, 2013. https://doi.org/10.2172/1096443.

Kim, H. J., Wan Kim, Sangjun Kang, Kyeryung Kim, and Sangpil Yun. "Fast Neutron and Gamma Induced Radiation Dose Monitoring during Nano-Particle Production by Proton Beam Irradiation." Progress in Nuclear Science and Technology 1, no. 0 (February 25, 2011): 198-201. https://doi.org/10.15669/pnst.1.198.

Kim, Sang In, Bong Hwan Kim, Jang Lyul Kim, and Jung Il Lee. "A Review of Neutron Scattering Correction for the Calibration of Neutron Survey Meters Using the Shadow Cone Method." Nuclear Engineering and Technology 47, no. 7 (December 1, 2015): 939-44. https://doi.org/10.1016/j.net.2015.07.005.

Klein, Horst, and Sonja Neumann. "Neutron and Photon Spectrometry with Liquid Scintillation Detectors in Mixed Fields." Nuclear Instruments and Methods in Physics Research Section A: Accelerators, Spectrometers, Detectors and Associated Equipment 476, no. 1-2 (January 1, 2002): 132-42. https://doi.org/10.1016/S0168-9002(01)01410-3.

Knoll, G. F. Radiation Detection and Measurement Glenn F. Knoll 3rd Ed 1999.Pdf, 1999.

Lakosi, L., C. Tam Nguyen, and J. Bagi. "Photoneutron Interrogation of Low-Enriched Uranium Induced by Bremsstrahlung from a 4MeV Linac." Nuclear Instruments and Methods in Physics Research Section B: Beam Interactions with Materials and Atoms 266, no. 2 (January 1, 2008): 295-300. https://doi.org/10.1016/j.nimb.2007.11.004.

Langford, T.J., E.J. Beise, H. Breuer, C.R. Heimbach, G. Ji, and J.S. Nico. "Development and Characterization of a High Sensitivity Segmented Fast Neutron Spectrometer (FaNS-2)." Journal of Instrumentation: An IOP and SISSA Journal 11 (January 2016). https://doi.org/10.1088/1748-0221/11/01/P01006.

Langner, D. G., J. E. Stewart, M. M. Pickrell, M. S. Krick, N. Ensslin, and W. C. Harker. "Application Guide to Neutron Multiplicity Counting." Los Alamos National Laboratory, Los Alamos, NM, November 1, 1998. https://doi.org/10.2172/1679.

LANL. "SOURCES-4C: Code System For Calculating Alpha,n; Spontaneous Fission; and Delayed Neutron Sources and Spectra.," July 2002.
https://rsicc.ornl.gov/codes/ccc/ccc6/ccc-661.html.

L'Annunziata, Michael F. Handbook of Radioactivity Analysis. Academic Press, 2012.

L'Annunziata, Michael F. Radioactivity: Introduction and History. Elsevier, 2007. https://doi.org/10.1016/B978-0-444-52715-8.X5000-2.

Lawrence, C. C., M. M. Flaska, M. Ojaruega, Andreas Enqvist, S. D. Clarke, S. A. Pozzi, and F. D. Becchetti. "Time-of-Flight Measurement for Energy-Dependent Intrinsic Neutron Detection Efficiency." In 2010 IEEE NUCLEAR SCIENCE SYMPOSIUM CONFERENCE RECORD (NSS/MIC), 110-13. IEEE Nuclear Science Symposium Conference Record. 345 E 47TH ST, NEW YORK, NY 10017 USA: IEEE, 2010.

Lee, Yong-Deok, R. C. Block, R. E. Slovacek, D. R. Harris, and N. M. Abdurrahman. "Neutron Tomographic Fissile Assay in Spent Fuel Using the Lead Slowing down Time Spectrometer." Nuclear Instruments and Methods in Physics Research Section A: Accelerators, Spectrometers, Detectors and Associated Equipment 459, no. 1-2 (February 21, 2001): 365-76. https://doi.org/10.1016/S0168-9002(00)01016-0.

Lehmann, E. H., P. Vontobel, and A. Hermann. "Non-Destructive Analysis of Nuclear Fuel by Means of Thermal and Cold Neutrons." Nuclear Instruments and Methods in Physics Research Section A: Accelerators, Spectrometers, Detectors and Associated Equipment 515, no. 3 (December 11, 2003): 745-59.

https://doi.org/10.1016/j.nima.2003.07.059.

Licata, M., M. D. Aspinall, M. Bandala, F. D. Cave, S. Conway, D. Gerta, H. M. O. Parker, N. J. Roberts, G. C. Taylor, and M. J. Joyce. "Depicting Corrosion-Born Defects in Pipelines with Combined Neutron/gamma Ray Backscatter: A Biomimetic Approach." Scientific Reports 10, no. 1 (January 30, 2020): 1486. https://doi.org/10.1038/s41598-020-58122-3.

Licata, M., and M. J. Joyce. "Concealed Nuclear Material Identification via Combined Fast-Neutron/gamma-Ray Computed Tomography (FNGCT): A Monte Carlo Study." Journal of Instrumentation 13, no. 02 (February 2018): P02013-P02013.

https://doi.org/10.1088/1748-0221/13/02/P02013.

Lopez-Revelles, A. J., J. P. Catalan, A. Kolsek, R. Juarez, R. Garcia, M. Garcia, and J. Sanz. "MCNP Model of the ITER Tokamak Complex." Fusion Engineering and Design, Special Issue: Proceedings of the 13th International Symposium on Fusion Nuclear Technology (ISFNT-13), 136 (November 1, 2018): 859-63.

https://doi.org/10.1016/j.fusengdes.2018.04.023.

Louka, Elli. Nuclear Weapons, Justice and the Law. Edward Elgar Publishing, 2011.

Lounsbury, M. "THE NATURAL ABUNDANCES OF THE URANIUM ISOTOPES." Canadian Journal of Chemistry 34, no. 3 (March 1956): 259-64. https://doi.org/10.1139/v56-039.

Lousteau, Angela L., Robert D. McElroy, Stephen Croft, and Jason P. Hayward. "Determining 235U Enrichment in Bulk Uranium Items Using Dual-Energy Interrogation with Delayed Neutron Measurement." Nuclear Instruments and Methods in Physics Research Section A: Accelerators, Spectrometers, Detectors and Associated Equipment 904 (October 1, 2018): 74-80. https://doi.org/10.1016/j.nima.2018.07.030.

Lucas, S. K. "Integral Proofs That 335/113 greater than Pi." University of South Australia, March 2005. http://educ.jmu.edu/ lucassk/Papers/intpi.pdf.

Magill, Joseph, and Jean Galy. Radioactivity Radionuclides Radiation. Springer Science and Business Media, 2005.

Marcath, M. J., T. H. Shin, A. Di Fulvio, S. D. Clarke, and S. A. Pozzi. "Correlations in Prompt Neutrons and Gamma-Rays from Cf-252 Spontaneous Fission." EPJ Web of Conferences 146 (2017): 04038. https://doi.org/10.1051/epjconf/201714604038.

Marques, F. M., M. Labiche, N. A. Orr, F. Sarazin, and J. C. Angelique. "Neutron Cross-Talk Rejection in a Modular Array and the Detection of Halo Neutrons." Nuclear Instruments and Methods in Physics Research Section A: Accelerators, Spectrometers, Detectors and Associated Equipment 450, no. 1 (August 1, 2000): 109-18. https://doi.org/10.1016/S0168-9002(00)00248-5.

Mashnik, S. G., J. S. Bull, H. G. Hughes, R. E. Prael, and A. J. Sierk. "Current Status of MCNP6 as a Simulation Tool Useful for Space and Accelerator Applications," 706-8. St. Petersburg, FL, USA, 2013. https://doi.org/10.1063/1.4826878.

McConn Jr, R.J., C.J. Gesh, R.T. Pagh, R.A. Rucker, and R.G. Williams II. "Compendium of Material Composition Data for Radiation Transport Modeling." Pacific Northwest National Laboratory, March 4, 2011.

MCNP. "MCNP - A General Monte Carlo N-Particle Transport Code, Version 5. Volume 2: User Guide." Los Alamos National Laboratory, April 24, 2003.

http://catatanstudi.files.wordpress.com/2009/10/mcnp5-manual-vol-ii.pdf.

Menlove, H. O., and G. E. Bosler. "Application of the Active Well Coincidence Counter (AWCC) to High-Enrichment Uranium Metal." Los Alamos National Lab., NM (US), August 1981. http://www.iaea.org/inis/collection/NCLCollectionStore/-Public/12/642/12642722.pdf.

Metropolis, N. "The Beginning of the Monte Carlo Method." Los Alamos Science Special Issue, 1987, 125-30.

Miller, Karen A., Howard O. Menlove, Martyn T. Swinhoe, and Johnna B. Marlow. "Monte Carlo Feasibility Study of an Active Neutron Assay Technique for Full-Volume

UF6 Cylinder Assay Using a Correlated Interrogation Source." Nuclear Instruments and Methods in Physics Research Section A: Accelerators, Spectrometers, Detectors and Associated Equipment 703 (March 1, 2013): 152-57.

https://doi.org/10.1016/j.nima.2012.10.128.

Mirion. "Neutron Detection and Counting," 2019. https://www.mirion.com/learning-center/nuclear-measurement-fundamental-principles/nuclear-measurement-fundamental-principle-neutron-detection-and-counting.

Mirzoyan, R., M. Laatiaoui, and M. Teshima. "Very High Quantum Efficiency PMTs with Bialkali Photo-Cathode." Nuclear Instruments and Methods in Physics Research Section A: Accelerators, Spectrometers, Detectors and Associated Equipment, Proceedings of the 4th International Conference on New Developments in Photodetection, 567, no. 1 (November 1, 2006): 230-32. https://doi.org/10.1016/j.nima.2006.05.094.

Nakamura, T., T. Kosako, and S. Iwai. "Environmental Neutron Measurements around Nuclear Facilities with Moderated-Type Neutron Detector." Health Physics 47, no. 5 (November 1984): 729-43.

Nave, R. "Inverse Square Law," 2019.

http://hyperphysics.phy-astr.gsu.edu/hbase/Forces/isq.html.

-. "Nuclear Fusion." Nuclear Fusion, 2019.

http://hyperphysics.phy-astr.gsu.edu/hbase/NucEne/fusion.html.

NDA. "Packaging of Plutonium Contaminated Material at the Waste Treatment Complex," January 14, 2013. https://rwm.nda.gov.uk/publication/summary-of-assessment-report-for-plutonium-contaminated-material-at-the-waste-treatment-complex-ext-to-final-and-periodic-review/?download.

-. "UK NDA Inventory: Plutonium Contaminated Materials Drums," 2016.

https://ukinventory.nda.gov.uk/wp-content/uploads/sites/18/2017/03/2F02.pdf.

Neumann, Dan A. "Neutron Scattering and Hydrogenous Materials." Materials Today 9, no. 1-2 (January 2006): 34-41. https://doi.org/10.1016/S1369-7021(05)71336-5.

Neutron Cross-Section. "Neutron Cross-Section." Nuclear Power, November 21, 2014. https://www.nuclear-power.net/neutron-cross-section/.

Nian, Victor. "Technology Perspectives from 1950 to 2100 and Policy Implications for the Global Nuclear Power Industry." Progress in Nuclear Energy 105 (May 1, 2018): 83-98. https://doi.org/10.1016/j.pnucene.2017.12.009.

NIST, and NCNR. "Neutron Scattering and Activation Estimation." Accessed May 2, 2018. https://www.ncnr.nist.gov/cgi-bin/neutcalc.

Noonan, William A. "Neutrons: It Is All in the Timing—The Physics of Nuclear Fission Chains and Their Detection." JOHNS HOPKINS APL TECHNICAL DIGEST 32, no. 5 (2014): 12.

Nowicki, Suzanne F., Stephen A. Wender, and Michael Mocko. "The Los Alamos Neutron Science Center Spallation Neutron Sources." Physics Procedia, Conference on the Application of Accelerators in Research and Industry, CAARI 2016, 30 October - 4 November 2016, Ft. Worth, TX, USA, 90 (January 1, 2017): 374-80.

https://doi.org/10.1016/j.phpro.2017.09.035.

Ohzu, A., M. Komeda, M. Kureta, N. Zaima, Y. Nakatsuka, and S. Nakashima. "Development of Non-Destructive Assay System Using Fast Neutron Direct Interrogation Method for Actual Uranium Waste Drums." Transactions of the Atomic Energy Society of Japan 15, no. 2 (2016): 115-27. https://doi.org/10.3327/taesj.J15.011.

Ojovan, M. I., and W. E. Lee. "Chapter 11 - Long-Lived Waste Radionuclides." In An Introduction to Nuclear Waste Immobilisation, edited by M. I. Ojovan and W. E. Lee, 115-23. Oxford: Elsevier, 2005. https://doi.org/10.1016/B978-008044462-8/50013-2.

Osborn, Jeremy M., Kevin J. Glennon, Evans D. Kitcher, Jonathan D. Burns, Charles M. Folden, and Sunil S. Chirayath. "Computational and Experimental Forensics Characterization of Weapons-Grade Plutonium Produced in a Thermal Neutron Environment." Nuclear Engineering and Technology 50, no. 6 (August 1, 2018): 820-28.

https://doi.org/10.1016/j.net.2018.04.017.

Panakkal, J. P., J. K. Ghosh, and P. R. Roy. "Nondestructive Characterization of Mixed Oxide Pellets in Welded Nuclear Fuel Pins by Neutron Radiography and Gamma-Autoradiography: Nondestructive Characterization of Materials, 3rd International Symposium, Saarbrucken (Germany), 3-6 Oct. 1988. Pp. 832-838. Edited by P. Holler, V.

Hauk, G. Dobmann, C.O. Ruud and R.E. Green. Springer-Verlag (1989)." NDT and E International 25, no. 4-5 (1992): 231-. http://dx.doi.org/10.1016/0963-8695(92)90240-H.

Parker, H. M. O., J. S. Beaumont, and M. J. Joyce. "Passive, Non-Intrusive Assay of Depleted Uranium." Journal of Hazardous Materials 364 (February 15, 2019): 293-99. https://doi.org/10.1016/j.jhazmat.2018.08.018.

Parker, Helen M. O., Michael D. Aspinall, Alex Couture, Francis D. Cave, Christopher Orr, Bryan Swinson, and Malcolm J. Joyce. "Active Fast Neutron Singles Assay of 235U Enrichment in Small Samples of Triuranium Octoxide." Progress in Nuclear Energy 93 (November 1, 2016): 59-66. https://doi.org/10.1016/j.pnucene.2016.07.022.

Parker, Helen M. O'D., and Malcolm J. Joyce. "The Use of Ionising Radiation to Image Nuclear Fuel: A Review." Progress in Nuclear Energy 85 (November 2015): 297-318. https://doi.org/10.1016/j.pnucene.2015.06.006.

Pickrell, M. M., A. Lavietes, Gavron, V., Henzlova, D., M. J. Joyce, Kouzes, R. T., and H. O. Menlove. "The IAEA Workshop on Requirements and Potential Technologies for Replacement of 3He Detectors in IAEA Safeguards Applications." Journal of the Institute of Nuclear Materials Management 41 (March 2013): 14-29.

PINCKNEY, THOMAS C., and SUZANNE GNAEGY. "EXPONENTIAL VERSUS LINEAR TRENDS: WHICH IS THE BEST FIT?" Pakistan Economic and Social Review 24, no. 2 (1986): 77-81.

Pino, F., L. Stevanato, D. Cester, G. Nebbia, L. Sajo-Bohus, and G. Viesti. "The Light Output and the Detection Efficiency of the Liquid Scintillator EJ-309." Applied Radiation and Isotopes: Including Data, Instrumentation and Methods for Use in Agriculture, Industry and Medicine 89 (July 2014): 79-84.

https://doi.org/10.1016/j.apradiso.2014.02.016.

Popeko, A. G., and G. M. Ter-Akopian. "Measurement of the 238U Spontaneous-Fission Halflife by Detecting Prompt Neutrons." Nuclear Instruments and Methods 178, no. 1 (December 1, 1980): 163-65. https://doi.org/10.1016/0029-554X(80)90871-X.

Pozzi, S. A. "Analysis of Neutron and Photon Detection Position for the Calibration of Plastic (BC-420) and Liquid (BC-501) Scintillators." Report. Digital Library, August 27, 2003. https://doi.org/10.2172/885588.

Pozzi, S. A., S. D. Clarke, M. Paff, A. Di Fulvio, and R. T. Kouzes. "Comparative Neutron Detection Efficiency in He-3 Proportional Counters and Liquid Scintillators." Nuclear Instruments and Methods in Physics Research Section A: Accelerators, Spectrometers, Detectors and Associated Equipment 929 (June 11, 2019): 107-12. https://doi.org/10.1016/j.nima.2019.03.027.

Prokopowicz, Rafal, and Krzysztof Pytel. "Determination of Nuclear Fuel Burn-up Axial Profile by Neutron Emission Measurement." Nuclear Instruments and Methods in Physics Research Section A: Accelerators, Spectrometers, Detectors and Associated Equipment 838 (December 1, 2016): 18-23. https://doi.org/10.1016/j.nima.2016.09.021.

Raoux, A. -C., A. Lyoussi, C. Passard, C. Denis, J. Loridon, J. Misraki, and P. Chany. "Transuranic Waste Assay by Neutron Interrogation and Online Prompt and Delayed Neutron Measurement." Nuclear Instruments and Methods in Physics Research Section B: Beam Interactions with Materials and Atoms 207, no. 2 (June 1, 2003): 186-94. https://doi.org/10.1016/S0168-583X(03)00451-8.

Redd, Nola Taylor, Live Science Contributor. "What Is Fission?" Live Science, September 19, 2012. https://www.livescience.com/23326-fission.html.

Reilly, D., N. Ensslin, J. Hastings Smith, and S. Kreiner. Passive Nondestructive Assay of Nuclear Materials PANDA. Los Alamos National Laboratory: United States Nuclear Regulatory Commission, 1993.

Roberts, J. H., Raymond Gold, and Roland J. Armani. "Spontaneous-Fission Decay Constant of 238U." Physical Review 174 (October 1, 1968): 1482-84.

https://doi.org/10.1103/PhysRev.174.1482.

Runkle, Robert C., David L. Chichester, and Scott J. Thompson. "Rattling Nucleons: New Developments in Active Interrogation of Special Nuclear Material." Nuclear Instruments and Methods in Physics Research Section A: Accelerators, Spectrometers, Detectors and Associated Equipment 663, no. 1 (January 21, 2012): 75-95.

https://doi.org/10.1016/j.nima.2011.09.052.

Rutherford Ernest. "Bakerian Lecture: Nuclear Constitution of Atoms." Proceedings of the Royal Society of London. Series A, Containing Papers of a Mathematical and Physical Character 97, no. 686 (July 1, 1920): 374-400.

https://doi.org/10.1098/rspa.1920.0040.

Sarwar, R., V. Astromskas, C.H. Zimmerman, G. Nutter, A.T. Simone, S. Croft, and M.J. Joyce. "An Event-Triggered Coincidence Algorithm for Fast-Neutron Multiplicity Assay Corrected for Cross-Talk and Photon Breakthrough." Nuclear Instruments and Methods in Physics Research Section A: Accelerators, Spectrometers, Detectors and Associated Equipment 903 (September 2018): 152-61.

https://doi.org/10.1016/j.nima.2018.06.056.

Sarwar, Rashed. "Real-Time Investigation of Temporal and Spatial Correlations in Fast Neutron Assay from Spontaneous and Stimulated Fission." Phd, Lancaster University, 2019. https://doi.org/10.17635/lancaster/thesis/618.

Schmitt, R. P., L. Cooke, G. Derrig, D. Fabris, B. Hurst, J. B. Natowitz, G. Nebbia, et al. "A Flexible 4pi Neutron Detector for In-Beam Studies: The Texas A and M Neutron Ball." Nuclear Instruments and Methods in Physics Research Section A: Accelerators, Spectrometers, Detectors and Associated Equipment 354, no. 2 (January 30, 1995): 487-95. https://doi.org/10.1016/0168-9002(94)01029-3.

Scionix Holland BV. "Assembly Diagram for Radiation Detector V94 A 94/3 M - EJ309 - E1 - X - Neg VS-1105-21," February 2012.

Sears, Varley F. "Neutron Scattering Lengths and Cross Sections." Neutron News 3, no. 3 (January 1, 1992): 26-37. https://doi.org/10.1080/10448639208218770.

Sharma, B. P. "Nuclear Reactors: Moderator and Reflector Materials." In Encyclopedia of Materials: Science and Technology, edited by K. H. Jürgen Buschow, Robert W. Cahn, Merton C. Flemings, Bernhard Ilschner, Edward J. Kramer, Subhash Mahajan, and Patrick Veyssière, 6365-69. Oxford: Elsevier, 2001. https://doi.org/10.1016/B0-08-043152-6/01126-8.

Shin, T. H., M. J. Marcath, A. DiFulvio, S. D. Clarke, and S. A. Pozzi. "Neutron Cross-Talk Characterization of Liquid Organic Scintillators." In 2015 IEEE Nuclear Science Symposium and Medical Imaging Conference (NSS/MIC), 1-4, 2015.

https://doi.org/10.1109/NSSMIC.2015.7581911.

Sills, R. J. "The Management of Plutonium (Alpha) Contaminated Waste Materials (PCM)." Progress in Nuclear Energy, Nuclear Waste Reprocessing, 13, no. 1 (January 1, 1984): 49-61. https://doi.org/10.1016/0149-1970(84)90006-4.

Sim, Cheul-Muu, TaeJoo Kim, Hwa Suk Oh, and Joon Cheol Kim. "Measurement of Ballooning Gap Size of Irradiated Fuels Using Neutron Radiography Transfer Method and HV Image Filter." Journal of the Korean Society for Nondestructive Testing 33, no. 2 (April 30, 2013): 212-18. https://doi.org/10.7779/JKSNT.2013.33.212.

Simpson, J. D., and Chichester, D. L. Tailoring the Neutron Spectrum from a 14-MeV Neutron Generator to Approximate a Spontaneous-Fission Spectrum. United States. National Nuclear Security Administration, 2011.

Slaninka, Alojz, Ondrej Slavik, and Vladimir Necas. "Uncertainty Analysis of In-Situ Gamma Spectrometry Measurements of Air Cleaning Filter Cartridges and 200L Drums by a HPGe Detector." Applied Radiation and Isotopes, Proceedings of the 17th International Conference on Radionuclide Metrology and its Applications (ICRM 2009), 68, no. 7 (July 1, 2010): 1273-77. https://doi.org/10.1016/j.apradiso.2009.11.012.

Slaughter, D., M Accatino, A Bernstein, J Candy, A Dougan, J Hall, A Loshak, et al. "Detection of Special Nuclear Material in Cargo Containers Using Neutron Interrogation," August 1, 2003. https://doi.org/10.2172/15005260.

Stevanato, L., D. Cester, G. Nebbia, and G. Viesti. "Neutron Detection in a High Gamma-Ray Background with EJ-301 and EJ-309 Liquid Scintillators." Nuclear Instruments and Methods in Physics Research Section A: Accelerators, Spectrometers, Detectors and Associated Equipment 690 (October 21, 2012): 96-101.

https://doi.org/10.1016/j.nima.2012.06.047.

Stewart, J. E., and George W. Eccleston. "Passive/Active Neutron Coincidence Counter." Application Note. Los Alamos, NM: LANL, April 1993.

https://www.lanl.gov/orgs/n/n1/appnotes/pa-ncc.pdf.

Stewart, J. E. and D. Reilly. "14. Principles of Total Neutron Counting." In PANDA - Passive Nondestructive Assay Manual, 407-34. LANL, 1991.

http://www.lanl.gov/orgs/n/n1/panda/00326409.pdf.

Strobl, M. "Neutron Matter Interaction." psi.ch, 2018. https://www.psi.ch/.

Sun, Hao, Chenglong Wang, Xiao Liu, Wenxi Tian, Suizheng Qiu, and Guanghui Su. "Reactor Core Design and Analysis for a Micronuclear Power Source." Frontiers in Energy Research 6 (2018). https://doi.org/10.3389/fenrg.2018.00014.

Tagziria, Hamid, Janos Bagi, Paolo Peerani, and Antony Belian. "Calibration, Characterisation and Monte Carlo Modelling of a Fast-UNCL." Nuclear Instruments and Methods in Physics Research Section A: Accelerators, Spectrometers, Detectors and Associated Equipment 687 (September 21, 2012): 82-91.

https://doi.org/10.1016/j.nima.2012.05.091.

Takada, Masashi, Kazuaki Yajima, So Kamada, Hiroshi Yasuda, and Takashi Nakamura. "Simulated Neutron Response Functions of Phoswich-Type Neutron Detector and Thin Organic Liquid Scintillator." Progress in Nuclear Science and Technology 2, no. 0 (October 1, 2011): 274-79. https://doi.org/10.15669/pnst.2.274.

Thanh, Tran Thien, Hoang Thi Kieu Trang, Huynh Dinh Chuong, Vo Hoang Nguyen, Le Bao Tran, Hoang Duc Tam, and Chau Van Tao. "A Prototype of Radioactive Waste Drum Monitor by Non-Destructive Assays Using Gamma Spectrometry." Applied Radiation and Isotopes, Proceedings of the 20th International Conference on Radionuclide Metrology and its Applications 8-11 June 2015, Vienna, Austria, 109 (March 1, 2016): 544-46. https://doi.org/10.1016/j.apradiso.2015.11.037.

The OU. "Unclear about Nuclear?" The Open University, 2019.

http://www.open.edu/openlearn/science-maths-technology/science/unclear-about-nuclear/content-section-0.

Tomanin, A., J. Paepen, P. Schillebeeckx, R. Wynants, R. Nolte, and A. Lavietes. "Characterization of a Cubic EJ-309 Liquid Scintillator Detector." Nuclear Instruments

and Methods in Physics Research Section A: Accelerators, Spectrometers, Detectors and Associated Equipment 756 (August 21, 2014): 45-54.

https://doi.org/10.1016/j.nima.2014.03.028.

Tomar, B. S., T. C. Kaushik, Sanjay Andola, Ramniranjan, R. K. Rout, Ashwani Kumar, D. B. Paranjape, et al. "Non-Destructive Assay of Fissile Materials through Active Neutron Interrogation Technique Using Pulsed Neutron (Plasma Focus) Device." Nuclear Instruments and Methods in Physics Research Section A: Accelerators, Spectrometers, Detectors and Associated Equipment 703 (March 1, 2013): 11-15.

https://doi.org/10.1016/j.nima.2012.11.027.

Tremsin, A. S., S. C. Vogel, M. Mocko, M. A. M. Bourke, V. Yuan, R. O. Nelson, D. W. Brown, and W. B. Feller. "Non-Destructive Studies of Fuel Pellets by Neutron Resonance Absorption Radiography and Thermal Neutron Radiography." Journal of Nuclear Materials 440, no. 1-3 (September 2013): 633-46.

https://doi.org/10.1016/j.jnucmat.2013.06.007.

Tsoulfanidis, Nicholas, and Sheldon Landsberger. Measurement and Detection of Radiation. CRC Press, 2010. UN. "Treaty on the Non-Proliferation of Nuclear Weapons." UN, July 1, 1968. https://www.un.org/disarmament/wmd/nuclear/npt/text.

Valkovic, Vladivoj, Davorin Sudac, Karlo Nad, and Jasmina Obhodas. "Container Inspection Utilizing 14 MeV Neutrons." IEEE Transactions on Nuclear Science 63, no. 3 (June 2016): 1536-43. https://doi.org/10.1109/TNS.2016.2521925.

Van Rossum, G. Python Software Foundation (version 2.7). Amsterdam, n.d. http://www.python.org.

Verbeke, J.M., M.K. Prasad, and N.J. Snyderman. "Neutron Crosstalk between Liquid Scintillators." Nuclear Instruments and Methods in Physics Research Section A: Accelerators, Spectrometers, Detectors and Associated Equipment 794 (September 2015): 127-40. https://doi.org/10.1016/j.nima.2015.04.019.

Verberck, Bart. "Building the Way to Fusion Energy." Nature Physics 12 (May 3, 2016): 395-97. https://doi.org/10.1038/nphys3752.

Verbinski, V. V., W. R. Burrus, T. A. Love, W. Zobel, N. W. Hill, and R. Textor. "Calibration of an Organic Scintillator for Neutron Spectrometry." Nuclear Instruments and Methods 65 (1968): 8-25. https://doi.org/10.1016/0029-554X(68)90003-7.

Wang, J, A Galonsky, J. J Kruse, P. D Zecher, F Deak, a Horvath, a Kiss, Z Seres, K Ieki, and Y Iwata. "Neutron Cross-Talk in a Multi-Detector System." Nuclear Instruments and Methods in Physics Research Section A: Accelerators, Spectrometers, Detectors and Associated Equipment 397, no. 2 (October 1, 1997): 380-90.

https://doi.org/10.1016/S0168-9002(97)00806-1.

Werner, C. J. "MCNP Users Manual - Code Version 6.2." LANL, 2017. X-5 Monte Carlo Team. "MCNP - A General Monte Carlo N-Particle Transport Code, Version 5." Los Alamos National Laboratory, March 10, 2005.

http://www.nucleonica.net/wiki/images/8/89/MCNPvolI.pdf.

Yoshioka, Tetsu, Takao Tsuruta, Hideki Iwano, and Tohru Danhara. "Spontaneous Fission Decay Constant of 238U Determined by SSNTD Method Using CR-39 and DAP Plates." Nuclear Instruments and Methods in Physics Research Section A: Accelerators, Spectrometers, Detectors and Associated Equipment 555, no. 1-2 (December 15, 2005): 386-95. https://doi.org/10.1016/j.nima.2005.09.014.

Yue, Qiang, Jingke He, Laurence Stamford, and Adisa Azapagic. "Nuclear Power in China: An Analysis of the Current and Near-Future Uranium Flows." Energy Technology 5, no. 5 (August 25, 2016): 681-91. https://doi.org/10.1002/ente.201600444.

Zaitseva, Natalia, Andrew Glenn, H. Paul Martinez, Leslie Carman, Iwona Pawełczak, Michelle Faust, and Stephen Payne. "Pulse Shape Discrimination with Lithium-Containing Organic Scintillators." Nuclear Instruments and Methods in Physics Research Section A: Accelerators, Spectrometers, Detectors and Associated Equipment 729 (November 21, 2013): 747-54. https://doi.org/10.1016/j.nima.2013.08.048.

A Surface flux images
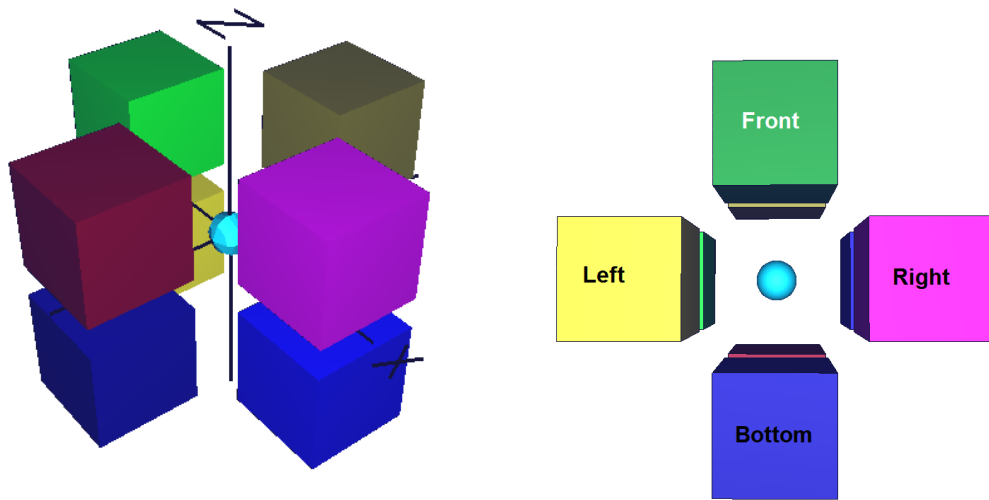
FIG. A.1: Reproduction of the geometry and nomenclature of the 4 by 2 detector arrangement.
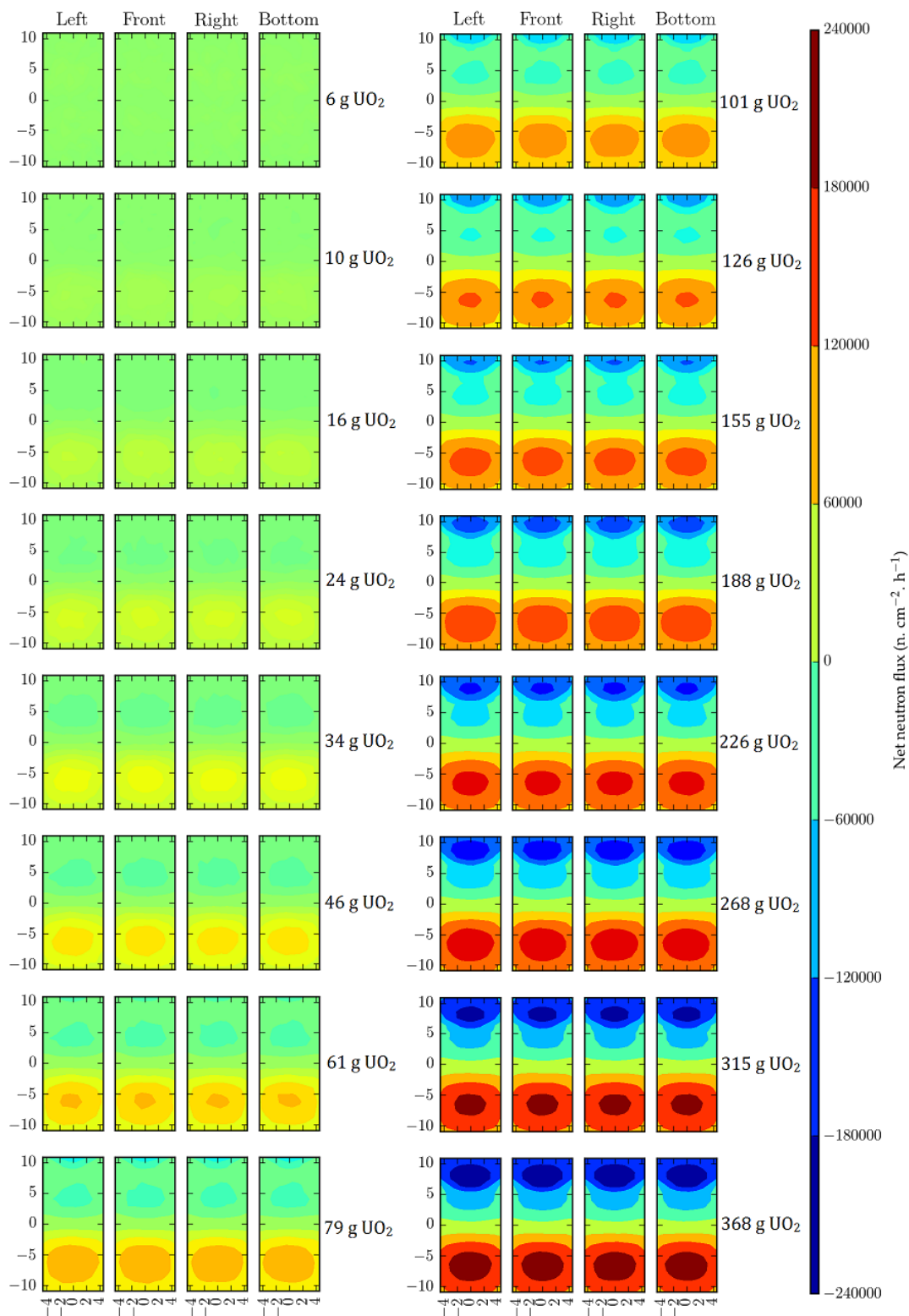
FIG. A.2: Simulated, net singles surface neutron flux in a 4 by 2 detector geometry during active assay with AmLi, at masses of UO_2 at 6 g (top), 101 g (middle), and 368 g (bottom). The axes represent the dimensions of the detector faces in centimetres. The detector labelling system is reproduced in A.1.
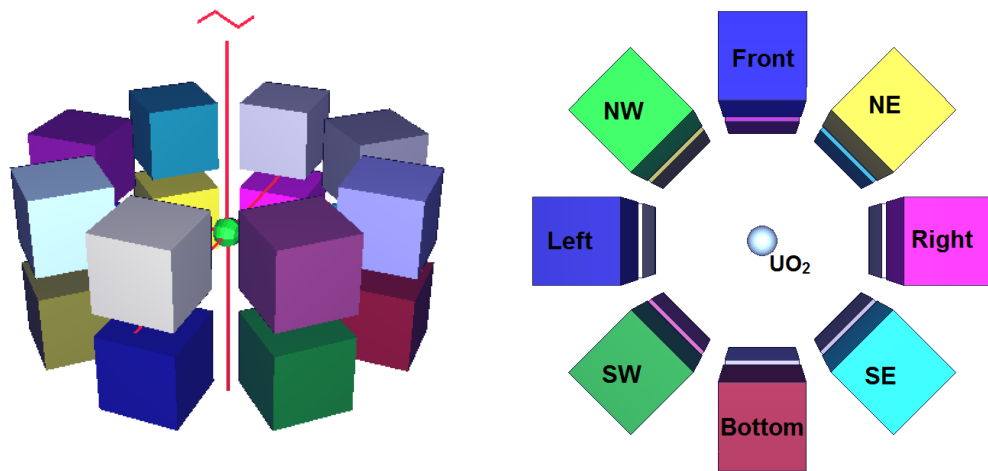
FIG. A.3: Reproduction of the geometry and nomenclature of the 8 by 2 detector arrangement.
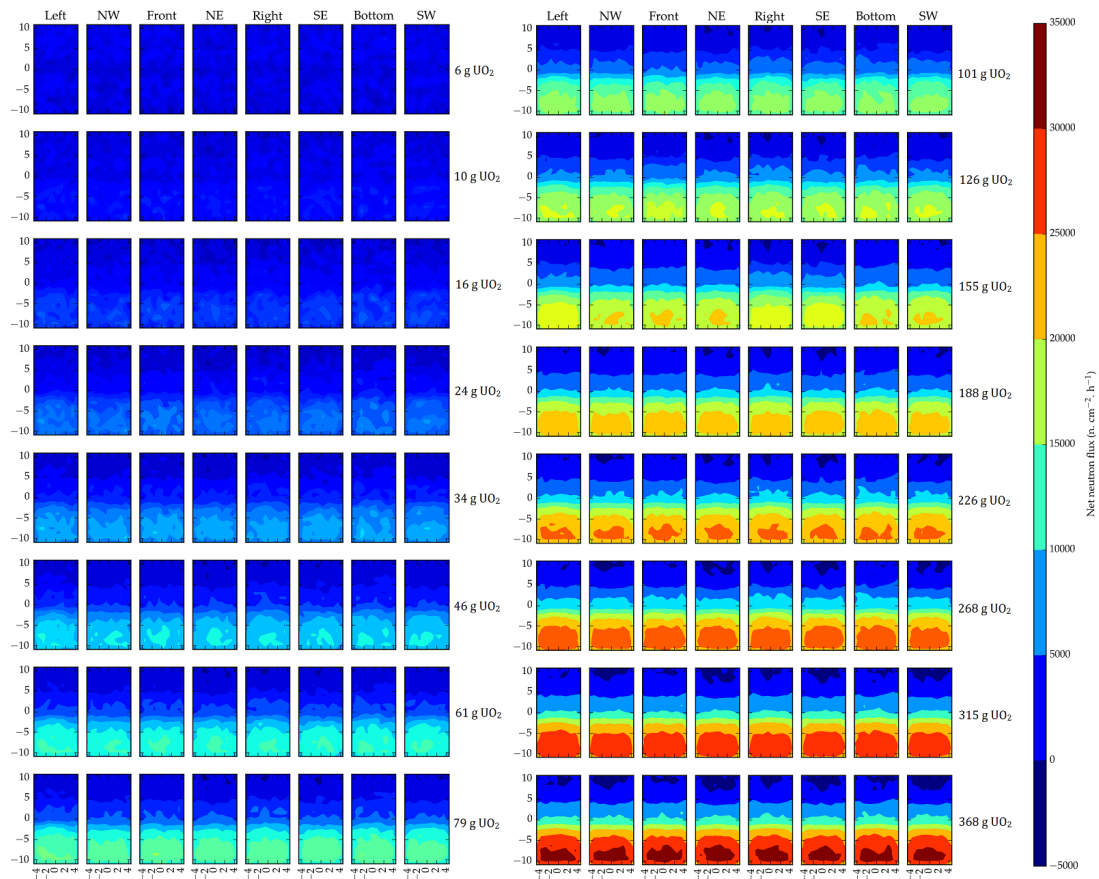
FIG. A.4: Simulated net singles surface neutron flux in a 8 by 2 detector geometry at masses of UO$_2$ from 6 g to 368 g. The axes represent the dimensions of the detector faces in centimetres. The detector labelling system is reproduced in A.3.
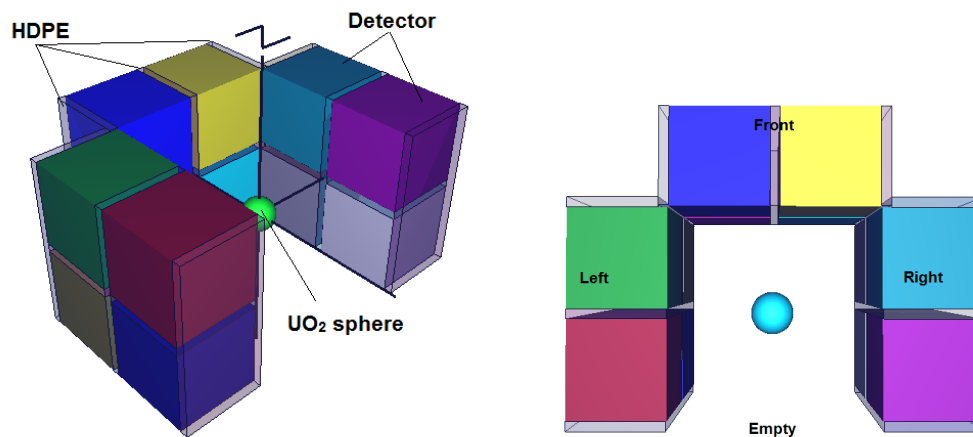
FIG. A.5: Reproduction of the geometry and nomenclature of the LS-UNCL detector arrangement.
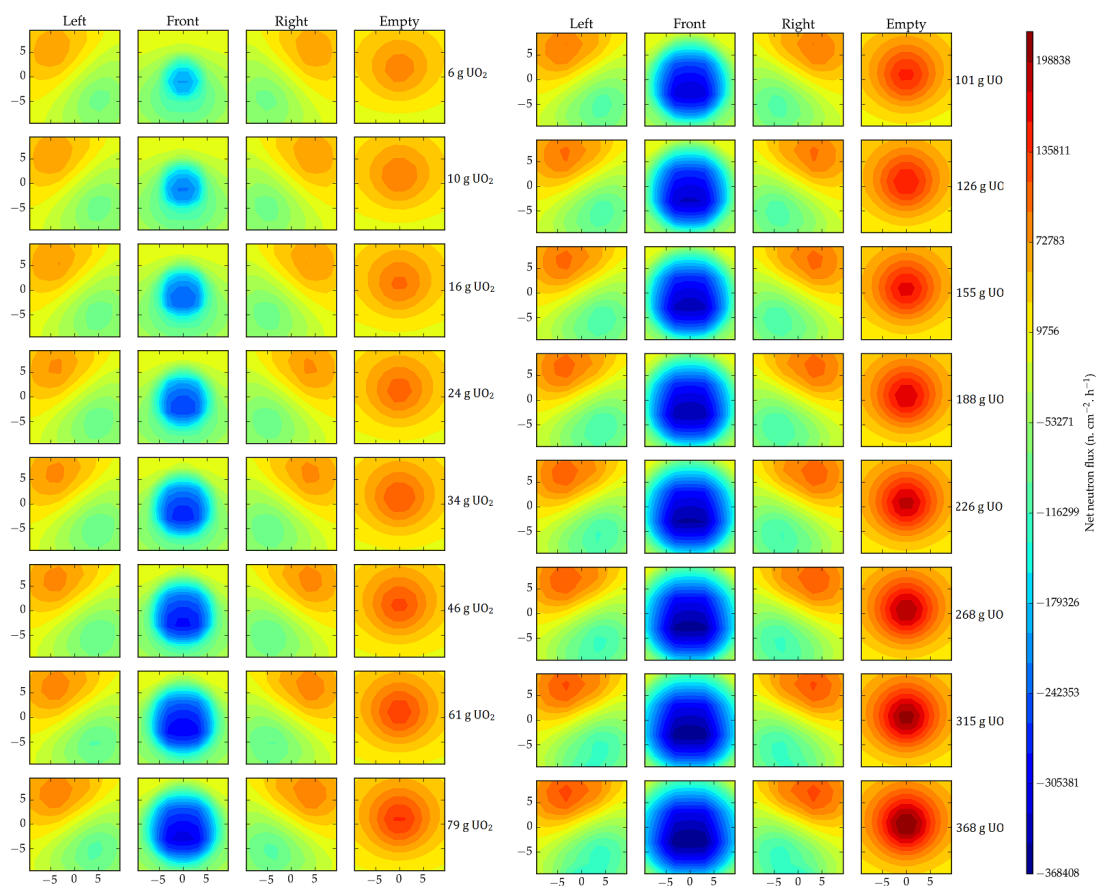
FIG. A.6: Simulated net singles surface neutron flux in a LS-UNCL detector geometry at masses of UO$_2$ from 6 g to 368 g. The axes represent the dimensions of the detector faces in centimetres. The detector labelling system is reproduced in A.5.

B Geometry optimisation example MCNP codes

An example of the MCNP code described in 4.1. We simulated the active assay of low enriched uranium with proposed geometries. We increased a sample mass of uranium oxide from 0 g to 368 g, whilst remaining at 3 % wt. enrichment. The simulated UO_2 was spherical in shape and its mass was increased by increasing the radius of the sphere in 1 mm increments from 5 mm to 20 mm. Details of the composition of each UO_2 sphere are included in Table 4.1. The UO_2 sphere was always placed at the centre of the MCNP universe. The code reproduced here is for double layer of eight detectors placed around a 1.3 mm radius sphere of UO_2.

```
message:

title   --  UO2 stimulated with an AmLi source ---
c
c
c  3 % UO2 pellet with 8 x 2 detectors
c  AmLi source below UO2 to stimulate fission
c  F2 tally on front surface of each detector at energies 0-10 MeV
c  F8 tally for pulse height in cell 80
c  9e8 neutrons runtime
c
c
c        *         *         *         *         *         *         *     **
c
```

```
c                          *** cell descriptions ***
c
10   1  -10.97       -1                  imp:n,p=1        $ Pellet 1
c                                            density in g/cm$^3$ (-ve)
c
20   5  -1.032       -2                  imp:n,p=1  $ detector 1
c
30   5  -1.032       -3                  imp:n,p=1  $ detector 2
c
40   5  -1.032       -4                  imp:n,p=1  $ detector 3
c
50   5  -1.032       -5                  imp:n,p=1  $ detector 4
c
80   5  -1.032       -8                  imp:n,p=1  $ detector 5
c
90   5  -1.032       -9                  imp:n,p=1  $ detector 6
c
100    5  -1.032       -10               imp:n,p=1  $ detector 7
c
110    5  -1.032       -11               imp:n,p=1  $ detector 8
c
120    5  -1.032       -12                imp:n,p=1  $ detector 9
c
130    5  -1.032       -13                imp:n,p=1  $ detector 10
c
140    5  -1.032       -14                imp:n,p=1  $ detector 11
c
150    5  -1.032       -15                imp:n,p=1  $ detector 12
c
160    5  -1.032       -16                imp:n,p=1  $ detector 13
c
170    5  -1.032       -17                imp:n,p=1  $ detector 14
c


                        *** cell descriptions ***
```

```
180   5  -1.032       -18                   imp:n,p=1  $ detector 15
c
190   5  -1.032       -19                   imp:n,p=1  $ detector 16
c
60   4  -0.002105   +1 +2 +3 +4 +5 +8 +9 +10 +11
       +12 +13 +14 +15 +16 +17 +18 +19 -6       imp:n,p=1 $ World
c
70   0               +6                     imp:n,p=0 $ Outside world
c
c    ***** Blank line***********

1   so   +1.3                       $ Sphere of UO2
2   rpp  -5 +5 +16 +26 -11.5 -1.5         $ detector 1
3   rpp  +16 +26 -5 +5 -11.5 -1.5         $ detector 2
4   rpp  -5 +5 -26 -16 -11.5 -1.5         $ detector 3
5   rpp  -26 -16 -5 +5 -11.5 -1.5         $ detector 4
8   rpp  -5 +5 +16 +26 +1.5 +11.5         $ detector 5
9   rpp  +16 +26 -5 +5 +1.5 +11.5         $ detector 6
10   rpp  -5 +5 -26 -16 +1.5 +11.5         $ detector 7
11   rpp  -26 -16 -5 +5 +1.5 +11.5         $ detector 8
12   box  -14.85 +7.77   1.5  -7.071 7.071 0  0 0 10  7.071 7.071 0 $ det 9
13   box  -14.85 +7.77 -11.5  -7.071 7.071 0  0 0 10  7.071 7.071 0 $ det 10
14   box  +14.85 +7.77   1.5  -7.071 7.071 0  0 0 10  7.071 7.071 0 $ det 11
15   box  +14.85 +7.77 -11.5  -7.071 7.071 0  0 0 10  7.071 7.071 0 $ det 12
16   box  -14.85 -21.92   1.5  -7.071 7.071 0  0 0 10  7.071 7.071 0 $ det 13
17   box  -14.85 -21.92 -11.5  -7.071 7.071 0  0 0 10  7.071 7.071 0 $ det 14
18   box  +14.85 -21.92   1.5  -7.071 7.071 0  0 0 10  7.071 7.071 0 $ det 15
19   box  +14.85 -21.92 -11.5  -7.071 7.071 0  0 0 10  7.071 7.071 0 $ det 16
6   so   +100                       $ sphere for the edge of world
c
c                        *** Data Cards after blank line***


c                        *** Source Card***
```

```
sdef POS=D1 ERG FPOS=D2

SI1 L 0 0 0 0 0 -2.3

SP1   .0000015 .9999985

DS2 S 3 4

SP3 -3 0.799 4.903               $ from Valentine 1997 Watt spectrum -3 a b

SI4 A 7.94e-10 3.162e-2 0.06 0.07 0.08 0.13 0.15 0.17 0.27 0.3 0.32 0.37
     0.41 1.5                         $ from NPL AmLi spectra measurement

SP4   0 3.18e-2 1.37e-2 1.437e-2 1.396e-2 2.041e-2 1.852e-2 1.862e-2
     1.022e-2 1.127e-2 1.027e-2 1.107e-2 9.161e-3 2.522e-5

c   From measured data (A allows use of non-rationalised data)

c   use (H and D for histograms and L for rationalised frequency data)

c

c      *        *        *        *        *        *        *        **

c

c                         *** Material Cards ***

c

c    3 % UO2

m1   92238 -0.855 92235 -0.026 8016 -0.119

c

c    Air

m4   6000 -0.000124 7014 -0.755268 &
     8016 -0.231781 18000 -0.012827

c

c    Plastic scintillator

m5   1001 -0.085000 6012 -0.015000

c

c                         *** Tally Cards ***

c

MODE n p

c

c  F1:N 10.2

c  E1 0.32 50

c  C1 -0.866 -0.5 0 0.5 0.866 1                     $ tallies angles of incidence
```

```
c
F4:N 20 30 40 50 80 90 100 110 120 130 140 150 160
      170 180 190
E4 0 1e-5 2e-5 0.5 1 1.5 2 2.5 3 3.5 4 4.5 5 5.5
      6 6.5 7 7.5 8 8.5 9 9.5 10
FC4 Flux in each detector
c
F2:N 2.4 3.2 4.3 5.1 12.2 14.6 16.5 18.1 T
E2 0 1e-5 2e-5 0.5 1 1.5 2 2.5 3 3.5 4 4.5 5 5.5 6 6.5 7 7.5 8 8.5 9 9.5 10
FC2 Flux across the surface of each detector facing the sources
c
FMESH14:n GEOM=XYZ ORIGIN=-5 +16 -11.5
        IMESH=+5
        IINTS=10
        JMESH=+16.1
        JINTS=1
        KMESH=+11.5
        KINTS=20
        EMESH=1.5 10        $ EMESH denotes energy bins
FC14 FMesh tally over S2.4 (FRONT) of an 8x2 array
      (the surface of 4 detectors)
c
FMESH24:n GEOM=XYZ ORIGIN=+16 -5 -11.5
        IMESH=+16.1
        IINTS=1
        JMESH=+5
        JINTS=10
        KMESH=+11.5
        KINTS=20
        EMESH=1.5 10        $ EMESH denotes energy bins
FC24 FMesh tally over S3.2 (RIGHT) of an 8x2 array
      (the surface of 4 detectors)
c
```

```
FMESH34:n GEOM=XYZ ORIGIN=-5 -16.1 -11.5

        IMESH=+5

        IINTS=10

        JMESH=-16.0

        JINTS=1

        KMESH=+11.5

        KINTS=20

        EMESH=1.5 10          $ EMESH denotes energy bins
FC34 FMesh tally over S4.3 (BOTTOM) of an 8x2 array

        (the surface of 4 detectors)

c

FMESH44:n GEOM=XYZ ORIGIN=-16.1 -5 -11.5

        IMESH=-16.0

        IINTS=1

        JMESH=+5

        JINTS=10

        KMESH=+11.5

        KINTS=20

        EMESH=1.5 10          $ EMESH denotes energy bins
FC44 FMesh tally over S5.1 (LEFT) of an 8x2 array

        (the surface of 4 detectors)

c

FMESH54:n GEOM=XYZ ORIGIN=+7.77 +7.77 -11.5

        IMESH=+14.84

        IINTS=10

        JMESH=+14.84

        JINTS=10

        KMESH=+11.5

        KINTS=20

        EMESH=1.5 10          $ EMESH denotes energy bins
FC54 FMesh tally over S14.6 (NE) of an 8x2 array

        (the surface of 4 detectors)

c
```

```
FMESH64:n GEOM=XYZ ORIGIN=+7.77 -14.84 -11.5

            IMESH=+14.84

            IINTS=10

            JMESH=-7.77

            JINTS=10

            KMESH=+11.5

            KINTS=20

            EMESH=1.5 10          $ EMESH denotes energy bins
FC64 FMesh tally over S18.1 (SE) of an 8x2 array

            (the surface of 4 detectors)

c

FMESH74:n GEOM=XYZ ORIGIN=-14.84 -14.84 -11.5

            IMESH=-7.77

            IINTS=10

          JMESH=-7.77

            JINTS=10

            KMESH=+11.5

            KINTS=20

            EMESH=1.5 10          $ EMESH denotes energy bins
FC74 FMesh tally over S16.5 (SW) of an 8x2 array

            (the surface of 4 detectors)

c

FMESH84:n GEOM=XYZ ORIGIN=-14.84 +7.77 -11.5

       IMESH=-7.77

       IINTS=10

       JMESH=+14.84

       JINTS=10

       KMESH=+11.5

       KINTS=20

       EMESH=1.5 10          $ EMESH denotes energy bins
FC84   FMesh tally over S14.6 (NW) of an 8x2 array

       (the surface of 4 detectors)

c
```

```
c          ** Print first 50 histories print table 110 ***

print 110                     $ add table 110 to minimum print-out

c

c                            *** time and nps cut cards ***

nps 900001364          $ nps stop simulation after 900001364 particles

c   tme 60                   $ ctme 1 - stop simulation after 1 min (60 sec)

c

c        *** Blank line terminator ***


End of File
```

C PCM Drum rig example MCNP code

MCNP-6 code for the simulation of 16 scintillation detectors (EJ-309) at half-height of a 200 l drum. The drum contains a lattice of 2451 elements of an air and PCM material. Each lattice has a 0.4 μg of plutonium/fluorine compound at the centre. In this example the ^{240}Pu abundance is 6 % wt. and there is no PuF$_4$ present. An (α, n) neutron fluence is introduced over the whole time period, and a burst of SF neutrons is released. At the same time as the SF neutrons, a detection gate is opened (as a time bin) then 4 ms pass and the same length time bin is opened again. F4 tallies are taken during these time-bins. For the scintillation detectors there is an energy threshold of 0.5 MeV.

```
message:

title  --  Hybrid-Innovus Project
c
c Drum-rig system filled with PCM material
c Light spattering of Pu throughout the drum (in a lattice)
c 0% PuF4
c remainder PuO2
c
c Isotopic compostions and neutron emission calcs in
c 239PU spreadsheet in googledrive/Phd/data
c
c         *         *         *         *         *         *         *     **
c
```

```
c                           *** cell descriptions ***
c
c Lattice Example
c
c  **** Drum   ****
 1  2 -7.84   -40 41 -42 (43:-44:45)  imp:n,p=1 $ Drum shell
 10 2 -7.84   40 -46                  imp:n,p=1 $ Top chime
 11 2 -7.84   40 -47                  imp:n,p=1 $ Bottom chime
 12 4 -0.001205 -45 44 -43 +30
       imp:n,p=1                               $ Contents of drum
c
c  **** Contents of drum - 2cm chopped hull in suspension
5 0 -30 -43 fill=3 imp:n,p=1
2 0 1 -2 3 -4 5 -6 u=3 lat=1 $ROW 1   Inner lattice size
       fill=-5:5 -5:5 -10:10
     2 2540r
     imp:n,p=1
 3 3 -11.46          -20         u=2   imp:n,p=1 $ puo pellet
 4 1 -0.7247      +20 -22     u=2   imp:n,p=1 $ pcm material
 6 4 -0.001205    22          u=2   imp:n,p=1 $ suspension material
c
c  **** Air filled universe  ****
 7 4 -0.001205  #101 #102 #103 #104 #105 #106 #107 #108   $ # = cell
     #109 #110 #111 #112 #113 #114 #115 #116
     -200 (40:-41:42) 46 47  imp:n,p=1 $ Universe
c
c  **** Detector volume for lattice ****
 1001 5 -0.959      -101               u=1   imp:n,p=1 $ Inside detector
 1002 208 -2.7      -102.3 101         u=1   imp:n,p=1 $ Detector skin
 1003 292 -0.30     -103 102.3         u=1   imp:n,p=1 $ PMT
 1004 4   -0.001205 +103.1 +102.3      u=1   imp:n,p=1 $ Air around PMT
c
c
```

```
c  **** Detector locations  ****
 101 0 -104  fill=1    *trcl=( 0 0 0) imp:n,p=1 $ inside detector
 102 like 101 but   *trcl=(0 0 0
      22.5 112.5 90   68.5 22.5 90   90 90 0)
 103 like 101 but   *trcl=(0 0 0
      45 135 90    45 45 90    90 90 0)
 104 like 101 but   *trcl=(0 0 0
      68.5 178.5 90   22.5 68.5 90   90 90 0)
 105 like 101 but   *trcl=(0 0 0
      270 180 90   0 270 90   90 90 0)
 106 like 101 but   *trcl=(0 0 0
      248.5 158.5 90   338.5 248.5 90   90 90 0)
 107 like 101 but   *trcl=(0 0 0
      68.5 77.5 90   22.5 68.5 90   90 90 0)
 108 like 101 but   *trcl=(0 0 0
      202.5 112.5 90   292.5 202.5 90   90 90 0)
 109 like 101 but   *trcl=(0 0 0
      180 90 90   270 180 90   90 90 0)
 110 like 101 but   *trcl=(0 0 0
      158.5 68.5 90   248.5 158.5 90   90 90 0)
 111 like 101 but   *trcl=(0 0 0
      135 45 90   225 135 90   90 90 0)
 112 like 101 but   *trcl=(0 0 0
      112.5 22.5 90   202.5 112.5 90   90 90 0)
 113 like 101 but   *trcl=(0 0 0
      90 0 90   180 90 90   90 90 0)
 114 like 101 but   *trcl=(0 0 0
      68.5 22.5 90   158.5 68.5 90   90 90 0)
 115 like 101 but   *trcl=(0 0 0
      45 45 90   135 45 90   90 90 0)
 116 like 101 but   *trcl=(0 0 0
      22.5 68.5 90   112.5 22.5 90   90 90 0)
 200 0 200         imp:n,p=0   $ Outside Universe
```

```
c  **** Surfaces  ****
c
c Create a box to store the fuel pins in
 1 px -2
 2 px 2
 3 py -2
 4 py 2
 5 pz -2
 6 pz 2
c
c Fuel Pins
 20 S 0 0 0    0.0001046 $ 8.73E-05 mg per lattice ~ 1mg throughout
 22 RPP -1.34 +1.34 -1.34 +1.34 -1.9 +1.9 $-42.55 +42.55
c
c Plutnium Oxide sphere
c 25 S 0 0 0    2.17
c
c Box for entire lattice
 30 rpp -21.999 +21.999 -21.999 +21.999 -41.999 +41.999
c 30 px -30
 31 px 30
 32 py -30
 33 py 30
 34 pz -30
 35 pz 30
c
c Drum Shell surfaces
 40 cz 29.2     $ Outer radius
 41 pz -43.8    $ Outer height
 42 pz 43.8
 43 cz 28.6     $ Inner radius
 430 cz 28.5999 $ work around for lattice
```

```
 44 pz -42.55  $ Inner radius

 45 pz 42.55

 46 RCC 0 0 14.6  0 0 4  29.85   $ Top chime

 47 RCC 0 0 -14.6  0 0 4  29.85   $ Bottom chime

c

c Detector body

101 RPP -4.8 4.8 32.7 44.3 -4.8 4.8   $ Inside detector

102 RPP -5   5   32.5 44.5 -5 5   $ Detector skin

103 RCC  0 44.5 0  0 20 0  3.9    $ PMT

104 RPP -4.999999 4.99999 32.500001 64.4999 -4.99999 4.99999  $ Detec-
tor Unit

c

c Edge of Universe

200 so 500

c

c

c                           *** Data Cards after blank line***


c                           *** Source Card***

c

c Distribution numbers used 1 2 7 8 20 21 22 30 31 32

c

SDEF  CEL=D1

     X=D2

     Y=D7

     Z=D8

     ERG=FCEL D20

     TME=FCEL D30

c

c          SF                    alpha,n

SI1 L (3<2[-5:5 -5:5 -10:10]<5) (3<2[-5:5 -5:5 -10:10]<5)

SP1    2.29e-4 2540r               6.76e-5 2540r   $ neutron prob-
ability for 0% PuF4
```

```
c Releasing 409000 shk of alpha,n neutrons and 409000 shk of SF neutrons
c calculated in s/s 239-Pu
c
c DS2 S 3 4
SI2 -0.000105 0.000105    $ for SF
SP2 0 1
c
SI7 -0.000105 0.000105
SP7 0 1
c
SI8 -0.000105 0.000105
SP8 0 1
c
DS20 S 21 2540r 22 2540r
SP21 -3 0.799 4.903 $ from Valentine 1997 Watt spectrum -3 a b
c calculated in S/S 239Pu from data Bliss 2000
c for 0% PuF4 - NEED TO CHANGE FOR OTHER COMPOSITIONS
SI22 L 0.064516129 0.193548387 0.35483871 0.419354839
        0.64516129 0.806451613 0.870967742 1 1.258064516
        1.709677419 1.903225806 2 2.258064516 2.35483871
        2.451612903 2.935483871 3.096774194 3.451612903
        3.580645161 3.677419355 3.774193548 3.967741935
SP22 0.361538462 0.323076923 0.315384615 0.307692308
        0.269230769 0.253846154 0.207692308 0.184615385
        0.292307692 0.461538462 0.584615385 0.623076923
        0.684615385 0.684615385 0.653846154 0.438461538
        0.369230769 0.184615385 0.076923077 0.046153846
        0.030769231 0
c
DS30 S 31 2540r 32<3 2540r
SI31 0 399 400 $ release SF n's at 400shks
SP31 0 0 1
SI32 0 1 2
```

```
SP32 0 1 0

SI3 0 409400 $ repeat (alpha,n) n's from 0-409000 shakes

SP3 0 1

c

c

c

c

c        *        *        *        *        *        *        *        **

c

c                              *** Material Cards ***

c

c

c

c

c PCM materials from SSL website (density 0.7424 g/cc3)

c  PCM material

m1    1001  -0.04800786

      6000  -0.26401486

      17000 -0.2269028

      13027 -0.08

      26054 -0.0034053

      26057 -0.00127938

      29063 -0.02766

      8016  -0.05958088

      25055 -0.00217

      26056 -0.0548958

      26058 -0.00017358

      29065 -0.01234

      14000 -0.01444212

      15031 -0.00004508

      16000 -0.0000294

      24000 -0.03724

      26000 -0.13753908
```

```
      28000 -0.01813

      11023 -0.00385764

      20000 -0.0042882

      29000 -0.004

c

c #   Carbon Steel    7.84g/cc (From PSC file)

m2    6000   -0.0006

      25055 -0.0035     26054  -0.056755

      26056 -0.91493    26057  -0.021323

      26058 -0.002893

c

c #--------------- Plutonium Material 11.46g/cc (calculated in s/s 239Pu)

c 0% PuF4 - 100 % PuO2

m3    8016 -0.118025

      94238 -0.000441

      94239 -0.824647

      94240 -0.052919

      94241 -0.003528

      94242 -0.000441

c      9019  -0.000000

c

c #----------------    Air     0.001205 g/cc (PNNL compendium)

m4    6000 -0.000124 7014 -0.755268 &

      8016 -0.231781 18000 -0.012827

c

c #----------------    Plastic scintillator  0.959g/cc (Copied from PSC file)

m5    1001     5.43              $ Liquid Organic Scintillator EJ309

      6000     4.35              $ Hydrocarbon -from Eljen Website

c

c #----------------    Zircaloy-4 cladding 6.56 g/cc

c m6   8016    -0.001196  24000    -0.000997

c     26000    -0.001994  40000    -0.981858

c     50000    -0.013955
```

```
c
c #------------------     Concrete Ordinary (NIST PNNL compendium) 2.3 g/cc
c m7     1001   -0.022100   6000    -0.002484
c        8016   -0.574930   11023   -0.015208
c        12000  -0.001266   13027   -0.019953
c        14000  -0.304627   19000   -0.010045
c        20000  -0.042951   26000   -0.006435
c
c #--------------     Detector skin (aluminium) 2.7 g/cc (From PSC file)
m208  13027     1  $ Aluminum
c
c #-------------- PMT electronics 80% metals, 10% organics and
c      10% inorganics 0.3 g/cc (PSC code)
m292  1001   -0.0201605
      6000   -0.1340751   8016   -0.0459444
      13027  -0.3000000   25055  -0.0010500
      26054  -0.0170265   26056  -0.2744790
      26057  -0.0063969   26058  -0.0008679
      29063  -0.1383000   29065  -0.0617000
c
c
c                        *** Tally Cards ***
c
MODE n p
phys:n
phys:p
c
c
c
c
F14:N (1001 < 101 102 103 104 105 106 107 108 109 110 111 112 113 114 115 116) T
FC14 Scintillation neutron flux tallies in detectors
E14 2e-5 0.5 50
```

```
T14 0 400 406 400400 400406

c T14 0 3 6 9 12 15 18 21 24 27 30 33 36 39 42 45 48 51 54 57

c      60 63 66 69 72 75 78 81 84 87 90

c

c                     $ 3 shakes= 30 ns

c                     3 from Sarwar 2018, 6400 from 3He literature

c                     takes 36 shakes for Ns to get to dets

c                     Start 3 shake gate at 3 to be 'event' triggered

c

F24:N (1001 < 101 102 103 104 105 106 107 108 109 110 111 112 113 114 115 116) T

FC24 3He neutron flux tallies in detectors

E24 2e-5 50

T24 0 400 8109 400400 408109

c

c                     $ 3 shakes= 30 ns

c                       3 from Sarwar 2018, 6400 from 3He literature

c                   8109=6400 * 1.267 as per Mirion data sheet

c                   8109+36shakes (to be 'event' triggered)

c                   takes 36 shakes for Ns to get to dets

c

c

c

c

c

c                       ** Print first 50 histories print table 110 ***

print 110            $ add table 110 to minimum print-out

c

c                       *** time and nps cut cards ***

nps 1e6                  $ nps 1E6 - stop simulation after 1E6 particles

c   tme 60               $ ctme 1 - stop simulation after 1 min (60 sec)

c

c      NDP     NDM    MCT NDMP DMMP0

PRDMP 1000000 100000 1
```

```
c prints tallies every 10 histories, continues the RUNTPE file every 1000
c MCT =1 tells MCNP to write tallies for plotting
c MPLOT TALLY=14 TFC P NONORM FREQ=1000000 FILE=ALL
c                         *** Blank line terminator ***
```

End of File